INAUGURAL-DISSERTATION

zur

Erlangung der Doktorwürde

an der

Gesamtfakultät für Mathematik,
Ingenieur- und Naturwissenschaften

der

Ruprecht-Karls-Universität
Heidelberg

vorgelegt von Diplom-Mathematiker

Stefan Meggendorfer

geboren in

Waiblingen (Rems-Murr), Deutschland

Datum der mündlichen Prüfung:

.....

Multilevel Schwarz Methods for Porous Media Problems

Betreuer: **Prof. Dr. Guido Kanschat**

Abstract

In this thesis, efficient overlapping multilevel Schwarz preconditioners are used to iteratively solve H^{div}-conforming finite element discretizations of models in poroelasticity, and an innovative two-scale multilevel Schwarz method is developed for the solution of pore-scale porous media models.

The convergence of two-level Schwarz methods is rigorously proven for Biot's consolidation model, as well as a Biot-Brinkman model by utilizing the conservation property of the discretization. The numerical performance of the proposed multiplicative and hybrid two-level Schwarz methods is tested in different problem settings by covering broad ranges of the parameter regimes, showing robust results in variations of the parameters in the system that are uniform in the mesh size. For extreme parameters a scaling of the system yields robustness of the iteration counts. Optimality of the relaxation factor of the hybrid method is investigated and the performance of the multilevel methods is shown to be nearly identical to the two-level case. The additional diffusion term in the Biot-Brinkman model yields a stabilization for high permeabilities.

Additionally, a homogenizing two-scale multilevel Schwarz preconditioner is developed for the iterative solution of high-resolution computations of flow in porous media at the pore scale, i.e., a Stokes problem in a periodically perforated domain. Different homogenized operators known from the literature are used as coarse-scale operators within a multilevel Schwarz preconditioner applied to H^{div}-conforming discretizations of an extended model problem. A comparison in the numerical performance tests shows that an operator of Brinkman type with optimized effective tensor yields the best performance results in an axisymmetric configuration and a moderately anisotropic geometry of the obstacles, outperforming Darcy and Stokes as coarse-scale operators, as well as a standard multigrid method, that serves as a benchmark test.

Zusammenfassung

In dieser Arbeit werden effiziente überlappende Multilevel-Schwarz-Vorkonditionierer verwendet, um H^{div}-konforme Finite-Elemente-Diskretisierungen von Modellen der Poroelastik iterativ zu lösen, und es wird eine innovative zweiskalige Multilevel-Schwarz-Methode für die Lösung von hochauflösenden Modellen für poröse Medien auf Porenskala entwickelt.

Die Konvergenz der Zweilevel-Schwarz-Methoden wird für das Konsolidierungsmodell von Biot sowie für ein Biot-Brinkman-Modell unter Ausnutzung der Erhaltungseigenschaft der Diskretisierung rigoros nachgewiesen. Die numerische Leistungsfähigkeit der vorgeschlagenen multiplikativen und hybriden Zwei-Level-Schwarz-Methoden wird in verschiedenen Problemstellungen getestet, indem eine große Bandbreite der Parameterbereiche abgedeckt wird. Dabei zeigen sich robuste Ergebnisse bei Variationen der Parameter des Systems, die einheitlich in der Gitterweite sind. Für extrem gewählte Parameter ergibt eine Skalierung des Systems eine Robustheit der Iterationszahlen. Die Optimalität des Relaxationsfaktors der hybriden Methode wird untersucht, und es wird gezeigt, dass die Leistung der Multilevel-Methoden nahezu identisch mit der des Zweilevel-Falls ist. Der zusätzliche Diffusionsterm im Biot-Brinkman-Modell führt zu einer Stabilisierung für hohe Permeabilitäten.

Zusätzlich wird ein homogenisierender zweiskaliger Multilevel-Schwarz-Vorkonditionierer für die iterative Lösung von hochauflösenden Berechnungen der Strömung in porösen Medien auf Porenskala entwickelt, d.h. für ein Stokes-Problem in einem periodisch perforierten Gebiet. Verschiedene homogenisierte Operatoren, die aus der Literatur bekannt sind, werden als Grobskalenoperatoren innerhalb eines mehrstufigen Schwarz-Vorkonditionierers verwendet, der auf H^{div}-konforme Diskretisierungen eines erweiterten Modellproblems angewendet wird. Ein Vergleich in den numerischen Leistungstests zeigt, dass ein Operator vom Brinkman-Typ mit einem optimierten effektiven Tensor die besten Ergebnisse in einer achsensymmetrischen Konfiguration sowie einer mäßig anisotropen Geometrie der Hindernisse liefert und dabei Darcy und Stokes als grobskalige Operatoren sowie ein Standard-Mehrgitterverfahren, das als Benchmark-Test dient, übertrifft.

Acknowledgements

First and foremost, I am sincerely grateful to my supervisor, Prof. Dr. Guido Kanschat, for his continued guidance, support and inspiration throughout my doctorate. Our discussions have been invaluable to my development as a researcher and have always helped me move forward. I thank you for your outstanding expertise, your patience, your always open ear, your innovative way of teaching, and for your openness, sincerity, and kindness with the people around you.

I would like to express my appreciation to Prof. Dr. Johannes Kraus for the highly productive collaboration on the Biot chapter and for the invitations to various conferences.

Furthermore, I want to thank my friend Prof. Dr. Robert Scheichl for the many valuable conversations as well as for proofreading the introduction of this dissertation – and for sharing the passion for mathematics and the mountains.

Additionally, I would like to thank Prof. Dr. sc. Filip Sadlo for the opportunity to participate in the "Visual Computing Group" within the "Waves to Weather" project of the DFG SFB-TRR 165.

I am also thankful to Prof. Dr. Vincent Heuveline for reviewing my thesis.

I am grateful to have met Prof. Dr. Andro Mikelić and learned about homogenization from him in a collaboration on a nonlinear consolidation model of Biot. His personality and expertise have left a lasting impression on me.

I would like to thank the members of the "Mathematical Methods of Simulation" group at the IWR for the pleasant working environment over the years. Especially, I would like to thank Dr. Daniel Arndt for his extensive support in deal.II, and my former roommates Dr. Pablo Lucero-Lorca and Dr. Julius Witte for all the fruitful discussions about C++ and multilevel Schwarz theory. I would also like to thank Felicitas Hirsch for her competent assistance with all formal matters at the university and Manfred Trunk for his reliable support as the system administrator. Furthermore, I am grateful to Freya Bretz, Dr. Andreas Rupp, Dr. Noman Shakir and the members of the neighboring groups at the IWR for many enjoyable coffee breaks and lunchtime conversations.

I would also like to acknowledge the development work of the Scientific Software Center of Heidelberg University, in particular Dr. Dominic Kempf, for his help in parallelizing

parts of the parameter studies.

Special thanks to Richa Shaunak for proofreading the text and making valuable suggestions.

Finally, I would like to thank my family and all my dear friends for their love and constant support.

Contents

Chapter 1

Introduction

In this thesis, we will use efficient multilevel Schwarz preconditioners to solve conservative finite element discretizations of equations in poroelasticity and develop innovative Schwarz methods for pore-scale porous media models.

1.1 Motivation and Perspective

Porous media models have wide-ranging applications in various fields such as groundwater hydrology, petroleum engineering, environmental science, and biomedicine. The models describe fluid flow through porous materials using partial differential equations, and are essential for understanding and predicting complex physical processes that occur in natural and engineered systems. In recent years, there has been growing interest in developing accurate and efficient numerical methods, including preconditioning techniques, for solving conservative finite element discretizations of porous media models in different application domains.

For instance, in groundwater hydrology, these models are used to study groundwater flow, contaminant transport, and remediation strategies for protecting water resources and managing environmental pollution [SWZY23]. In petroleum engineering, porous media models are used to simulate fluid flow and transport in oil and gas reservoirs for optimal reservoir management and enhanced oil recovery strategies [DTDPP16]. In environmental science, porous media models are used to simulate pollutant transport in soils and aquifers, and to assess the impact of human activities on the environment [Bru94].

In biomedicine, porous media models are increasingly used to model organic tissues for better understanding of tissue behavior, disease progression, and treatment planning. For example, porous media models have been developed to simulate osmotic swelling of brain cells due to fluid absorption [Mal15], drug distribution in the vitreous body of the

human eye [DFS17], and the growth of tumors [FC18].

Since analytical solutions are often limited to simple settings, numerical simulations are typically required for most applications in porous media. Conservative finite element discretizations have gained popularity due to their accuracy in capturing complex multiphysics phenomena [KR10, KR18, HK18, HKLP19, GRH$^+$19, HKK$^+$22, LY22, WCWZ22]. However, these discretizations result in large and ill-conditioned linear systems of equations, which are challenging to solve efficiently and robustly.

To address this challenge, preconditioning of linear systems is commonly employed to improve the condition of the system matrix and enhance the convergence of iterative solvers. Various preconditioning strategies have been proposed for porous media models, but there is ongoing research and development to further improve their effectiveness, particularly for conservative finite element discretizations.

In this thesis, we focus on developing preconditioning techniques for conservative finite element discretizations of porous media models. The proposed research aims to investigate and develop overlapping two-level and multilevel Schwarz methods for H^{div}-conforming discretizations of Biot's consolidation model and the Biot-Brinkman model, as well as a two-scale multilevel Schwarz method as a preconditioner for highly resolved computations of flow in porous media. The convergence of the proposed methods will be rigorously proven, and their robustness will be investigated through extensive numerical experiments.

To be precise, we examine overlapping two-level and multilevel Schwarz preconditioning methods for the following three distinct sets of equations that describe different physical properties of the porous medium under consideration, which are modeled at different observation length and time scales. Through the analysis of these equations, our objective is to develop more efficient numerical methods for simulating these processes, which will facilitate a comprehensive understanding of the complex physical phenomena occurring within the porous medium.

The first set of equations is Biot's quasi-static model of consolidation [Bio41], which describes the seepage flow of a viscous fluid through an elastic solid porous structure. It is the prototypical example of linear poroelasticity and it couples on a macroscopic length scale the deformation $\boldsymbol{u}$ of the elastic solid matrix via the pressure p with the

seepage velocity $\boldsymbol{v}$ in a continuum-mechanical approach at constant temperature by

$$\begin{aligned} -\operatorname{div}(2\mu\boldsymbol{\varepsilon}(\boldsymbol{u}) + \lambda \operatorname{div}(\boldsymbol{u})\boldsymbol{I}) + \alpha\nabla p &= \boldsymbol{f} && \text{in } \Omega \times (0,T), \\ \boldsymbol{v} + \boldsymbol{K}\nabla p &= \boldsymbol{0} && \text{in } \Omega \times (0,T), \\ -\alpha \operatorname{div} \partial_t \boldsymbol{u} - \operatorname{div} \boldsymbol{v} - c_s \partial_t p &= g && \text{in } \Omega \times (0,T), \end{aligned}$$

where Ω denotes the porous reservoir and $(0,T)$ the time interval. We will apply the theory of overlapping two-level Schwarz methods as proposed by [TW10] to these equations and test its performance also in a multilevel setup.

The second one is a quasi-static Biot-Brinkman model [HKK+22], which follows the same continuum-mechanical approach on a macroscopic observational length scale as Biot's consolidation model by coupling the deformation $\boldsymbol{u}$, the pressure p and the seepage velocity $\boldsymbol{v}$. But instead of Darcy's law [Dar56], a diffusion term is added to the equations of the fluid flow as suggested by Brinkman [Bri49]. The model is given by

$$\begin{aligned} -\operatorname{div}(2\mu\boldsymbol{\varepsilon}(\boldsymbol{u}) + \lambda \operatorname{div} \boldsymbol{u}) + \alpha\nabla p &= \boldsymbol{f} && \text{in } \Omega \times (0,T), \\ -\nu\Delta\boldsymbol{v} + \boldsymbol{K}^{-1}\boldsymbol{v} + \nabla p &= \boldsymbol{0} && \text{in } \Omega \times (0,T), \\ -\alpha \operatorname{div} \partial_t \boldsymbol{u} - \operatorname{div} \boldsymbol{v} - c_s \partial_t p &= g && \text{in } \Omega \times (0,T). \end{aligned}$$

While Darcy's law is widely accepted, there is still ongoing discussion about the validity of the Brinkman equations. Especially in the context of poroelasticity, the Biot-Brinkman model is rather new and has not been derived mathematically, yet. But it has potential in modeling highly permeable porous media as it stabilizes the simulations in these cases, which will be observed in the calculations later on.

The last one is the steady Stokes system on a perforated fluid domain Ω^ε modeling the fully resolved fluid flow through a non-deformable porous medium at pore scale by the equations

$$\begin{aligned} -\mu\Delta\boldsymbol{v}^\varepsilon + \nabla p^\varepsilon &= \boldsymbol{f} && \text{in } \Omega^\varepsilon, \\ \operatorname{div} \boldsymbol{v}^\varepsilon &= 0 && \text{in } \Omega^\varepsilon. \end{aligned}$$

The domain Ω^ε is arranged by periodically repeated standard periodicity cells Y_i^ε of size ε containing solid obstacles. We aim to determine the fluid velocity $\boldsymbol{v}^\varepsilon$ and the pressure p^ε on a microscopic length scale. To solve the equations, we extend the work of [Neu96, NJW01] and develop a two-scale multilevel Schwarz preconditioner based on

homogenized coarse scale operators for this model problem.

1.2 Scientific Contribution and Outline

In this section, we provide an overview of the structure of this thesis and explain the author's scientific contributions.

Parts of the work were funded by the German Science Foundation (DFG) within the Transregional Collaborative Research Center SFB/TRR 165 "Waves to Weather", resulting in a publication about an energy-based visualization approach for time-dependent 2D flow fields. The results have been published in [HMH+19].

As part of the research presented in this work, the author has also contributed code to the C++-based finite element software library DEAL.II [ABF+22].

The structure of this thesis is as follows.

Chapter 2 forms the theoretical basis of this dissertation. Specifically, the algorithms and theory of iterative solvers and Schwarz preconditioners for conservative finite element discretizations are introduced, on which the analysis of the later chapters builds. As a preliminary chapter, it introduces the notation and recapitulates existing results from the literature only, while no new results by the author are presented.

In Chapter 3, the two-level Schwarz method is applied to the case of H^{div}-conforming finite element discretizations of Biot's consolidation model in a three-field formulation, scaled such that only three physical parameters are present in the system. These famous equations by Biot model a large variety of poroelastic materials, from saturated porous rocks to organic tissue.

A major contribution of the author is the proof of a stable decomposition (Theorem 3.11) in Section 3.4.3 for overlapping multiplicative and additive two-level Schwarz methods applied to the Biot model. For the proof, the system is first transformed into an equivalent, symmetric and positive definite, singularly perturbed two-field formulation, for which the abstract convergence theory introduced in Chapter 2 applies. A special decomposition of the underlying function spaces with respect to the kernel of the divergence operator then yields the proof of the stable decomposition. Due to the robustness in the perturbation parameter, the convergence proof finally follows by establishing local stability and a strengthened Cauchy-Schwarz inequality. While the proof is formulated in 2D only, we point out that most of the argumentation holds true in 3D as well. The relevant parts, which require separate consideration, are elaborated in the course of the

section.

To confirm the validity of the theoretical analysis, numerical experiments are presented for a test case with homogeneous boundary values and isotropic constant permeabilities in Section 3.5.2, showing the robust performance of the methods in the model parameters and its uniformity in the mesh size. The discretizations under consideration are mixed, equal-order Raviart-Thomas finite elements with matching pressure space, such that the discretization is H^{div}-conforming and therefore mass-conservative. Different polynomial degrees are considered and discussed, where a main focus is on finite elements of second order ($k = 2$) as well as on lowest order ($k = 0$).

The multiplicative two-level Schwarz method yields better performance results than the hybrid method in all calculations. The methods are robust in the ratio $\frac{\lambda}{\mu}$ of the Lamé constants, even in the nearly incompressible case $\lambda \gg \mu$, as well as in the scaled specific storage coefficient. The dependence of the convergence proof on the inverse of the scaled permeability tensor can only be slightly observed in the experiments and does not restrict the applicability of the two-level Schwarz methods. Numerical instabilities originating in extremely large chosen parameters are remedied by the use of a scaling of the system matrix so that the parameters stay in reasonable ranges. In the lowest order case, an additional equalization of the system matrix, in the form of another scaling with respect to the mesh size, is necessary to obtain uniformity with a refinement of the mesh. The resulting methods then appear to be robust.

In addition to the experiments with homogeneous boundary conditions, tests are also performed for the case of mixed Dirichlet-Neumann boundary conditions in Section 3.5.3. A short discussion about the choice of the set of patches shows that patches on the boundary need to be included for this test configuration. But whereas for the multiplicative method patches containing only one cell can be excluded from the set of patches, the performance of the hybrid method benefits considerably when these are included.

The performance of the method depends in this test case on the permeability rather than on its inverse. Using a scaling as for the homogeneous case yields robustness also for very high permeabilities. In addition, the performance in the remaining parameters is comparable to that of the first test case.

In Section 3.5.4 we discuss the optimal choice of the relaxation factor for the hybrid two-level Schwarz method. As it turns out, it only needs to compensate for the effect of adding the overlapping patches, such that a choice of approximately 0.25 yields the best

results.

The efficiency of the two-level methods translates also to the multilevel Schwarz methods as presented in Section 3.5.5. Although the coarse space solve is relaxed, the performance results are nearly the same as in the two-level case. The number of iterations GMRES takes to converge when preconditioned with the hybrid multilevel Schwarz method can be reduced by additional smoothing steps. An additional pre-smoothing in case of the multiplicative method does not lead to a further reduction of the iteration counts, demonstrating the already very good performance of the multiplicative algorithm.

In Chapter 4, mass conservative finite element discretizations of the Biot-Brinkman equations are considered, where an additional diffusion term stabilizes Biot's consolidation model for highly permeable material settings. To prove convergence of the two-level Schwarz methods, the ideas from Chapter 3 are extended to the current case, yielding similar dependencies of the constants in the proof of the stable decomposition with an additional dependence on the viscosity coefficient. In the numerical experiments of Section 4.3.1, the additional diffusion term yields a stabilization of the iteration counts when the reciprocal κ^{-1} of the permeability constant is varied, especially for the case of high permeabilities in a channel-flow example, whereas the method also stays robust for all other considered parameter ranges. Numerical instabilities due to extremely large values of the Lamé parameter λ from elasticity, originating in the squaring of the diagonal entries of the system matrix within GMRES, can be handled by a scaling of the system, leading to an overall robust scheme in the practical application of the method.

In Chapter 5, a homogenizing two-scale multilevel Schwarz preconditioner is developed and applied to a fully resolved pore-scale porous media flow model, i.e., a laminar Stokes flow through a periodically perforated domain. The model problem is extended to the entire domain by using a Brinkman law and then discretized by an H^{div}-conforming mixed finite element method. To derive an efficient preconditioner, homogenized operators known from the literature and discretized with the same type of finite element method as the extended Stokes equations are used as coarse-scale operators within a multilevel Schwarz method on levels where the structure of the perforated domain cannot be resolved anymore by the mesh.

First performance tests with the analytical homogenized operators show the necessity of optimizing the effective tensors of the homogenized Brinkman and Darcy operators with respect to the iteration counts of GMRES. Scanning the parameter spaces yields a

dependence of the Brinkman operator on the penalty constant of the extension. It turns out that a homogenized Brinkman law as coarse-scale operator with optimized effective tensor yields the best convergence results of GMRES, outperforming the homogenized and optimized Darcy operator as well as the standard multigrid method. Another optimization of the Brinkman operator with respect to the geometry of the obstacles by combining the knowledge of a homogenized Darcy operator, derived by the two-scale convergence method, with the optimization process developed for the Brinkman operator yields the best results for moderately anisotropic geometries.

Finally, Chapter 6 offers an outlook on the potential of preconditioning fully resolved poroelastic media computations using Biot's nonlinear equations of poroelasticity at finite strain. Specifically, we propose a two-scale multilevel Schwarz preconditioner that leverages Biot's linear consolidation model or the Biot-Brinkman model as homogenized coarse-scale operator. In addition, Section 6.2 briefly discusses the imposition of strong or weak interface conditions inside the domain to extend a physical phase accurately to an extended (virtual) region. We provide examples for Stokes flow, linear elasticity, and a fluid structure interaction problem. A summary of the topics covered concludes this thesis in Section 6.3.

Chapter 2

Theoretical Foundations

This chapter serves as an introduction to iterative solvers for linear systems of equations, and the two-level and multilevel Schwarz methods to be used as preconditioners for finite element discretizations of partial differential equations. In addition to the algorithms, the abstract theory for the two-level Schwarz methods for H^{div}-conforming finite element discretization spaces is presented, which will build the foundation of the convergence results later in this thesis. In this chapter, only existing results from the literature are recapitulated and no new results by the author are presented.

Section 2.1 begins with notation and the basic theory of functional analysis. Divergence-conforming finite element spaces and their matching pressure spaces are introduced in Section 2.2. Iterative algorithms and their convergence theorems are introduced in Section 2.3, focusing on Krylov subspace solvers. The two-level Schwarz method as a domain decomposition approach for preconditioning systems of equations arising from finite element discretizations of partial differential equations are presented in Section 2.4. Here, the abstract framework is first introduced and then the theory for overlapping decompositions of H^{div}-conforming discretizations is specified. The Chapter ends with an extension to multilevel algorithms, i.e., the classical multigrid method with domain decomposition smoothers.

2.1 Notation and Function Spaces

We start with some remarks on notation and introduce basic concepts of differential calculus and functional analysis as far as they are necessary for the analysis in this work. Especially, we introduce the notation of Lebesgue and Sobolev spaces. All results of this section are standard and can be studied in every common introduction to functional analysis, see for example [Alt06, Dob10, Eva10].

2.1.1 Basic Notation

The set of integers $\{0, 1, 2, ...\}$ is denoted by $\mathbb{N}$ and the set of real numbers by $\mathbb{R}$. The absolute value for real numbers a is given by $|a|$. On the n-dimensional Euclidean vector space $\mathbb{R}^n$ the dot product $\boldsymbol{a} \cdot \boldsymbol{b} = \sum_{i=1}^n a_i b_i$ defines an inner product $(\boldsymbol{a}, \boldsymbol{b}) = \boldsymbol{a} \cdot \boldsymbol{b}$, and a norm is given by the 2-norm $\|\boldsymbol{a}\|_2 = (\boldsymbol{a}, \boldsymbol{a})^{1/2}$. Obviously, the 2-norm is equal to the absolute value in one dimension. Whenever we have vector valued quantities we will use boldface letters, and otherwise normal letters. For vectors $\boldsymbol{v} = (v_1, \dots, v_n) \in \mathbb{R}^n$ and matrices $\boldsymbol{A} \in \mathbb{R}^{n \times n}$ we occasionally use the notation $(v_i)_{i=1}^n$ and $(A_{ij})_{i,j=1}^n$ to specify entries. The transpose of a matrix $\boldsymbol{A} \in \mathbb{R}^{m \times n}$ is denoted by $\boldsymbol{A}^T \in \mathbb{R}^{n \times m}$. In definitions of operators and bilinear forms we will sometimes use the operator $\forall$ as abbreviation of the phrase "for all". We will use c and C as generic positive and real constants that might differ in estimates from line to line. If a constant c depends on some given quantity q we mark this by c_q. Further, the usual definition for the Landau symbols o and O is used to describe asymptotic growth, i.e., for functions $f, g \colon X \subset \mathbb{R} \to \mathbb{R}$ it holds $f = o(g)$, if and only if $\lim_{x \to a} \left| \frac{f(x)}{g(x)} \right| = 0$, and it holds $f = O(g)$, if and only if $\limsup_{x \to a} \left| \frac{f(x)}{g(x)} \right| < \infty$, where $a \in \mathbb{R} \cup \{-\infty, \infty\}$.

2.1.2 Differential Calculus

Next, we introduce the notation of differential calculus. Therefore, we assume that $\Omega \subset \mathbb{R}^d$, $d \in \{2, 3\}$, is an open and bounded set with Lipschitz boundary $\partial\Omega$ and outer unit normal vector $\boldsymbol{n}$. Let $f : \Omega \to \mathbb{R}$ be a scalar function and $\boldsymbol{g} = (g_1, \dots, g_d) : \Omega \to \mathbb{R}^d$ be a vector valued function. The gradient is defined in terms of the nabla operator

$$\nabla f = (\partial_1 f, \dots, \partial_d f), \qquad \nabla \boldsymbol{g} = (\partial_j g_i)_{i,j=1}^d,$$

where the partial derivatives of f at a given point $\boldsymbol{x} \in \Omega$ are given by

$$\partial_i f(\boldsymbol{x}) = \frac{\partial f(\boldsymbol{x})}{\partial x_i} = \lim_{h \to 0} \frac{f(\boldsymbol{x} + h\boldsymbol{e}_i) - f(\boldsymbol{x})}{h}. \tag{2.1}$$

Here, $\boldsymbol{e}_i$ is the i-th canonical unit-vector of $\mathbb{R}^d$. A function is called continuously differentiable, if the limit in (2.1) exists for every $i = 1, ..., d$. Derivatives of higher order are defined with the help of multi-indices $\alpha = (\alpha_1, ..., \alpha_m) \in \mathbb{N}^m$ of order $|\alpha| = \alpha_1 + ... + \alpha_m$

by

$$\partial^\alpha f = \partial_1^{\alpha_1} \cdots \partial_d^{\alpha_d} f.$$

Furthermore, ∇^k denotes the tensor of all partial derivatives of order $k \in \mathbb{N}$. We define the divergence of a vector field by

$$\operatorname{div} \boldsymbol{g} = \nabla \cdot \boldsymbol{g} = \sum_{i=1}^{d} \partial_i g_i.$$

For matrix valued functions $\boldsymbol{F} : \Omega \to \mathbb{R}^{d\times d}$ the divergence is defined column wise as

$$\operatorname{div} \boldsymbol{F} = \nabla \cdot \boldsymbol{F} = \left(\sum_{j=1}^{d} F_i \right)_{i=1}^{d}.$$

By combination of divergence and gradient one gets the Laplacian

$$\Delta f = \operatorname{div} \nabla f = \sum_{i=1}^{d} \partial_i^2 f, \qquad \Delta \boldsymbol{g} = \operatorname{div} \nabla \boldsymbol{g} = \left(\sum_{j=1}^{d} \partial_j^2 g_i \right)_{i=1}^{d},$$

that describes, for example, diffusion processes like fluid flow or heat. The curl operator, describing the rotation of a vector field $\boldsymbol{g} : \Omega \subset \mathbb{R}^3 \to \mathbb{R}^3$, is defined via the cross product in three space dimensions, i.e.,

$$\mathbf{curl}\, \boldsymbol{g} = \nabla \times \boldsymbol{g} = \left(\partial_2 g_3 - \partial_3 g_2, \partial_3 g_1 - \partial_1 g_3, \partial_1 g_2 - \partial_2 g_1\right). \tag{2.2}$$

In two space dimensions $\Omega \subset \mathbb{R}^2$ the curl operator is defined for scalar functions $f : \Omega \to \mathbb{R}$ by

$$\mathbf{curl}\, f = (\partial_2 f, -\partial_1 f), \tag{2.3}$$

and for vector valued functions $\boldsymbol{g} : \Omega \to \mathbb{R}^2$ by

$$\operatorname{curl} \boldsymbol{g} = \partial_1 \boldsymbol{g}_2 - \partial_2 \boldsymbol{g}_1. \tag{2.4}$$

2.1.3 Function Spaces

Having the definitions of the differential operators at hand, we come to the introduction of the most important function spaces for continuous functions as well as Lebesgue-measurable functions.

By $C^m(\bar{\Omega})$ we denote the function space of continuous functions on the closure $\bar{\Omega} = \Omega \cup \partial\Omega$ that are continuously differentiable up to the order $|\alpha| \leq m$, and by $C_0^\infty(\Omega)$ the space of infinitely differentiable functions with compact support in Ω. The latter plays a central role in the definition and approximability of Lebesgue and Sobolev spaces. $C^m(\bar{\Omega})$ becomes a Banach space by defining the norm

$$\|f\|_{C^m(\bar{\Omega})} = \sum_{|\alpha|\leq m} \sup_{\boldsymbol{x}\in\bar{\Omega}} |\partial^\alpha f(\boldsymbol{x})|.$$

Further,

$$(f,g)_\Omega = (f,g)_{L^2(\Omega)} = \int_\Omega f(\boldsymbol{x}) \cdot g(\boldsymbol{x})\, d\boldsymbol{x}$$

defines an inner product on the usual Hilbert space $L^2(\Omega)$ consisting of all Lebesgue measurable and square integrable functions $f : \Omega \to \mathbb{R}$, for which the graph norm

$$\|f\|_\Omega = \|f\|_{L^2(\Omega)} = \sqrt{(f,f)_\Omega}$$

is bounded, i.e., $\|f\|_\Omega < \infty$. The set of Lebesgue measurable functions consists of equivalence classes, since its functions are defined only up to subsets $Z \subset \Omega$ with zero Lebesgue measure $|Z| = \int_Z dx = 0$. Additionally, we define the space $L_0^2(\Omega)$ of mean-value free functions in $L^2(\Omega)$ by

$$L_0^2(\Omega) = \left\{ f \in L^2(\Omega) \ : \ \int_\Omega f(\boldsymbol{x})\, d\boldsymbol{x} = 0 \right\}.$$

Furthermore, let $L^\infty(\Omega)$ be the Lebesgue space of measurable functions for which $\|f\|_{L^\infty(\Omega)} < \infty$, where

$$\|f\|_{L^\infty(\Omega)} = \inf_{|Z|=0} \sup_{\boldsymbol{x}\in\Omega\setminus Z} |f(\boldsymbol{x})|.$$

The space of Lebesgue-measurable and square-integrable functions $f : (a, b) \to Y$ mapping from an open interval $(a, b) \subset \mathbb{R}$ to a Banach space Y with norm $\|\cdot\|_Y$ is denoted by $L^2(a, b; Y)$ and its norm is defined by

$$\|f\|_{L^2(a,b;Y)} = \left(\int_a^b \|f\|_Y^2 \, d\boldsymbol{x} \right)^{\frac{1}{2}}.$$

Beneath the gradient for continuously differentiable functions we introduce the weak gradient $\partial^\alpha f$ of order $|\alpha|$, where α again is a multi-index, to allow for a definition of differentiability of locally Lebesgue measurable functions f. Its definition is motivated by the formula for partial integration and given by $\partial^\alpha f = g$, if there exists a function g such that for all $\varphi \in C_0^\infty(\Omega)$

$$\int_\Omega f(\boldsymbol{x}) \partial^\alpha \varphi(\boldsymbol{x}) \, d\boldsymbol{x} = (-1)^\alpha \int_\Omega g(\boldsymbol{x}) \varphi(\boldsymbol{x}) \, d\boldsymbol{x}.$$

With the definition of weak gradients we are able to introduce the Sobolev space

$$H^m(\Omega) = \left\{ f \in L^2(\Omega) \, : \, \partial^\alpha f \in L^2(\Omega) \text{ for all } |\alpha| \leq m \right\},$$

with norm

$$\|f\|_{H^m(\Omega)} = \left(\sum_{|\alpha| \leq m} \|\partial^\alpha f\|_\Omega^2 \right)^{\frac{1}{2}},$$

and semi-norm

$$|f|_{H^m(\Omega)} = \left(\sum_{|\alpha| = m} \|\partial^\alpha f\|_\Omega^2 \right)^{\frac{1}{2}}.$$

On $H^m(\Omega)$ an inner product is given by

$$(f, g)_{H^m(\Omega)} = \sum_{k=0}^{m} (\nabla^k f, \nabla^k g)_\Omega.$$

Every function in the space $H^m(\Omega)$ can be approximated by continuous functions, since $C^\infty(\Omega) \cap H^m(\Omega)$ is dense in $H^m(\Omega)$. Furthermore, the space $H_0^m(\Omega)$ is defined as the

closure of $C_0^\infty(\Omega)$ with respect to the norm $\|\cdot\|_{H^m(\Omega)}$. For functions in the Sobolev spaces $H^m(\Omega)$ a trace operator $\mathrm{tr} : H^m(\Omega) \to L^2(\partial\Omega)$ can be defined as the restriction

$$\mathrm{tr}\, u = u\big|_{\partial\Omega},$$

which is linear and bounded, and thus

$$\big\|\mathrm{tr}\, u\big\|_{\partial\Omega} \leq \big\|u\big\|_{H^m(\Omega)}.$$

On $H_0^1(\Omega)$ norm and inner product are given by

$$\big\|f\big\|_{H_0^1(\Omega)} = \big\|\nabla f\big\|_\Omega$$

and

$$\big(f, g\big)_{H_0^1(\Omega)} = \big(\nabla f, \nabla g\big)_\Omega,$$

respectively. With the help of the trace operator the space $H_0^1(\Omega)$ can be identified with the space of H^1-functions with zero boundary-values.

Product spaces $X \times ... \times X$ consisting of the same space X, i.e. vector-valued spaces, are denoted by X^n or $[X]^n$, for example

$$[L^2(\Omega)]^2 = L^2(\Omega) \times L^2(\Omega), \qquad [H_0^1(\Omega)]^3 = H_0^1(\Omega) \times H_0^1(\Omega) \times H_0^1(\Omega).$$

Since the norms and inner products of Lebesgue and Sobolev spaces are defined via the dot product, we can simply inherit the norms from the one dimensional case. With this notation, the vector-valued space $H^{\mathrm{div}}(\Omega)$ is defined by

$$H^{\mathrm{div}}(\Omega) = \Big\{\boldsymbol{g} \in [L^2(\Omega)]^d \ : \ \mathrm{div}\, \boldsymbol{g} \in L^2(\Omega)\Big\},$$

and the subspace $H_0^{\mathrm{div}}(\Omega)$ with vanishing normal component by

$$H_0^{\mathrm{div}}(\Omega) = \Big\{\boldsymbol{g} \in H^{\mathrm{div}}(\Omega) \ : \ \boldsymbol{g} \cdot \boldsymbol{n} = 0 \text{ on } \partial\Omega\Big\}.$$

Norm $\|\cdot\|_{H^{\mathrm{div}}(\Omega)}$, semi-norm $|\cdot|_{H^{\mathrm{div}}(\Omega)}$ and inner product $(\cdot,\cdot)_{H^{\mathrm{div}}(\Omega)}$ for functions in

$H^{\mathrm{div}}(\Omega)$ are given by

$$\begin{aligned}\|\boldsymbol{g}\|_{H^{\mathrm{div}}(\Omega)} &= \left(\|\boldsymbol{g}\|_{\Omega}^2 + \|\operatorname{div}\boldsymbol{g}\|_{\Omega}^2\right)^{\frac{1}{2}},\\ |\boldsymbol{g}|_{H^{\mathrm{div}}(\Omega)} &= \|\operatorname{div}\boldsymbol{g}\|_{\Omega},\end{aligned}$$

and

$$(\boldsymbol{f},\boldsymbol{g})_{H^{\mathrm{div}}(\Omega)} = (\boldsymbol{f},\boldsymbol{g})_{\Omega} + (\operatorname{div}\boldsymbol{f},\operatorname{div}\boldsymbol{g})_{\Omega}.$$

In line with the definition of the curl operator for two- or three-dimensional vector valued functions in (2.2) and (2.3), respectively, as well as for two-dimensional scalar functions in (2.4), the space $H^{\mathrm{curl}}(\Omega)$ consists of all Lebesgue-measurable and square integrable functions with Lebesgue-measurable and square integrable curl operator. For functions in $H^{\mathrm{curl}}(\Omega)$, norm, semi-norm and inner product are defined by

$$\begin{aligned}\|\boldsymbol{g}\|_{H^{\mathrm{curl}}(\Omega)} &= \left(\|\boldsymbol{g}\|_{\Omega}^2 + \|\mathbf{curl}\,\boldsymbol{g}\|_{\Omega}^2\right)^{\frac{1}{2}},\\ |\boldsymbol{g}|_{H^{\mathrm{curl}}(\Omega)} &= \|\mathbf{curl}\,\boldsymbol{g}\|_{\Omega},\end{aligned}$$

and

$$(\boldsymbol{f},\boldsymbol{g})_{H^{\mathrm{curl}}(\Omega)} = (\boldsymbol{f},\boldsymbol{g})_{\Omega} + (\mathbf{curl}\,\boldsymbol{f},\mathbf{curl}\,\boldsymbol{g})_{\Omega},$$

where $\boldsymbol{f}$ and $\boldsymbol{g}$ this time stand for vector valued, as well as for scalar functions to generalize the definition. Further, let $\boldsymbol{t}$ be the unit tangent vector on the boundary $\partial\Omega$, for example, in 2D it is given by $\boldsymbol{t} = (-n_2, n_1)$. Then, the tangential component $\boldsymbol{g}_t = \boldsymbol{g}\cdot\boldsymbol{t}$ of a vector $\boldsymbol{g}$ is

$$\boldsymbol{g}_t = \begin{cases}\boldsymbol{n}\times\boldsymbol{g}, & \text{for } d=2,\\ \boldsymbol{g}-(\boldsymbol{g}\cdot\boldsymbol{n})\boldsymbol{n} = (\boldsymbol{n}\times\boldsymbol{g})\times\boldsymbol{n}, & \text{for } d=3.\end{cases}$$

The subspace of $H^{\mathrm{curl}}(\Omega)$ with vanishing tangential component on $\partial\Omega$ is denoted by $H_0^{\mathrm{curl}}(\Omega)$.

Remark 2.1. *In 2D we have a strong relation between the spaces $H^{\mathrm{curl}}(\Omega)$ and $H^{\mathrm{div}}(\Omega)$, since a vector $\boldsymbol{u} = (u_1, u_2)$ belongs to $H^{\mathrm{curl}}(\Omega)$, if and only if the vector $\boldsymbol{v} = (-u_2, u_1)$*

belongs to $H^{\mathrm{div}}(\Omega)$, see [TW10, Lemma A.20].

2.2 H^{div}-conforming Finite Element Methods

This section serves as introduction to finite element spaces, and especially to mixed finite elements with H^{div}-conforming spaces $V_h \subset H^{\mathrm{div}}(\Omega)$ and their matching pressure spaces $Q_h \subset L^2(\Omega)$, such that

$$\operatorname{div} V_h = Q_h. \tag{2.5}$$

The presentation will be restricted to Raviart-Thomas finite element spaces [RT77, Ned80, Ned86] on rectangular and hexahedral cells, and we will mainly follow [FB91, Chapter III] for this matter. The definitions of other H^{div}-conforming finite element spaces such as the Raviart-Thomas elements on triangles and tetrahedra, as well as the Brezzi-Douglas-Marini elements BDM_k [BDM85], and the Brezzi-Douglas-Fortin-Marini elements $BDFM_{k+1}$ [BDFM87] can also be found in [FB91, Chapter III]. Moreover, the ABF_k finite element space is introduced in [ABF02], and a compilation of all these spaces with its matching pressure spaces for triangles/tetrahedra as well as for quadrilaterals/hexahedra can be found in [KR10, Table 1].

The benefit of combinations of spaces as in (2.5) is the accurate integration of the mass balance equation in discretizations of Stokes- or Darcy-like systems such as

$$\begin{aligned} \boldsymbol{L}(\boldsymbol{u}) + \nabla p &= \boldsymbol{f}, \qquad \text{in } \Omega, \\ \operatorname{div} \boldsymbol{u} + \gamma p &= g, \qquad \text{in } \Omega, \end{aligned} \tag{2.6}$$

where $\boldsymbol{L}(\boldsymbol{u}) = -\Delta \boldsymbol{u}$ or $\boldsymbol{L}(\boldsymbol{u}) = \boldsymbol{u}$, $\gamma \geq 0$. With a proper definition of the bilinear form $a_h(\cdot,\cdot)$ (see for example Chapter 4) the mixed finite element discretization of system (2.6) regarding the space $V_h \times Q_h$ chosen as in (2.5) reads

$$\begin{aligned} a_h(\boldsymbol{u}_h, \boldsymbol{\varphi}) + \big(p_h, \operatorname{div} \boldsymbol{\varphi}\big)_\Omega &= \big(\boldsymbol{f}, \boldsymbol{\varphi}\big)_\Omega \qquad \forall \boldsymbol{\varphi} \in V_h, \\ \big(q, \operatorname{div} \boldsymbol{u}_h\big)_\Omega + \big(\gamma p_h, q\big)_\Omega &= \big(g, q\big)_\Omega \qquad \forall q \in Q_h, \end{aligned} \tag{2.7}$$

where

$$\operatorname{div} \boldsymbol{u}_h + \gamma p_h = g_h \tag{2.8}$$

is fulfilled point-wise, provided g_h is chosen adequately as element of Q_h. Thus, (2.8) becomes an algebraic constraint of the discretized first equation of (2.7). With this approach parameter-robust and locking-free discretizations can be obtained for Darcy (by construction), as well as for Stokes, nearly incompressible elasticity, and poroelasticity, see for example [CKS06, HKXZ15, KR18, HKLP19].

Let the computational domain $\Omega \subset \mathbb{R}^d$, $d \in \{2, 3\}$, be an open, bounded and convex set with Lipschitz-boundary $\partial\Omega$ and outer unit normal vector $\boldsymbol{n}$. Let further $\mathcal{T}_h$ be a family of shape regular triangulations of Ω into closed quadrilateral or hexaedral mesh cells $T \in \mathcal{T}_h$ with diameter $h_T = \mathrm{diam}(T)$, where $h = \max_{T\in\mathcal{T}_h} h_T$ denotes the mesh size. Each cell T is obtained by an affine transformation $\Psi_T : \widehat{T} \to T$ from the reference cell $\widehat{T} = [0, 1]^d$. On $\widehat{T}$ the space of all polynomials of degree not larger than $k \in \mathbb{N}$ is denoted by $\widehat{P}_k(\widehat{T})$. Further, the space of polynomials of degree not larger than k_i in $\boldsymbol{x}_i$ for $1 \le i \le d$ is defined by

$$\widehat{P}_{k_1,\dots,k_d}(\widehat{T}) = \Big\{ p : \widehat{T} \to \mathbb{R} \ : \ p(\boldsymbol{x}_1, \dots, \boldsymbol{x}_d) = \sum_{i_1 \le k_1, \dots, i_d \le k_d} a_{i_1 \cdots i_d} \boldsymbol{x}_1^{i_1} \cdots \boldsymbol{x}_d^{i_d} \Big\}.$$

Let

$$\widehat{Q}_k(\widehat{T}) = \begin{cases} \widehat{P}_{k,k}(\widehat{T}), & \text{for } d = 2, \\ \widehat{P}_{k,k,k}(\widehat{T}), & \text{for } d = 3, \end{cases}$$

then the space of H^{div}-conforming Raviart-Thomas functions on the reference cell is defined by

$$\widehat{RT}_k(\widehat{T}) = [\widehat{Q}_k(\widehat{T})]^d + \boldsymbol{x}\widehat{Q}_k(\widehat{T}),$$

which is equivalent to

$$\widehat{RT}_k(\widehat{T}) = \begin{cases} \widehat{P}_{k+1,k}(\widehat{T}) \times \widehat{P}_{k,k+1}(\widehat{T}) & \text{for } d = 2, \\ \widehat{P}_{k+1,k,k}(\widehat{T}) \times \widehat{P}_{k,k+1,k}(\widehat{T}) \times \widehat{P}_{k,k,k+1}(\widehat{T}) & \text{for } d = 3. \end{cases}$$

With the help of the mapping Ψ_T the polynomial spaces $P_k(T)$, $Q_k(T)$, and $RT_k(T)$ on a cell $T = \Psi_T(\widehat{T})$ are now obtained by a change of variables using a Piola transformation [FB91, eq. III.1.45]. See also [AFW06, p. 10] where this is described as pullback. This

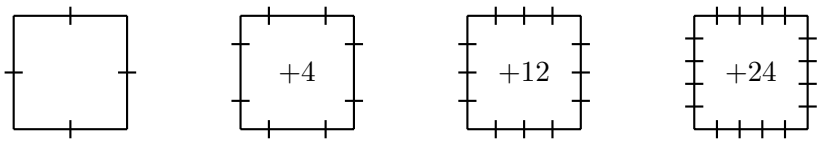

Figure 2.1: Distribution of the degrees of freedom of Raviart-Thomas finite elements with continuity of the normal flux (marked by a stroke at the boundary) and additional interior degrees of freedom, see [FB91, Fig. III.13].

procedure is necessary to preserve normal components and therefore the divergence. With these definitions we define the H^{div}-conforming space RT_k, as well as the space Q_k of discontinuous finite element functions by

$$RT_k(\Omega) = \Big\{ \boldsymbol{v} \in H^{\mathrm{div}}(\Omega) \ : \ \boldsymbol{v}\big|_T \in RT_k(T) \quad \forall T \in \mathcal{T}_h \Big\},$$
$$Q_k(\Omega) = \big\{ v \in L^2(\Omega) \ : \ v\big|_T \in Q_k(T) \quad \forall T \in \mathcal{T}_h \big\}.$$

The spaces $RT_k = RT_k(\Omega)$ and $Q_k = Q_k(\Omega)$ are defined such that

$$\operatorname{div} RT_k = Q_k.$$

The degrees of freedom of RT_k are chosen in order to assure continuity of the normal flux $\boldsymbol{v} \cdot \boldsymbol{n}$ at interfaces of elements, as sketched in Figure 2.1.

Let $W(T) = \big\{ \boldsymbol{\varphi} \in L^s(T) \ : \ \operatorname{div} \boldsymbol{\varphi} \in L^2(\Omega), s > 2 \big\}$. For the interpolation operator $I^h \colon W(T) \to RT_k(T)$ and the L^2-projection Π^h on $Q_k(T)$ it holds the important commuting property

$$\operatorname{div} I^h = \Pi^h \operatorname{div}.$$

For later use we further define the space P_k of discontinuous functions of total degree at most k on T, and the space S_k of continuous finite element functions by

$$P_k(\Omega) = \big\{ v \in L^2(\Omega) \ : \ v\big|_T \in P_k(T) \quad \forall T \in \mathcal{T}_h \big\},$$
$$S_k(\Omega) = \big\{ v \in C^0(\Omega) \ : \ v\big|_T \in Q_k(T) \quad \forall T \in \mathcal{T}_h \big\}.$$

2.3 Iterative Solution Algorithms

A main goal in scientific computing is to deliver reliable methods for the calculation of real world application scenarios coming from different fields of science and engineering, making simulations of real world problems possible and efficient. Very often, these methods result in large linear systems of equations that need to be solved, where increasing their accuracy typically goes along with a growing number of unknowns and equations. Thus, from a certain point, direct solution algorithms as the Gauss elimination become unpractical because of their high need of memory and time consumption to invert the corresponding system matrix. A way out, reducing these effects and making it possible to drop the memory usage of the computer hardware to a minimum, is to use state-of-the-art Krylov subspace methods like the conjugate gradient (CG) [HS52], the minimum residual (MinRes) [PS75], or the generalized minimal residual method (GMRES) [SS86]. These projection methods, which are going to be introduced in this section, are based on minimization processes in so-called Krylov subspaces and iteratively approximate the solution of a linear system

$$\boldsymbol{A}\boldsymbol{x} = \boldsymbol{b} \tag{2.9}$$

while using matrix-vector products only. Especially in the case of finite element discretizations of partial differential equations, which result in large and sparse system matrices $\boldsymbol{A}$, this allows for massively parallel implementations of the solution algorithms, because the whole system can easily be decomposed into small parts by using the strong link between the geometry of the computational domain and the matrix and vector entries. Krylov subspace methods could in principle be used as direct solvers, since they solve equations of the form (2.9) in $\mathbb{R}^n$ in at most n iterations, assumed that they are applied in exact arithmetic. Obviously, this is not the case for computations on modern workstations, such that their actual potency is as iterative solver. Although there are counter examples, where they produce iterates with the same accuracy until the last iteration, where the residual finally and suddenly drops to zero (assuming exact arithmetic), Krylov subspace methods perform often very well in practical computations. A good overview and many details about iterative methods for sparse linear systems can be found for example in [Saa03].

A simple iterative solution algorithm, not a Krylov subspace method, is the Richardson

iteration. As a prototypical iterative solution algorithm it serves as theoretical tool in the later analysis of Schwarz methods, but will not directly be used in practical calculations. Given the linear system of equations (2.9) and a starting vector $\boldsymbol{x}_0$, the Richardson iteration approximates $\boldsymbol{x}$ by transforming the system into a fixed point equation and solving it by using the iteration

$$\boldsymbol{x}_k = (\boldsymbol{I} - \boldsymbol{A})\boldsymbol{x}_{k-1} + \boldsymbol{b}, \qquad k = 1, \ldots, n, \tag{2.10}$$

where $\boldsymbol{I}$ is the identity matrix. Convergence of the Richardson iteration (2.10) is guaranteed, if the spectral radius of $\boldsymbol{I} - \boldsymbol{A}$ is less than one, see [Saa03, Theorem 4.1].

Linear systems with a sparse symmetric positive definite matrix $\boldsymbol{A}$ can be solved with the CG algorithm, which is a Krylov subspace method and one of the best known iterative techniques for this situation, [Saa03, p. 187]. Let $\left\{\boldsymbol{x}^k\right\}_{k\geq 0}$ be the sequence of iterates generated by Algorithm 2.1. Then, convergence is guaranteed by

$$\|\boldsymbol{x}_k - \boldsymbol{x}\|_{\boldsymbol{A}} \leq 2\left(\frac{\sqrt{\kappa(\boldsymbol{A})} - 1}{\sqrt{\kappa(\boldsymbol{A})} + 1}\right)^k \|\boldsymbol{x}_0 - \boldsymbol{x}\|_{\boldsymbol{A}}, \tag{2.11}$$

with the norm

$$\|\boldsymbol{x}\|_{\boldsymbol{A}} = (\boldsymbol{A}\boldsymbol{x}, \boldsymbol{x})^{1/2},$$

and the condition number

$$\kappa(\boldsymbol{A}) = \frac{|\lambda_{\max}(\boldsymbol{A})|}{|\lambda_{\min}(\boldsymbol{A})|},$$

where $\lambda_{\max}(\boldsymbol{A})$ and $\lambda_{\min}(\boldsymbol{A})$ denote the largest and smallest eigenvalue of $\boldsymbol{A}$, respectively. For a proof of (2.11) see [Saa03, p. 205].

In case of unsymmetric and possibly indefinite problems GMRES can be applied to solve a linear system of equations iteratively. Convergence can be shown with respect to the residual for diagonalizable matrices $\boldsymbol{A} \in \mathbb{R}^{N\times N}$ in the form $\boldsymbol{A} = \boldsymbol{T}\boldsymbol{D}\boldsymbol{T}^{-1}$, where $\boldsymbol{D} = \operatorname{diag}(\lambda_1, ..., \lambda_N)$ with eigenvalues arranged in increasing order. Therefore, assume that all λ_i are contained in the ellipse $E(c, d, a)$ in the complex plane with center $c \in \mathbb{R}$, focal distance $d \in \mathbb{R}$, and large half-axis $a \in \mathbb{R}$, such that $0 \notin E(c, d, a)$. Then, the

Algorithm 2.1 CG [Saa03, Algorithm 6.18]

Require: $\boldsymbol{A}$, $\boldsymbol{b}$, $\boldsymbol{x}_0$

1. Compute $\boldsymbol{r}_0 = \boldsymbol{b} - \boldsymbol{A}\boldsymbol{x}_0$, $\boldsymbol{p}_0 = \boldsymbol{r}_0$
2. **for** $j = 0, 1, \ldots,$ until convergence **do**
3. $\quad \alpha_j = (\boldsymbol{r}_j, \boldsymbol{r}_j) \,/\, (\boldsymbol{A}\boldsymbol{p}_j, \boldsymbol{p}_j)$
4. $\quad \boldsymbol{x}_{j+1} = \boldsymbol{x}_j + \alpha_j \boldsymbol{p}_j$
5. $\quad \boldsymbol{r}_{j+1} = \boldsymbol{r}_j - \alpha_j \boldsymbol{A}\boldsymbol{p}_j$
6. $\quad \beta_j = (\boldsymbol{r}_{j+1}, \boldsymbol{r}_{j+1}) \,/\, (\boldsymbol{r}_j, \boldsymbol{r}_j)$
7. $\quad \boldsymbol{p}_{j+1} = \boldsymbol{r}_{j+1} + \beta_j \boldsymbol{p}_j$
8. **end for**
9. **return** $\boldsymbol{x}_k$ ▷ where k is the last iteration

Algorithm 2.2 GMRES [Saa03, Algorithm 6.9]

Require: $\boldsymbol{A}$, $\boldsymbol{b}$, $\boldsymbol{x}_0$

1. Compute $\boldsymbol{r}_0 = \boldsymbol{b} - \boldsymbol{A}\boldsymbol{x}_0$, $\beta = \|\boldsymbol{r}_0\|_2$, and $\boldsymbol{v}_1 = \boldsymbol{r}_0/\beta$
2. **for** $j = 1, \ldots, k$ **do**
3. $\quad$ Compute $\boldsymbol{w}_j = \boldsymbol{A}\boldsymbol{v}_j$
4. $\quad$ **for** $i = 1, \ldots, j$ **do**
5. $\quad\quad h_{ij} = (\boldsymbol{w}_j, \boldsymbol{v}_i)$
6. $\quad\quad \boldsymbol{w}_j = \boldsymbol{w}_j - h_{ij}\boldsymbol{v}_i$
7. $\quad$ **end for**
8. $\quad h_{j+1,j} = \|\boldsymbol{w}_j\|_2$
9. $\quad$ **if** $(h_{j+1,j} = 0)$ set $k = j$ and **go to** Line 12
10. $\quad \boldsymbol{v}_{j+1} = \boldsymbol{w}_j / h_{j+1,j}$
11. **end for**
12. Define matrices $\boldsymbol{H}_k = (h_{ij})_{1 \le i \le k+1, 1 \le j \le k}$, and $\boldsymbol{V}_k = (\boldsymbol{v}_1, \ldots, \boldsymbol{v}_k)$
13. Compute $\boldsymbol{y}_k$, minimizer of $\|\boldsymbol{e}_1/\beta - \bar{\boldsymbol{H}}_k\|_2$
14. **return** $\boldsymbol{x}_k = \boldsymbol{x}_0 + \boldsymbol{V}_k \boldsymbol{y}_k$

residual $\boldsymbol{r}_k = \boldsymbol{b} - \boldsymbol{A}\boldsymbol{x}_k$ at the k-th step in Algorithm 2.2 satisfies

$$\left\|\boldsymbol{r}_k\right\|_2 \leq \kappa(\boldsymbol{T}) \frac{C_k(\frac{a}{d})}{C_k(\frac{c}{d})} \left\|\boldsymbol{r}_0\right\|_2, \tag{2.12}$$

where $C_k(z) = (z + \sqrt{z^2 - 1})^k + (z + \sqrt{z^2 - 1})^{-k}$. For a proof see [Saa03, p. 206]. In practice, when $\boldsymbol{A}$ is ill-conditioned and has real spectrum, i.e., $a \approx d$, $c + a = \lambda_{\max}$, $c - a = \lambda_{\min}$, one can use the approximate expression

$$\frac{C_k(\frac{a}{d})}{C_k(\frac{c}{d})} \approx \left(1 - \frac{2}{\sqrt{\kappa(\boldsymbol{A})}}\right)^k$$

instead of (2.12), compare [EG10, p. 409] and also [Saa03, p. 207]. For symmetric positive-definite problems, and when exact arithmetic is considered, GMRES is mathematically equivalent to the minimum residual method (MinRes) [PS75], for which we have the convergence result

$$\left\|\boldsymbol{r}_k\right\|_{\boldsymbol{A}} \leq 2 \left(\frac{\sqrt{\kappa(\boldsymbol{A})} - 1}{\sqrt{\kappa(\boldsymbol{A})} + 1}\right)^k \left\|\boldsymbol{r}_0\right\|_{\boldsymbol{A}}, \tag{2.13}$$

similar to (2.11) but with respect to the residual, see [GR11].

As one can see in (2.11), (2.13), and (2.12), the convergence of Krylov subspace methods is highly dependent on the condition number $\kappa(\boldsymbol{A})$. Since $\kappa(\boldsymbol{A})$ is typically dependent on the mesh size for finite element discretizations of partial differential equations and grows with the size of $\boldsymbol{A}$ the use of a preconditioner is crucial for the solution process. Preconditioning can be done, for example, by multiplying (2.9) with a positive definite matrix $\boldsymbol{P}$, called preconditioner, such that

$$\boldsymbol{P}\boldsymbol{A}\boldsymbol{x} = \boldsymbol{P}\boldsymbol{b}. \tag{2.14}$$

Then, the preconditioned system (2.14) is solved instead of the original system (2.9) with the new matrix $\boldsymbol{P}\boldsymbol{A}$ and the new right hand side $\boldsymbol{P}\boldsymbol{b}$. Another option is to insert the identity $\boldsymbol{I} = \boldsymbol{P}\boldsymbol{P}^{-1}$, such that $\boldsymbol{A}\boldsymbol{P}\boldsymbol{P}^{-1}\boldsymbol{x} = \boldsymbol{b}$ and substitute $\boldsymbol{y} = \boldsymbol{P}^{-1}\boldsymbol{x}$, which results in solving the preconditioned system in two steps

$$\boldsymbol{A}\boldsymbol{P}\boldsymbol{y} = \boldsymbol{b}, \qquad \boldsymbol{x} = \boldsymbol{P}\boldsymbol{y}.$$

One can also use combinations of both options. Either way, we aim to have a better condition number $\kappa(\boldsymbol{PA})$ or $\kappa(\boldsymbol{AP})$ smaller than the original $\kappa(\boldsymbol{A})$ and at best independent of the size of $\boldsymbol{A}$, i.e., independent of the targeted accuracy, while building the preconditioned matrix $\boldsymbol{PA}$ or $\boldsymbol{AP}$ is actually cheap. Meaning, that the building process is far cheaper than creating the inverse $\boldsymbol{P} = \boldsymbol{A}^{-1}$. In this context, if the rate of convergence of an iterative method is independent of the size of the system, we say that the algorithm is optimal. The discussion of optimal preconditioned iterative methods for models describing poroelastic and porous media is the central goal of the following chapters in this thesis.

2.4 Two-level Schwarz Preconditioner

Schwarz methods go back to 1870, where Schwarz presented the first known domain decomposition method in [Sch70]. Originally, Schwarz proposed his alternating method to provide a theoretical tool for the proof of existence and uniqueness of solutions of Laplace's equation on complicated two-dimensional domains, cf. [GW14]. Nowadays, the method is successfully applied as solver or preconditioner in various situations, providing a powerful tool in the solution of partial differential equations. In the following section we introduce the concept of two-level overlapping Schwarz methods, develop their convergence theory in an abstract framework, and apply it to the case of H^{div}-conforming finite element spaces as proposed by [TW10].

2.4.1 Algorithm

Let V be a real-valued finite-dimensional Hilbert space with norm $\|\cdot\|$ and let V^* denote its dual space. V is meant to be a finite element space in the further analysis. Let $a(\cdot,\cdot) : V \times V \to \mathbb{R}$ be a symmetric, continuous and coercive bilinearform, i.e.,

$$a\big(u,v\big) = a\big(v,u\big), \qquad a\big(u,v\big) \leq c\,\|u\|\,\|v\|\,, \qquad a\big(u,u\big) \geq c\,\|u\|^2\,,$$

for all $u, v \in V$. We consider the problem of finding $u \in V$, such that

$$a\big(u,v\big) = f(v) \qquad \forall v \in V, \tag{2.15}$$

for given functional $f \in V^*$. Problem (2.15) has a unique solution by the Riesz representation theorem. Further, we assume that there is a decomposition of V into a sum

$$V = V_0 + \sum_{j=1}^{J} V_j \tag{2.16}$$

of local subspaces $V_j \subset V$ and a global coarse space $V_0 \subset V$. The local spaces V_j correspond to a partition of the underlying computational domain $\Omega \subset \mathbb{R}^d$ into subdomains $\Omega_j \subset \Omega$. Functions in V_j are extended by zero to the whole space V, such that

$$V_j = \{v_j \in V \ : \ v_j = 0 \text{ in } \Omega \setminus \Omega_j\}.$$

On these spaces we define local bilinear forms $a_j(\cdot,\cdot) : V_j \to V_j$ and a coarse bilinear form $a_0(\cdot,\cdot) : V_0 \to V_0$ as restrictions of $a(\cdot,\cdot)$ to the corresponding spaces, equipped with homogeneous Dirichlet boundaries, by

$$\begin{aligned} a_j\big(u_j, v_j\big) &= a\big(u_j, v_j\big) \qquad \forall u_j, v_j \in V_j, \\ a_0\big(u_0, v_0\big) &= a\big(u_0, v_0\big) \qquad \forall u_0, v_0 \in V_0. \end{aligned} \tag{2.17}$$

Further we define Ritz-projections $P_j \colon V \to V_j$ by

$$a_j\big(P_j u, v_j\big) = a\big(u, v_j\big) \qquad \forall v_j \in V_j.$$

An additive two-level Schwarz operator is given by

$$P_{\text{ad}} = \omega \sum_{j=0}^{J} P_j,$$

where ω is a relaxation factor that deals with the overlap and also tunes the algorithm. With the error propagation operator

$$E_{\text{mu}} = (I - P_J) \cdots (I - P_1)(I - P_0)$$

we define a multiplicative two-level Schwarz operator P_{mu} by

$$P_{\text{mu}} = I - E_{\text{mu}}.$$

A hybrid version that is additive on the local spaces and multiplicative with respect to the coarse space is defined by

$$P_{\text{hyb}} = I - E_{\text{hyb}}, \qquad E_{\text{hyb}} = \left(I - \omega \sum_{j=1}^{J} P_j \right) (I - P_0) \left(I - \omega \sum_{j=1}^{J} P_j \right).$$

2.4.2 Abstract Convergence Theory

To prove convergence of the two-level Schwarz operators defined in Section 2.4, we follow [TW10] and assume to have a stable decomposition, as well as local stability and strengthened Cauchy-Schwarz inequalities as formulated in Assumptions 2.2 to 2.4. All proofs of this Section can be found in [TW10, chapter 2].

Assumption 2.2 (Stable decomposition)**.** *There exists a constant C_0, such that every $u \in V$ admits a decomposition*

$$u = \sum_{j=0}^{J} u_j, \qquad \{u_j \in V_j, 0 \leq j \leq J\}$$

that satisfies

$$\sum_{j=0}^{J} a_j\big(u_j, u_j\big) \leq C_0 a\big(u, u\big).$$

Assumption 2.3 (Local stability)**.** *For each $0 \leq j \leq J$ there exists a constant $C_1 > 0$, such that*

$$a\big(u_j, u_j\big) \leq C_1 a_j\big(u_j, u_j\big),$$

for $u_j \in \text{range}(P_j) \subset V_j$.

Assumption 2.4 (Strengthened Cauchy-Schwarz inequalities)**.** *For $1 \leq i, j \leq J$ there exist constants $0 \leq \varepsilon_{ij} \leq 1$ such that*

$$\big|a\big(u_i, u_j\big)\big| \leq \varepsilon_{ij} a\big(u_i, u_i\big)^{\frac{1}{2}} a\big(u_j, u_j\big)^{\frac{1}{2}},$$

for $u_i \in V_i$, $u_j \in V_j$. The spectral radius of $\mathcal{E} = \{\varepsilon_{ij}\}$ is denoted by $\rho(\mathcal{E})$.

Due to the stable decomposition formulated in Assumption 2.2, we are able to find a lower bound of the minimal eigenvalue $\lambda_{\min}(P_{\text{ad}})$, ensuring the invertibility of P_{ad}. A value of C_0 close to one is desirable, and thus, orthogonal subspaces V_j would be best. The aim of the strengthened Cauchy-Schwarz inequalities, Assumption 2.4, together with the local stability, Assumption 2.3, is to obtain an upper bound for the maximal eigenvalue $\lambda_{\max}(P_{\text{ad}})$. The Cauchy-Schwarz inequalities are trivially valid with $\varepsilon_{ij} = 1$, but we are highly interested in better bounds, since this would lead to a spectral radius $\rho(\mathcal{E}) = J$, growing linearly with the number of subdomains V_j. Again, the best bound is reached for orthogonal subspaces. All three assumptions are also needed to limit the norm of the error propagation operator E_{mu} leading to a convergence proof of the multiplicative operator P_{mu}.

Remark 2.5. *Assumption 2.3 is trivial with $C_1 = 1$, when exact solvers are chosen, as we have done in the definition of the local and coarse bilinear forms in* (2.17)*. Nevertheless, we need to make this assumption here, since we will define methods with non-inherited coarse bilinear forms in the following chapters.*

Since P_{ad} is symmetric, we can use the conjugate gradient algorithm to solve the preconditioned system

$$\boldsymbol{P}_{\text{ad}}\boldsymbol{u} = \boldsymbol{g}_{\text{ad}}.$$

The conjugate gradient algorithm converges, if the condition number of the positive-definite and symmetric system matrix is bounded. Hence, in the following proposition, we give a bound of the condition number

$$\kappa(\boldsymbol{P}_{\text{ad}}) = \frac{\lambda_{\max}(\boldsymbol{P}_{\text{ad}})}{\lambda_{\min}(\boldsymbol{P}_{\text{ad}})},$$

where the maximal and minimal eigenvalues of $\boldsymbol{P}_{\text{ad}}$ are given by

$$\lambda_{\max}(\boldsymbol{P}_{\text{ad}}) = \sup_{u \in V} \frac{a\big(P_{\text{ad}}u, u\big)}{a\big(u, u\big)}, \qquad \lambda_{\min}(\boldsymbol{P}_{\text{ad}}) = \inf_{u \in V} \frac{a\big(P_{\text{ad}}u, u\big)}{a\big(u, u\big)}.$$

Proposition 2.6. *Let Assumptions 2.2, 2.3 and 2.4 be satisfied, then it holds for the*

smallest and largest eigenvalues of the additive Schwarz operator

$$\lambda_{\min}(\boldsymbol{P}_{ad}) \geq \frac{1}{C_0}, \qquad \lambda_{\max}(\boldsymbol{P}_{ad}) \leq C_1(\rho(\mathcal{E}) + 1),$$

thus, the condition number of the additive Schwarz operator is bounded by

$$\kappa(\boldsymbol{P}_{ad}) \leq C_0 C_1(\rho(\mathcal{E}) + 1).$$

The multiplicative Schwarz operator P_{mu} is not symmetric, therefore we solve the preconditioned system

$$\boldsymbol{P}_{\text{mu}}\boldsymbol{u} = \boldsymbol{g}_{\text{mu}}$$

with a simple Richardson iteration. To guarantee convergence, the norm of the error propagation operator E_{mu}

$$\left\|E_{\text{mu}}\right\|_a = \left(\sup_{u \in V} \frac{a\big(E_{\text{mu}}u, E_{\text{mu}}u\big)}{a\big(u,u\big)}\right)^{\frac{1}{2}}$$

is strictly bounded by one in Proposition 2.7.

Proposition 2.7. *Let Assumption 2.2, 2.3 and 2.4 be satisfied and* $0 < C_1 < 2$*. Then the error propagation operator* $E_{mu} = I - P_{mu}$ *of the multiplicative Schwarz method satisfies*

$$\left\|E_{mu}\right\|_a^2 \leq 1 - \frac{2 - C_1}{\left(2\hat{C}_1^2\rho(\mathcal{E})^2 + 1\right) C_0} < 1,$$

where $\hat{C}_1 = \max(1, C_1)$.

The hybrid operator P_{hyb} is again symmetric, and thus we can use the conjugate gradient algorithm to solve the preconditioned system

$$\boldsymbol{P}_{\text{hyb}}\boldsymbol{u} = \boldsymbol{g}_{\text{hyb}}.$$

Convergence of the hybrid method, which is the two-level version of a classical multigrid algorithm with an additive domain decomposition smoother, has not been investigated by [TW10]. Instead, they proved convergence for a quite similar hybrid operator $I -$

$(I - P_0)\left(I - \sum_{j=1}^{J} P_j\right)(I - P_0)$, that was introduced by Mandel in [Man94], which is also additive with respect to the local contributions and multiplicative regarding the coarse space. As P_{hyb} is closely related to this hybrid operator due to Mandel, and lies as a combination of the additive and multiplicative methods in between those operators, we expect convergence also for the hybrid method P_{hyb}, when Assumptions 2.2 to 2.4 have been verified. Additionally, the convergence analysis of P_{hyb} as special case of a multigrid V-cycle has been investigated, for example by [Bra93, Yse93, Saa03, DGTZ07]. Although we specialize our analysis to two-level methods we refer to the literature for the multilevel case, see also Section 2.5.

2.4.3 Overlapping Methods

In Section 2.4.2 the decomposition (2.16) of the global space V into a sum of local subspaces V_j was quite general and not made explicit. In this section we will specify the theory for the case of overlapping partitions of the underlying computational domain Ω into patches Ω_j. In order to develop the convergence analysis for this case we need to assume that there is a sufficient overlap of the patches, and that the covering of the partition is finite.

Let the computational domain $\Omega \subset \mathbb{R}^d$ be an open, bounded and convex set with Lipschitz-boundary, and let $\mathcal{T}_h$ be a family of shape regular triangulations of Ω into closed mesh cells T with diameter $h_T = \operatorname{diam}(T)$, where $h = \max_{T \in \mathcal{T}_h} h_T$ denotes the mesh size. The subdomains $\Omega_j \subset \Omega$, called patches, are assumed to be unions of cells such that each patch is the interior of a union of neighboring cells. Further, let $\mathcal{T}_H$ be a quasi-uniform coarse triangulation of Ω_0 with mesh size $H \geq h$.

Assumption 2.8 (Sufficient overlap)**.** *There is a constant $\delta > 0$ that measures the size of overlaps between the subdomains Ω_j, such that*

$$c_2 h \leq \delta \leq c_3 H$$

for constants $c_2 > 0$ and $c_3 > 0$.

Assumption 2.9 (Finite covering)**.** *The partition $\{\Omega_j\}_{j=1}^{J}$ can be colored using at most N^c colors, in such a way that subregions with the same color are disjoint.*

In case of overlapping methods we need a partition of unity for the construction of

local functions u_j on each patch Ω_j. The properties that are needed are summarized in the following Proposition 2.10 and a proof can be found in [TW10, Lemma 3.4].

Proposition 2.10. *Let Assumptions 2.8 and 2.9 be given, then there is a piecewise d-linear partition of unity $\{\theta_j\}_{j=1}^J$ relative to the overlapping partition $\{\Omega_j\}_{j=1}^J$ such that for all $j = 1, \dots, J$*

$$\operatorname{supp}(\theta_j) \subset \overline{\Omega_j},$$

and for all $x \in \overline{\Omega}$ there holds

$$\sum_{j=1}^{J} \theta_j(x) = 1 \tag{2.18}$$

with $0 \leq \theta_j(x) \leq 1$. Moreover,

$$\left\|\nabla \theta_j\right\|_{L^\infty(\Omega)} \leq \frac{c}{\delta},$$

where δ is the constant from Assumption 2.8.

With these preliminaries a stable decomposition can be proven for the case of overlapping partitions. The theorem goes back to [DW87] and a proof can be found in [TW10, Lemma 3.13].

Proposition 2.11. *Given Assumptions 2.8 and 2.9 there exists a constant $C > 0$, such that every $u \in V$ admits a decomposition*

$$u = \sum_{j=0}^{J} u_j, \qquad \{u_j \in V_j, 0 \leq j \leq J\},$$

relative to the overlapping partition $\{\Omega_j\}_{j=1}^J$, that satisfies

$$\sum_{j=0}^{J} a_j\big(u_j, u_j\big) \leq C \left(1 + \frac{H}{\delta}\right) a\big(u, u\big).$$

The convergence of the two-level overlapping Schwarz methods is now guaranteed by Proposition 2.11 and the theorems of Section 2.4.2 with stability constant $C_0 = C\left(1 + \frac{H}{\delta}\right)$,

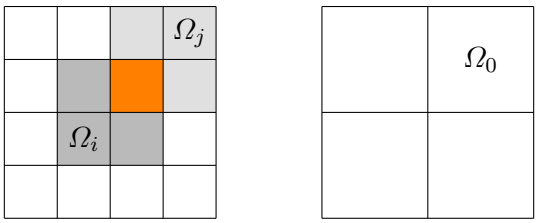

Figure 2.2: Overlapping patches (left) and corresponding hierarchical coarse mesh (right).

as well as the bound of the spectral radius $\rho(\mathcal{E}) \leq N^c$, which is a direct consequence of Assumption 2.9. A typical choice of the coarse space in case of hierarchical meshes is to choose it one level coarser than the computational mesh, as well as one layer of cells as overlap between the patches, compare Figure 2.2. Then $H = 2h$ and $\delta = h$, resulting in the constant $C_0 = 3C$.

2.4.4 Two-level Methods for H^{div}-conforming Finite Elements

In the following chapters of this thesis we will mainly use discretization spaces containing H^{div}-conforming finite element functions to gain mass conservative discretizations of the given model problems in poroelasticity and porous media flow. The construction of a decomposition (2.16) needs to take into account that the divergence is represented properly, such that the H^{div}-conformity is conserved by the preconditioner. Thus, we need to partition the computational domain Ω into overlapping subdomains Ω_j, consisting of at least 4 cells in 2D surrounding a vertex (or 8 cells in 3D), so called vertex patches, such that the divergence of the given finite element functions can be represented in every node. In 3D the size of the patches can be reduced to so called edge patches, which consist of 4 cells surrounding an edge, see [AFW00, p. 207]. An illustration in a 2D example of lowest order Raviart-Thomas functions is given in Figure 2.3. Here you can see, that nodes in the interior of the domain always need four surrounding cells, which form a patch to represent the curl, that describes the rotation of a vector field properly. In this example we take the $\mathbf{curl} = (\partial_2, -\partial_1)$ in favor of the divergence $\text{div} = (\partial_1, \partial_2)\cdot$ (note the dot) due to their close relation to each other (compare Remark 2.1) and the ability of the curl to give a far more placative visualization here. Additionally in the right picture with three patches you can see the need of an overlap of one layer of cells between two patches, such that the curl is represented here as well. Without overlap the partition

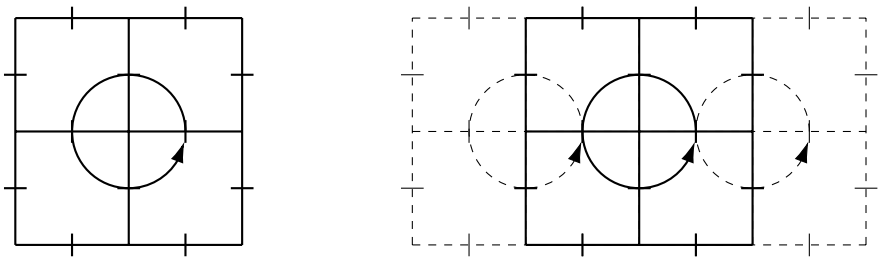

Figure 2.3: Representation of the curl on one patch (left) and on overlapping patches (right).

would not be able to treat the curl on vertices at their boundaries correctly, since the overlap assures that all vertices have a surrounding layer of cells, such that all portions of the curl (or divergence) operator are captured.

The first study on domain decomposition preconditioners for H^{div}-conforming finite element functions was done by Arnold, Falk, Winther for two dimensional Raviart-Thomas finite element functions in [AFW97], followed by [AFW98, AFW00], and Hiptmair [Hip96, Hip97], as well as Hiptmair, Hoppe [HH99], handling both two and three dimensional cases; cf. [TW10, p. 273]. These studies build on earlier works, where the domain decomposition methods are directly used as solvers, see for example [EW92, VW92].

In order to prove convergence for the H^{div}-conforming case a proof of the stable decomposition for bilinear form

$$\big(\boldsymbol{u},\boldsymbol{v}\big)_{H^{\mathrm{div}}(\Omega)} = \big(\boldsymbol{u},\boldsymbol{v}\big)_{\Omega} + \big(\operatorname{div}\boldsymbol{u},\operatorname{div}\boldsymbol{v}\big)_{\Omega}, \qquad \boldsymbol{u},\boldsymbol{v}\in V\subset H^{\mathrm{div}}(\Omega), \tag{2.19}$$

needs to treat the kernel V^0 of the divergence operator and its orthogonal complement $V^{\perp}$ with respect to bilinear form (2.19) seperately, where kernel and orthogonal complement are defined by

$$V^0 = \big\{\boldsymbol{u}^0\in V \;:\; \operatorname{div}\boldsymbol{u}^0 = 0\big\},$$

and

$$V^{\perp} = \Big\{\boldsymbol{u}^{\perp}\in V \;:\; \big(\boldsymbol{u}^{\perp},\boldsymbol{v}^0\big)_{H^{\mathrm{div}}(\Omega)} = 0 \quad \forall \boldsymbol{v}^0\in V^0\Big\},$$

respectively. Therefore, a Helmholtz decomposition is used to write V as the sum

$$V = V^0 \oplus V^\perp.$$

Whereas it is not important for functions in the orthogonal complement $V^\perp$ to stay locally orthogonal, it is important for functions in the kernel V^0 to find a decomposition that is divergence-free also in the local contributions, compare also [LWXZ07]. To this end the fact is used that divergence-free functions $\boldsymbol{u}^0 \in V^0$ can be represented as curl of H^1-functions s, i.e.,

$$\boldsymbol{u}^0 = \mathbf{curl}\, s,$$

for which we find a decomposition $s = \sum_{j=0}^{J} s_j$ stable in $H^1(\Omega)$, namely,

$$\sum_{j=0}^{J} |s_j|^2_{H^1(\Omega)} \leq c_{H,\delta} |s|^2_{H^1(\Omega)}$$

for some constant $c_{H,\delta} = C\left(1 + \frac{H}{\delta}\right) > 0$, see Proposition 2.11. By choosing $\boldsymbol{u}^0_j = \mathbf{curl}\, s_j$ we have constructed a decomposition $\boldsymbol{u}^0 = \sum_{j=0}^{J} \boldsymbol{u}^0_j$ that is stable and stays in the kernel locally since

$$\sum_{j=0}^{J} \|\boldsymbol{u}^0_j\|^2_\Omega = \sum_{j=0}^{J} \|\mathbf{curl}\, s_j\|^2_\Omega = \sum_{j=0}^{J} |s_j|^2_{H^1(\Omega)}$$
$$\leq c_{H,\delta} |s|^2_{H^1(\Omega)} = c_{H,\delta} \|\mathbf{curl}\, s\|^2_\Omega = c_{H,\delta} \|\boldsymbol{u}^0\|^2_\Omega.$$

This sketches a main idea of the proof of the following two Propositions 2.12 and 2.13. The full proof can be found in [TW10, p. 285 f]. It goes back to [VW92] for the two-dimensional case, and to [Hip97] in three dimensions.

Proposition 2.12. *Every $\boldsymbol{v} \in V^0_h$ admits a decomposition of the form $\boldsymbol{v} = \sum_{j=0}^{J} \boldsymbol{v}_j$, $\boldsymbol{v}_j \in V^0_j$, which satisfies the bound*

$$\sum_{j=0}^{J} \|\boldsymbol{v}_j\|^2_\Omega \leq c \left(1 + \frac{H^2}{\delta^2}\right) \|\boldsymbol{v}\|^2_\Omega.$$

Proposition 2.13. *Let $\nu > 0$ be a positive constant. Every $\boldsymbol{v} \in V_h^{\perp}$ admits a decomposition of the form $v = \sum_{j=0}^{J} \boldsymbol{v}_j$, $\boldsymbol{v}_j \in V_j$, which satisfies the bound*

$$\sum_{j=0}^{J} \left(\|\boldsymbol{v}_j\|_{\Omega}^2 + \nu \|\operatorname{div} \boldsymbol{v}_j\|_{\Omega}^2 \right) \leq c \left(1 + \frac{H^2}{\delta^2} \right) \left(\|\boldsymbol{v}\|_{\Omega}^2 + \nu \|\operatorname{div} \boldsymbol{v}\|_{\Omega}^2 \right),$$

for a constant $c > 0$ independent of ν.

2.4.5 Remarks on the Implementation

Let $\boldsymbol{A}$ be the system matrix, $\boldsymbol{f}$ be the coefficient vector of the right hand side f, and $\boldsymbol{u}$ be the coefficient vector of the solution u corresponding to problem (2.15) after choosing a basis of the finite element space V. Then, we aim to solve linear systems of equations

$$\boldsymbol{A}\boldsymbol{u} = \boldsymbol{f}. \tag{2.20}$$

In practice, if we want to apply the Schwarz preconditioners from Section 2.4 to system (2.20), we need to introduce prolongation and restriction matrices to deal with the zero-extension of the local spaces V_j to the global space V and its effect on the matrices of the preconditioner. The prolongation matrices are defined as interpolation operators $\boldsymbol{R}_j^T \colon V_j \to V$, whereas the restrictions $\boldsymbol{R}_j \colon V \to V_j$ are just their transposed. Let $\boldsymbol{A}_j$ be the local matrices corresponding to the local bilinear forms in (2.17). Let further $\tilde{\boldsymbol{A}}_j \in \mathbb{R}^{N_j \times N_j}$ be the local matrices defined only on patch Ω_j, where $N_j = \dim(V_j)$ denotes the number of degrees of freedom on patch Ω_j specified by the dimension of the local finite element space V_j. Then the local matrices $\boldsymbol{A}_j \in \mathbb{R}^{N_\Omega \times N_\Omega}$, $N_\Omega = \dim(V)$, are given by

$$\boldsymbol{A}_j = \boldsymbol{R}_j^T \tilde{\boldsymbol{A}}_j \boldsymbol{R}_j$$

and their inverses by

$$\boldsymbol{A}_j^{-1} = \boldsymbol{R}_j^T \tilde{\boldsymbol{A}}_j^{-1} \boldsymbol{R}_j, \tag{2.21}$$

assumimg that the local matrices $\tilde{\boldsymbol{A}}_j$ are positive definite. For the coarse space V_0 we define $\boldsymbol{R}_0^T$, $\boldsymbol{R}_0$ and $\boldsymbol{A}_0$ accordingly. Let $\boldsymbol{P}_{\mathrm{ad}}$, $\boldsymbol{P}_{\mathrm{mu}}$, and $\boldsymbol{P}_{\mathrm{hyb}}$ be the matrix representations of the corresponding operators P_{ad}, P_{mu}, and P_{hyb}, respectively. A closer look into the

Algorithm 2.3 Multiplicative two-level Schwarz preconditioner

The action of $\boldsymbol{A}_{\text{mu}}^{-1}$ on a vector $\boldsymbol{g}$ is given by:

1. $\boldsymbol{x}_0 = \boldsymbol{R}_0^T \tilde{\boldsymbol{A}}_0^{-1} \boldsymbol{R}_0 \boldsymbol{g}$ ▷ coarse space correction
2. **for** $j = 1, \ldots, J$ **do**
3. $\quad \boldsymbol{x}_j = \boldsymbol{x}_{j-1} + \boldsymbol{R}_j^T \tilde{\boldsymbol{A}}_j^{-1} \boldsymbol{R}_j (\boldsymbol{g} - \boldsymbol{A}\boldsymbol{x}_{j-1})$ ▷ local smoothing
4. **end for**
5. Assign: $\boldsymbol{A}_{\text{mu}}^{-1}\boldsymbol{g} = \boldsymbol{x}_J$

projection operators $\boldsymbol{P}_j$ shows that they can be written as

$$\boldsymbol{P}_j = \boldsymbol{A}_j^{-1}\boldsymbol{A}, \qquad 0 \leq j \leq J, \tag{2.22}$$

and thus, $\boldsymbol{P}_{\text{ad}} = \sum_{j=0}^{J} \boldsymbol{A}_j^{-1}\boldsymbol{A}$. Defining the preconditioner $\boldsymbol{A}_{\text{ad}}^{-1} = \sum_{j=0}^{J} \boldsymbol{A}_j^{-1}$ leads to the preconditioned system

$$\boldsymbol{A}_{\text{ad}}^{-1}\boldsymbol{A}\boldsymbol{u} = \boldsymbol{A}_{\text{ad}}^{-1}\boldsymbol{f},$$

or equivalently

$$\boldsymbol{P}_{\text{ad}}\boldsymbol{u} = \boldsymbol{g}_{\text{ad}},$$

where the right hand side is given by $\boldsymbol{g}_{\text{ad}} = \boldsymbol{A}_{\text{ad}}^{-1}\boldsymbol{f}$. Due to (2.22) the according Schwarz operators in the multiplicative and hybrid cases can also be written as $\boldsymbol{P}_{\text{mu}} = \boldsymbol{A}_{\text{mu}}^{-1}\boldsymbol{A}$ and $\boldsymbol{P}_{\text{hyb}} = \boldsymbol{A}_{\text{hyb}}^{-1}\boldsymbol{A}$, with appropriately defined preconditioners $\boldsymbol{A}_{\text{mu}}^{-1}$ and $\boldsymbol{A}_{\text{hyb}}^{-1}$. By defining the right hand sides $\boldsymbol{g}_{\text{hyb}} = \boldsymbol{A}_{\text{hyb}}^{-1}\boldsymbol{f}$ and $\boldsymbol{g}_{\text{mu}} = \boldsymbol{A}_{\text{mu}}^{-1}\boldsymbol{f}$ this leads to the equivalent preconditioned systems

$$\boldsymbol{P}_{\text{mu}}\boldsymbol{u} = \boldsymbol{g}_{\text{mu}}, \qquad \boldsymbol{P}_{\text{hyb}}\boldsymbol{u} = \boldsymbol{g}_{\text{hyb}}.$$

The implementation of the additive operator P_{ad} is straight forward, since it is only the sum of the local and coarse projections. In the case of the multiplicative operator P_{mu} and the hybrid operator P_{hyb}, the action of the preconditioners applied to a vector is presented in pseudo-code in Algorithm 2.3 and Algorithm 2.4, respectively; compare also [TW10, Section 2.6]. The code is written in form of a subspace correction algorithm as it is known from multigrid methods with a local smoothing part, where the contributions of the patches are applied to the current residual, and a coarse space correction part, cf.

Algorithm 2.4 Hybrid two-level Schwarz preconditioner

The action of $\boldsymbol{A}_{\text{hyb}}^{-1}$ on a vector $\boldsymbol{g}$ is given by:

1. $\boldsymbol{x}_0 = \boldsymbol{0}$
2. **for** $j = 1, \ldots, J$ **do**
3. $\quad \boldsymbol{x}_j = \boldsymbol{x}_{j-1} + \omega \boldsymbol{R}_j^T \tilde{\boldsymbol{A}}_j^{-1} \boldsymbol{R}_j \boldsymbol{g}$ ▷ local smoothing
4. **end for**
5. $\boldsymbol{x}_{J+1} = \boldsymbol{x}_J + \boldsymbol{R}_0^T \tilde{\boldsymbol{A}}_0^{-1} \boldsymbol{R}_0 (\boldsymbol{g} - \boldsymbol{A}\boldsymbol{x}_J)$ ▷ coarse space correction
6. $\boldsymbol{r} = \boldsymbol{g} - \boldsymbol{A}\boldsymbol{x}_{J+1}$
7. **for** $j = J+2, \ldots, 2J+1$ **do**
8. $\quad \boldsymbol{x}_j = \boldsymbol{x}_{j-1} + \omega \boldsymbol{R}_j^T \tilde{\boldsymbol{A}}_j^{-1} \boldsymbol{R}_j \boldsymbol{r},$ ▷ local smoothing
9. **end for**
10. Assign: $\boldsymbol{A}_{\text{hyb}}^{-1} \boldsymbol{g} = \boldsymbol{x}_{2J+1}$

[Xu92, Bra93].

Extension to Positive Semi-definite Systems

In case of positive definite problems the local and coarse matrices $\tilde{\boldsymbol{A}}_j$ and $\tilde{\boldsymbol{A}}_0$ can simply be inverted and then applied against the system matrix $\boldsymbol{A}$, see (2.21) and (2.22). This cannot be done when the matrices $\tilde{\boldsymbol{A}}_j$ and $\tilde{\boldsymbol{A}}_0$ have a non-trivial kernel, i.e., when the formulation of the local problems is not positive definite, but positive semi-definite. For example, Stokes flow with no-slip boundary conditions implies a solution that is defined only up to a constant. To reach a unique solution an additional constraint has to be formulated, such as forcing the mean-value of the pressure to be zero. Typically, this is realized by adjusting the solution after the problem has been solved for an arbitrary constant, which leads to the problem of solving linear systems where the corresponding matrix does not have full rank. In this case of linear systems with a non-trivial kernel we cannot invert the local matrices $\tilde{\boldsymbol{A}}_j$ as in (2.21), but we can build the pseudoinvers $\tilde{\boldsymbol{A}}_j^{\dagger}$ by using a singular value decomposition (SVD) that factorizes $\tilde{\boldsymbol{A}}_j$ into $\tilde{\boldsymbol{A}}_j = \boldsymbol{U}_j \boldsymbol{\Sigma}_j \boldsymbol{V}_j^T$, where $\boldsymbol{U}_j, \boldsymbol{V}_j$ are orthogonal matrices and $\boldsymbol{\Sigma}_j$ is a diagonal matrix with as many non-zero diagonal elements, called singular values, as the rank of $\tilde{\boldsymbol{A}}_j$. With the help of the pseudoinvers $\boldsymbol{\Sigma}^{\dagger}$ of $\boldsymbol{\Sigma}$, built by inverting every non-zero diagonal element of $\boldsymbol{\Sigma}$, the pseudoinvers of $\tilde{\boldsymbol{A}}_j$ is now given by

$$\tilde{\boldsymbol{A}}_j^{\dagger} = \boldsymbol{V}_j \boldsymbol{\Sigma}_j^{\dagger} \boldsymbol{U}_j^T.$$

Remark 2.14. *The implementation of the algorithms presented in this thesis is matrix-based. That means, that the system matrix, as well as the matrices of the preconditioner, are assembled globally before starting the solution process. That makes the code quite storage consuming essentially for higher mesh levels, and limits the calculations to the storage capacity of the machine. When changing the implementation to a matrix-free one, the large global matrix is not assembled beforehand, but only small local matrices are used to provide an implementation of the required matrix-vector-multiplications. Here, looping over all mesh cells, one assembles a local cell-matrix to compute the matrix-vector-multiplication on each cell, and adds all local contributions to the global iteration vector. This has the benefit of reducing the storage usage of the code drastically and making larger and even exa-scale computations possible. In this context I would like to refer to the work of Witte, Arndt, Kanschat in [WAK21] and [Wit22] for recent research on high-performance computing with multilevel Schwarz methods.*

2.5 Multilevel Schwarz Preconditioner

In this section the two-level domain decomposition algorithms already developed in the last section will be extended to a multilevel setup. Both two-level Schwarz operators from Section 2.4, the hybrid as well as the multiplicative version, appear to be special cases of a multigrid V-cycle algorithm, as will be presented in the latter.

When using a two-level Schwarz method the coarse problem is assumed to be solved exactly, which makes a major part of the computational costs, since the dimension of the coarse space grows with refinement of the mesh. Multilevel algorithms reduce this cost of the coarse solver by transferring the residual over several levels to a coarse level, where solving the entire coarse system is actually cheap. It is therefore promising to use multilevel algorithms in favor of the two-level versions, because their design leads to optimal complexity of the algorithms. The idea of multigrid methods goes back to the 1960's to a paper of Fedorenko in [Fed64]. In the following decades, the method has been developed with a tremendous amount of scientific research. The multigrid method has successfully been applied to finite difference, as well as finite element discretizations of partial differential equations in a very broad field of applications. Whereas the overall multigrid scheme has few variations, as for example the variable V-cycle or the W-cycle, the performance of the multigrid method relies heavily on the design of the smoother. Choices range from different kinds of matrix decompositions, which has been the first

methods in use, to quite sophisticated smoothers that rely on the analytical structure of the underlying problem, or even doesn't care about it at all by acting algebraically on the matrix, only. Nowadays, multigrid algorithms are typically used as preconditioner inside iterative Krylov subspace solvers, as already outlined for the two-level Schwarz methods in Section 2.4. Although we will not examine the convergence proof of the multilevel methods in the later chapters, we refer to [Xu92, Bra93, Yse93, Saa03, DGTZ07, Bra13] for an overview of the analysis.

2.5.1 Multigrid Algorithm

We assume having a hierarchy of nested meshes

$$\mathcal{T}_{h_0} \subset \mathcal{T}_{h_1} \subset \cdots \mathcal{T}_{h_L} = \mathcal{T}_h$$

and corresponding finite element spaces

$$V_{h_0} \subset V_{h_1} \subset \cdots V_{h_L} = V_h$$

to mesh sizes $h_0 < h_1 < \ldots < h_L = h$. On the finest level L we aim to solve the following abstract problem: find $u_h \in V_h$ such that

$$a_h\big(u_h, v_h\big) = f(v_h) \qquad \forall v_h \in V_h,$$

where $a_h(\cdot,\cdot) : V_h \times V_h \to \mathbb{R}$ is a coercive and continuous bilinearform, and $f \in V_h^*$. For the construction of the multilevel preconditioner we consider on each level ℓ the problem of finding $u_\ell \in V_\ell = V_{h_\ell}$ such that

$$a_\ell\big(u_\ell, v_\ell\big) = f(v_\ell) \qquad \forall v_\ell \in V_\ell, \tag{2.23}$$

where the bilinearform is defined by $a_\ell(\cdot,\cdot) = a_{h_\ell}(\cdot,\cdot)$. As algebraic analogue we rewrite the level problems (2.23) as

$$\boldsymbol{A}_\ell \boldsymbol{u}_\ell = \boldsymbol{f}_\ell, \qquad \text{for } \ell \in \{1, \ldots, L\}.$$

Algorithm 2.5 Multigrid V-cycle

Let $\boldsymbol{M}_0 = \boldsymbol{A}_0^{-1}$. Let $\boldsymbol{S}_\ell$ be a suitable smoother, and let m_{pre} and m_{post} be the number of pre-smoothing and post-smoothing steps, respectively, on each level. Recursively define the action of $\boldsymbol{M}_\ell$ on a vector $\boldsymbol{b}_\ell$ as follows:

1. Pre-smoothing: let $\boldsymbol{x}_0 = \boldsymbol{0}$ and compute for $i = 1, \dots, m_{\text{pre}}$
$$\boldsymbol{x}_i = \boldsymbol{x}_{i-1} + \boldsymbol{S}_\ell \left(\boldsymbol{b}_\ell - \boldsymbol{A}_\ell \boldsymbol{x}_{i-1}\right)$$
2. Coarse grid correction:
$$\boldsymbol{x}_{m_{\text{pre}}+1} = \boldsymbol{x}_{m_{\text{pre}}} + \boldsymbol{R}_{\ell-1}^T \boldsymbol{M}_{\ell-1} \boldsymbol{R}_{\ell-1} \left(\boldsymbol{b}_\ell - \boldsymbol{A}_\ell \boldsymbol{x}_{m_{\text{pre}}}\right)$$
3. Post-smoothing: for $i = m_{\text{pre}} + 2, \dots, m_{\text{pre}} + m_{\text{post}} + 1$ compute
$$\boldsymbol{x}_i = \boldsymbol{x}_{i-1} + \boldsymbol{S}_\ell \left(\boldsymbol{b}_\ell - \boldsymbol{A}_\ell \boldsymbol{x}_{i-1}\right)$$
4. Assign: $\boldsymbol{M}_\ell \boldsymbol{b}_\ell = \boldsymbol{x}_{m_{\text{pre}}+m_{\text{post}}+1}$

Furthermore, for transferring between the levels we define the restriction operators $\boldsymbol{R}_\ell : V_{\ell+1} \to V_\ell$ as L^2-projection, i.e.,

$$\left(\boldsymbol{R}_\ell u_{\ell+1}, v_\ell\right)_\Omega = \left(u_{\ell+1}, v_\ell\right)_\Omega \qquad \forall v_\ell \in V_\ell,$$

for given $u_{\ell+1} \in V_{\ell+1}$, and the prolongation operators $\boldsymbol{R}_\ell^T : V_\ell \to V_{\ell+1}$ such that

$$\left(\boldsymbol{R}_\ell^T u_\ell, v_{\ell+1}\right)_\Omega = \left(u_\ell, \boldsymbol{R}_\ell v_{\ell+1}\right)_\Omega \qquad \forall u_\ell \in V_\ell, v_{\ell+1} \in V_{\ell+1}.$$

For convenience we write the restriction and prolongation matrices with the same symbol as the operators. The application of the multigrid V-cycle $\boldsymbol{M}_\ell$ to a vector is then defined in Algorithm 2.5, compare for example [Bra93, Saa03, KLM17].

2.5.2 Domain Decomposition Smoother

For the definition of the smoother we will use the domain decomposition approach of the Schwarz operators of the foregoing section and apply it to each level. To this end, we will quickly need to recapitulate the definitions of the spaces and operators and adapt the notation to the multilevel setup. We decompose the finite element space V_ℓ on each

level $\ell \in \{1, \dots, L\}$ into the sum

$$V_\ell = \sum_{j=1}^{J} V_{\ell,j}$$

of local subspaces $V_{\ell,j} \subset V_\ell$, which correspond to an overlapping partition into patches $\Omega_{\ell,j}$ on level ℓ. As before, functions in $V_{\ell,j}$ are extended by zero to the whole space V_ℓ. With the local bilinearforms

$$a_{\ell,j}\big(u_{\ell,j}, v_{\ell,j}\big) = a_\ell\big(u_{\ell,j}, v_{\ell,j}\big) \qquad \forall u_{\ell,j}, v_{\ell,j} \in V_{\ell,j},$$

equipped with homogeneous Dirichlet boundary values on $\partial\Omega_{\ell,j}$, we can define the Ritz-projections $P_{\ell,j} : V_\ell \to V_{\ell,j}$ by

$$a_{\ell,j}\big(P_{\ell,j}u_\ell, v_{\ell,j}\big) = a_\ell\big(u_\ell, v_{\ell,j}\big) \qquad \forall v_{\ell,j} \in V_{\ell,j}.$$

On level ℓ, an additive one-level Schwarz method is then defined by

$$P_{\mathrm{ad},\ell} = \omega \sum_{j=1}^{J} P_{\ell,j},$$

and a multiplicative one-level Schwarz method by

$$P_{\mathrm{mu},\ell} = I - E_\ell^{\mathrm{mu}}, \qquad E_\ell^{\mathrm{mu}} = (I - P_{\ell,J}) \cdots (I - P_{\ell,1})\,.$$

To define the additive smoother $\boldsymbol{A}_{\mathrm{ad},\ell}^{-1}$, as well as the multiplicative smoother $\boldsymbol{A}_{\mathrm{mu},\ell}^{-1}$, we follow Section 2.4.5 and use

$$\boldsymbol{P}_{\ell,j} = \boldsymbol{A}_{\ell,j}^{-1}\boldsymbol{A}_\ell, \qquad 1 \le j \le J,$$

to rewrite the matrix representations of the one-level methods $P_{\mathrm{ad},\ell}$ and $P_{\mathrm{mu},\ell}$ as

$$\boldsymbol{P}_{\mathrm{ad},\ell} = \boldsymbol{A}_{\mathrm{ad},\ell}^{-1}\boldsymbol{A}_\ell, \qquad \boldsymbol{P}_{\mathrm{mu},\ell} = \boldsymbol{A}_{\mathrm{mu},\ell}^{-1}\boldsymbol{A}_\ell.$$

For the implementation, we again define the prolongation operator $\boldsymbol{R}_{\ell,j}^T : V_{\ell,j} \to V_\ell$ as interpolation, and the restriction $\boldsymbol{R}_{\ell,j} : V_\ell \to V_{\ell,j}$ as its transpose to write the local

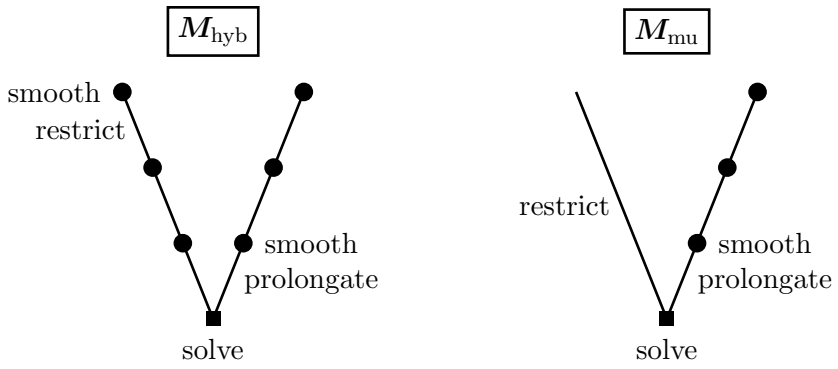

Figure 2.4: Hybrid and multiplicative multilevel Schwarz preconditioner.

inverses as

$$\boldsymbol{A}_{\ell,j}^{-1} = \boldsymbol{R}_{\ell,j}^{T} \tilde{\boldsymbol{A}}_{\ell,j} \boldsymbol{R}_{\ell,j},$$

compare (2.21), and also the discussion in Section 2.4.5.

2.5.3 Schwarz Preconditioner

Finally, we are able to define the symmetric hybrid multilevel Schwarz preconditioner $\boldsymbol{M}_{\text{hyb}}$ by setting $\boldsymbol{M}_{\text{hyb}} = \boldsymbol{M}_L$ in Algorithm 2.5 with $\boldsymbol{A}_{\text{ad},\ell}^{-1}$ as smoother, and with $m_{\text{pre}} = m_{\text{post}}$ smoothing steps.

Further, the multiplicative multilevel Schwarz preconditioner $\boldsymbol{M}_{\text{mu}}$ is defined by $\boldsymbol{M}_{\text{mu}} = \boldsymbol{M}_L$ in Algorithm 2.5 with $\boldsymbol{A}_{\text{mu},\ell}^{-1}$ as smoother, and with $m_{\text{pre}} = 0$, as well as $m_{\text{post}} = 1$ as smoothing steps. Note, that the choice of $m_{\text{pre}} = 0$ basically means skipping the pre-smoothing, implying that $\boldsymbol{M}_{\text{mu},\ell}$ is not symmetric.

For an illustration of the action of both preconditioners see Figure 2.4.

Remark 2.15. *By setting $h_0 = h/2$ we easily see that the hybrid and the multiplicative two-level Schwarz methods from Section 2.4 are special cases of the hybrid and multiplicative multilevel Schwarz methods of this section, respectively.*

Chapter 3

Two-level Schwarz Preconditioner for Biot's Consolidation Model

In this chapter, the theory of the two-level Schwarz methods as introduced in Chapter 2 is applied to H^{div}-conforming finite element discretizations of Biot's quasi-static consolidation model. The main theoretical result is the proof of the stable decomposition in Section 3.4.3, which is the most important ingredient in the proof of convergence of the methods as preconditioner in state-of-the-art Krylov subspace solvers. The idea here is to use the mass-conservation property of the discretization to derive an equivalent, nearly-singular, positive-definite system that allows us to prove stability of arbitrary decompositions of the finite element functions. The special structure of the system implies a parameter dependence of the method on the inverse of the permeability tensor, which cannot be avoided in the proof. Nevertheless, this dependence can only be slightly observed in the numerical experiments and does not restrict the applicability of the solver, which is demonstrated by various numerical simulations in Section 3.5 testing the performance of the preconditioned iterative solvers in a two-level and a multilevel setup. The numerical performance of the solver is excellent, showing uniform results in the simulations in the mesh size, robust for all considered regimes of the parameters in the system, especially for the ratio $\frac{\lambda}{\mu}$ of the Lamé constants of elasticity, even in the nearly incompressible case $\lambda \gg \mu$, as well as for the ratio $\frac{c_s \mu}{\alpha^2}$ of the specific storage coefficient c_s and the Biot-Willis constant α. To our knowledge, the successful application of this monolithic approach of overlapping two- and multilevel Schwarz methods to H^{div}-conforming discretizations of the equations in poroelasticity is novel in the literature.

In the field of linear poroelasticity, the physical behavior of saturated porous and elastic materials is described. Examples of such materials can be found in various types of rock such as sandstone, as well as in clay, wet sand or concrete, but also in organic tissue such as liver, brain or articular cartilage. The equations governing poroelastic

media have been invented and developed by the engineer Biot in a series of works [Bio35, Bio41, Bio55, Bio72] starting in 1935, based on the pioneering work of Terzaghi [Ter25] in 1925. The quasi-static model we will focus on was suggested by Biot in [Bio41] by hypothesizing the form of the macroscopic constitutive relations of poroelastic materials and generalized to anisotropic solids in [Bio55]. It is a combination of linear elasticity describing the deformation of a solid body, and Darcy's law, which describes fluid flow through a porous medium. Instead of a heterogeneous description that incorporates the finescale behavior of such materials as fluid-structure interaction problem, models of Biot type follow a continuum mechanical approach and describe the effective behavior of poroelastic materials on a macroscopic length scale.

The research on theory and applications of this topic has been and is still in ongoing progress in the scientific community, as it is for the development of numerical solvers.

About three decades after the engineering approach of Biot a formal mathematical derivation of the linear model has been proposed by Burridge, Keller in [BK81] using homogenization theory. Mathematically rigorous derivations have been presented by Sanchez-Palencia in [SP80] and by Nguetseng in [Ngu90].

Discretizations for Biot's consolidation model have been developed since the late 1960's, see [Chr68, SW69, YYN71], where mainly continuous finite element spaces were employed, besides a few attempts with finite difference and finite volume methods. The most popular numerical methods have been standard finite element discretizations due to their ability to address complicated domains, but they suffer from inaccuracies called locking for certain parameter ranges involving spurious pressure oscillations, see [Yi17] and the literature cited therein, which is in parts already known from discretizations in linear elasticity when the material is nearly incompressible or thin, see [BS92, Arn81] as well as [Bra13, Kapitel VI §4]. This pushed the development of discretizations towards finite element methods that are robust with respect to the parameters in the system to avoid locking. Such methods were found in mixed finite element formulations, where different approaches were being pursued, such as discontinuous and continuous mixed Galerkin methods [Phi05, PW07a, PW07b, PW08, Lee16, Lee18], also for a total-stress formulation in [ORB16], a least-squares mixed finite element method [TPS08], different stabilization techniques [AGLR08, RGHZ16], also for hybrid mixed finite elements [NRH19], space-time variational mixed finite element formulations [BRK17], and nonconforming mixed methods [Yi13, Yi14, HRGZ17], without any claim to completeness of this list.

For their iterative solution different methods have been proposed, such as stress splitting schemes [MW13, MWW14, CWT15, BRK17, BBN$^+$17, HKLW20, AKW23], domain decomposition methods [FWR13, Flo18], an Uzawa-type algorithm [HKLP20], block preconditioners [FBG10, ABB12, CWT15, CWF16, LMW17, AGH$^+$19], and multigrid preconditioners [GR17, AHH$^+$22].

Lately, the conservation of mass became an especially relevant feature that has been addressed by H^{div}-conforming mixed finite elements [KR18, HK18, HKLP19], by finite elements based on enrichment [GRH$^+$19, LY22] and by mixed virtual finite elements [WCWZ22].

We will focus on H^{div}-conforming mixed finite element discretizations proposed by [KR18, HK18, HKLP19], as they provide locking-free and mass conserving schemes. Since these discretizations result in large saddle-point systems, ill-conditioned with respect to standard finite element bases, effective preconditioners are needed for their iterative solution.

To this end, Hong and Kraus developed a block-diagonal preconditioner in [HK18, HKLP19] that is based on parameter-dependent norms, which they apply to a mass conservative H^{div}-conforming three-field mixed finite element discretization of Biot's quasi-static consolidation model, as well as a multiple-network poroelastic system. They show robustness of their scheme and provide numerical tests.

In [BKMRB21], Boon et. al. apply a block preconditioner to a mixed finite element discretization of a total-pressure four-field formulation of Biot's consolidation model using Taylor-Hood as well as H^{div}-conforming mixed finite element spaces. In their numerical results they present robustness of the condition numbers for the case where an LU factorization is used to invert the blocks, which is of little practical applicability for large scale computations due to the growing size of the blocks. An approximate inversion of the blocks yields suboptimal results.

Jayadharan, Khattatov and Yotov apply a domain decomposition approach with non-overlapping subdomains to a five-field fully coupled H^{div}-conforming mixed formulation in [JKY21]. They use a reduction of the subdomain problems to an interface problem for a Lagrange multiplier, beneath two splitting approaches. Beneath the fact that their discretization yields very large systems due to the five-field formulation, their numerical experiments show deteriorating iteration counts of GMRES and CG for all three methods.

None of these approaches has successfully applied the Schwarz theory to H^{div}-conforming

finite element discretizations of Biot's consolidation model, which is our motivation and goal for this chapter.

The structure of this chapter is as follows.

The quasi-static model of linear consolidation by Biot is introduced as a three-field formulation in Section 3.1 and discretized in Section 3.2 by a family of H^{div}-conforming mixed finite element methods as proposed in [KR18, HK18, HKLP19]. Section 3.3 defines multiplicative and hybrid overlapping two-level Schwarz methods for preconditioning the resulting saddle point systems and thus providing efficient solvers. The convergence of the methods is proven in Section 3.4. In Section 3.5, numerical tests are described and their results are presented showing that the dependence of the convergence constants on the permeability tensor can only be observed slightly and do not restrict the applicability of the method. A scaling leads to robustness even with extremely large chosen parameters. Moreover, the optimal choice of the relaxation factor of the hybrid two-level Schwarz is investigated and the performance of the multilevel Schwarz methods are examined.

3.1 Biot's Linear Consolidation Model

Biot's consolidation model in three-field formulation couples the displacement field $\boldsymbol{u}$ of the solid component, the seepage velocity $\boldsymbol{v}$ of the fluid, and the pressure p in a fully saturated porous medium at constant temperature in a linear model. It is posed on a computational domain $\Omega \subset \mathbb{R}^d$ with $d = 2$ or $d = 3$ on a time interval $(0, T)$. In strong form, Biot's quasi-static model of consolidation reads

$$\begin{aligned} -\operatorname{div}\left(2\mu\boldsymbol{\varepsilon}(\boldsymbol{u}) + \lambda \operatorname{div}(\boldsymbol{u})\boldsymbol{I}\right) + \alpha\nabla p &= \boldsymbol{f} && \text{in } \Omega \times (0,T), \\ \boldsymbol{v} + \boldsymbol{K}\nabla p &= \boldsymbol{0} && \text{in } \Omega \times (0,T), \\ -\alpha \operatorname{div} \partial_t \boldsymbol{u} - \operatorname{div} \boldsymbol{v} - c_s \partial_t p &= g && \text{in } \Omega \times (0,T), \end{aligned} \tag{3.1}$$

with initial conditions $\boldsymbol{u}(0) = \boldsymbol{u}_0$, and $p(0) = p_0$, such that (3.1) is satisfied at time $t = 0$. For existence, uniqueness, and regularity of solutions of (3.1) we refer to [Žen84] as well as to [Sho00] and the literature cited therein. An introduction to the equations of poroelasticity from a physical point of view as well as an overview over the constants can, for example, be found in [DC93, Cou04]. In these works and the literature cited therein, application scenarios, as well as a discussion of boundary settings and famous problems as Mandel's problem [Man53] can be found here as well. The equations are derived and

explained in the following.

To start with, linearity of the model is assured by the hypothesis of small perturbations, which consists of the hypothesis of small displacements

$$\left\| \frac{1}{L} \boldsymbol{u} \right\| \ll 1,$$

where L is the characteristic observation length scale, the hypothesis of infinitesimal small transformations

$$\left\| \nabla \boldsymbol{u} \right\| \ll 1,$$

as well as the hypothesis of small variations of the Lagrangian porosity and the fluid mass density, see [Cou04, Chapter 5]. The effective stress of the elastic medium is described by Hooke's law, a linearized model in elasticity. It obeys the constitutive equation

$$\boldsymbol{\sigma}_{\text{eff}}(\boldsymbol{u}) = 2\mu \boldsymbol{\varepsilon}(\boldsymbol{u}) + \lambda \operatorname{div}(\boldsymbol{u}) \boldsymbol{I},$$

where $\boldsymbol{I}$ is the identity tensor and the linearized strain tensor is given by

$$\boldsymbol{\varepsilon}(\boldsymbol{u}) = \frac{1}{2} \left(\nabla \boldsymbol{u} + \nabla \boldsymbol{u}^T \right).$$

The physical parameters $\lambda \geq 0$ and $\mu > 0$ denote the Lamé constants defined in terms of Young's modulus E and Poisson ratio ν by

$$\lambda = \frac{\nu E}{(1+\nu)(1-2\nu)}, \qquad \text{and} \qquad \mu = \frac{E}{2(1+\nu)}.$$

For an introduction to the theory of elasticity and the relations of the constants we refer to [Cia88].

The total stress $\boldsymbol{\sigma}(\boldsymbol{u})$ of the poroelastic medium is defined as the sum of the effective stress $\boldsymbol{\sigma}_{\text{eff}}(\boldsymbol{u})$ and the stress $\alpha p \boldsymbol{I}$ due to the pore pressure, where the Biot-Willis constant α [BW57] takes values between zero and one and represents unaccounted volume changes, for instant small air inclusions in soil [KR18]. For soft soils like sand or clay α is considered to be one or very close to one, whereas for rocks as sandstone or granite it might take smaller values around 0.2 to 0.9, cf. [DC93]. With a given force $\boldsymbol{f}$ the constitutive

equations are given by

$$-\operatorname{div}(\boldsymbol{\sigma}_{\text{eff}}(\boldsymbol{u}) - \alpha p \boldsymbol{I}) = \boldsymbol{f} \qquad \text{in } \Omega \times (0,T).$$

The Biot-Willis constant α couples the equations of elasticity via the pore pressure with Darcy's law

$$\boldsymbol{v} = -\boldsymbol{K}\nabla p \qquad \text{in } \Omega \times (0,T),$$

where $\boldsymbol{K}$ is the symmetric positive-definite permeability tensor of the saturated porous medium. It is assumed that $\boldsymbol{K}$ is bounded in the sense that there are positive constants $C_{\boldsymbol{K}} \geq c_{\boldsymbol{K}} > 0$, such that

$$c_{\boldsymbol{K}} \|\boldsymbol{v}\|_{\Omega}^2 \leq \left(\boldsymbol{K}^{-1}\boldsymbol{v}, \boldsymbol{v}\right)_{\Omega} \leq C_{\boldsymbol{K}} \|\boldsymbol{v}\|_{\Omega}^2 \qquad \forall \boldsymbol{v} \in [L^2(\Omega)]^d. \tag{3.2}$$

In the simplest case, we consider a permeability tensor of the form $\boldsymbol{K} = \kappa \boldsymbol{I}$, constant over Ω and constant over the time interval $(0,T)$ with the scalar constant κ satisfying

$$0 < c_{\boldsymbol{K}} \leq \kappa^{-1} \leq C_{\boldsymbol{K}} < \infty.$$

The set of equations is completed by introducing the mass balance equation

$$-\alpha \operatorname{div} \partial_t \boldsymbol{u} - \operatorname{div} \boldsymbol{v} - c_s \partial_t p = g \qquad \text{in } \Omega \times (0,T),$$

with a given sink or source term g, and the specific storage coefficient $c_s \geq 0$. The constant c_s combines the compressibility and the porosity of the medium and is a measure of the amount of fluid that can be forced into the medium by pressure increments at constant volume, cf. [Sho00].

Semi-discretization in time by the backward Euler method to time step size $\tau > 0$ results in a sequence of semi-discrete and static problems of the form

$$\begin{aligned} -2\mu \operatorname{div} \boldsymbol{\varepsilon}(\boldsymbol{u}) - \lambda \nabla \operatorname{div} \boldsymbol{u} + \alpha \nabla p &= \boldsymbol{f} && \text{in } \Omega, \\ \boldsymbol{v} + \boldsymbol{K}\nabla p &= \boldsymbol{0} && \text{in } \Omega, \\ -\frac{\alpha}{\tau} \operatorname{div} \boldsymbol{u} - \operatorname{div} \boldsymbol{v} - \frac{c_s}{\tau} p &= \bar{g} && \text{in } \Omega, \end{aligned} \tag{3.3}$$

in each time step, where $\bar{g} = g - \frac{\alpha}{\tau} \operatorname{div} \boldsymbol{u}_{\text{old}} - \frac{c_s}{\tau} p_{\text{old}}$ with $\boldsymbol{u}_{\text{old}}$ and p_{old} taken from the previous time step and all other quantities referring to the new time step. We point out that the specific time discretization is irrelevant, since all implicit methods will result in the necessity of solving systems of similar kind. Furthermore, we note that $\boldsymbol{u}/\tau$ has the unit of speed and α is dimensionless. Hence, it is dimensionally meaningful to add $(\alpha \operatorname{div} \boldsymbol{u})/\tau$ and $\operatorname{div} \boldsymbol{v}$ and p/τ in the last equation.

Following [HKLP19] we transform (3.3) into a symmetric problem by proper scaling and substitution of variables. Therefore, we transform (3.3) into

$$\begin{aligned} -\operatorname{div} \boldsymbol{\varepsilon}(\boldsymbol{u}) - \tfrac{\lambda}{2\mu} \nabla \operatorname{div} \boldsymbol{u} + \tfrac{\alpha}{2\mu} \nabla p &= \tfrac{1}{2\mu} \boldsymbol{f} && \text{in } \Omega, \\ \tfrac{\alpha}{2\mu} \boldsymbol{K}^{-1} \boldsymbol{v} + \tfrac{\alpha}{2\mu} \nabla p &= \boldsymbol{0} && \text{in } \Omega, \\ -\operatorname{div} \boldsymbol{u} - \tfrac{\tau}{\alpha} \operatorname{div} \boldsymbol{v} - \tfrac{c_s}{\alpha} p &= \tfrac{\tau}{\alpha} \bar{g} && \text{in } \Omega. \end{aligned}$$

By substitution of the variables and right hand side

$$\tilde{\boldsymbol{v}} = \frac{\tau}{\alpha} \boldsymbol{v}, \qquad \tilde{p} = \frac{\alpha}{2\mu} p, \qquad \tilde{\boldsymbol{f}} = \frac{1}{2\mu} \boldsymbol{f}, \qquad \tilde{g} = \frac{\tau}{\alpha} g - \operatorname{div} \boldsymbol{u}_{\text{old}} - \frac{c_s}{\alpha} p_{\text{old}},$$

as well as the physical parameters

$$\tilde{\lambda} = \frac{\lambda}{2\mu}, \qquad \tilde{\boldsymbol{K}}^{-1} = \frac{\alpha^2}{2\mu\tau} \boldsymbol{K}^{-1}, \qquad \tilde{c_s} = \frac{2\mu c_s}{\alpha^2}, \tag{3.4}$$

we obtain the rescaled system

$$\begin{aligned} -\operatorname{div} \boldsymbol{\varepsilon}(\boldsymbol{u}) + \tilde{\lambda} \nabla (\operatorname{div} \boldsymbol{u}) + \nabla \tilde{p} &= \tilde{\boldsymbol{f}} && \text{in } \Omega, \\ \tilde{\boldsymbol{K}}^{-1} \tilde{\boldsymbol{v}} + \nabla \tilde{p} &= \boldsymbol{0} && \text{in } \Omega, \\ -\operatorname{div} \boldsymbol{u} - \operatorname{div} \tilde{\boldsymbol{v}} - \tilde{c_s} \tilde{p} &= \tilde{g} && \text{in } \Omega. \end{aligned} \tag{3.5}$$

Since this is the normalized system we build our analysis on, we will omit the tilde symbol from here on.

This system is closed by proper boundary conditions. As usual, essential boundary conditions enter the definitions of the function spaces $U \subset [H^1(\Omega)]^d$ and $V \subset H^{\text{div}}(\Omega)$ for displacement and seepage velocity, respectively. We will choose a particular combination of boundary conditions in the presentation and analysis of the two-level algorithm in Sections 3.3 and 3.4, although one might also want to consider other combinations

for which certain arguments and basic estimates have to be adapted and exchanged accordingly. The general assumptions that are required to conduct an analysis similar to the one presented in this work are as follows.

Assumption 3.1. *The boundary conditions on the spaces U and V are such that:*

1. *The seepage velocity $\boldsymbol{v}$ is uniquely determined.*

2. *Korn's inequality [Kor08] holds for $\boldsymbol{u}$ in the continuous setting as well as for $\boldsymbol{u}_h$ in the discrete setting. For sufficient conditions in the continuous case we refer to [DV02] and the literature cited therein. For the discrete case, see [Bre04].*

3. *The pressure space Q is chosen such that the operator* $\operatorname{div}\colon V \to Q$ *is surjective. The boundary conditions on U are compatible such that also* $\operatorname{div}\colon U \to Q$ *is surjective.*

To give one example, which applies to the setting of the analysis presented in Section 3.4, Korn's inequality

$$\frac{1}{c_e}\|\nabla \boldsymbol{u}\|_{\Omega}^2 \leq \|\boldsymbol{\varepsilon}(\boldsymbol{u})\|_{\Omega}^2 \leq \|\nabla \boldsymbol{u}\|_{\Omega}^2$$

holds for all $\boldsymbol{u} \in [H_0^1(\Omega)]^d$. In line with this, we assume on the whole boundary a homogeneous Dirichlet (no-slip) boundary condition on $\boldsymbol{u}$ and a Neumann boundary condition on p, which translates to an essential condition on $\boldsymbol{v}$. Accordingly, we choose

$$U = [H_0^1(\Omega)]^d, \qquad V = H_0^{\operatorname{div}}(\Omega), \qquad Q = L_0^2(\Omega).$$

The weak formulation of (3.5) is then: find $(\boldsymbol{u}, \boldsymbol{v}, p) \in U \times V \times Q$, such that

$$\begin{aligned} e(\boldsymbol{u}, \boldsymbol{\varphi}) + \lambda d(\boldsymbol{u}, \boldsymbol{\varphi}) - b(p, \boldsymbol{\varphi}) &= (\boldsymbol{f}, \boldsymbol{\varphi})_{\Omega} && \forall \boldsymbol{\varphi} \in U, \\ k(\boldsymbol{v}, \boldsymbol{\psi}) - b(p, \boldsymbol{\psi}) &= 0 && \forall \boldsymbol{\psi} \in V, \\ -b(q, \boldsymbol{u}) - b(q, \boldsymbol{v}) - c_s(p, q)_{\Omega} &= (g, q)_{\Omega} && \forall q \in Q, \end{aligned} \tag{3.6}$$

with bilinear forms

$$\begin{aligned} e(\boldsymbol{u}, \boldsymbol{\varphi}) &= (\boldsymbol{\varepsilon}(\boldsymbol{u}), \boldsymbol{\varepsilon}(\boldsymbol{\varphi}))_{\Omega}, & d(\boldsymbol{u}, \boldsymbol{\varphi}) &= (\operatorname{div} \boldsymbol{u}, \operatorname{div} \boldsymbol{\varphi})_{\Omega}, \\ b(p, \boldsymbol{\psi}) &= (p, \operatorname{div} \boldsymbol{\psi})_{\Omega}, & k(\boldsymbol{v}, \boldsymbol{\psi}) &= (\boldsymbol{K}^{-1}\boldsymbol{v}, \boldsymbol{\psi})_{\Omega}. \end{aligned}$$

3.2 Mass Conservative Discretization

The model problem (3.6) is discretized by a family of strongly mass-conserving mixed methods as proposed in [KR18, HK18, HKLP19], where the displacement and seepage velocity fields are approximated in suitable H^{div}-conforming spaces U_h and V_h and the pressure space Q_h consists of piecewise polynomial functions discontinuous at element interfaces such that the condition

$$\operatorname{div} U_h = Q_h, \qquad \operatorname{div} V_h = Q_h, \tag{3.7}$$

is satisfied. By choosing the spaces as in (3.7) the discrete mass equation

$$-\operatorname{div} \boldsymbol{u}_h - \operatorname{div} \boldsymbol{v}_h - c_s p_h = g_h$$

is fulfilled pointwise, which serves as key ingredient for the convergence analysis in Section 3.4 of the two-level Schwarz methods introduced in Section 3.3. The combined finite element space for the mixed method is then defined by

$$X_h = U_h \times V_h \times Q_h.$$

Examples for such combinations of spaces are given by the triplets $RT_k \times RT_k \times Q_k$, $BDM_k \times RT_{k-1} \times P_{k-1}$ or $BDFM_k \times RT_{k-1} \times P_{k-1}$. Since the space U_h is not H^1-conforming, a discrete interior penalty discontinuous Galerkin bilinear form $e_h(\cdot,\cdot)$ is used to approximate $e(\cdot,\cdot)$ as detailed below.

Let $\mathcal{T}_h$ be a family of shape regular triangulations of the computational domain Ω into mesh cells T with diameter $h_T = \operatorname{diam}(T)$ where $h = \max_{T\in\mathcal{T}_h} h_T$ denotes the mesh size. Let $\Gamma_{I,h}$ be the set of all interior faces (edges in two dimensions) of $\mathcal{T}_h$, and $\Gamma_{B,h}$ be the set of all faces on the boundary $\partial\Omega$. For every face $F \in \Gamma_{I,h}$ there are two neighboring cells $T_+, T_- \in \mathcal{T}_h$ such that $F = \partial T_+ \cap \partial T_-$. Let $\boldsymbol{n}$ be the unit outward normal vector pointing from T_+ to T_-. On every face $F \in \Gamma_{I,h}$ and for any $\boldsymbol{\varphi} \in [L^2(\Omega)]^d$ and $\boldsymbol{\tau} \in [L^2(\Omega)]^{d\times d}$, we define jump $[\![\,]\!]$ and average $\{\!\{\,\}\!\}$ by

$$[\![\boldsymbol{\varphi}]\!] = \boldsymbol{\varphi}_+ - \boldsymbol{\varphi}_-, \qquad \{\!\{\boldsymbol{\tau}\boldsymbol{n}\}\!\} = \frac{1}{2}\left(\boldsymbol{\tau}_+ + \boldsymbol{\tau}_-\right)\boldsymbol{n},$$

where $\boldsymbol{\varphi}_{\pm} = \boldsymbol{\varphi}\big|_{T_{\pm}}$ and $\boldsymbol{\tau}_{\pm} = \boldsymbol{\tau}\big|_{T_{\pm}}$. Further, on the broken Sobolev space

$$[H^1(\Omega, \mathcal{T}_h)]^d = \left\{ \boldsymbol{\varphi} \in [L^2(\Omega)]^d \ : \ \boldsymbol{\varphi}\big|_T \in [H^1(T)]^d \right\}$$

we introduce the discrete norm

$$\|\boldsymbol{\varphi}\|_{1,h} = \left(\sum_{T \in \mathcal{T}_h} \|\nabla \boldsymbol{\varphi}\|_T^2 + \sum_{F \in \Gamma_{I,h}} \frac{1}{h} \|[\![\boldsymbol{\varphi}]\!]\|_F^2 + \sum_{B \in \Gamma_{B,h}} \frac{1}{h} \|\boldsymbol{\varphi}\|_B^2 \right)^{\frac{1}{2}}. \tag{3.8}$$

Following the work of [Arn82, Nit71] we choose an interior penalty discontinuous Galerkin approximation of $e(\cdot,\cdot)$ in the nonconforming space U_h. Therefore, on $U_h \times U_h$ we define the symmetric discrete bilinear form

$$\begin{aligned} e_h(\boldsymbol{u}_h, \boldsymbol{\varphi}) = & \sum_{T \in \mathcal{T}_h} \big(\boldsymbol{\varepsilon}(\boldsymbol{u}_h), \boldsymbol{\varepsilon}(\boldsymbol{\varphi})\big)_T + \sum_{F \in \Gamma_{I,h}} \frac{\eta}{h} \big([\![\boldsymbol{u}_h]\!], [\![\boldsymbol{\varphi}]\!]\big)_F \\ & - \sum_{F \in \Gamma_{I,h}} \big(\{\!\{\boldsymbol{\varepsilon}(\boldsymbol{u}_h)\boldsymbol{n}\}\!\}, [\![\boldsymbol{\varphi}]\!]\big)_F - \sum_{F \in \Gamma_{I,h}} \big([\![\boldsymbol{u}_h]\!], \{\!\{\boldsymbol{\varepsilon}(\boldsymbol{\varphi})\boldsymbol{n}\}\!\}\big)_F \\ & + \sum_{B \in \Gamma_{B,h}} \frac{\eta}{h} \big(\boldsymbol{u}_h, \boldsymbol{\varphi}\big)_B \\ & - \sum_{B \in \Gamma_{B,h}} \big(\boldsymbol{\varepsilon}(\boldsymbol{u}_h)\boldsymbol{n}, \boldsymbol{\varphi}\big)_B - \sum_{B \in \Gamma_{B,h}} \big(\boldsymbol{u}_h, \boldsymbol{\varepsilon}(\boldsymbol{\varphi})\boldsymbol{n}\big)_B. \end{aligned}$$

Here, the penalty parameter $\eta > 0$ is chosen large enough to ensure coercivity of $e_h(\cdot,\cdot)$, i.e., there is a positive constant c such that

$$e_h(\boldsymbol{\varphi}, \boldsymbol{\varphi}) \geq c \|\boldsymbol{\varphi}\|_{1,h}^2 \quad \forall \boldsymbol{\varphi} \in U_h. \tag{3.9}$$

We assume that the boundary conditions are chosen such that this relation, which is a discrete form of Korn's inequality, holds as formulated in Assumption 3.1, cf. [Bre04] in this context. In addition to (3.9) we have continuity of $e_h(\cdot,\cdot)$ in the norm $\|\cdot\|_{1,h}$, i.e.,

$$e_h(\boldsymbol{u}_h, \boldsymbol{\varphi}) \leq c \|\boldsymbol{u}_h\|_{1,h} \|\boldsymbol{\varphi}\|_{1,h} \quad \forall \boldsymbol{u}_h, \boldsymbol{\varphi} \in U_h. \tag{3.10}$$

Since U_h is H^{div}-conforming, the form $b(\boldsymbol{u}, \boldsymbol{\varphi}) = (\operatorname{div} \boldsymbol{u}, \operatorname{div} \boldsymbol{\varphi})_\Omega$ does not need a penalty formulation. The mass-conserving mixed method based on the finite element space X_h

can then be represented as

$$\mathbb{A}_h\left(\begin{pmatrix}\boldsymbol{u}_h\\ \boldsymbol{v}_h\\ p_h\end{pmatrix},\begin{pmatrix}\boldsymbol{\varphi}\\ \boldsymbol{\psi}\\ q\end{pmatrix}\right)=\mathbb{F}_h\left(\begin{pmatrix}\boldsymbol{\varphi}\\ \boldsymbol{\psi}\\ q\end{pmatrix}\right), \tag{3.11}$$

where the discrete bilinear form $\mathbb{A}_h(\cdot,\cdot): X_h \times X_h \to \mathbb{R}$ is defined by

$$\begin{aligned}\mathbb{A}_h\left(\begin{pmatrix}\boldsymbol{u}_h\\ \boldsymbol{v}_h\\ p_h\end{pmatrix},\begin{pmatrix}\boldsymbol{\varphi}\\ \boldsymbol{\psi}\\ q\end{pmatrix}\right) =& e_h(\boldsymbol{u}_h,\boldsymbol{\varphi})+\lambda d(\boldsymbol{u}_h,\boldsymbol{\varphi})+k(\boldsymbol{v}_h,\boldsymbol{\psi})\\ &-b(p_h,\boldsymbol{\varphi}+\boldsymbol{\psi})-b(q,\boldsymbol{u}_h+\boldsymbol{v}_h)-c_s(p_h,q)_\Omega\end{aligned}$$

and the right hand side is given by

$$\mathbb{F}_h\left(\begin{pmatrix}\boldsymbol{\varphi}\\ \boldsymbol{\psi}\\ q\end{pmatrix}\right)=(\boldsymbol{f},\boldsymbol{\varphi})_\Omega+(g_h,q)_\Omega,$$

with g_h chosen as the L^2-projection $\Pi^h g$. System (3.11) is consistent and has a unique solution, which has been proven in [KR18] and follows essentially by the special choice of H^{div}-conforming discretization spaces, coercivity (3.9), continuity (3.10) and the discrete inf-sup conditions, see for example [BBF13, HL02, SST03, Bre74],

$$\inf_{q\in Q_h}\sup_{\boldsymbol{\varphi}\in U_h}\frac{(\operatorname{div}\boldsymbol{\varphi},q)_\Omega}{\|\boldsymbol{\varphi}\|_{1,h}\|q\|_\Omega}\geq\gamma_u>0$$

and

$$\inf_{q\in Q_h}\sup_{\boldsymbol{\psi}\in V_h}\frac{(\operatorname{div}\boldsymbol{\psi},q)_\Omega}{\|\boldsymbol{\psi}\|_{H^{\mathrm{div}}(\Omega)}\|q\|_\Omega}\geq\gamma_v>0.$$

From [KR18, Theorem 3] we know that the error for the spatial semi-discretization with $RT_k\times RT_k\times Q_k$-elements for all times $t>0$ satisfies

$$\mu\|\boldsymbol{u}_h(t)-\boldsymbol{u}(t)\|_{1,h}^2\leq ch^{2k}\left(M+\mu\|u(t)\|_{H^{k+1}(\Omega)}^2\right),$$

and

$$c_s\big\|p_h(t)-p(t)\big\|_{\Omega}^2+\big\|\boldsymbol{K}^{-1/2}(\boldsymbol{v}_h-\boldsymbol{v})\big\|_{L^2(0,t;L^2(\Omega))}^2 \\ \leq ch^{2k}\left(M+c_s\big\|p(t)\big\|_{H^{k+1}(\Omega)}^2\right),$$

where $M=\alpha^2\left\|\partial_t \operatorname{div}\boldsymbol{u}\right\|_{L^2(0,T;H^{k+1}(\Omega))}^2+\left\|\boldsymbol{v}\right\|_{L^2(0,T;H^{k+1}(\Omega))}^2$. Further, under the assumption

$$\big|\tilde{\boldsymbol{u}}(t)-\boldsymbol{u}(t)\big|_{H^{\operatorname{div}}(\Omega)}^2\leq c_{\mu,\lambda}h^{2k+2}\big|\operatorname{div}\boldsymbol{u}(t)\big|_{H^{k+1}(\Omega)}$$

for the error of the Ritz-projection $\tilde{\boldsymbol{u}}$ to the exact solution $\boldsymbol{u}$ in the H^{div}-seminorm the authors obtain an additional bound for the divergence of the displacement

$$\lambda\big|\boldsymbol{u}_h(t)-\boldsymbol{u}(t)\big|_{H^{\operatorname{div}}(\Omega)}^2\leq c_{\mu,\lambda}h^{2k+2}\left(M+\lambda\big\|\operatorname{div}\boldsymbol{u}(t)\big\|_{H^{k+1}(\Omega)}^2\right),$$

as well as the improved result

$$c_s\big\|p_h(t)-p(t)\big\|_{\Omega}^2+\big\|\boldsymbol{K}^{-1/2}(\boldsymbol{v}_h-\boldsymbol{v})\big\|_{L^2(0,t;L^2(\Omega))}^2 \\ \leq c_{\mu,\lambda}h^{2k+2}\left(M+c_s\big\|p(t)\big\|_{H^{k+1}(\Omega)}^2\right).$$

3.3 Two-level Algorithm

In this section we define a monolithic two-level algorithm for the mixed problem (3.11) as outlined in Section 2.4. The method differs from partitioned solvers, which rely on and exploit the block structure of the system.

For $j=1,\dots,J$ let the vertex patch Ω_j be the subdomain consisting of all mesh cells touching the vertex $\mathbf{p}_j$. This could be the union of 4 quadrilaterals or 6 triangles (in 2D), or 8 hexahedra (in 3D) for inner vertices of uniform mesh partitions. With the subdomains Ω_j we associate subspaces $X_j\subset X_h$. To this end, we define

$$U_j=U_h\cap H_0^{\operatorname{div}}(\Omega_j),\qquad V_j=V_h\cap H_0^{\operatorname{div}}(\Omega_j),\qquad Q_j=Q_h\cap L_0^2(\Omega_j),$$

continued by zero on $\Omega\setminus\Omega_j$, and set

$$X_j=U_j\times V_j\times Q_j.$$

Moreover, for $H > h$ let $\mathcal{T}_H$ be a triangulation of the coarse domain $\Omega_0 = \Omega$ such that the associated subspace $X_0 = X_H \subset X_h$. Then, X_0 plays the role of a global coarse space and we can decompose X_h into an overlapping sum by

$$X_h = X_0 + \sum_{j=1}^{J} X_j.$$

For $j = 1, \dots, J$ we introduce local bilinear forms $\mathbb{A}_j(\cdot,\cdot) : X_j \times X_j \to \mathbb{R}$ as restrictions of $\mathbb{A}_h(\cdot,\cdot)$ to X_j, as well as a coarse bilinear form $\mathbb{A}_0(\cdot,\cdot) : X_0 \times X_0 \to \mathbb{R}$ by

$$\mathbb{A}_j\left(\begin{pmatrix}\boldsymbol{u}_j\\ \boldsymbol{v}_j\\ p_j\end{pmatrix}, \begin{pmatrix}\boldsymbol{\varphi}_j\\ \boldsymbol{\psi}_j\\ q_j\end{pmatrix}\right) = \mathbb{A}_h\left(\begin{pmatrix}\boldsymbol{u}_j\\ \boldsymbol{v}_j\\ p_j\end{pmatrix}, \begin{pmatrix}\boldsymbol{\varphi}_j\\ \boldsymbol{\psi}_j\\ q_j\end{pmatrix}\right) \qquad \forall \begin{pmatrix}\boldsymbol{u}_j\\ \boldsymbol{v}_j\\ p_j\end{pmatrix}, \begin{pmatrix}\boldsymbol{\varphi}_j\\ \boldsymbol{\psi}_j\\ q_j\end{pmatrix} \in X_j,$$

$$\mathbb{A}_0\left(\begin{pmatrix}\boldsymbol{u}_0\\ \boldsymbol{v}_0\\ p_0\end{pmatrix}, \begin{pmatrix}\boldsymbol{\varphi}_0\\ \boldsymbol{\psi}_0\\ q_0\end{pmatrix}\right) = \omega_0^{-1}\mathbb{A}_H\left(\begin{pmatrix}\boldsymbol{u}_0\\ \boldsymbol{v}_0\\ p_0\end{pmatrix}, \begin{pmatrix}\boldsymbol{\varphi}_0\\ \boldsymbol{\psi}_0\\ q_0\end{pmatrix}\right) \qquad \forall \begin{pmatrix}\boldsymbol{u}_0\\ \boldsymbol{v}_0\\ p_0\end{pmatrix}, \begin{pmatrix}\boldsymbol{\varphi}_0\\ \boldsymbol{\psi}_0\\ q_0\end{pmatrix} \in X_0,$$

where the coarse bilinear form is scaled by a relaxation factor $0 < \omega_0 < 1$. In practice we will set $\omega_0 = 1$, but we need to define it for the convergence analysis. Further, we define projections $P_j \colon X_h \to X_j$ and $P_0 \colon X_h \to X_0$ by

$$\mathbb{A}_j\left(P_j\begin{pmatrix}\boldsymbol{u}_h\\ \boldsymbol{v}_h\\ p_h\end{pmatrix}, \begin{pmatrix}\boldsymbol{\varphi}_j\\ \boldsymbol{\psi}_j\\ q_j\end{pmatrix}\right) = \mathbb{A}_h\left(\begin{pmatrix}\boldsymbol{u}_h\\ \boldsymbol{v}_h\\ p_h\end{pmatrix}, \begin{pmatrix}\boldsymbol{\varphi}_j\\ \boldsymbol{\psi}_j\\ q_j\end{pmatrix}\right) \qquad \forall \begin{pmatrix}\boldsymbol{\varphi}_j\\ \boldsymbol{\psi}_j\\ q_j\end{pmatrix} \in X_j, \tag{3.12}$$

for $j = 0, 1, \dots, J$. Note, that the bilinear form $e_H(\cdot,\cdot)$ is not inherited from $e_h(\cdot,\cdot)$ although $X_H \subset X_h$, because it differs in the face and boundary terms. Thus, P_0 is not a projection, since consequently $\mathbb{A}_0(\cdot,\cdot)$ differs from $\mathbb{A}_h(\cdot,\cdot)$.

With the specification of the P_j and P_0 in (3.12) we recall the definition of the multiplicative Schwarz operator $P_{\text{mu}} : X_h \to X_h$, the additive Schwarz operator $P_{\text{ad}} : X_h \to X_h$, and the hybrid Schwarz operator $P_{\text{hyb}} : X_h \to X_h$ from Section 2.4 by

$$P_{\text{mu}} = I - E_{\text{mu}}, \qquad E_{\text{mu}} = (I - P_J) \cdots (I - P_1)(I - P_0), \tag{3.13}$$

and

$$P_{\text{ad}} = \sum_{j=0}^{J} P_j, \tag{3.14}$$

as well as

$$P_{\text{hyb}} = I - E_{\text{hyb}}, \qquad E_{\text{hyb}} = \left(I - \omega \sum_{j=1}^{J} P_j \right) (I - P_0) \left(I - \omega \sum_{j=1}^{J} P_j \right),$$

where ω is a relaxation factor that depends on the overlap and can also be used for tuning the method.

3.4 Convergence Analysis

There is no immediate convergence analysis for subspace correction methods for saddle point problems. Therefore, we follow [Sch99] and transform (3.11) into an equivalent, singularly perturbed problem for any fixed $c_s > 0$. Then, we prove robust convergence with respect to $c_s \to 0$, cf. [AFW97, LWXZ07, KM15] by applying the abstract two-level Schwarz theory as introduced in Section 2.4.

In order to be able to apply the two-level Schwarz framework for symmetric, positive definite operators, we first transform system (3.11) into an equivalent, symmetric and positive definite (Lemma 3.4), singularly perturbed problem in Section 3.4.1. Then, we follow the abstract theory of two-level Schwarz methods for H^{div}-conforming finite element discretizations as introduced in Section 2.4. First, we make the standard Assumptions 2.8 and 2.9 on the covering $\{\Omega_j\}_{j=1}^J$ of the domain Ω, see [TW10, AFW97, FK01]. In addition, we need to verify Assumptions 2.2 to 2.4.

As a preparatory step for the proof of Assumption 2.2 we decompose the product space W_h on which the singularly perturbed problem is formulated into an orthogonal sum with respect to the kernel of a divergence operator in Section 3.4.2. In Section 3.4.3 we then provide a main result of this chapter by proving Theorem 3.11, i.e., the stable decomposition of arbitrary finite element functions in W_h. In Section 3.4.4 we will then proof the local stability in Lemma 3.12, and the strengthened Cauchy-Schwarz inequalities in Lemma 3.13.

All this gives us a bound for the condition number of the preconditioned singularly

perturbed system. Since this bound is robust in the perturbation parameter c_s, even in the case $c_s \to 0$, and we have equivalence of the singularly perturbed problem and the discrete three-field formulation (3.11) this proves the following two Theorems 3.2 and 3.3.

Theorem 3.2. *The multiplicative two-level Schwarz method* (3.13) *converges uniformly in the mesh size h and is robust with respect to the rescaled material parameters λ and c_s.*

Theorem 3.3. *The additive two-level Schwarz method* (3.14) *converges independently of the mesh size h and the rescaled material parameters λ and c_s.*

The rest of this section is devoted to the proof of the stated preliminaries.

3.4.1 An Equivalent, Singularly Perturbed Problem

As shown in [KR18, HKLP19], strong mass conservation can be recovered from system (3.11) by using H^{div}-conforming discretizations for the displacement field and seepage velocity in combination with piecewise polynomial approximations of the pressure if the discrete spaces match. To be more precise, the discrete mass balance equation

$$-\operatorname{div} \boldsymbol{u}_h - \operatorname{div} \boldsymbol{v}_h - c_s p_h = g_h$$

is fulfilled point-wise if the condition (3.7) is met. This allows us to substitute

$$p_h = -c_s^{-1} \left(\operatorname{div} \boldsymbol{u}_h + \operatorname{div} \boldsymbol{v}_h + g_h \right)$$

and obtain the equivalent, singularly perturbed system

$$\begin{aligned} e_h(\boldsymbol{u}_h, \boldsymbol{\varphi}) + \lambda d(\boldsymbol{u}_h, \boldsymbol{\varphi}) + c_s^{-1} d(\boldsymbol{u}_h + \boldsymbol{v}_h, \boldsymbol{\varphi}) &= (\boldsymbol{f}, \boldsymbol{\varphi})_\Omega - c_s^{-1} (g_h, \operatorname{div} \boldsymbol{\varphi})_\Omega \\ k(\boldsymbol{v}_h, \boldsymbol{\psi}) + c_s^{-1} d(\boldsymbol{u}_h + \boldsymbol{v}_h, \boldsymbol{\psi}) &= -c_s^{-1} (g_h, \operatorname{div} \boldsymbol{\psi})_\Omega \end{aligned}$$

for all $(\boldsymbol{\varphi}, \boldsymbol{\psi}) \in W_h = U_h \times V_h$. We rewrite this system as

$$\mathscr{A}_h \left(\begin{pmatrix} \boldsymbol{u}_h \\ \boldsymbol{v}_h \end{pmatrix}, \begin{pmatrix} \boldsymbol{\varphi} \\ \boldsymbol{\psi} \end{pmatrix} \right) = \mathscr{F}_h \left(\begin{pmatrix} \boldsymbol{\varphi} \\ \boldsymbol{\psi} \end{pmatrix} \right)$$

with

$$\mathscr{A}_h\left(\begin{pmatrix}\boldsymbol{u}_h\\ \boldsymbol{v}_h\end{pmatrix},\begin{pmatrix}\boldsymbol{\varphi}\\ \boldsymbol{\psi}\end{pmatrix}\right)=A_h\left(\begin{pmatrix}\boldsymbol{u}_h\\ \boldsymbol{v}_h\end{pmatrix},\begin{pmatrix}\boldsymbol{\varphi}\\ \boldsymbol{\psi}\end{pmatrix}\right)+D\left(\begin{pmatrix}\boldsymbol{u}_h\\ \boldsymbol{v}_h\end{pmatrix},\begin{pmatrix}\boldsymbol{\varphi}\\ \boldsymbol{\psi}\end{pmatrix}\right), \tag{3.15}$$

where the bilinear forms $A_h(\cdot,\cdot)$ and $D(\cdot,\cdot)$ are defined on $W_h \times W_h$ by

$$\begin{aligned} A_h\left(\begin{pmatrix}\boldsymbol{u}_h\\ \boldsymbol{v}_h\end{pmatrix},\begin{pmatrix}\boldsymbol{\varphi}\\ \boldsymbol{\psi}\end{pmatrix}\right) &= e_h(\boldsymbol{u}_h,\boldsymbol{\varphi})+k(\boldsymbol{v}_h,\boldsymbol{\psi}),\\ D\left(\begin{pmatrix}\boldsymbol{u}_h\\ \boldsymbol{v}_h\end{pmatrix},\begin{pmatrix}\boldsymbol{\varphi}\\ \boldsymbol{\psi}\end{pmatrix}\right) &= \lambda d(\boldsymbol{u}_h,\boldsymbol{\varphi})+c_s^{-1}d(\boldsymbol{u}_h+\boldsymbol{v}_h,\boldsymbol{\varphi}+\boldsymbol{\psi}) \end{aligned} \tag{3.16}$$

and the right hand side is given by

$$\mathscr{F}_h\left(\begin{pmatrix}\boldsymbol{\varphi}\\ \boldsymbol{\psi}\end{pmatrix}\right)=(\boldsymbol{f},\boldsymbol{\varphi})_{\Omega}-c_s^{-1}(g_h,\operatorname{div}(\boldsymbol{\varphi}+\boldsymbol{\psi}))_{\Omega}.$$

Lemma 3.4. *The form $\mathscr{A}_h(\cdot,\cdot)$ defines a symmetric, positive definite bilinear form on W_h.*

Proof. It is clear by definition that $\mathscr{A}_h(\boldsymbol{w}_h,\boldsymbol{w}_h)\geq 0$ for all $\boldsymbol{w}_h\in W_h$, and also $\mathscr{A}_h(\boldsymbol{w}_h,\boldsymbol{w}_h)=0$, if $\boldsymbol{w}_h=\boldsymbol{0}$. Therefore, let $\mathscr{A}_h(\boldsymbol{w}_h,\boldsymbol{w}_h)=0$ for $\boldsymbol{w}_h=(\boldsymbol{u}_h,\boldsymbol{v}_h)\in W_h$. Then, the choice of the boundary values as formulated in Assumption 3.1 for the displacement, as well as the seepage velocity, together with

$$\mathscr{A}_h\left(\begin{pmatrix}\boldsymbol{u}_h\\ \boldsymbol{v}_h\end{pmatrix},\begin{pmatrix}\boldsymbol{u}_h\\ \boldsymbol{v}_h\end{pmatrix}\right)\geq c\|\boldsymbol{u}_h\|_{1,h}^2+c_{\boldsymbol{K}}\|\boldsymbol{v}_h\|_{\Omega}^2,$$

implies $\boldsymbol{w}_h=\boldsymbol{0}$. The symmetry of $\mathscr{A}_h(\cdot,\cdot)$ follows by the symmetry of the bilinear forms $e_h(\cdot,\cdot)$, $k(\cdot,\cdot)$ and $d(\cdot,\cdot)$. □

Similar to Section 3.3 we choose local subspaces $W_j\subset W_h$ associated with the subdomains Ω_j, such that

$$W_j=U_j\times V_j$$

as well as a global coarse space $W_0=U_H\times V_H$, which provide a decomposition of W_h

into an overlapping sum of subspaces, i.e.,

$$W_h = W_0 + \sum_{j=1}^{J} W_j.$$

Note, that every $\boldsymbol{w}_h \in W_h$ then admits a decomposition of the form

$$\boldsymbol{w}_h = \sum_{j=0}^{J} \boldsymbol{w}_j, \qquad \boldsymbol{w}_j \in W_j. \tag{3.17}$$

For $j = 1, \ldots, J$ we introduce the local bilinear forms $\mathscr{A}_j(\cdot,\cdot) : W_j \times W_j \to \mathbb{R}$ as restrictions of $\mathscr{A}_h(\cdot,\cdot)$ to W_j and a coarse bilinear form $\mathscr{A}_0(\cdot,\cdot) : W_0 \times W_0 \to \mathbb{R}$ as $\mathscr{A}_0(\cdot,\cdot) = \mathscr{A}_H(\cdot,\cdot)$. Analogously to (3.12) we define the projections $P_j \colon W_h \to W_j$ and the projection-like operator $P_0 \colon W_h \to W_0$ by

$$\mathscr{A}_j\left(P_j\begin{pmatrix}\boldsymbol{u}_h\\ \boldsymbol{v}_h\end{pmatrix}, \begin{pmatrix}\boldsymbol{\varphi}_j\\ \boldsymbol{\psi}_j\end{pmatrix}\right) = \mathscr{A}_h\left(\begin{pmatrix}\boldsymbol{u}_h\\ \boldsymbol{v}_h\end{pmatrix}, \begin{pmatrix}\boldsymbol{\varphi}_j\\ \boldsymbol{\psi}_j\end{pmatrix}\right) \qquad \forall \begin{pmatrix}\boldsymbol{\varphi}_j\\ \boldsymbol{\psi}_j\end{pmatrix} \in W_j.$$

3.4.2 Decomposition of the Spaces according to $\ker(D)$

Our goal in Section 3.4.3 is to prove that for any $\boldsymbol{w}_h \in W_h$, any decomposition of the form (3.17) is stable under the global and local bilinear forms $\mathscr{A}_h(\cdot,\cdot) : W_h \times W_h \to \mathbb{R}$ and $\mathscr{A}_j(\cdot,\cdot) : W_j \times W_j \to \mathbb{R}$, respectively. As a preparatory step we decompose the space W_h into the orthogonal sum

$$W_h = \ker(D) \oplus \ker(D)^{\perp} \tag{3.18}$$

of the kernel of the summed divergence operator

$$W_h^0 = \ker(D) = \left\{ \begin{pmatrix}\boldsymbol{u}_h\\ \boldsymbol{v}_h\end{pmatrix} \in W_h \;:\; D\left(\begin{pmatrix}\boldsymbol{u}_h\\ \boldsymbol{v}_h\end{pmatrix}, \begin{pmatrix}\boldsymbol{\varphi}\\ \boldsymbol{\psi}\end{pmatrix}\right) = 0 \quad \forall \begin{pmatrix}\boldsymbol{\varphi}\\ \boldsymbol{\psi}\end{pmatrix} \in W_h \right\}$$

and its $A_h(\cdot,\cdot)$-orthogonal complement

$$\ker(D)^{\perp} = \left\{ \begin{pmatrix}\boldsymbol{u}_h\\ \boldsymbol{v}_h\end{pmatrix} \in W_h \;:\; A_h\left(\begin{pmatrix}\boldsymbol{u}_h\\ \boldsymbol{v}_h\end{pmatrix}, \begin{pmatrix}\boldsymbol{\varphi}\\ \boldsymbol{\psi}\end{pmatrix}\right) = 0 \quad \forall \begin{pmatrix}\boldsymbol{\varphi}\\ \boldsymbol{\psi}\end{pmatrix} \in \ker(D) \right\},$$

cf. [AFW97, Hip97]. To this end we introduce the discrete Helmholtz-decompositions

$$U_h = U_h^0 \oplus U_h^\perp, \qquad V_h = V_h^0 \oplus V_h^\perp,$$

of U_h and V_h into their divergence-free subspaces U_h^0 and V_h^0, and their $e_h(\cdot,\cdot)$-orthogonal and $k(\cdot,\cdot)$-orthogonal complements, respectively, cf. [AFW10, KM15],

$$\begin{aligned} U_h^\perp &= \big\{ \boldsymbol{u}_h \in U_h \ : \ e_h\big(\boldsymbol{u}_h, \boldsymbol{\varphi}\big) = 0 \quad \forall \boldsymbol{\varphi} \in U_h^0 \big\}, \\ V_h^\perp &= \big\{ \boldsymbol{v}_h \in V_h \ : \ k\big(\boldsymbol{v}_h, \boldsymbol{\psi}\big) = 0 \quad \forall \boldsymbol{\psi} \in V_h^0 \big\}. \end{aligned}$$

The following lemma characterizes $W_h^0 = \ker(D) \subset W_h$.

Lemma 3.5. *For $\lambda > 0$ there holds*

$$W_h^0 = \ker(D) = U_h^0 \times V_h^0, \qquad W_h^\perp = \ker(D)^\perp = U_h^\perp \times V_h^\perp.$$

Proof. First, let $(\boldsymbol{u}_h, \boldsymbol{v}_h) \in \ker(D)$. Setting $\boldsymbol{\varphi} = \boldsymbol{u}_h$ and $\boldsymbol{\psi} = \boldsymbol{v}_h$ in

$$D\left(\begin{pmatrix}\boldsymbol{u}_h \\ \boldsymbol{v}_h\end{pmatrix}, \begin{pmatrix}\boldsymbol{\varphi} \\ \boldsymbol{\psi}\end{pmatrix}\right) = \lambda d\big(\boldsymbol{u}_h, \boldsymbol{\varphi}\big) + c_s^{-1} d\big(\boldsymbol{u}_h + \boldsymbol{v}_h, \boldsymbol{\varphi} + \boldsymbol{\psi}\big)$$

shows that a necessary condition is $\operatorname{div} \boldsymbol{u}_h = 0$, and as a consequence also $\operatorname{div} \boldsymbol{v}_h = 0$. Thus, $\ker(D) \subset U_h^0 \times V_h^0$. On the other hand, $(\boldsymbol{u}_h^0, \boldsymbol{v}_h^0) \in U_h^0 \times V_h^0$ implies immediately

$$D\left(\begin{pmatrix}\boldsymbol{u}_h^0 \\ \boldsymbol{v}_h^0\end{pmatrix}, \begin{pmatrix}\boldsymbol{\varphi} \\ \boldsymbol{\psi}\end{pmatrix}\right) = 0$$

for arbitrary $(\boldsymbol{\varphi}, \boldsymbol{\psi}) \in W_h$, and we have $U_h^0 \times V_h^0 \subset \ker(D)$. The statement for $W_h^\perp$ follows directly due to its definition as orthogonal complement to W_h^0 in (3.18). □

Note that for all $\boldsymbol{w}_h^0 = (\boldsymbol{u}_h^0, \boldsymbol{v}_h^0) \in W_h^0$ and $\boldsymbol{\pi}_h = (\boldsymbol{\varphi}_h, \boldsymbol{\psi}_h) \in W_h$, there holds

$$\mathscr{A}_h\left(\boldsymbol{w}_h^0, \boldsymbol{\pi}_h\right) = e_h\big(\boldsymbol{u}_h^0, \boldsymbol{\varphi}_h\big) + k\big(\boldsymbol{v}_h^0, \boldsymbol{\psi}_h\big). \tag{3.19}$$

Remark 3.6. *For $\lambda = 0$ the space $\ker(D)$ is larger, because D is then defined by*

$d\left(\boldsymbol{u}_h + \boldsymbol{v}_h, \boldsymbol{\varphi}_h + \boldsymbol{\psi}_h\right)$ *only and therefore*

$$\ker(D) = U_h^0 \times V_h^0 + \Big\{(\boldsymbol{u}, \boldsymbol{v}) \in U_h^\perp \times V_h^\perp \ : \ \operatorname{div} \boldsymbol{u} = -\operatorname{div} \boldsymbol{v}\Big\}.$$

3.4.3 Stable Decomposition

The main result of this section is Theorem 3.11. Before we can prove it, we begin by recalling known facts from the literature and showing some auxiliary results.

In order to represent divergence free functions in the displacement space U_h^0 we introduce the space

$$S(\Omega, \mathcal{T}_h) = \big\{s_h \in H_0^1(\Omega) \ : \ s_h|_T \in H^2(T) \text{ for all } T \in \mathcal{T}_h\big\},$$

which is equipped with the discrete norm

$$\big\|s_h\big\|_{2,h} = \left(\sum_{T\in\mathcal{T}_h} \big\|\nabla^2 s_h\big\|_T^2 + \sum_{F\in\Gamma_{I,h}} \frac{1}{h}\big\|[\![\partial_n s_h]\!]\big\|_F^2 + \sum_{B\in\Gamma_{B,h}} \frac{1}{h}\big\|\partial_n s_h\big\|_B^2\right)^{\frac{1}{2}}. \quad (3.20)$$

Following [KS14], the bilinear form $e_h(\cdot,\cdot)$ on the divergence free subspace is algebraically equivalent to the bilinear form of a C^0-interior penalty formulation of a corresponding biharmonic problem by assigning velocities $\boldsymbol{u}_h = \mathbf{curl}\, s_h$, where $\boldsymbol{u}_h$ belongs to the discrete stream function space $S(\Omega, \mathcal{T}_h)$. Using arguments as in [KS14], it is easy to see that in two space dimensions there holds the elementary identity

$$\big\|\mathbf{curl}\, s_h\big\|_{1,h} = \big\|s_h\big\|_{2,h}, \quad \forall s_h \in S(\Omega, \mathcal{T}_h), \quad (3.21)$$

where $\mathbf{curl} = (\partial_2, -\partial_1)$. Indeed, since in two dimensions, $\mathbf{curl}\, s_h$ is just the rotated gradient, equality of the bulk term is obvious. Comparing the jump terms in the definition (3.8) with (3.20), the latter contains only the jump of $\partial_n s_h$, while in the former we consider the jump of the whole vector $\mathbf{curl}\, s_h$. Since $s_h \in H^2(T)$ for every cell, the trace of $\mathbf{curl}\, s_h$ is defined on every interface. Furthermore, its tangential derivatives from both adjacent cells coincide almost everywhere, such that for an interior face F there holds

$$\big\|[\![\mathbf{curl}\, s_h]\!]\big\|_F = \big\|[\![\nabla s_h]\!]\big\|_F = \big\|[\![\partial_n s_h]\!]\big\|_F.$$

On the boundary, the definition of $S(\Omega, \mathcal{T}_h)$ immediately implies that the tangential derivative vanishes and thus $\|\mathbf{curl}\, s_h\|_B = \|\partial_n s_h\|_B$. We point out that we did not verify the identity (3.21) for the three dimensional case $\Omega \subset \mathbb{R}^3$ and leave this special matter for future work.

Next, we recall a result from [BW05, Lemma 4.2] showing that functions in $S(\Omega, \mathcal{T}_h)$ have a stable decomposition with respect to the norm (3.20).

Proposition 3.7. *Every $s \in S(\Omega, \mathcal{T}_h)$ admits a decomposition $s = \sum_{j=0}^{J} s_j$ with $s_j \in S(\Omega_j, \mathcal{T}_h)$, $s_0 \in S(\Omega_0, \mathcal{T}_H)$, such that*

$$\|s_0\|_{2,H}^2 + \sum_{j=1}^{J} \|s_j\|_{2,h}^2 \leq c \left(1 + \frac{H^4}{\delta^4}\right) \|s\|_{2,h}^2$$

for some constant $c > 0$.

The above results suffice to prove the stability of the decomposition of the divergence free subspace of U_h with respect to the elasticity energy norm.

Lemma 3.8. *Every function $\boldsymbol{u}^0 \in U_h^0$ admits a decomposition of the form $\boldsymbol{u}^0 = \sum_{j=0}^{J} \boldsymbol{u}_j^0$ with $\boldsymbol{u}_j^0 \in U_j^0$, which satisfies the bound*

$$e_H(\boldsymbol{u}_0^0, \boldsymbol{u}_0^0) + \sum_{j=1}^{J} e_h(\boldsymbol{u}_j^0, \boldsymbol{u}_j^0) \leq c \left(1 + \frac{H^4}{\delta^4}\right) e_h(\boldsymbol{u}^0, \boldsymbol{u}^0)$$

for some constant $c > 0$.

Proof. For every $\boldsymbol{u}^0 \in U_h^0$ there exists a unique stream function $s \in S(\Omega, \mathcal{T}_h)$, such that

$$\boldsymbol{u}^0 = \mathbf{curl}\, s.$$

Now we decompose $s = \sum_{j=0}^{J} s_j$ and choose

$$\boldsymbol{u}_j^0 = \mathbf{curl}\, s_j,$$

such that $\boldsymbol{u}_j^0 \in U_j^0$ and by linearity of the curl

$$\boldsymbol{u}^0 = \sum_{j=0}^{J} \boldsymbol{u}_j^0.$$

Continuity of $e_h(\cdot,\cdot)$, the stability of the decomposition in Proposition 3.7 and identity (3.21) yield

$$\begin{aligned} e_H(\boldsymbol{u}_0^0,\boldsymbol{u}_0^0)+\sum_{j=1}^J e_h(\boldsymbol{u}_j^0,\boldsymbol{u}_j^0) &\le c\left(\big\|\mathbf{curl}\, s_0\big\|_{1,H}^2+\sum_{j=1}^J\big\|\mathbf{curl}\, s_j\big\|_{1,h}^2\right)\\ &= c\left(\big\|s_0\big\|_{2,H}^2+\sum_{j=1}^J\big\|s_j\big\|_{2,h}^2\right)\le c\left(1+\frac{H^4}{\delta^4}\right)\big\|s\big\|_{2,h}^2\\ &= c\left(1+\frac{H^4}{\delta^4}\right)\big\|\mathbf{curl}\, s\big\|_{1,h}^2\le c\left(1+\frac{H^4}{\delta^4}\right)e_h\big(\boldsymbol{u}^0,\boldsymbol{u}^0\big), \end{aligned}$$

where we have used Korn's inequality (3.9) in the last estimate. □

Next, we show that also $U_h^\perp$ has a stable decomposition with respect to the elasticity bilinear form.

Lemma 3.9. *Every function $\boldsymbol{u}^\perp\in U_h^\perp$ admits a decomposition of the form $\boldsymbol{u}^\perp=\sum_{j=0}^J\boldsymbol{u}_j^1$ with $\boldsymbol{u}_j^1\in U_j$, which satisfies the bound*

$$e_H\big(\boldsymbol{u}_0^1,\boldsymbol{u}_0^1\big)+\sum_{j=1}^J e_h\big(\boldsymbol{u}_j^1,\boldsymbol{u}_j^1\big)\le c\left(1+\frac{H^2}{\delta^2}\right)e_h\big(\boldsymbol{u}^\perp,\boldsymbol{u}^\perp\big) \tag{3.22}$$

for some constant $c>0$.

Proof. We use the construction in [TW10, chapter 10] and adapt it to the bilinear form $e_h(\cdot,\cdot)$. To this end we introduce the semicontinuous space U^+ containing functions which can be characterized as the image of U_h under an orthogonal projection $\Theta^\perp\colon H_0^{\mathrm{div}}(\Omega)\to H_0^{\mathrm{div},\perp}(\Omega)$, i.e., $U^+=\Theta^\perp(U_h)$, which is defined by

$$\Theta^\perp\boldsymbol{u}=\boldsymbol{u}-\mathbf{curl}\, w,$$

where $w\in H_0^{\mathbf{curl},\perp}(\Omega)$ satisfies

$$\big(\mathbf{curl}\, w,\mathbf{curl}\, v\big)_\Omega=\big(\boldsymbol{u},\mathbf{curl}\, v\big)_\Omega,\quad \forall v\in H_0^\perp(\mathbf{curl};\Omega).$$

Here $H_0^{\mathrm{div},\perp}(\Omega)$ and $H_0^{\mathbf{curl},\perp}(\Omega)$ denote the orthogonal complements of the divergence-

free and curl-free subspaces

$$H_0^{\mathrm{div},0}(\Omega) = \Big\{ \boldsymbol{v} \in H_0^{\mathrm{div}}(\Omega) \ : \ \mathrm{div}\, \boldsymbol{v} = 0 \Big\},$$
$$H_0^{\mathbf{curl},0}(\Omega) = \Big\{ v \in H_0^{\mathrm{curl}}(\Omega) \ : \ \mathbf{curl}\, v = \mathbf{0} \Big\},$$

of $H_0^{\mathrm{div}}(\Omega)$ and $H_0^{\mathrm{curl}}(\Omega)$ in the $(\cdot,\cdot)_{H^{\mathrm{div}}(\Omega)}$ and $(\cdot,\cdot)_{H^{\mathrm{curl}}(\Omega)}$ inner products, respectively, i.e.,

$$H_0^{\mathrm{div}}(\Omega) = H_0^{\mathrm{div},0}(\Omega) \oplus H_0^{\mathrm{div},\perp}(\Omega), \tag{3.23}$$
$$H_0^{\mathrm{curl}}(\Omega) = H_0^{\mathbf{curl},0}(\Omega) \oplus H_0^{\mathbf{curl},\perp}(\Omega). \tag{3.24}$$

Note that the decompositions (3.23) and (3.24) are both L^2-orthogonal as well. The finite dimensional space U^+ is not a finite element space, however the divergence of these functions are finite element functions.

Further, we define the projection $P^h \colon H_0^{\mathrm{div}}(\Omega) \to U^+$ by

$$\big(\mathrm{div}\, \Big(P^h \boldsymbol{u} - \boldsymbol{u} \Big), \mathrm{div}\, \boldsymbol{\varphi} \big)_\Omega = 0, \quad \forall \boldsymbol{\varphi} \in U^+.$$

From [TW10, Lemma 10.12] for convex Ω, we have the approximation property

$$\big\| \boldsymbol{u}^\perp - P^h \boldsymbol{u}^\perp \big\|_\Omega \leq c\, h \big\| \mathrm{div}\, \boldsymbol{u}^\perp \big\|_\Omega \qquad \forall \boldsymbol{u}^\perp \in U_h^\perp. \tag{3.25}$$

Then, for P^h there holds

$$\big\| P^h \boldsymbol{u}^\perp \big\|_{H^{\mathrm{div}}(\Omega)} \leq c_\Omega \big\| \boldsymbol{u}^\perp \big\|_{H^{\mathrm{div}}(\Omega)}, \quad \forall \boldsymbol{u}^\perp \in U_h^\perp$$

with a constant c_Ω depending on Ω. It follows immediately from [CKS05, Proposition 4.6] that for another constant c, depending on mesh grading and shape regularity, we have

$$\big\| P^h \boldsymbol{u}^\perp \big\|_{1,h} \leq c \big\| \boldsymbol{u}^\perp \big\|_{1,h}. \tag{3.26}$$

For the L^2-projection $\Pi^H \colon [L^2(\Omega)]^d \to U_0$ onto the coarse space U_0 there holds

$$\big\| \boldsymbol{u} - \Pi^H \boldsymbol{u} \big\|_\Omega \leq c\, H \big\| \boldsymbol{u} \big\|_{1,h}. \tag{3.27}$$

Additionally, we have H^1-stability of Π^H, i.e.,

$$\left\|\Pi^H \boldsymbol{u}\right\|_{1,h} \leq c\left\|\boldsymbol{u}\right\|_{1,h}. \tag{3.28}$$

We are now ready to choose

$$\begin{aligned}\boldsymbol{u}_0^1 &= \Pi^H P^h \boldsymbol{u}^\perp,\\ \boldsymbol{u}_j^1 &= I^h\left(\theta_j\left(\boldsymbol{u}^\perp - \boldsymbol{u}_0^1\right)\right),\end{aligned}$$

where I^h is the canonical interpolation into U_h and $\{\theta_j\}_{j=1}^J$ the piecewise linear partition of unity defined in (2.18). We point at the fact that $\boldsymbol{u}_j^1 \in U_j$ is not necessarily a function in $U_j^\perp$.

Let $\tilde{\boldsymbol{u}} = \boldsymbol{u}^\perp - \boldsymbol{u}_0^1$. Noting that on each cell $T \in \mathcal{T}_h$, the function $\theta_j\tilde{\boldsymbol{u}}$ is polynomial and hence

$$\left\|I^h\left(\theta_j\tilde{\boldsymbol{u}}\right)\right\|_{1,h} \leq c\left\|\theta_j\tilde{\boldsymbol{u}}\right\|_{1,h}. \tag{3.29}$$

By continuity of the bilinear form $e_H(\cdot,\cdot)$, the bounds (3.28) and (3.26), and coercivity of $e_h(\cdot,\cdot)$ we get

$$\begin{aligned}e_H\big(\boldsymbol{u}_0^1, \boldsymbol{u}_0^1\big) &\leq c\left\|\Pi^H P^h \boldsymbol{u}^\perp\right\|_{1,h}^2\\ &\leq c\left\|P^h\boldsymbol{u}^\perp\right\|_{1,h}^2 \leq c\left\|\boldsymbol{u}^\perp\right\|_{1,h}^2 \leq c\, e_h\big(\boldsymbol{u}^\perp, \boldsymbol{u}^\perp\big)\end{aligned} \tag{3.30}$$

and

$$\left\|\tilde{\boldsymbol{u}}\right\|_{1,h}^2 \leq c\left(\left\|\boldsymbol{u}^\perp\right\|_{1,h}^2 + \left\|\Pi^H P^h \boldsymbol{u}^\perp\right\|_{1,h}^2\right) \leq c\, e_h\big(\boldsymbol{u}^\perp, \boldsymbol{u}^\perp\big). \tag{3.31}$$

By (3.25), (3.27), and using $h \leq H$, we obtain

$$\begin{aligned}\left\|\tilde{\boldsymbol{u}}\right\|_\Omega &\leq \left\|\boldsymbol{u}^\perp - P^h\boldsymbol{u}^\perp\right\|_\Omega + \left\|P^h\boldsymbol{u}^\perp - \Pi^H P^h \boldsymbol{u}^\perp\right\|_\Omega\\ &\leq c\, h\left\|\operatorname{div}\boldsymbol{u}^\perp\right\|_\Omega + c\, H\left\|\boldsymbol{u}^\perp\right\|_{1,h}\\ &\leq c\, H\left\|\boldsymbol{u}^\perp\right\|_{1,h}.\end{aligned} \tag{3.32}$$

Using continuity of $e_h(\cdot,\cdot)$, (3.29), the properties of θ_j, (3.32), (3.31), and coercivity of

$e_h(\cdot,\cdot)$, as well as the finite covering Assumption 2.9, we get

$$\begin{aligned}\sum_{j=1}^{J} e_h\big(\boldsymbol{u}_j^1,\boldsymbol{u}_j^1\big) &\le c\sum_{j=1}^{J}\big\|I^h\left(\theta_j\tilde{\boldsymbol{u}}\right)\big\|_{1,h}^2 \le c\sum_{j=1}^{J}\big\|\theta_j\tilde{\boldsymbol{u}}\big\|_{1,h}^2\\ &\le c\sum_{j=1}^{J}\Bigg(\sum_{T\in\mathcal{T}_h}\Big(\big\|\nabla\theta_j\big\|_{L^\infty(T)}^2\big\|\tilde{\boldsymbol{u}}\big\|_T^2+\big\|\theta_j\nabla\tilde{\boldsymbol{u}}\big\|_T^2\Big)\\ &\qquad+\sum_{F\in\Gamma_{I,h}}\frac{1}{h}\big\|\theta_j[\![\tilde{\boldsymbol{u}}]\!]\big\|_F^2+\sum_{B\in\Gamma_{B,h}}\frac{1}{h}\big\|\theta_j\tilde{\boldsymbol{u}}\big\|_B^2\Bigg)\\ &\le c\frac{1}{\delta^2}\big\|\tilde{\boldsymbol{u}}\big\|_\Omega^2+c\big\|\tilde{\boldsymbol{u}}\big\|_{1,h}^2\\ &\le c\left(1+\frac{H^2}{\delta^2}\right)e_h\big(\boldsymbol{u}^\perp,\boldsymbol{u}^\perp\big).\end{aligned}\tag{3.33}$$

Finally, combining (3.30) and (3.33) results in the desired estimate (3.22). □

Moreover, W_h^0 has a stable decomposition with respect to $\mathscr{A}_h(\cdot,\cdot)$.

Lemma 3.10. *Every $\boldsymbol{w}^0=(\boldsymbol{u}^0,\boldsymbol{v}^0)\in W_h^0$ admits a decomposition of the form*

$$\boldsymbol{w}^0=\sum_{j=0}^{J}\boldsymbol{w}_j^0,\qquad \boldsymbol{w}_j^0\in W_j^0,$$

which satisfies the bound

$$\sum_{j=0}^{J}\mathscr{A}_j\left(\boldsymbol{w}_j^0,\boldsymbol{w}_j^0\right)\le c\left(1+\frac{H^4}{\delta^4}\right)\mathscr{A}_h\left(\boldsymbol{w}^0,\boldsymbol{w}^0\right)$$

for some constant $c>0$ independent of the model parameters and of J.

Proof. By Lemma 3.8, every $\boldsymbol{u}^0\in U_h^0$ has a decomposition $\boldsymbol{u}^0=\sum_{J=0}^{J}\boldsymbol{u}_j^0$ with $\boldsymbol{u}_j^0\in U_j^0$, such that

$$e_H\big(\boldsymbol{u}_0^0,\boldsymbol{u}_0^0\big)+\sum_{j=1}^{J}e_h\big(\boldsymbol{u}_j^0,\boldsymbol{u}_j^0\big)\le c\left(1+\frac{H^4}{\delta^4}\right)e_h\big(\boldsymbol{u}^0,\boldsymbol{u}^0\big),$$

with $\boldsymbol{u}_j^0=\mathbf{curl}\,s_j$, where s_j is chosen as in the proof of Lemma 3.8.

Further, by a classical result in domain decomposition theory that goes back to [DW94], every $r \in S(\Omega, \mathcal{T}_h)$ has a decomposition $r = \sum_{j=0}^{J} r_j$, such that

$$\sum_{j=0}^{J} \|r_j\|_{H^1(\Omega)}^2 \leq c \left(1 + \frac{H}{\delta}\right) \|r\|_{H^1(\Omega)}^2.$$

By choosing $\boldsymbol{v}_j^0 = \mathbf{curl}\, r_j$, we get for the second term in (3.19)

$$\begin{aligned} \sum_{j=0}^{J} k(\boldsymbol{v}_j^0, \boldsymbol{v}_j^0) &\leq C_{\boldsymbol{K}} \sum_{j=0}^{J} \|\mathbf{curl}\, r_j\|_{\Omega}^2 = C_{\boldsymbol{K}} \sum_{j=0}^{J} \|r_j\|_{H^1(\Omega)}^2 \\ &\leq c\, C_{\boldsymbol{K}} \left(1 + \frac{H}{\delta}\right) \|r\|_{H^1(\Omega)}^2 = c\, C_{\boldsymbol{K}} \left(1 + \frac{H}{\delta}\right) \|\mathbf{curl}\, r\|_{\Omega}^2 \\ &\leq c\, \frac{C_{\boldsymbol{K}}}{c_{\boldsymbol{K}}} \left(1 + \frac{H}{\delta}\right) k(\boldsymbol{v}^0, \boldsymbol{v}^0) \end{aligned} \tag{3.34}$$

where we have used (3.2). The assertion of the lemma follows then by choosing $\boldsymbol{w}_j^0 = \left(\boldsymbol{u}_j^0, \boldsymbol{v}_j^0\right)_{\Omega} = (\mathbf{curl}\, s_j, \mathbf{curl}\, r_j)_{\Omega} \in W_j^0$ for all $j = 0, \ldots, J$. □

We are ready to state and prove our main result.

Theorem 3.11 (Stable decomposition)**.** *Every $\boldsymbol{w} \in W_h$ admits a decomposition of the form*

$$\boldsymbol{w} = \sum_{j=0}^{J} \boldsymbol{w}_j, \qquad \boldsymbol{w}_j \in W_j,$$

which satisfies the bound

$$\sum_{j=0}^{J} \mathscr{A}_j(\boldsymbol{w}_j, \boldsymbol{w}_j) \leq c_{\boldsymbol{K},\Omega} \left(1 + \frac{H^4}{\delta^4}\right) \mathscr{A}_h(\boldsymbol{w}, \boldsymbol{w}),$$

for some constant $c_{\boldsymbol{K},\Omega} > 0$ independent of the model parameters λ and c_s in the discrete bilinear form $\mathscr{A}_h(\cdot,\cdot)$ defined in (3.15)–(3.16) and independent of the number of subdomains J as well as of the discretization parameter h, but dependent on Ω and $\boldsymbol{K}$.

Proof. For $\boldsymbol{w} = \mathbf{0}$ the result is trivial. So let $\boldsymbol{w} \in W_h$, $\boldsymbol{w} \neq \mathbf{0}$, be arbitrary. To start with,

we decompose $\boldsymbol{w}$ in the form

$$\boldsymbol{w} = \begin{pmatrix} \boldsymbol{u} \\ \boldsymbol{v} \end{pmatrix} = \begin{pmatrix} \boldsymbol{u}^0 \\ \boldsymbol{v}^0 \end{pmatrix} + \begin{pmatrix} \boldsymbol{u}^\perp \\ \boldsymbol{v}^\perp \end{pmatrix},$$

with $(\boldsymbol{u}^0, \boldsymbol{v}^0) \in U^0 \times V^0$ and $(\boldsymbol{u}^\perp, \boldsymbol{v}^\perp) \in U^\perp \times V^\perp$. Since we need to control the term $d(\boldsymbol{u}+\boldsymbol{v}, \boldsymbol{u}+\boldsymbol{v})$, we define $\boldsymbol{\varphi} = \boldsymbol{u}^\perp + \boldsymbol{v}^\perp$ and decompose it into $\boldsymbol{\varphi} = \boldsymbol{\varphi}^0 + \boldsymbol{\varphi}^\perp$, $\boldsymbol{\varphi}^0 \in V^0$, where $\boldsymbol{\varphi}^0$ and $\boldsymbol{\varphi}^\perp$ are orthogonal with respect to $k(\cdot,\cdot)$. Then, the decomposition of $\boldsymbol{w}$ that we will use in our proof reads as

$$\begin{aligned} \boldsymbol{w} = \begin{pmatrix} \boldsymbol{u} \\ \boldsymbol{v} \end{pmatrix} &= \begin{pmatrix} \boldsymbol{u}^0 \\ \boldsymbol{v}^0 \end{pmatrix} + \begin{pmatrix} \boldsymbol{u}^\perp \\ -\boldsymbol{u}^\perp \end{pmatrix} + \begin{pmatrix} \boldsymbol{0} \\ \boldsymbol{\varphi} \end{pmatrix} \\ &= \begin{pmatrix} \boldsymbol{u}^0 \\ \boldsymbol{v}^0 \end{pmatrix} + \begin{pmatrix} \boldsymbol{0} \\ \boldsymbol{\varphi}^0 \end{pmatrix} + \begin{pmatrix} \boldsymbol{u}^\perp \\ -\boldsymbol{u}^\perp \end{pmatrix} + \begin{pmatrix} \boldsymbol{0} \\ \boldsymbol{\varphi}^\perp \end{pmatrix} \\ &=: \boldsymbol{w}^0 + \boldsymbol{w}^1 + \boldsymbol{w}^2 + \boldsymbol{w}^3. \end{aligned} \tag{3.35}$$

We decompose each component of each summand in (3.35) according to

$$\begin{aligned} &\sum_{j=0}^{J} \boldsymbol{u}_j^0 = \boldsymbol{u}^0, && \sum_{j=0}^{J} \boldsymbol{v}_j^0 = \boldsymbol{v}^0, && \sum_{j=0}^{J} \boldsymbol{\varphi}_j^0 = \boldsymbol{\varphi}^0, \\ &\sum_{j=0}^{J} \boldsymbol{u}_j^1 = \boldsymbol{u}^\perp, && \sum_{j=0}^{J} \boldsymbol{v}_j^1 = \boldsymbol{v}^\perp, && \sum_{j=0}^{J} \boldsymbol{\varphi}_j^1 = \boldsymbol{\varphi}^\perp, \end{aligned}$$

where $\boldsymbol{u}_j^0 \in U_j^0$, $\boldsymbol{v}_j^0 \in V_j^0$, $\boldsymbol{\varphi}_j^0 \in V_j^0$, $\boldsymbol{u}_j^1 \in U_j$, $\boldsymbol{v}_j^1 \in V_j$ and $\boldsymbol{\varphi}_j^1 \in V_j$ are specified below. The superscript 1 of $\boldsymbol{u}_j^1$, $\boldsymbol{v}_j^1$ and $\boldsymbol{\varphi}_j^1$ indicates that these terms are not orthogonal. Now, we define $\boldsymbol{w}_j = \boldsymbol{w}_j^0 + \boldsymbol{w}_j^1 + \boldsymbol{w}_j^2 + \boldsymbol{w}_j^3$, where

$$\begin{aligned} &\boldsymbol{w}_j^0 = \begin{pmatrix} \boldsymbol{u}_j^0 \\ \boldsymbol{v}_j^0 \end{pmatrix} \in W_j^0, && \boldsymbol{w}_j^1 = \begin{pmatrix} \boldsymbol{0} \\ \boldsymbol{\varphi}_j^0 \end{pmatrix} \in W_j^0, \\ &\boldsymbol{w}_j^2 = \begin{pmatrix} \boldsymbol{u}_j^1 \\ -\boldsymbol{u}_j^1 \end{pmatrix} \in W_j, && \boldsymbol{w}_j^3 = \begin{pmatrix} \boldsymbol{0} \\ \boldsymbol{\varphi}_j^1 \end{pmatrix} \in W_j, \end{aligned}$$

and herewith estimate

$$\sum_{j=0}^{J} \mathscr{A}_j\left(\boldsymbol{w}_j, \boldsymbol{w}_j\right) \leq c \sum_{j=0}^{J} \left(\mathscr{A}_j\left(\boldsymbol{w}_j^0, \boldsymbol{w}_j^0\right) + \mathscr{A}_j\left(\boldsymbol{w}_j^1, \boldsymbol{w}_j^1\right) + \mathscr{A}_j\left(\boldsymbol{w}_j^2, \boldsymbol{w}_j^2\right) + \mathscr{A}_j\left(\boldsymbol{w}_j^3, \boldsymbol{w}_j^3\right)\right). \tag{3.36}$$

In the kernel W_h^0 we have by Lemma 3.10 for $\boldsymbol{w}^0 = (\boldsymbol{u}^0, \boldsymbol{v}^0) \in W_h^0$

$$\begin{aligned}\sum_{j=0}^{J} \mathscr{A}_j\left(\boldsymbol{w}_j^0, \boldsymbol{w}_j^0\right) &= e_H(\boldsymbol{u}_j^0, \boldsymbol{u}_j^0) + \sum_{j=1}^{J} e_h(\boldsymbol{u}_j^0, \boldsymbol{u}_j^0) + \sum_{j=0}^{J} k(\boldsymbol{v}_j^0, \boldsymbol{v}_j^0) \\ &\leq c_{H,\delta}\left(e_h(\boldsymbol{u}^0, \boldsymbol{u}^0) + k(\boldsymbol{v}^0, \boldsymbol{v}^0)\right) = c_{H,\delta}\mathscr{A}_h\left(\boldsymbol{w}^0, \boldsymbol{w}^0\right). \end{aligned} \tag{3.37}$$

For the decomposition in the orthogonal complement $W_h^\perp$, we will use the stability estimates

$$k(\boldsymbol{\varphi}^0, \boldsymbol{\varphi}^0) \leq k(\boldsymbol{\varphi}, \boldsymbol{\varphi}) = k(\boldsymbol{u}^\perp + \boldsymbol{v}^\perp, \boldsymbol{u}^\perp + \boldsymbol{v}^\perp), \tag{3.38}$$

$$k(\boldsymbol{\varphi}^\perp, \boldsymbol{\varphi}^\perp) \leq k(\boldsymbol{\varphi}, \boldsymbol{\varphi}) = k(\boldsymbol{u}^\perp + \boldsymbol{v}^\perp, \boldsymbol{u}^\perp + \boldsymbol{v}^\perp). \tag{3.39}$$

Further, we note that

$$d(\boldsymbol{\varphi}^\perp, \boldsymbol{\varphi}^\perp) = d(\boldsymbol{\varphi}, \boldsymbol{\varphi}) = d(\boldsymbol{u}^\perp + \boldsymbol{v}^\perp, \boldsymbol{u}^\perp + \boldsymbol{v}^\perp). \tag{3.40}$$

Then, the stability of the L^2-decomposition (3.34) and the estimate (3.38) yield

$$\begin{aligned}\sum_{j=0}^{J} \mathscr{A}_j\left(\boldsymbol{w}_j^1, \boldsymbol{w}_j^1\right) &= \sum_{j=0}^{J} k(\boldsymbol{\varphi}_j^0, \boldsymbol{\varphi}_j^0) \leq c_{H,\delta} k(\boldsymbol{\varphi}^0, \boldsymbol{\varphi}^0) \\ &\leq c_{H,\delta}\left(k(\boldsymbol{u}^\perp, \boldsymbol{u}^\perp) + k(\boldsymbol{v}^\perp, \boldsymbol{v}^\perp)\right). \end{aligned} \tag{3.41}$$

Moreover, by Lemma 3.9 and [TW10, AFW97], we have

$$\begin{aligned}\sum_{j=0}^{J} \mathscr{A}_j\left(\boldsymbol{w}_j^2, \boldsymbol{w}_j^2\right) &= e_H(\boldsymbol{u}_0^1, \boldsymbol{u}_0^1) + \sum_{j=1}^{J} e_h(\boldsymbol{u}_j^1, \boldsymbol{u}_j^1) + \sum_{j=0}^{J} \left(k(\boldsymbol{u}_j^1, \boldsymbol{u}_j^1) + \lambda d(\boldsymbol{u}_j^1, \boldsymbol{u}_j^1)\right) \\ &\leq c_{H,\delta}\left(e_h(\boldsymbol{u}^\perp, \boldsymbol{u}^\perp) + k(\boldsymbol{u}^\perp, \boldsymbol{u}^\perp) + \lambda d(\boldsymbol{u}^\perp, \boldsymbol{u}^\perp)\right). \end{aligned}$$

Again, by [TW10, AFW97], stability estimate (3.39), and equality (3.40), we have

$$\begin{aligned}\sum_{j=0}^{J} \mathscr{A}_j\left(\boldsymbol{w}_j^3, \boldsymbol{w}_j^3\right) &= \sum_{j=0}^{J} \left(k\big(\boldsymbol{\varphi}_j^1, \boldsymbol{\varphi}_j^1\big) + c_s^{-1} d\big(\boldsymbol{\varphi}_j^1, \boldsymbol{\varphi}_j^1\big)\right) \\ &\leq c_{H,\delta}\left(k\big(\boldsymbol{\varphi}^\perp, \boldsymbol{\varphi}^\perp\big) + c_s^{-1} d\big(\boldsymbol{\varphi}^\perp, \boldsymbol{\varphi}^\perp\big)\right) \\ &\leq c_{H,\delta}\left(k\big(\boldsymbol{u}^\perp, \boldsymbol{u}^\perp\big) + k\big(\boldsymbol{v}^\perp, \boldsymbol{v}^\perp\big) + c_s^{-1} d\big(\boldsymbol{u}^\perp + \boldsymbol{v}^\perp, \boldsymbol{u}^\perp + \boldsymbol{v}^\perp\big)\right).\end{aligned} \tag{3.42}$$

Due to the special choice of the decomposition (3.35), the term $k\left(\boldsymbol{u}^\perp, \boldsymbol{u}^\perp\right)$ arises in (3.42), which we further estimate using the Poincaré inequality

$$k\big(\boldsymbol{u}^\perp, \boldsymbol{u}^\perp\big) \leq c_{\boldsymbol{K},\Omega} e_h\big(\boldsymbol{u}^\perp, \boldsymbol{u}^\perp\big) \tag{3.43}$$

with a constant $c_{\boldsymbol{K},\Omega}$ depending on the domain Ω and the permeability coefficient $\boldsymbol{K}$. Thus, collecting the estimates (3.36), (3.37), and (3.41)–(3.43), we obtain with $\boldsymbol{w}^\perp = (\boldsymbol{u}^\perp, \boldsymbol{v}^\perp) \in W_h^\perp$

$$\begin{aligned}&\sum_{j=0}^{J} \mathscr{A}_j\left(\boldsymbol{w}_j, \boldsymbol{w}_j\right) \\ &\leq c_{H,\delta}\Big(e_h\big(\boldsymbol{u}^0, \boldsymbol{u}^0\big) + k\big(\boldsymbol{v}^0, \boldsymbol{v}^0\big) + k\big(\boldsymbol{u}^\perp, \boldsymbol{u}^\perp\big) \\ &\qquad + e_h\big(\boldsymbol{u}^\perp, \boldsymbol{u}^\perp\big) + k\big(\boldsymbol{v}^\perp, \boldsymbol{v}^\perp\big) + \lambda d\big(\boldsymbol{u}^\perp, \boldsymbol{u}^\perp\big) + c_s^{-1} d\big(\boldsymbol{u}^\perp + \boldsymbol{v}^\perp, \boldsymbol{u}^\perp + \boldsymbol{v}^\perp\big)\Big) \\ &\leq c_{H,\delta,\boldsymbol{K},\Omega}\Big(\mathscr{A}_h\left(\boldsymbol{w}^0, \boldsymbol{w}^0\right) + \mathscr{A}_h\left(\boldsymbol{w}^\perp, \boldsymbol{w}^\perp\right)\Big) \\ &= c_{H,\delta,\boldsymbol{K},\Omega} \mathscr{A}_h\left(\boldsymbol{w}, \boldsymbol{w}\right)\end{aligned}$$

where the constant $c_{H,\delta,\boldsymbol{K},\Omega}$ for a proper overlap δ depends only on $\boldsymbol{K}$ and Ω. □

3.4.4 Local Stability and Strengthened Cauchy-Schwarz Inequalities

It remains to verify Assumptions 2.3 and 2.4.

Since we have chosen exact bilinear forms in the definition of the local components

$$\mathscr{A}_j\left(\begin{pmatrix}\boldsymbol{u}_j \\ \boldsymbol{v}_j\end{pmatrix}, \begin{pmatrix}\boldsymbol{u}_j \\ \boldsymbol{v}_j\end{pmatrix}\right) = \mathscr{A}_h\left(\begin{pmatrix}\boldsymbol{u}_j \\ \boldsymbol{v}_j\end{pmatrix}, \begin{pmatrix}\boldsymbol{u}_j \\ \boldsymbol{v}_j\end{pmatrix}\right) \qquad \text{for } j =, 1 \ldots, J,$$

it suffices to prove Assumption 2.3 only for the coarse bilinear form $\mathscr{A}_0(\cdot,\cdot)$, compare also Remark 2.5.

Lemma 3.12 (Local stability)**.** *For each $\boldsymbol{w}_0 \in W_0$ it holds*

$$\mathscr{A}_h(\boldsymbol{w}_0,\boldsymbol{w}_0) \leq \omega_0 \frac{H}{h} \mathscr{A}_0(\boldsymbol{w}_0,\boldsymbol{w}_0),$$

with $\omega_0 < 1$, such that $\omega_0 \frac{H}{h} < 2$.

Proof. On the coarse space, we have chosen a non-inherited form for the approximation of the elasticity bilinear form, namely $e_H(\cdot,\cdot)$ instead of $e_h(\cdot,\cdot)$, which differs in the face and boundary terms because of the different cell size $H \geq h$. Due to the continuity of the coarse displacement functions $\boldsymbol{u}_0 = \boldsymbol{u}_H \in U_0$ on every coarse cell, the jump terms $\|[\![\boldsymbol{u}_H]\!]\|_F$ vanish for all faces F that lie in the interior of a coarse cell. Therefore, we have

$$e_h\big(\boldsymbol{u}_0,\boldsymbol{u}_0\big) \leq \frac{H}{h} e_H\big(\boldsymbol{u}_0,\boldsymbol{u}_0\big). \tag{3.44}$$

Since all other terms of the coarse space operator $\mathscr{A}_0(\cdot,\cdot)$ are chosen to be exact, the statement of Lemma 3.12 follows by estimate (3.44). □

The relaxation factor ω_0 is essentially defined for the convergence analysis, such that the coarse bilinear form is scaled enough to assure $\omega_0 \frac{H}{h} < 2$ and thus Assumption 2.3 is fulfilled. Such a relaxation parameter can always be introduced, but we are not free to scale the local and coarse bilinear forms arbitrarily, since a small ω_0 will result in small corrections of the error, and in a large constant C_0 of the stable decomposition resulting in poor bounds for the largest eigenvalue, see [TW10, p. 41] and [SBG96, p. 155]. In practice such a relaxation is not necessary and we will set $\omega_0 = 1$.

Lemma 3.13 (Strengthened Cauchy-Schwarz inequalities)**.** *For $1 \leq i,j \leq J$ there exist constants $0 \leq \varepsilon_{ij} \leq 1$ such that*

$$|\mathscr{A}_h(\boldsymbol{w}_i,\boldsymbol{w}_j)| \leq \varepsilon_{ij} \mathscr{A}_h(\boldsymbol{w}_i,\boldsymbol{w}_i)^{\frac{1}{2}} \mathscr{A}_h(\boldsymbol{w}_j,\boldsymbol{w}_j)^{\frac{1}{2}},$$

for $\boldsymbol{w}_i \in W_i$, $\boldsymbol{w}_j \in W_j$.

Proof. The existence of the constants ε_{ij} is a direct consequence of the Cauchy-Schwarz-inequality. To get a small bound we take a look a bit more in detail. The local function

$\boldsymbol{w}_i$ has support only on the patch Ω_i and is continued by zero on the rest of the domain $\Omega \setminus \Omega_i$. Since two functions, $\boldsymbol{w}_i$ and $\boldsymbol{w}_j$, have common support only in the intersection $\Omega_i \cap \Omega_j$, we immediately get values $\varepsilon_{ij} < 1$. □

3.5 Numerical Tests

The performance and robustness of the proposed Schwarz preconditioners defined in section 3.3 shall be examined in a series of numerical tests, covering a large variety of the parameter regimes, as well as different kinds of boundary values. We restrict the presentation to the case of isotropic permeabilities $\boldsymbol{K} = \kappa \boldsymbol{I}$ and demonstrate the robustness of the two-level Schwarz preconditioners for the case of H^{div}-conforming discretizations of Biot's quasi-static consolidation model with $RT_k \times RT_k \times Q_k$ finite elements. The implementation has been done in C++ and is based on the finite element library DEAL.II [ABF+22], as well as on existing code that was available in the group at the IWR at the time of writing this thesis. Parts of the code use the linear algebra software package LAPACK [ABB+99].

In Section 3.5.1 we introduce a first test scenario with homogeneous Dirichlet boundary values, for which the performance of the multiplicative and hybrid two-level Schwarz methods is tested in Section 3.5.2 by measuring the iteration counts of GMRES. Starting with a short investigation on different polynomial degrees $k = 0, \ldots, 3$, the robustness of the methods with respect to the parameters λ, κ^{-1} and c_s is tested. The two-level Schwarz methods show robust iteration numbers, where the dependence on the inverse permeability enters the results only slightly, without restricting the applicability of the proposed methods. For extremely large values of λ and for values of κ^{-1} very close to zero, numerical instabilities occur that can be remedied by scaling the system. In Section 3.5.3 another test case is introduced, covering mixed Dirichlet-Neumann boundary conditions. For this scenario the inclusion of boundary patches improves the performance results of the hybrid method. Furthermore, the dependence on the permeability appears to be switched. Otherwise, the results are similar to the test case with homogeneous boundary values. In Section 3.5.4, the optimal choice of the relaxation factor of the hybrid two-level Schwarz method is investigated. In Section 3.5.5, the multilevel Schwarz method is examined.

3.5.1 Test Case with Homogeneous Dirichlet Boundary Values

The setting of this first numerical test has been taken from [HKLP19, section 6.1]. It is constructed such that the solution is divergence-free in the displacement component and is otherwise strongly dominated by the pressure. It serves somewhat as prototypical test case for the later examples, since the local problems always have homogeneous boundary values and a mean-value free pressure in all of the following problems. The setting is defined as follows. Let the force $\boldsymbol{f}$ and the source g be given by

$$\boldsymbol{f} = \begin{pmatrix} 900\partial_x\boldsymbol{\varphi} - \partial_y^3\boldsymbol{\varphi} - \partial_x^2\partial_y\boldsymbol{\varphi} \\ 900\partial_y\boldsymbol{\varphi} + \partial_x^3\boldsymbol{\varphi} + \partial_x\partial_y^2\boldsymbol{\varphi} \end{pmatrix}, \qquad g = 900\kappa\Delta\boldsymbol{\varphi} - c_s(900\boldsymbol{\varphi} - 1),$$

where $\boldsymbol{\varphi}$ is defined on the square $\Omega = (0,1) \times (0,1)$ by

$$\boldsymbol{\varphi} = x^2(x-1)^2y^2(y-1)^2.$$

Homogeneous Dirichlet boundary conditions are prescribed for the solid displacement $\boldsymbol{u}$ as well as for the normal direction of the seepage velocity $\boldsymbol{v}$ on the whole boundary $\partial\Omega$, i.e.,

$$\boldsymbol{u} = 0 \quad \text{on } \partial\Omega, \qquad \boldsymbol{v} \cdot \boldsymbol{n} = 0 \quad \text{on } \partial\Omega.$$

Here, $\boldsymbol{n}$ describes the unit outward normal vector. The solution of this partial differential equation is defined up to an additive constant for the pressure p. Thus, we search for a mean-value free solution in the pressure component satisfying

$$\int_\Omega p \, dx = 0.$$

The exact solution to this system is in $\boldsymbol{H}_{\boldsymbol{0}}^{\boldsymbol{1}}(\Omega) \times \boldsymbol{H}_{\boldsymbol{0}}^{\boldsymbol{\mathrm{div}}}(\Omega) \times L_0^2(\Omega)$ by construction and given by

$$\boldsymbol{u} = \begin{pmatrix} \partial_y\boldsymbol{\varphi} \\ -\partial_x\boldsymbol{\varphi} \end{pmatrix}, \qquad \boldsymbol{v} = -900\kappa\nabla p, \qquad p = 900\boldsymbol{\varphi} - 1. \tag{3.45}$$

A visualization of a sample calculation can be found in Figure 3.1.

For the tests the domain Ω is divided into $2^{2\ell}$ squares, each of size $h = 2^{-\ell}$, where ℓ

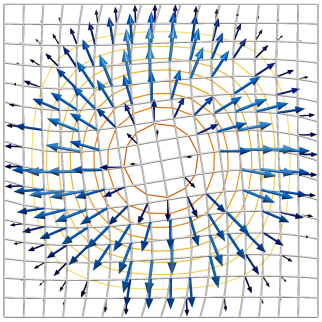

Figure 3.1: Visualization of an example calculation of the experiment with homogeneous boundary conditions. The arrows illustrate the flux of the seepage velocity, the isolines show the pressure and the displacement is visualized by the deformation of the grid. The magnitudes are exaggerated in favor of the representation.

denotes the corresponding level on which the calculations are performed. To discretize the partial differential equations we use the triplets $RT_k \times RT_k \times Q_k$, $k \geq 0$, of equal order Raviart-Thomas and discontinuous cell-wise polynomial finite element functions, such that we have matching spaces satisfying

$$\operatorname{div} RT_k = Q_k.$$

The dimension of the finite element space $RT_k \times RT_k \times Q_k$, as well as the additional data of the mesh is summarized in Table 3.1. The resulting discrete linear system is solved with a preconditioned GMRES method until the starting residual has been reduced by a factor of 10^{-8}. Note, that the Richardson iteration has only been used for the analysis, while in the numerical application scenarios the potentially faster GMRES algorithm is taken instead. As preconditioner we use the overlapping two-level Schwarz methods described in Section 3.3. Therefore, we define vertex patches that are made out of four cells surrounding every vertex in the interior of Ω. For an illustration of the vertex patches see Figure 2.2. The relaxation parameter of the hybrid Schwarz preconditioner P_{hyb} is chosen to be $\omega = 0.25$ to compensate the effect of adding the overlapping patches,

			Dofs		
ℓ	h	Cells	$k=0$	$k=1$	$k=2$
0	1	1	9	28	57
1	1/2	4	28	96	204
2	1/4	16	96	352	768
3	1/8	64	352	1344	2976
4	1/16	256	1344	5248	11712
5	1/32	1024	5248	20736	46464
6	1/64	4096	20736	82432	185088
7	1/128	16384	82432	328704	738816

Table 3.1: Discretization data of the finite element space $RT_k \times RT_k \times Q_k$.

which have an overlap of size $\delta = h$. In case of the multiplicative method P_{mu} no such relaxation for the patches is needed. The coarse space is always assembled one level below the actual level, i.e., $H = 2h$ leading to a constant factor $\frac{H}{\delta} = 2$. As noted after the proof of Lemma 3.12 no additional relaxation factor is required for the coarse space correction in the following tests, i.e., $\omega_0 = 1$, although the factor $\frac{H}{\delta}$ is not strictly less than two. To solve the local problems on each vertex patch, as well as the coarse problem, we use a singular value decomposition (SVD) from LAPACK that takes the one-dimensional kernel of the pressure component into account.

3.5.2 Performance of the Two-level Schwarz Preconditioners

To start the discussion of the performance of the multiplicative and hybrid two-level Schwarz preconditioners P_{mu} and P_{hyb}, we perform calculations for different polynomial degrees $k = 0, \dots, 3$ of the above described test setting in Section 3.5.1 on different mesh refinement levels and record the iteration counts that the preconditioned GMRES method takes to reduce the norm of the starting residual $\boldsymbol{r}_0$ up to a factor of 10^{-8}, such that the norm of the current residual $\|\boldsymbol{r}_k\|_2$ is below the relative tolerance $10^{-8} \|\boldsymbol{r}_0\|_2$.

For $k = 0$ and $k = 1$ we observe some sort of stiffness of the methods compared to polynomial degrees $k \geq 2$ as can be seen in a sample calculation with $\lambda = 100$, $\kappa = 1$, and $c_s = 0$ in Table 3.2.

For the hybrid method the numbers drop from around 22 for $k = 1$ to approximately 14 for $k = 2$, and are then constant for all degrees $k \geq 2$. The multiplicative method produces similar results, where we can observe iteration counts around 15 for polynomial

	P_{mu}				P_{hyb}			
h	$k=0$	1	2	3	$k=0$	1	2	3
1/4	7	8	5	3	7	15	15	14
1/8	12	13	6	3	15	20	15	14
1/16	14	15	6	2	24	22	14	14
1/32	15	15	6	2	27	22	13	13

Table 3.2: Comparison of multiplicative Schwarz preconditioner P_{mu} and hybrid Schwarz preconditioner P_{hyb} with respect to different polynomial degrees $k = 0, ..., 3$ for $RT_k \times RT_k \times Q_k$. Calculated with $\lambda = 100$, $\kappa^{-1} = 1$, $c_s = 0$.

degrees $k \leq 1$, which drop to 6 for $k = 2$. For $k \geq 2$ the iteration counts of P_{mu} reduce even further until they reach 1 for $k \geq 4$, since the method then resolves the polynomial structure of the given solution (3.45) exactly.

A polynomial degree of $k = 2$ seems to give a good balance of effort and performance, thus, we will focus on this case in the following tests. For a comprehensive overview, we will also cover the lowest-order variant $k = 0$ later on.

We continue by comparing the performance of P_{mu} and P_{hyb} with respect to different choices of patches in the case $k = 2$. Therefore, we consider the following possibilities:

1. non-overlapping cell patches, where each patch consists of a single cell,
2. overlapping vertex patches without boundary patches, where the corresponding vertex is located at the boundary $\partial\Omega$,
3. overlapping vertex patches with boundary patches, but without single cell patches, where the corresponding vertex is located in a corner,
4. overlapping vertex patches with boundary patches and with single cell patches.

In Table 3.3 we see that the number of iterations deteriorates for non-overlapping cell patches as expected from the analysis in Section 2.4.4. Selecting overlapping vertex patches yields uniform iteration counts for the multiplicative and the hybrid operator, while for the multiplicative method it makes no difference whether boundary patches are included or not, since the required iteration count remains at about 4. For the hybrid method, we observe a small beneficial effect of incorporating boundary patches, but no further improvement when single cell patches are included. Since the number of iterations only decreases from about 14 when boundary patches are excluded to 12 when boundary

	P_{mu}				P_{hyb}			
h	cp	vp	vpb	vpbs	cp	vp	vpb	vpbs
1/4	17	4	4	4	30	15	12	11
1/8	19	5	4	4	33	15	13	12
1/16	23	5	4	4	32	14	12	12
1/32	25	4	4	4	34	14	12	11

Table 3.3: Comparison of iteration counts of GMRES for different choices of patches: cell patches (cp), vertex patches without boundary patches (vp), vertex patches with boundary patches but without single cell patches (vpb), vertex patches with boundary patches and with single cell patches (vpbs). Multiplicative two-level Schwarz P_{mu}, hybrid two-level Schwarz P_{hyb}. Homogeneous boundaries, $RT_2 \times RT_2 \times Q_2$, $\lambda = \kappa^{-1} = 1$, $c_s = 0$.

patches are included, we choose the less expensive version without boundary patches for both the hybrid method and the multiplicative method for the following performance tests.

Robustness for $k = 2$

We now discuss the performance of GMRES with respect to a variety of parameters in the system for polynomial degree $k = 2$.

In order not to overwhelm the reader with numbers, we restrict the presentation to the four cases, where λ, κ^{-1}, $\lambda = \kappa^{-1}$ and c_s are varied while the other parameters remain constant, since this covers the most important test cases for demonstrating the robustness of the method for all parameter ranges. In particular, the case $c_s > 0$ is not as interesting mathematically, since the system is then no longer a saddle point system and is therefore easier to solve. As explained in detail in [Phi05, Sec. 5.2] in the context of locking, "a null constrained specific storage coefficient value, $c_s \approx 0$, appears to be a necessary condition for numerical problems to occur". Thus, we neglect the cases where λ or κ^{-1} is varied together with c_s in the presentation, since the numbers are constant in these cases anyway. Since the parameters λ, κ^{-1} and c_s are rescaled quantities, see (3.4), their robustness transports directly to all physical parameters in the system, i.e., the Lamé constants, the permeability, the Biot-Willis constant, and the specific storage capacity, as well as the time step size.

	P_{mu}						P_{hyb}					
h	$\lambda =$ 0	1	10^2	10^4	10^6	10^8	0	1	10^2	10^4	10^6	10^8
1/4	4	4	5	5	5	5	15	15	15	14	14	13
1/8	5	5	6	6	6	6	15	15	15	15	15	13
1/16	4	5	6	6	6	6	14	14	14	14	14	12
1/32	4	4	6	6	6	6	14	14	13	13	13	11

Table 3.4: Iteration counts of GMRES with respect to λ. Multiplicative two-level Schwarz (left), hybrid two-level Schwarz (right). Homogeneous boundaries, $RT_2 \times RT_2 \times Q_2$, $\kappa^{-1} = 1$, $c_s = 0$.

Starting with the constant λ in Table 3.4, we observe robust iteration numbers for all $0 \leq \lambda \leq 10^8$ for the multiplicative Schwarz preconditioner P_{mu} as well as for the hybrid version P_{hyb}, even in the nearly incompressible case, i.e., when λ becomes very large. Both produce constant iteration counts for $0 \leq \lambda \leq 1$ and $\lambda > 1$, with P_{mu} needing only 4 iterations for small values of λ and 6 for large values, while P_{hyb} needs 14 and 13, respectively, to converge. Only for the case $\lambda = 10^8$ GMRES converges slightly earlier in the hybrid case with about two fewer iterations. As from the convergence proof expected, we cannot observe a dependence of the Schwarz methods with respect to λ. In this table, as in all following calculations for this first test case, we see that the multiplicative Schwarz preconditioner outperforms the hybrid method by about one-third to one-half of the iterations.

In the practical calculations with extremely large parameters, numerical instabilities of GMRES occur due to the large values generated in the course of the calculation, especially for κ^{-1}, but also for λ. Numerical instabilities also occur in the case of κ^{-1} very close to zero, since the matrix is then almost singular. For such parameter ranges, building the (pseudo-)inverses of the local patch matrices and of the global coarse-matrix becomes difficult or breaks down, even when using the robust but expensive SVD. This happens because of the squaring of the diagonal entries of the system matrix amplifying the already large (or small) values, compare Algorithm 2.2, and leading to an inaccurate pseudo-inverse. For example, in the case $\kappa^{-1} = 10^{-8}$, the iteration counts of GMRES deteriorate with decreasing mesh size h for both the multiplicative two-level Schwarz method and the hybrid method. This is even more evident for $\lambda = \kappa^{-1} \geq 10^6$, where the numbers exceed 100 iterations even for coarse meshes $h \leq \frac{1}{8}$. Furthermore, for $\kappa^{-1} = 10^{-6}$ and for $\lambda = \kappa^{-1} = 10^{-8}$ calculating the SVD of the coarse matrix aborts.

To avoid these difficulties and stabilize the computations, we scale the linear system with a suitable scaling matrix so that the numbers remain within a reasonable range. Therefore, consider that the system is given in the form $\boldsymbol{A}\boldsymbol{x} = \boldsymbol{f}$ with the block vector $\boldsymbol{x} = (\boldsymbol{u}, \boldsymbol{v}, \boldsymbol{p})^T$ and the system matrix

$$\boldsymbol{A} = \begin{pmatrix} \boldsymbol{E} + \lambda \boldsymbol{D} & \boldsymbol{0} & \boldsymbol{B}^T \\ \boldsymbol{0} & \kappa^{-1}\boldsymbol{M} & \boldsymbol{B}^T \\ \boldsymbol{B} & \boldsymbol{B} & c_s \boldsymbol{C} \end{pmatrix}.$$

This system is preconditioned from the left and the right with a diagonal scaling matrix

$$\boldsymbol{S} = \begin{pmatrix} s_\lambda \boldsymbol{I} & \boldsymbol{0} & \boldsymbol{0} \\ \boldsymbol{0} & s_\kappa \boldsymbol{I} & \boldsymbol{0} \\ \boldsymbol{0} & \boldsymbol{0} & \boldsymbol{I} \end{pmatrix},$$

where $s_\lambda, s_\kappa > 0$ are suitable scalar values and the identity $\boldsymbol{I}$ and the null-matrix $\boldsymbol{0}$ have dimensions according to the finite element spaces U_h, V_h and Q_h. The resulting preconditioned system is then given by

$$\begin{aligned} \boldsymbol{SASy} &= \boldsymbol{Sf}, \\ \boldsymbol{x} &= \boldsymbol{Sy}, \end{aligned} \tag{3.46}$$

with the scaling factors chosen as $s_\lambda = 1/\sqrt{\lambda}$ and $s_\kappa = \sqrt{\kappa}$ such that the system matrix $\boldsymbol{A}$ is scaled as

$$\boldsymbol{SAS} = \begin{pmatrix} \frac{1}{\lambda}\boldsymbol{E} + \boldsymbol{D} & \boldsymbol{0} & \frac{1}{\sqrt{\lambda}}\boldsymbol{B}^T \\ \boldsymbol{0} & \boldsymbol{M} & \sqrt{\kappa}\boldsymbol{B}^T \\ \frac{1}{\sqrt{\lambda}}\boldsymbol{B} & \sqrt{\kappa}\boldsymbol{B} & c_s \boldsymbol{C} \end{pmatrix}.$$

In the following tests, we will use the scaling (3.46) in the cases summarized above.

The implementation of this scaling was realized in two steps. The first equation of (3.46) is scaled in the assembly process by multiplying the local matrices and vectors on each cell with the scaling matrix $\boldsymbol{S}$. After the linear system is iteratively solved, the global result vector $\boldsymbol{y}$ is then rescaled by another multiplication with $\boldsymbol{S}$, yielding the solution vector $\boldsymbol{x}$. In this way, the system matrix as well as the patch matrices and the coarse matrix are equivalently transformed and retransformed according to (3.46). Furthermore,

		κ^{-1}								
	h	10^{-8}	10^{-6}	10^{-4}	10^{-2}	1	10^{2}	10^{4}	10^{6}	10^{8}
P_{mu}	1/4	1	1	3	3	4	5	6	6	6
	1/8	2	2	3	4	5	5	6	6	6
	1/16	2	2	3	4	5	5	5	6	6
	1/32	2	2	3	4	4	4	5	6	7
P_{hyb}	1/4	9	10	11	12	15	15	15	16	15
	1/8	10	10	11	13	15	15	15	16	16
	1/16	10	10	10	12	14	14	14	15	15
	1/32	9	9	10	12	14	14	14	13	16

Table 3.5: Iteration counts of GMRES with respect to κ^{-1}. Multiplicative two-level Schwarz (top), hybrid two-level Schwarz (bottom). Homogeneous boundaries, $RT_2 \times RT_2 \times Q_2$, $\lambda = 1$, $c_s = 0$.

		$\lambda = \kappa^{-1}$								
	h	10^{-8}	10^{-6}	10^{-4}	10^{-2}	1	10^{2}	10^{4}	10^{6}	10^{8}
P_{mu}	1/4	1	3	2	3	4	5	6	6	6
	1/8	2	3	2	4	5	6	6	6	6
	1/16	2	3	2	4	5	6	6	6	6
	1/32	2	3	2	3	4	6	6	6	6
P_{hyb}	1/4	9	10	11	12	15	15	14	14	14
	1/8	10	10	11	13	15	15	15	15	15
	1/16	10	10	11	12	14	14	14	14	14
	1/32	9	9	10	12	14	13	13	13	13

Table 3.6: Iteration counts of GMRES with respect to $\lambda = \kappa^{-1}$. Multiplicative two-level Schwarz (top), hybrid two-level Schwarz (bottom). Homogeneous boundaries, $RT_2 \times RT_2 \times Q_2$, $c_s = 0$.

	P_{mu}				P_{hyb}			
h	$c_s =$ 0	10^{-10}	10^{-4}	1	0	10^{-10}	10^{-4}	1
1/4	4	4	4	4	15	15	15	15
1/8	5	5	5	5	15	15	15	15
1/16	5	5	5	5	14	14	14	14
1/32	4	4	4	4	14	14	14	14

Table 3.7: Iteration counts of GMRES with respect to c_s. Multiplicative two-level Schwarz (left), hybrid two-level Schwarz (right). Homogeneous boundaries, $RT_2 \times RT_2 \times Q_2$, $\lambda = \kappa^{-1} = 1$.

the method also allows for a matrix-free implementation of the code.

We go on with investigating the performance of the multiplicative and hybrid two-level Schwarz methods with respect to κ^{-1} in Table 3.5. The theoretical dependence of the constant C_0 in the stable decomposition on the inverse of the permeability does not restrict us in the practical application of the method and can only slightly be observed in this test scenario, see Table 3.5, where the numbers of the multiplicative Schwarz preconditioner increase from 2 to 7 over the whole range of $10^{-8} \leq \kappa^{-1} \leq 10^{8}$. Also in the hybrid case, the numbers start at 9 and grow to 16, which is no restriction at all for the applicability of the method. The observed numerical instabilities for $\kappa \leq 10^{-6}$ were resolved by scaling the system according to (3.46), resulting in a very low iteration count of only 2 for P_{mu} and about 9 for P_{hyb}.

Similar results can be observed for $\lambda = \kappa^{-1}$ in Table 3.6. The numbers are robust with slight variations for large and for small values. Both methods the multiplicative and the hybrid method are more sensitive for large values of $\kappa^{-1} = \lambda$ as the numbers deteriorate for values greater than 10^6, but again, scaling the system for these values leads to robust iteration counts with comparable results as in Table 3.5. Moreover, the dependence on κ^{-1} is only slightly apparent and does not restrict the applicability of the method.

Finally, Table 3.7 shows constant iteration numbers when the specific storage coefficient c_s is varied.

Robustness for $k = 0$

We continue with the same tests for polynomial degree $k = 0$. For the multiplicative two-level Schwarz method in the lowest order case $RT_0 \times RT_0 \times Q_0$ we use the scaling (3.46). For the hybrid two-level Schwarz method, however, we use a scaling in h additionally to the scaling already described. Therefore, we choose another diagonal scaling matrix

$$\boldsymbol{S}_h = \begin{pmatrix} h\boldsymbol{I} & \boldsymbol{0} & \boldsymbol{0} \\ \boldsymbol{0} & \sqrt{h}\boldsymbol{I} & \boldsymbol{0} \\ \boldsymbol{0} & \boldsymbol{0} & \boldsymbol{I} \end{pmatrix}$$

to precondition the system $\boldsymbol{A}\boldsymbol{x} = \boldsymbol{f}$ as

$$\begin{aligned} \boldsymbol{S}_h\boldsymbol{S}\boldsymbol{A}\boldsymbol{S}\boldsymbol{S}_h\boldsymbol{y} &= \boldsymbol{S}_h\boldsymbol{S}\boldsymbol{f} \\ \boldsymbol{x} &= \boldsymbol{S}_h\boldsymbol{S}\boldsymbol{y}. \end{aligned} \tag{3.47}$$

	P_{mu}						P_{hyb}					
h	$\lambda =$ 0	1	10^2	10^4	10^6	10^8	0	1	10^2	10^4	10^6	10^8
1/16	8	8	13	12	11	10	15	15	18	17	16	15
1/32	9	8	14	13	12	10	15	16	18	17	16	14
1/64	9	8	15	14	12	11	16	17	18	17	15	14
1/128	9	8	15	15	13	12	16	17	17	16	14	13

Table 3.8: Iteration counts of GMRES with respect to λ. P_{mu} with scaling (3.46), P_{hyb} with scaling (3.47). Homogeneous boundaries, $RT_0 \times RT_0 \times Q_0$, $\kappa^{-1} = 1$, $c_s = 0$.

		κ^{-1}								
	h	10^{-8}	10^{-6}	10^{-4}	10^{-2}	1	10^2	10^4	10^6	10^8
P_{mu}	1/16	4	3	5	7	8	9	13	14	14
	1/32	4	3	5	7	8	8	11	15	15
	1/64	4	3	5	7	8	8	9	15	15
	1/128	4	4	6	7	8	8	9	15	16
P_{hyb}	1/16	9	9	12	12	15	15	18	19	19
	1/32	9	9	11	13	16	17	17	19	19
	1/64	8	8	11	13	17	18	17	19	20
	1/128	7	8	11	13	17	18	17	19	20

Table 3.9: Iteration counts of GMRES with respect to κ^{-1}. P_{mu} with scaling (3.46), P_{hyb} with scaling (3.47). Homogeneous boundaries, $RT_0 \times RT_0 \times Q_0$, $\lambda = 1$, $c_s = 0$.

		$\lambda = \kappa^{-1}$								
	h	10^{-8}	10^{-6}	10^{-4}	10^{-2}	1	10^2	10^4	10^6	10^8
P_{mu}	1/16	4	3	5	7	8	14	14	14	14
	1/32	4	3	5	7	8	15	15	15	15
	1/64	4	3	5	7	8	15	15	15	15
	1/128	4	4	6	8	8	15	16	16	41
P_{hyb}	1/16	9	9	11	12	15	20	21	21	21
	1/32	9	9	10	12	16	21	22	22	22
	1/64	8	8	10	12	17	22	22	22	22
	1/128	7	8	10	13	17	21	22	22	22

Table 3.10: Iteration counts of GMRES with respect to $\lambda = \kappa^{-1}$. P_{mu} with scaling (3.46), P_{hyb} with scaling (3.47). Homogeneous boundaries, $RT_0 \times RT_0 \times Q_0$, $c_s = 0$.

	P_{mu}				P_{hyb}			
h	$c_s =$ 0	10^{-10}	10^{-4}	1	0	10^{-10}	10^{-4}	1
1/16	8	8	8	8	15	15	15	15
1/32	8	8	8	8	16	16	16	16
1/64	8	8	8	8	17	17	17	17
1/128	8	8	8	8	17	17	17	17

Table 3.11: Iteration counts of GMRES with respect to c_s. boundaries, $RT_0 \times RT_0 \times Q_0$, $\lambda = \kappa^{-1} = 1$.

This is necessary since the hybrid preconditioner P_{hyb} is much more sensitive regarding the mesh size in the lowest order case, which has already been observed in Table 3.2, where the iteration numbers of GMRES deteriorate with a refinement of the mesh for $k = 0$. In the following, we only show the iteration numbers calculated with scaling (3.47), since the numbers otherwise deteriorate for $k = 0$.

Using scaling (3.47) for P_{hyb}, the numbers now flatten out as the mesh size decreases, dropping considerably from 27 without scaling (Table 3.2) to 18 with scaling (Table 3.8) for $\lambda = 10^2$ and $h = \frac{1}{32}$. In Table 3.8, the situation is now comparable to the case $k = 2$ (cf. Table 3.4), except that the iteration numbers are about twice as large when λ is varied for the multiplicative algorithm, and only about two iterations more are needed in the hybrid case. For P_{mu}, the same division of the ranges is observed with 8 to 9 iterations for $\lambda \leq 1$ and 15 to 12 iterations for $\lambda \geq 10^2$, while the numbers for P_{hyb} are again somewhat more homogeneous, ranging from 17 to 13 iterations.

The dependence on the inverse of the permeability can be observed for both Schwarz methods in Table 3.9, since the numbers rise from 4 to 16 for the multiplicative method and from 8 to 20 for the hybrid method.

Very similar results occur also for the case $\lambda = \kappa^{-1}$ in Table 3.10. Again, the dependence on κ^{-1} enters the results only slightly and does not restrict the applicability of the preconditioners at all. When calculating with the multiplicative method we observe with 41 iterations an outlier for $\lambda = \kappa^{-1} = 10^8$ and $h = \frac{1}{128}$.

In Table 3.11 the specific storage capacity is varied giving constant numbers for the whole range considered.

3.5.3 Performance for Mixed Dirichlet-Neumann Boundary Values

The second test scenario describes the flow through a porous and elastic channel. The elastic solid is clamped from the left and the right and free to move on top and bottom. The fluid has a prescribed inflow in normal direction on the left boundary, homogeneous boundary conditions on top and bottom, and a free outflow on the right boundary. The setting is illustrated in Figure 3.2 and the definition given in the following. We define three different parts of the boundary of the domain $\Omega = (0,1) \times (0,1)$ by

$$\Gamma_{in} = \{x_1 = 0\}, \qquad \Gamma_{out} = \{x_1 = 1\}, \qquad \Gamma_{wall} = \{x_2 = 0\} \cup \{x_2 = 1\},$$

where $\boldsymbol{x} = (x_1, x_2) \in \mathbb{R}^2$, on which we prescribe boundary conditions for the solid displacement and the seepage velocity by

$$\begin{aligned} \boldsymbol{u} &= \boldsymbol{0} && \text{on } \Gamma_{in} \cup \Gamma_{out}, && \boldsymbol{\sigma}(\boldsymbol{u}) \cdot \boldsymbol{n} = \boldsymbol{0}, && \text{on } \Gamma_{wall}, \\ \boldsymbol{v} \cdot (-\boldsymbol{n}) &= 0.5 && \text{on } \Gamma_{in}, && \boldsymbol{v} \cdot \boldsymbol{n} = 0 && \text{on } \Gamma_{wall}, \end{aligned}$$

as well as for the pressure

$$p = 0 \quad \text{on } \Gamma_{out}.$$

External forces as well as sink or source terms are eliminated by setting

$$\boldsymbol{f} = \begin{pmatrix} 0 \\ 0 \end{pmatrix}, \qquad g = 0.$$

For the mixed Dirichlet-Neumann boundary condition of the displacement $\boldsymbol{u}$ we need to change the interior penalty bilinearform $e_h(\boldsymbol{u}, \boldsymbol{\varphi})$ such that the set of boundary faces $\Gamma_{B,h}$ contains all faces on $\Gamma_{in} \cup \Gamma_{out}$, but not the faces on Γ_{wall}. Furthermore, all degrees of freedom that belong to the normal component of $\boldsymbol{u}$ on $\Gamma_{in} \cup \Gamma_{out}$, and of $\boldsymbol{v}$ on $\Gamma_{in} \cup \Gamma_{wall}$ need to be constrained. To incorporate the inhomogeneous boundary condition of the seepage velocity, we assemble the system with a homogeneous boundary condition on $\Gamma_{in} \cup \Gamma_{wall}$ and use Newton's method as an outer solver with a starting vector that has the correct inhomogeneous boundary values. Then, the boundary values of the starting vector are transported to all following vectors in the Newton iteration.

The resulting system is solved again with GMRES preconditioned by the multiplicative

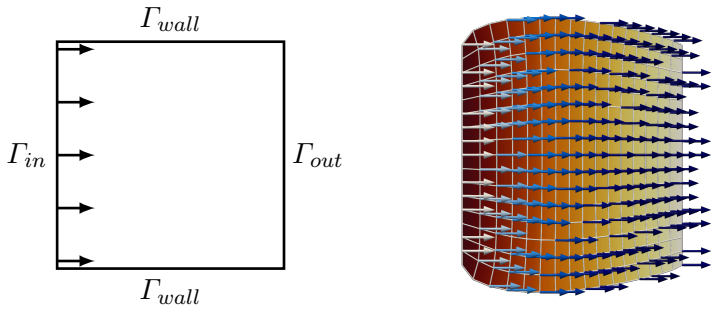

Figure 3.2: Flow through a poroelastic tube. The arrows illustrate the flux of the seepage velocity, the displacement is visualized by the deformation of the grid, the pressure is shown via the background color. The magnitudes are exaggerated in favor of the representation.

	P_{mu}		P_{hyb}	
h	ex	in	ex	in
1/4	9	8	17	15
1/8	8	8	20	15
1/16	8	8	20	15
1/32	8	8	19	15

Table 3.12: Comparison: Iteration counts of GMRES when single cell patches are included (in) vs. excluded (ex). Multiplicative two-level Schwarz P_{mu}, hybrid two-level Schwarz P_{hyb}. Mixed boundaries, $RT_2 \times RT_2 \times Q_2$, $\lambda = \kappa^{-1} = 1$, $c_s = 0$.

and hybrid two-level Schwarz operators defined in Section 3.3 and solved until the starting residual is reduced by a factor of 10^{-8}.

This time, we include also vertex patches where the corresponding vertex lies at the boundary $\partial\Omega$, so-called boundary patches. These patches are made out of two cells, if the corresponding vertex lies on an edge. For vertices located in a corner the resulting patches are called single cell patches, since they contain only one cell. As it turns out, we need to include boundary patches in this test scenario with mixed Dirichlet-Neumann boundary conditions, since otherwise the calculations fail. But, whereas boundary patches have to be added to the set of patches, single cell patches can be left out for the multiplicative Schwarz method. Their absence does not lead to a decrease of efficiency as the iteration numbers are the same, as can be seen in Table 3.12 for the multiplicative operator

	P_{mu}						P_{hyb}					
h	$\lambda =$ 0	1	10^2	10^4	10^6	10^8	0	1	10^2	10^4	10^6	10^8
1/4	10	9	8	4	1	1	15	15	14	10	4	3
1/8	9	8	6	4	1	1	15	15	14	11	5	5
1/16	9	8	6	4	1	1	15	15	14	11	5	5
1/32	8	8	6	4	1	1	13	15	14	11	5	5

Table 3.13: Iterations of GMRES with respect to λ. P_{mu} without single cell patches, P_{hyb} with single cell patches included. Mixed boundaries, $RT_2 \times RT_2 \times Q_2$, $\kappa^{-1} = 1$, $c_s = 0$.

P_{mu}. For the hybrid Schwarz method, however, we clearly have a beneficial effect on the iteration counts of GMRES, if single cell patches are included, see the columns for P_{hyb} in Table 3.12, where the numbers drop from about 19 to 15, when single cell patches are included. This particularly holds true in case of varying λ and c_s, whereas in case of larger values of $\kappa^{-1} \geq 10^2$ the effect is notably smaller with only one iteration difference. For the following tests we thus include boundary patches for both operators, but use single cell patches only for the calculations with P_{hyb}.

In Table 3.13 we see that the iterations of GMRES are robust in λ and only for $\lambda \geq 10^6$ do we observed a numerical instability for P_{mu} and P_{hyb}. For both cases, a scaling as in (3.46) leads to robustness even in the nearly incompressible case, with five iterations for the hybrid method and only one iteration for P_{mu}.

In Table 3.14 we observe robust iteration counts of GMRES with respect to κ^{-1} for both, the multiplicative and the hybrid operator. In this test scenario with mixed Dirichlet-Neumann boundary conditions the scaling (3.46) is important. We encountered a dependence of the iterations with respect to the permeability κ rather than on the reciprocal κ^{-1} when no scaling is used, see Table 4.2 for the case $\nu = 0$. To be precise, the iteration counts grow when κ^{-1} tends to zero, i.e., when κ becomes large, which is in contrast to the convergence proof of Section 3.4. In particular, the multiplicative method without scaling shows deteriorating iteration counts for smaller becoming κ^{-1} and requires 50 iterations to converge for $\kappa^{-1} = 10^{-8}$. Although not displayed in the tables, the hybrid operator behaves similar as expected and is even more sensitive for small values of $\kappa^{-1} \leq 10^{-4}$ than the multiplicative operator. Nevertheless, with the scaling (3.46) the iteration numbers are limited and even decrease for $\kappa^{-1} \leq 10^{-4}$, leading to robustness of the numbers, as we can see in Table 3.14.

		κ^{-1}								
	h	10^{-8}	10^{-6}	10^{-4}	10^{-2}	1	10^{2}	10^{4}	10^{6}	10^{8}
P_{mu}	1/4	8	8	8	8	9	6	6	4	4
	1/8	5	5	6	8	8	5	6	4	4
	1/16	5	5	6	8	8	5	5	4	4
	1/32	5	5	6	8	8	5	5	4	4
P_{hyb}	1/4	20	20	22	25	15	11	11	8	9
	1/8	12	14	15	18	15	11	11	9	9
	1/16	12	14	15	18	15	11	11	10	9
	1/32	13	14	16	18	15	11	11	10	9

Table 3.14: Iterations of GMRES with respect to κ^{-1}. P_{mu} without single cell patches, P_{hyb} with single cell patches included. Mixed boundaries, $RT_2 \times RT_2 \times Q_2$, $\lambda = 1$, $c_s = 0$.

		$\lambda = \kappa^{-1}$								
	h	10^{-8}	10^{-6}	10^{-4}	10^{-2}	1	10^{2}	10^{4}	10^{6}	10^{8}
P_{mu}	1/4	9	8	8	6	9	5	4	4	4
	1/8	5	5	6	5	8	5	4	3	4
	1/16	5	5	6	5	8	5	4	3	4
	1/32	5	5	6	5	8	5	4	3	8
P_{hyb}	1/4	20	21	23	11	15	10	8	8	8
	1/8	12	14	15	11	15	11	8	7	7
	1/16	12	14	15	11	15	11	8	7	8
	1/32	12	14	16	11	15	11	9	8	13

Table 3.15: Iterations of GMRES with respect to $\lambda = \kappa^{-1}$. P_{mu} without single cell patches, P_{hyb} with single cell patches included. Mixed boundaries, $RT_2 \times RT_2 \times Q_2$, $c_s = 0$.

	P_{mu}				P_{hyb}			
h	$c_s =$ 0	10^{-10}	10^{-5}	1	0	10^{-10}	10^{-5}	1
1/4	9	9	9	9	15	15	15	15
1/8	8	8	8	8	15	15	15	15
1/16	8	8	8	8	15	15	15	15
1/32	8	8	8	8	15	15	15	15

Table 3.16: Iterations of GMRES with respect to c_s. P_{mu} without single cell patches, P_{hyb} with single cell patches included. Mixed boundaries, $RT_2 \times RT_2 \times Q_2$, $\lambda = \kappa^{-1} = 1$.

In the case $\lambda = \kappa^{-1}$ the effects of the numerical instability for large values observed for λ and the dependence on the permeability for values of κ^{-1} close to zero accumulate, leading to an increase of the number of iterations even for values closer to 1, when no scaling is used. Again, scaling the system leads to robustness of the iteration counts, as shown in Table 3.15, in which we focus on the scaled system only, since the effects of numerical instabilities and dependence on κ have already been discussed.

Finally, Table 3.16 shows constant iteration numbers for P_{mu}, as well as for P_{hyb}, when the storage capacity c_s is varied.

3.5.4 Optimal Relaxation Parameter

In the preceding test cases the numerical test runs were performed with a fixed relaxation parameter $\omega = 0.25$. In the following, the optimality of this parameter will be discussed. To this end we measure the iteration counts of GMRES for varying values of ω in different scenarios to track possible dependencies regarding the model parameters.

As test case we choose the problem setting as described in Section 3.5.1 with homogeneous boundary conditions and mean-value free pressure, as well as the channel flow scenario of Section 3.5.3. The calculations in Figure 3.3 are performed for the finite element space $RT_2 \times RT_2 \times Q_2$. The test results for the different values of the parameters λ, κ^{-1} and c_s are calculated on mesh level 4, which corresponds to $h = \frac{1}{16}$ with 256 cells and 11712 degrees of freedom. As default scenario we choose the saddle point problem determined by the choice $\lambda = \kappa^{-1} = 1$, $c_s = 0$, for which the tests regarding the mesh size h are performed. If one parameter is chosen differently as the default, this is explicitly indicated, such that for example the line corresponding to $\kappa^{-1} = 10^6$ refers to the case $\lambda = 1$, $\kappa^{-1} = 10^6$, $c_s = 0$.

In case of homogeneous boundary values in Figure 3.3, we observe the lowest iteration counts in the range $0.26 \leq w \leq 0.3$ for different values of the parameters λ, κ^{-1} and c_s, and in the range $0.27 \leq w \leq 0.3$ when the mesh size h is varied in the default case.

In the poroelastic channel flow scenario the lowest iteration counts lie between 0.24 and 0.27. We detect the lowest count for $\lambda = 10^4$ at $\omega = 0.29$, for $c_s = 1$ at 0.26, and for varying mesh size in the default case at $\omega = 0.25$, when $h = \frac{1}{32}$.

Throughout the calculations shown in Figure 3.3 we observe the lowest iteration counts for ω between 0.27 and 0.28, independently of the model parameters, the mesh size or the choice of boundary conditions. Nevertheless, optimal iteration counts can be detected at

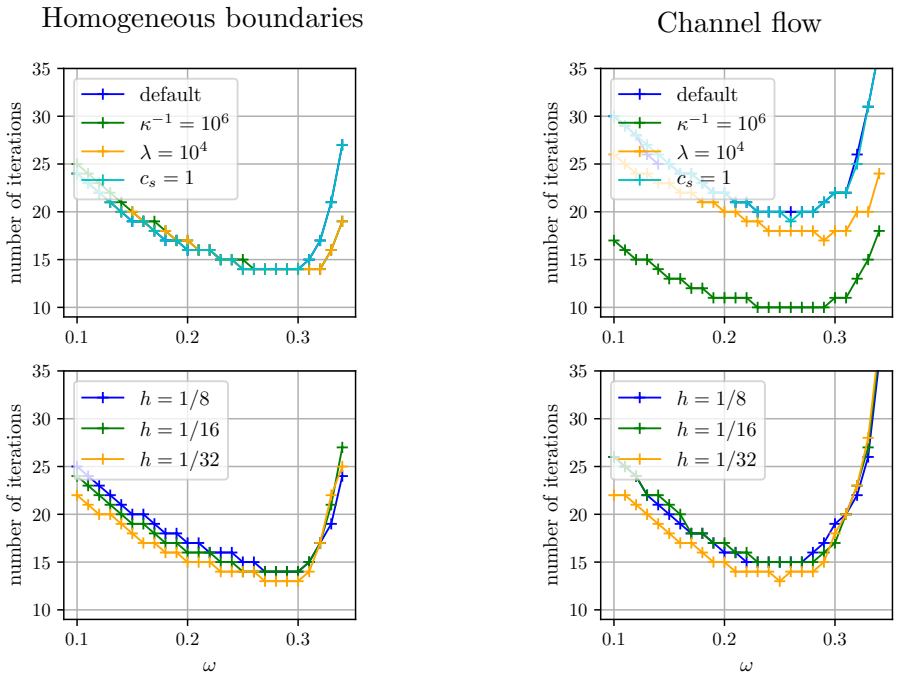

Figure 3.3: Optimality of relaxation parameter ω of hybrid Schwarz method with respect to iteration counts of GMRES. "default" refers to $\lambda = \kappa^{-1} = 1$, $c_s = 0$.

or close to the choice $\omega = 0.25$.

3.5.5 Multilevel Schwarz

In this section we provide tests for the multilevel Schwarz methods as introduced in Section 2.5 for the test case with homogeneous boundary conditions from Section 3.5.1.

We start with a brief investigation of different versions of the multiplicative and hybrid multilevel methods in Table 3.17. Therefore, in addition to the multiplicative multilevel Schwarz $\boldsymbol{M}_{\text{mu}}$, we introduce a symmetric multiplicative Schwarz method $\boldsymbol{M}_{\text{mu}}^{*}$ that also performs the pre-smoothing steps by setting $m_{\text{pre}} = 1$ in Algorithm 2.5 and applies the local contributions of the post-smoothing on each level in reversed order of the pre-smoothing. Furthermore, we consider hybrid multilevel Schwarz methods $\boldsymbol{M}_{\text{hyb}}^{m}$ with several smoothing steps m, where the number of pre-smoothing and post-smoothing steps is equal. With this notation, it holds for the hybrid preconditioner $\boldsymbol{M}_{\text{hyb}} = \boldsymbol{M}_{\text{hyb}}^{1}$.

h	$\boldsymbol{M}_{\text{mu}}$	$\boldsymbol{M}^*_{\text{mu}}$	$\boldsymbol{M}_{\text{hyb}}$	$\boldsymbol{M}^2_{\text{hyb}}$	$\boldsymbol{M}^3_{\text{hyb}}$	$\boldsymbol{M}^4_{\text{hyb}}$
1/8	5	4	16	11	8	7
1/16	5	5	17	11	8	7
1/32	5	5	18	11	8	7
1/64	5	5	19	11	8	6

Table 3.17: Comparison of different multiplicative and hybrid multilevel Schwarz algorithms for test case with homogeneous boundaries. $\lambda = \kappa^{-1} = 1$, $c_s = 0$.

In Table 3.17 we observe that an additional pre-smoothing in case of the multiplicative multilevel Schwarz method does not lead to a reduction of the iteration counts of GMRES, thus, it is sufficient in practice to use $\boldsymbol{M}_{\text{mu}}$ in favor of $\boldsymbol{M}^*_{\text{mu}}$.

For the hybrid operator we see a beneficial influence of the number of smoothing steps on the performance of GMRES in Table 3.17. A second smoothing step stabilizes the convergence of the hybrid method, but at least three to four smoothing steps are necessary to reach a comparable number of iterations as the multiplicative preconditioner $\boldsymbol{M}_{\text{mu}}$. That means, that a total amount of more than six to eight times as much smoothing operations are needed for the hybrid preconditioner.

We then examine the robustness of the multilevel Schwarz preconditioners with respect to the parameters λ, κ^{-1} and c_s. The presentation is restricted to the polynomial degree $k = 2$ and we comment in each table when scaling is used.

As before, the multiplicative Schwarz method gives better results than the hybrid method, the dependence on κ^{-1} is observed only very slightly in the computations, and numerical instabilities can be remedied by the scaling described in Section 3.5.2. The performance results for the multiplicative multilevel Schwarz method are essentially the same as in the two-level setting. Throughout the calculations, GMRES preconditioned by $\boldsymbol{M}_{\text{mu}}$ requires only about 1 to 2 iterations more to converge than an exact solution at level $L-1$, cf. Tables 3.18 to 3.21 with Tables 3.4 to 3.7. The hybrid operator, however, turns out to be more sensitive than the multiplicative operator with about 5 to 11 iterations more.

Both multilevel methods seem to be more stable to higher values of λ and κ^{-1}, so that numerical instabilities do not occur as quickly as with the two-level methods. This is because the coarsest matrix at level $\ell_0 = 0$ is much smaller and therefore easier to invert than at $\ell_0 = L-1$. Thus, both multilevel Schwarz methods are effective preconditioners

	$\boldsymbol{M}_{\text{mu}}$						$\boldsymbol{M}_{\text{hyb}}$					
h	$\lambda = 0$	1	10^2	10^4	10^6	10^8	0	1	10^2	10^4	10^6	10^8
1/16	5	5	7	7	7	4	17	17	19	19	20	20
1/32	5	5	8	8	8	5	18	18	21	21	21	22
1/64	5	5	8	8	8	5	18	19	23	23	24	24
1/128	5	5	8	8	8	6	19	19	24	25	25	33

Table 3.18: Iteration counts of GMRES with respect to λ for multiplicative multilevel Schwarz (left) and hybrid multilevel Schwarz (right). Homogeneous boundaries, $RT_2 \times RT_2 \times Q_2$.

		κ^{-1}								
	h	10^{-8}	10^{-6}	10^{-4}	10^{-2}	1	10^2	10^4	10^6	10^8
$\boldsymbol{M}_{\text{mu}}$	1/16	1	2	3	4	5	5	7	7	7
	1/32	1	2	3	4	5	5	7	8	8
	1/64	1	3	3	5	5	5	7	8	8
	1/128	2	3	3	5	5	5	7	8	8
$\boldsymbol{M}_{\text{hyb}}$	1/16	11	12	13	15	17	17	18	20	19
	1/32	11	12	13	16	18	18	20	22	21
	1/64	11	13	14	17	19	19	20	23	24
	1/128	12	13	15	18	19	19	20	24	26

Table 3.19: Iteration counts of GMRES with respect to κ^{-1}. Multiplicative multilevel Schwarz (top), hybrid multilevel Schwarz (bottom). Homogeneous boundaries, $RT_2 \times RT_2 \times Q_2$.

		$\lambda = \kappa^{-1}$								
	h	10^{-8}	10^{-6}	10^{-4}	10^{-2}	1	10^2	10^4	10^6	10^8
$\boldsymbol{M}_{\text{mu}}$	1/16	1	2	3	4	5	7	7	7	7
	1/32	1	2	3	4	5	8	8	8	8
	1/64	1	2	3	4	5	8	8	8	8
	1/128	2	2	3	4	5	8	8	8	8
$\boldsymbol{M}_{\text{hyb}}$	1/16	12	12	13	15	17	19	19	20	20
	1/32	11	12	13	16	18	21	21	21	21
	1/64	11	12	14	17	19	23	23	24	24
	1/128	12	13	14	18	19	24	25	25	26

Table 3.20: Iteration counts of GMRES with respect to $\lambda = \kappa^{-1}$. Multiplicative multilevel Schwarz (top), hybrid multilevel Schwarz (bottom). Homogeneous boundaries, $RT_2 \times RT_2 \times Q_2$, $c_s = 0$.

	$\boldsymbol{M}_{\text{mu}}$				$\boldsymbol{M}_{\text{hyb}}$			
h	$c_s =$ 0	10^{-10}	10^{-4}	1	0	10^{-10}	10^{-4}	1
1/16	5	5	5	5	17	17	17	17
1/32	5	5	5	5	18	18	18	18
1/64	5	5	5	5	19	19	19	19
1/128	5	5	5	5	19	19	19	19

Table 3.21: Iteration counts of GMRES with respect to c_s. Multiplicative multilevel Schwarz (left), hybrid multilevel Schwarz (right). Homogeneous boundaries, $RT_2 \times RT_2 \times Q_2$.

for Biot's consolidation model.

3.6 Conclusion

In this chapter we have successfully applied overlapping Schwarz methods to H^{div}-conforming discretizations of Biot's consolidation model. We proved convergence of the two-level methods independent of the rescaled model parameters λ and c_s, as well as the discretization parameter h and the number of subdomains J for a proper choice of the overlap δ and the mesh size H of the coarse space. The dependence on the inverse of the rescaled permeability constant κ^{-1} has no deteriorating effect on the robustness of the method when a test case with homogeneous boundary conditions is considered. On the contrary, for large values of κ^{-1} the iteration numbers stay bounded and for small values of κ^{-1} the numbers even decrease.

In a test scenario with mixed Dirichlet-Neumann boundary values the dependence appears to be on κ rather than on its reciprocal. Numerical instabilities caused by extremely large chosen parameters could be remedied by scaling the system.

The relaxation factor of the hybrid Schwarz method only needs to compensate that the contributions of the local vertex patches are summed, which was confirmed in a numerical optimality study.

In addition to the discussion of the two-level Schwarz methods, we have presented tests that go beyond the analysis of this chapter by relaxing the coarse space solve to the case of multiplicative and hybrid multilevel methods. As already seen in the two-level case, the multilevel Schwarz methods perform very well and produce flat iteration counts of GMRES robust in the parameter ranges.

Chapter 4

Two-level Schwarz Preconditioner for Highly Permeable Poroelasticity

The quasi-static Biot-Brinkman model

$$\begin{aligned} -\operatorname{div}(2\mu\boldsymbol{\varepsilon}(\boldsymbol{u}) + \lambda \operatorname{div}\boldsymbol{u}) + \alpha\nabla p &= \boldsymbol{f} && \text{in } \Omega \times (0,T), \\ -\nu\Delta\boldsymbol{v} + \boldsymbol{K}^{-1}\boldsymbol{v} + \nabla p &= \boldsymbol{0} && \text{in } \Omega \times (0,T), \\ -\alpha \operatorname{div}\partial_t\boldsymbol{u} - \operatorname{div}\boldsymbol{v} - c_s\partial_t p &= g && \text{in } \Omega \times (0,T). \end{aligned} \tag{4.1}$$

describes the flow of a fluid through an elastic porous solid in an open bounded domain $\Omega \subset \mathbb{R}^d$ over a time interval $(0,T)$. As Biot's consolidation model, it couples the displacement field $\boldsymbol{u}$ of the solid component, the seepage velocity $\boldsymbol{v}$ of the fluid and the pressure p in a fully saturated porous medium, where the elastic behavior of the material is assumed to be linear and described by the stress-strain relation of Hooke's law with the Lamé constants $\lambda, \mu > 0$ of elasticity. But instead of Darcy's law a diffusion term is added to the equations of fluid flow through a porous solid,

$$-\nu\Delta\boldsymbol{v} + \boldsymbol{K}^{-1}\boldsymbol{v} + \nabla p = \boldsymbol{0} \qquad \text{in } \Omega \times (0,T),$$

as suggested by Brinkman in [Bri49]. Here, $\nu > 0$ denotes a viscosity constant, that might be different to the viscosity of the fluid, and $\boldsymbol{K}$ is a tensor that is linked to the permeability of the medium, for which we assume that it is bounded in the sense of (3.2). Moreover, α denotes the Biot-Willis constant from Biot's consolidation model, but here applied to the coupling of the equations of elasticity with Brinkman's equations, and $c_s \geq 0$ is the specific storage coefficient that allows for some additional compressibility of the medium within the mass balance equation.

The aim of using Brinkman's equations instead of Darcy's law is to stabilize the equations for higher permeabilities, when the fraction of the pore-volume compared to

the total volume is at a critical size, i.e., when the pore-volume is large compared to the volume of the solid matrix.

As one can see, the Biot-Brinkman model (4.1) is a generalization of Biot's linear consolidation model (3.1) and both are equivalent in the limit case $\nu \to 0$. However, due to the additional diffusion term, the properties of the solution space for the fluid changes in the limit $\nu = 0$, and thus, the Biot-Brinkman equations are structurally different from Biot's consolidation model. To be precise, for $\nu > 0$ we search for a solution $\boldsymbol{v}$ that is more regular and at least in $[H^1(\Omega)]^d$, instead of $H^{\text{div}}(\Omega)$ when $\nu = 0$. Moreover, the boundary condition of the seepage velocity is different to the case $\nu = 0$. Where in Biot's model we had to prescribe the normal component on the boundary $\partial\Omega$ only, now the whole boundary function is taken into account.

The model follows a continuum mechanical approach and is described as a bulk medium from a macroscopic point of view. To our knowledge, a mathematically rigorous derivation of the equations has not been examined, yet.

In [RTL19], the derivation of a model close to (4.1) has been presented, where Rohan, Turjanicová and Lukeš rigorously derive a set of equations that describes a Biot-Darcy-Brinkman model in the context of double-porous media. For the derivation, they employ the two-scale homogenization theory, where the effective macroscopic equations are derived from a microstructure model and a mesoscopic intermediate model.

Hong et. al. consider generalized Biot-Brinkman equations in [HKK+22] that are equivalent to (4.1) for the case of one fluid. They employ a mass conservative discretization with H^{div}-conforming mixed finite element spaces and propose a block-diagonal preconditioner analogously to [HKLP19].

We follow the same methodology as in chapter Chapter 3 outlined in the following.

In Section 4.1 the Biot-Brinkman model is discretized by H^{div}-conforming finite element spaces using an interior penalty discontinuous Galerkin formulation for the elasticity form, as well as for the additional diffusion term in the Brinkman equations. Section 4.2 treats the application of the overlapping two-level Schwarz preconditioner to the discrete system and proves its convergence. Finally, in Section 4.3 the performance of the Schwarz method is tested in a series of experiments, showing the stabilizing effect of the additional diffusion term in cases of otherwise deteriorating iteration numbers of GMRES due to the permeability dependence.

4.1 Mass Conservative Discretization

As in Chapter 3 we first discretize (4.1) in time by the backward Euler method, then scale the system and finally employ an H^{div}-conforming finite element method that results in a mass conservative discretization.

Semi-discretization in time by the backward Euler method to time step size $\tau > 0$, as well as a scaling and substitution of variables leads to symmetric problems of the form

$$\begin{aligned} -\operatorname{div}\left(\boldsymbol{\varepsilon}(\boldsymbol{u}) + \tilde{\lambda}\operatorname{div}\boldsymbol{u}\right) + \nabla\tilde{p} &= \tilde{\boldsymbol{f}} && \text{in } \Omega, \\ -\tilde{\nu}\Delta\tilde{\boldsymbol{v}} + \tilde{\boldsymbol{K}}^{-1}\tilde{\boldsymbol{v}} + \nabla\tilde{p} &= \boldsymbol{0} && \text{in } \Omega, \\ -\operatorname{div}\boldsymbol{u} - \operatorname{div}\tilde{\boldsymbol{v}} - \tilde{c_s}\tilde{p} &= \tilde{g} && \text{in } \Omega, \end{aligned} \tag{4.2}$$

where the seepage velocity and the pressure are substituted by

$$\tilde{\boldsymbol{v}} = \frac{\tau}{\alpha}\boldsymbol{v}, \quad \tilde{p} = \frac{\alpha}{2\mu}p,$$

and the right hand side is changed to

$$\tilde{\boldsymbol{f}} = \frac{1}{2\mu}\boldsymbol{f}, \qquad \tilde{g} = \frac{\tau}{\alpha}g - \operatorname{div}\boldsymbol{u}_{\mathrm{old}} - \frac{c_s}{\alpha}p_{\mathrm{old}},$$

with $\boldsymbol{u}_{\mathrm{old}}$ and p_{old} taken from the previous time step and all other quantities referring to the new time step. Furthermore, the parameters of the system are substituted by

$$\tilde{\nu} = \frac{\alpha^2}{2\mu\tau}\nu, \qquad \tilde{\boldsymbol{K}}^{-1} = \frac{\alpha^2}{2\mu\tau}\boldsymbol{K}^{-1}, \qquad \tilde{\lambda} = \frac{\lambda}{2\mu}, \qquad \tilde{c_s} = \frac{2\mu c_s}{\alpha^2}. \tag{4.3}$$

The tilde symbol will be skipped in the following for convenience, since this is the normalized system of equations, that we build our analysis on.

We assume homogeneous Dirichlet boundary conditions on the displacement and on the seepage velocity and define

$$U = [H_0^1(\Omega)]^d, \qquad V = [H_0^1(\Omega)]^d, \qquad Q = L_0^2(\Omega).$$

The weak formulation of (4.2) is then: find $(\boldsymbol{u}, \boldsymbol{v}, p) \in U \times V \times Q$, such that

$$\begin{aligned} e(\boldsymbol{u}, \boldsymbol{\varphi}) + \lambda d(\boldsymbol{u}, \boldsymbol{\varphi}) - b(p, \boldsymbol{\varphi}) &= (\boldsymbol{f}, \boldsymbol{\varphi})_\Omega && \forall \boldsymbol{\varphi} \in U, \\ \nu a(\boldsymbol{v}, \boldsymbol{\psi}) + k(\boldsymbol{v}, \boldsymbol{\psi}) - b(p, \boldsymbol{\psi}) &= \boldsymbol{0} && \forall \boldsymbol{\psi} \in V, \\ -b(q, \boldsymbol{u}) - b(q, \boldsymbol{v}) - c_s(p, q)_\Omega &= (g, q)_\Omega && \forall q \in Q, \end{aligned} \tag{4.4}$$

with bilinear forms

$$\begin{aligned} e(\boldsymbol{u}, \boldsymbol{\varphi}) &= (\boldsymbol{\varepsilon}(\boldsymbol{u}), \boldsymbol{\varepsilon}(\boldsymbol{\varphi}))_\Omega, & d(\boldsymbol{u}, \boldsymbol{\varphi}) &= (\operatorname{div} \boldsymbol{u}, \operatorname{div} \boldsymbol{\varphi})_\Omega, \\ b(p, \boldsymbol{\psi}) &= (p, \operatorname{div} \boldsymbol{\psi})_\Omega, & k(\boldsymbol{v}, \boldsymbol{\psi}) &= (\boldsymbol{K}^{-1} \boldsymbol{v}, \boldsymbol{\psi})_\Omega, \\ a(\boldsymbol{u}, \boldsymbol{\psi}) &= (\nabla \boldsymbol{u}, \nabla \boldsymbol{\psi})_\Omega. \end{aligned}$$

We go on with the discretization of (4.4) by a family of H^{div}-conforming mixed finite element methods, such that

$$\operatorname{div} U_h = Q_h, \qquad \operatorname{div} V_h = Q_h,$$

leading to the conservation of the discrete mass, such that the equation

$$-\operatorname{div} \boldsymbol{u}_h - \operatorname{div} \boldsymbol{v}_h - c_s p_h = g_h$$

is fulfilled pointwise.

The discretization space is $X_h = U_h \times V_h \times Q_h$ and we adopt the notation and discretization as in Section 3.2, especially the definition of bilinear form $e_h(\cdot, \cdot)$ as discrete interior penalty discontinuous Galerkin approximation of $e(\cdot, \cdot)$.

For the equation of Brinkman to model porous media flow we now have to consider the additional diffusion term. Where in the Darcy case, we simply could use a L^2-term, we now have to introduce another interior penalty discretization as approximation of $a(\cdot, \cdot)$, which complicates the discrete formulation but is necessary due to the H^{div}-conformity of the discretization space and to approximate the second order bilinear form $a(\cdot, \cdot)$.

Therefore, we define on $V_h \times V_h$ the discrete bilinear form

$$\begin{aligned} a_h(\boldsymbol{u}_h, \boldsymbol{\varphi}) = &\sum_{T\in\mathcal{T}_h} \big(\nabla \boldsymbol{u}_h, \nabla \boldsymbol{\varphi}\big)_T + \sum_{F\in\Gamma_{I,h}} \frac{\eta_a}{h} \big([\![\boldsymbol{u}_h]\!], [\![\boldsymbol{\varphi}]\!]\big)_F \\ &- \sum_{F\in\Gamma_{I,h}} \big(\{\!\{\nabla \boldsymbol{u}_h \boldsymbol{n}\}\!\}, [\![\boldsymbol{\varphi}]\!]\big)_F - \sum_{F\in\Gamma_{I,h}} \big([\![\boldsymbol{u}_h]\!], \{\!\{\nabla \boldsymbol{\varphi} \boldsymbol{n}\}\!\}\big)_F \\ &+ \sum_{B\in\Gamma_{B,h}} \frac{\eta_a}{h} \big(\boldsymbol{u}_h, \boldsymbol{\varphi}\big)_B - \sum_{B\in\Gamma_{B,h}} \big(\nabla \boldsymbol{u}_h \boldsymbol{n}, \boldsymbol{\varphi}\big)_B - \sum_{B\in\Gamma_{B,h}} \big(\boldsymbol{u}_h, \nabla \boldsymbol{\varphi} \boldsymbol{n}\big)_B. \end{aligned} \tag{4.5}$$

The penalty parameter $\eta_a > 0$ is chosen large enough to ensure coercivity of $a_h(\cdot,\cdot)$

$$a_h(\boldsymbol{\psi}, \boldsymbol{\psi}) \geq c \big\|\boldsymbol{\psi}\big\|_{1,h}^2 \qquad \forall \boldsymbol{\psi} \in V_h. \tag{4.6}$$

In addition, continuity of $a_h(\cdot,\cdot)$ holds in the norm $\|\cdot\|_{1,h}$,

$$a_h(\boldsymbol{v}_h, \boldsymbol{\psi}) \leq c \big\|\boldsymbol{v}_h\big\|_{1,h} \big\|\boldsymbol{\psi}\big\|_{1,h} \qquad \forall \boldsymbol{v}_h, \boldsymbol{\psi} \in V_h. \tag{4.7}$$

The mass conserving mixed method based on the finite element space X_h can then be represented as

$$\mathbb{A}_h^a \left(\begin{pmatrix} \boldsymbol{u}_h \\ \boldsymbol{v}_h \\ p_h \end{pmatrix}, \begin{pmatrix} \boldsymbol{\varphi} \\ \boldsymbol{\psi} \\ q \end{pmatrix} \right) = \mathbb{F}_h \left(\begin{pmatrix} \boldsymbol{\varphi} \\ \boldsymbol{\psi} \\ q \end{pmatrix} \right), \tag{4.8}$$

where the discrete bilinear form $\mathbb{A}_h^a(\cdot,\cdot) : X_h \times X_h \to \mathbb{R}$ is defined by

$$\begin{aligned} \mathbb{A}_h^a \left(\begin{pmatrix} \boldsymbol{u}_h \\ \boldsymbol{v}_h \\ p_h \end{pmatrix}, \begin{pmatrix} \boldsymbol{\varphi} \\ \boldsymbol{\psi} \\ q \end{pmatrix} \right) =& e_h(\boldsymbol{u}_h, \boldsymbol{\varphi}) + \lambda d(\boldsymbol{u}_h, \boldsymbol{\varphi}) + \nu a_h(\boldsymbol{v}_h, \boldsymbol{\psi}) + k(\boldsymbol{v}_h, \boldsymbol{\psi}) \\ &- b(p_h, \boldsymbol{\varphi} + \boldsymbol{\psi}) - b(q, \boldsymbol{u}_h + \boldsymbol{v}_h) - c_s(p_h, q)_\Omega \end{aligned}$$

and the right hand side is given by

$$\mathbb{F}_h \left(\begin{pmatrix} \boldsymbol{\varphi} \\ \boldsymbol{\psi} \\ q \end{pmatrix} \right) = (\boldsymbol{f}, \boldsymbol{\varphi})_\Omega + (g_h, q)_\Omega,$$

with g_h chosen as the L^2-projection $\Pi^h g$. For the choice of $H(\mathrm{div})$-conforming discretization spaces the following discrete inf-sup conditions hold, see, e.g. [BBF13, HL02, SST03, Bre74])

$$\inf_{q\in Q_h}\sup_{\boldsymbol{\varphi}\in U_h}\frac{\left(\operatorname{div}\boldsymbol{\varphi},q\right)_\Omega}{\|\boldsymbol{\varphi}\|_{1,h}\|q\|_\Omega}\geq\gamma_u>0 \tag{4.9}$$

and

$$\inf_{q\in Q_h}\sup_{\boldsymbol{\psi}\in V_h}\frac{\left(\operatorname{div}\boldsymbol{\psi},q\right)_\Omega}{\|\boldsymbol{\psi}\|_{1,h}\|q\|_\Omega}\geq\gamma_v>0. \tag{4.10}$$

For existence of solutions we follow [HKK+22] and refer to [HW11] for the existence of general saddle point problems. Existence of solutions of system (4.8) follows then by coercivity (3.9) and (4.6), continuity (3.10) and (4.7), as well as the discrete inf-sup conditions (4.9) and (4.10).

4.2 Two-level Schwarz Convergence Analysis

The definition of the overlapping two-level Schwarz method for the Biot-Brinkman model is analogous to Section 3.3 with the bilinear form $\mathbb{A}_h^a(\cdot,\cdot)$ instead of $\mathbb{A}_h(\cdot,\cdot)$. The convergence proof follows the same ideas as for Biot's consolidation model in Section 3.4, i.e., transforming problem (4.8) into an equivalent singularly perturbed problem using the mass conservation property of the H^{div}-conforming discretization, then decomposing the spaces according to the kernel of the divergence operator, and finally proving for the Assumptions 2.2 to 2.4, with the proof of the stable decomposition forming the main part of the convergence proof. As a result we get the following two theorems.

Theorem 4.1. *The multiplicative two-level Schwarz method converges with a contraction number independent of the mesh size h and the material parameters λ and c_s.*

Theorem 4.2. *The additive two-level Schwarz method converges independently of the mesh size h and the material parameters λ and c_s.*

We will go very quickly through the proof in this chapter and work out the differences to the proof of Biot's consolidation model, only. For a detailed discussion of all statements we refer the reader to Section 3.4. Nevertheless, we will examine the proof of the stable

decomposition in full length to be able to track the changing dependencies of the constants and parameters.

Substitution of the point-wise fulfilled discrete mass equation

$$-\operatorname{div} \boldsymbol{u}_h - \operatorname{div} \boldsymbol{v}_h - c_s p_h = g_h$$

in (4.8) leads to the equivalent, singularly perturbed problem

$$\begin{aligned} e_h(\boldsymbol{u}_h, \boldsymbol{\varphi}) + \lambda d(\boldsymbol{u}_h, \boldsymbol{\varphi}) + c_s^{-1} d(\boldsymbol{u}_h + \boldsymbol{v}_h, \boldsymbol{\varphi}) &= (\boldsymbol{f}, \boldsymbol{\varphi})_\Omega - c_s^{-1} (g_h, \operatorname{div} \boldsymbol{\varphi})_\Omega, \\ \nu a_h(\boldsymbol{v}_h, \boldsymbol{\psi}) + k(\boldsymbol{v}_h, \boldsymbol{\psi}) + c_s^{-1} d(\boldsymbol{u}_h + \boldsymbol{v}_h, \boldsymbol{\psi}) &= -c_s^{-1} (g_h, \operatorname{div} \boldsymbol{\psi})_\Omega, \end{aligned}$$

for all $(\boldsymbol{\varphi}, \boldsymbol{\psi}) \in W_h = U_h \times V_h$. We rewrite this system as

$$\mathscr{A}_h^a \left(\begin{pmatrix} \boldsymbol{u}_h \\ \boldsymbol{v}_h \end{pmatrix}, \begin{pmatrix} \boldsymbol{\varphi} \\ \boldsymbol{\psi} \end{pmatrix} \right) = \mathscr{F}_h \left(\begin{pmatrix} \boldsymbol{\varphi} \\ \boldsymbol{\psi} \end{pmatrix} \right)$$

with

$$\mathscr{A}_h^a \left(\begin{pmatrix} \boldsymbol{u}_h \\ \boldsymbol{v}_h \end{pmatrix}, \begin{pmatrix} \boldsymbol{\varphi} \\ \boldsymbol{\psi} \end{pmatrix} \right) = A_h^a \left(\begin{pmatrix} \boldsymbol{u}_h \\ \boldsymbol{v}_h \end{pmatrix}, \begin{pmatrix} \boldsymbol{\varphi} \\ \boldsymbol{\psi} \end{pmatrix} \right) + D \left(\begin{pmatrix} \boldsymbol{u}_h \\ \boldsymbol{v}_h \end{pmatrix}, \begin{pmatrix} \boldsymbol{\varphi} \\ \boldsymbol{\psi} \end{pmatrix} \right), \tag{4.11}$$

where the bilinear forms $A_h^a(\cdot, \cdot)$ and $D(\cdot, \cdot)$ are defined on $W_h \times W_h$ by

$$\begin{aligned} A_h^a \left(\begin{pmatrix} \boldsymbol{u}_h \\ \boldsymbol{v}_h \end{pmatrix}, \begin{pmatrix} \boldsymbol{\varphi} \\ \boldsymbol{\psi} \end{pmatrix} \right) &= e_h(\boldsymbol{u}_h, \boldsymbol{\varphi}) + \nu a_h(\boldsymbol{v}_h, \boldsymbol{\psi}) + k(\boldsymbol{v}_h, \boldsymbol{\psi}), \\ D \left(\begin{pmatrix} \boldsymbol{u}_h \\ \boldsymbol{v}_h \end{pmatrix}, \begin{pmatrix} \boldsymbol{\varphi} \\ \boldsymbol{\psi} \end{pmatrix} \right) &= \lambda d(\boldsymbol{u}_h, \boldsymbol{\varphi}) + c_s^{-1} d(\boldsymbol{u}_h + \boldsymbol{v}_h, \boldsymbol{\varphi} + \boldsymbol{\psi}), \end{aligned} \tag{4.12}$$

and the right hand side is given by

$$\mathscr{F}_h \left(\begin{pmatrix} \boldsymbol{\varphi} \\ \boldsymbol{\psi} \end{pmatrix} \right) = (\boldsymbol{f}, \boldsymbol{\varphi})_\Omega - c_s^{-1} (g_h, \operatorname{div}(\boldsymbol{\varphi} + \boldsymbol{\psi}))_\Omega.$$

Further, we introduce the decomposition

$$W_h = \ker(D) \oplus \ker(D)^{\perp, a}$$

into the space of divergence free functions $\ker(D)$ and the orthogonal complement

$$\ker(D)^{\perp,a} = \left\{ \begin{pmatrix} \boldsymbol{u} \\ \boldsymbol{v} \end{pmatrix} \in W_h \ : \ A_h^a\left(\begin{pmatrix} \boldsymbol{u} \\ \boldsymbol{v} \end{pmatrix}, \begin{pmatrix} \boldsymbol{\varphi} \\ \boldsymbol{\psi} \end{pmatrix} \right) = 0 \quad \forall \begin{pmatrix} \boldsymbol{\varphi} \\ \boldsymbol{\psi} \end{pmatrix} \in \ker(D) \right\}.$$

The space $\ker(D)^{\perp,a}$ differs slightly from Chapter 3 in that $a_h(\cdot,\cdot)$ occurs in the defining bilinear form $A_h^a(\cdot,\cdot)$. The representation of $\ker(D)$ in terms of a decomposition of the underlying spaces U_h and V_h is done in the same way as before. Let

$$U_h = U_h^0 \oplus U_h^{\perp}, \qquad V_h = V_h^0 \oplus V_h^{\perp,a},$$

where U_h^0 and V_h^0 denote the divergence free subspaces of U_h and V_h, respectively, and

$$\begin{aligned} U_h^{\perp} &= \left\{ \boldsymbol{u} \in U_h \ : \ e_h(\boldsymbol{u}, \boldsymbol{\varphi}) = 0 \quad \forall \boldsymbol{\varphi} \in U_h^0 \right\}, \\ V_h^{\perp,a} &= \left\{ \boldsymbol{v} \in V_h \ : \ \nu a_h(\boldsymbol{v}, \boldsymbol{\psi}) + k(\boldsymbol{v}, \boldsymbol{\psi}) = 0 \quad \forall \boldsymbol{\psi} \in V_h^0 \right\}. \end{aligned}$$

Note that we use the weighted scalar product $\nu a_h(\cdot,\cdot) + k\,(\cdot,\cdot)$ in the definition of $V_h^{\perp,a}$. Thus, for $\lambda > 0$ there holds

$$W_h^0 := \ker(D) = U_h^0 \times V_h^0, \qquad W_h^{\perp,a} := \ker(D)^{\perp,a} = U_h^{\perp} \times V_h^{\perp,a}.$$

Next, we prove Assumptions 2.3 and 2.4.

Lemma 4.3 (Local stability)**.** *For each $\boldsymbol{w}_0 \in W_0$ there exists a constant $C_1 > 0$, such that*

$$\mathscr{A}_h^a(\boldsymbol{w}_0, \boldsymbol{w}_0) \leq \omega_0 \frac{H}{h} \mathscr{A}_0^a(\boldsymbol{w}_0, \boldsymbol{w}_0)\,,$$

with $\omega_0 < 1$, such that $\omega_0 \frac{H}{h} < 2$.

Proof. The proof follows directly by the proof of Lemma 3.12, as well as continuity (4.7) and coercivity (4.6) of bilinearform $a_h(\cdot,\cdot)$. □

The strengthened Cauchy-Schwarz inequalities depend only on the geometric structure of the local spaces, i.e., the overlap and the fact that we can apply the normal Cauchy-Schwarz inequality. Thus, the proof has already been given in Lemma 3.13.

Lemma 4.4 (Strengthened Cauchy-Schwarz inequalities)**.** *For $1 \leq i, j \leq J$ there exist constants $0 \leq \varepsilon_{ij} \leq 1$ such that*

$$|\mathscr{A}_h^a(\boldsymbol{w}_i, \boldsymbol{w}_j)| \leq \varepsilon_{ij} \mathscr{A}_h^a(\boldsymbol{w}_i, \boldsymbol{w}_i)^{\frac{1}{2}} \mathscr{A}_h^a(\boldsymbol{w}_j, \boldsymbol{w}_j)^{\frac{1}{2}},$$

for $\boldsymbol{w}_i \in W_i$, $\boldsymbol{w}_j \in W_j$.

For a proof of the stable decomposition in Theorem 4.7 we need decomposition properties of the bilinear form $a_h(\cdot,\cdot)$ in addition to the preliminary considerations of Section 3.4.3. A close look at Lemma 3.8 and Lemma 3.9 shows that we have already proved the corresponding properties for the bilinear form $a_h(\cdot,\cdot)$ and used Korn's inequality to obtain the result for $e_h(\cdot,\cdot)$. Thus, we have the following two statements in the kernel V_h^0 and the orthogonal complement $V_h^\perp$.

Lemma 4.5. *Every function $\boldsymbol{v}^0 \in V_h^0$ admits a decomposition of the form $\boldsymbol{v}^0 = \sum_{j=0}^J \boldsymbol{v}_j^0$ with $\boldsymbol{v}_j^0 \in V_j^0$, which satisfies the bound*

$$a_H(\boldsymbol{v}_0^0, \boldsymbol{v}_0^0) + \sum_{j=1}^J a_h(\boldsymbol{v}_j^0, \boldsymbol{v}_j^0) \leq c \left(1 + \frac{H^4}{\delta^4}\right) a_h(\boldsymbol{v}^0, \boldsymbol{v}^0)$$

for some constant $c > 0$.

Lemma 4.6. *Every function $\boldsymbol{v}^\perp \in V_h^\perp$ admits a decomposition of the form $\boldsymbol{v}^\perp = \sum_{j=0}^J \boldsymbol{v}_j^1$ with $\boldsymbol{v}_j^1 \in V_j$, which satisfies the bound*

$$a_H(\boldsymbol{v}_0^1, \boldsymbol{v}_0^1) + \sum_{j=1}^J a_h(\boldsymbol{v}_j^1, \boldsymbol{v}_j^1) \leq c \left(1 + \frac{H^2}{\delta^2}\right) a_h(\boldsymbol{v}^\perp, \boldsymbol{v}^\perp)$$

for some constant $c > 0$.

With these two lemmas we are now in a position to state and prove the main result of this section, namely Theorem 4.7. The proof follows the ideas of the proof of Theorem 3.11, but extends it to the current case by taking care of the additional interior penalty formulation of the diffusion term and working out all the specifications that have to be made in this case.

Theorem 4.7 (Stable decomposition)**.** *Every $\boldsymbol{w} \in W_h$ admits a decomposition of the form*

$$\boldsymbol{w} = \sum_{j=0}^{J} \boldsymbol{w}_j, \qquad \boldsymbol{w}_j \in W_j,$$

which satisfies the bound

$$\sum_{j=0}^{J} \mathscr{A}_j^a(\boldsymbol{w}_j, \boldsymbol{w}_j) \leq c_{\boldsymbol{K},\nu} \left(1 + \frac{H^4}{\delta^4}\right) \mathscr{A}_h^a(\boldsymbol{w}, \boldsymbol{w}),$$

for some constant $c_{\boldsymbol{K},\nu} > 0$ independent of the model parameters λ and c_s in the discrete bilinear form $\mathscr{A}_h^a(\cdot,\cdot)$ defined in (4.11)–(4.12) and independent of the number of subdomains J as well as of the discretization parameters h and τ.

Proof. We decompose $\boldsymbol{w}$ as

$$\begin{aligned} \boldsymbol{w} = \begin{pmatrix} \boldsymbol{u} \\ \boldsymbol{v} \end{pmatrix} &= \begin{pmatrix} \boldsymbol{u}^0 \\ \boldsymbol{v}^0 \end{pmatrix} + \begin{pmatrix} \boldsymbol{u}^\perp \\ -\boldsymbol{u}^\perp \end{pmatrix} + \begin{pmatrix} \boldsymbol{0} \\ \boldsymbol{\varphi} \end{pmatrix} \\ &= \begin{pmatrix} \boldsymbol{u}^0 \\ \boldsymbol{v}^0 \end{pmatrix} + \begin{pmatrix} \boldsymbol{0} \\ \boldsymbol{\varphi}^0 \end{pmatrix} + \begin{pmatrix} \boldsymbol{u}^\perp \\ -\boldsymbol{u}^\perp \end{pmatrix} + \begin{pmatrix} \boldsymbol{0} \\ \boldsymbol{\varphi}^\perp \end{pmatrix} = \boldsymbol{w}^0 + \boldsymbol{w}^1 + \boldsymbol{w}^2 + \boldsymbol{w}^3, \end{aligned} \tag{4.13}$$

with $(\boldsymbol{u}^0, \boldsymbol{v}^0) \in U^0 \times V^0$ and $(\boldsymbol{u}^\perp, \boldsymbol{v}^\perp) \in U^\perp \times V^\perp$, $\boldsymbol{\varphi} = \boldsymbol{u}^\perp + \boldsymbol{v}^\perp$ and the decomposition $\boldsymbol{\varphi} = \boldsymbol{\varphi}^0 + \boldsymbol{\varphi}^\perp$, $\boldsymbol{\varphi}^0 \in V^0$, where $\boldsymbol{\varphi}^0$ and $\boldsymbol{\varphi}^\perp$ are orthogonal with respect to the weighted bilinear form $\nu a_h(\cdot,\cdot) + k\,(\cdot,\cdot)$. Further, we decompose each component of each summand in (4.13) according to

$$\begin{aligned} &\sum_{j=0}^{J} \boldsymbol{u}_j^0 = \boldsymbol{u}^0, && \sum_{j=0}^{J} \boldsymbol{v}_j^0 = \boldsymbol{v}^0, && \sum_{j=0}^{J} \boldsymbol{\varphi}_j^0 = \boldsymbol{\varphi}^0, \\ &\sum_{j=0}^{J} \boldsymbol{u}_j^1 = \boldsymbol{u}^\perp, && \sum_{j=0}^{J} \boldsymbol{v}_j^1 = \boldsymbol{v}^\perp, && \sum_{j=0}^{J} \boldsymbol{\varphi}_j^1 = \boldsymbol{\varphi}^\perp, \end{aligned}$$

where $\boldsymbol{u}_j^0 \in U_j^0$, $\boldsymbol{v}_j^0 \in V_j^0$, $\boldsymbol{\varphi}_j^0 \in V_j^0$, $\boldsymbol{u}_j^1 \in U_j$, $\boldsymbol{v}_j^1 \in V_j$ and $\boldsymbol{\varphi}_j^1 \in V_j$. The superscript 1 of $\boldsymbol{u}_j^1$, $\boldsymbol{v}_j^1$ and $\boldsymbol{\varphi}_j^1$ indicates, that these terms are not orthogonal. Now, we define $\boldsymbol{w}_j :=$

$\boldsymbol{w}_j^0 + \boldsymbol{w}_j^1 + \boldsymbol{w}_j^2 + \boldsymbol{w}_j^3$, where

$$\boldsymbol{w}_j^0 = \begin{pmatrix} \boldsymbol{u}_j^0 \\ \boldsymbol{v}_j^0 \end{pmatrix} \in W_j^0, \qquad \boldsymbol{w}_j^1 = \begin{pmatrix} \boldsymbol{0} \\ \boldsymbol{\varphi}_j^0 \end{pmatrix} \in W_j^0,$$
$$\boldsymbol{w}_j^2 = \begin{pmatrix} \boldsymbol{u}_j^1 \\ -\boldsymbol{u}_j^1 \end{pmatrix} \in W_j, \qquad \boldsymbol{w}_j^3 = \begin{pmatrix} \boldsymbol{0} \\ \boldsymbol{\varphi}_j^1 \end{pmatrix} \in W_j,$$

and estimate

$$\begin{aligned} \sum_{j=0}^{J} \mathscr{A}_j^a(\boldsymbol{w}_j, \boldsymbol{w}_j) \leq c \sum_{j=0}^{J} \big(& \mathscr{A}_j^a\big(\boldsymbol{w}_j^0, \boldsymbol{w}_j^0\big) + \mathscr{A}_j^a\big(\boldsymbol{w}_j^1, \boldsymbol{w}_j^1\big) \\ & + \mathscr{A}_j^a\big(\boldsymbol{w}_j^2, \boldsymbol{w}_j^2\big) + \mathscr{A}_j^a\big(\boldsymbol{w}_j^3, \boldsymbol{w}_j^3\big)\big) . \end{aligned} \tag{4.14}$$

In the kernel W_h^0 we have by Lemma 3.10 and Lemma 4.5 for $\boldsymbol{w}^0 = (\boldsymbol{u}^0, \boldsymbol{v}^0)^T \in W_h^0$

$$\begin{aligned} \sum_{j=0}^{J} \mathscr{A}_j^a\big(\boldsymbol{w}_j^0, \boldsymbol{w}_j^0\big) =& e_H\big(\boldsymbol{u}_0^0, \boldsymbol{u}_0^0\big) + \sum_{j=1}^{J} e_h\big(\boldsymbol{u}_j^0, \boldsymbol{u}_j^0\big) \\ & + \nu a_H\big(\boldsymbol{v}_0^0, \boldsymbol{v}_0^0\big) + \nu \sum_{j=1}^{J} a_h\big(\boldsymbol{v}_j^0, \boldsymbol{v}_j^0\big) + \sum_{j=0}^{J} k\big(\boldsymbol{v}_j^0, \boldsymbol{v}_j^0\big) \\ \leq & c_{H,\delta} \left(e_h\big(\boldsymbol{u}^0, \boldsymbol{u}^0\big) + \nu a_h\big(\boldsymbol{v}^0, \boldsymbol{v}^0\big) + k\big(\boldsymbol{v}^0, \boldsymbol{v}^0\big)\right) = c_{H,\delta} \mathscr{A}_h^a\big(\boldsymbol{w}^0, \boldsymbol{w}^0\big) . \end{aligned} \tag{4.15}$$

For the decomposition in the orthogonal complement $W_h^{\perp,a}$ we will use the stability estimates

$$\nu a_h\big(\boldsymbol{\varphi}^0, \boldsymbol{\varphi}^0\big) + k\big(\boldsymbol{\varphi}^0, \boldsymbol{\varphi}^0\big) \leq \nu a_h\big(\boldsymbol{u}^\perp + \boldsymbol{v}^\perp, \boldsymbol{u}^\perp + \boldsymbol{v}^\perp\big) + k\big(\boldsymbol{u}^\perp + \boldsymbol{v}^\perp, \boldsymbol{u}^\perp + \boldsymbol{v}^\perp\big), \tag{4.16}$$

and

$$\nu a_h\big(\boldsymbol{\varphi}^\perp, \boldsymbol{\varphi}^\perp\big) + k\big(\boldsymbol{\varphi}^\perp, \boldsymbol{\varphi}^\perp\big) \leq \nu a_h\big(\boldsymbol{u}^\perp + \boldsymbol{v}^\perp, \boldsymbol{u}^\perp + \boldsymbol{v}^\perp\big) + k\big(\boldsymbol{u}^\perp + \boldsymbol{v}^\perp, \boldsymbol{u}^\perp + \boldsymbol{v}^\perp\big) \tag{4.17}$$

By Lemma 4.5, the stability of the L^2-decomposition (3.34) and stability estimate (4.16)

we get

$$\begin{aligned}\sum_{j=0}^{J} \mathscr{A}_j^a\big(\boldsymbol{w}_j^1, \boldsymbol{w}_j^1\big) &= \nu a_H\big(\boldsymbol{\varphi}_0^0, \boldsymbol{\varphi}_0^0\big) + \nu \sum_{j=1}^{J} a_h\big(\boldsymbol{\varphi}_j^0, \boldsymbol{\varphi}_j^0\big) + \sum_{j=0}^{J} k\big(\boldsymbol{\varphi}_j^0, \boldsymbol{\varphi}_j^0\big) \\ &\leq c_{H,\delta}\left(\nu a_h\big(\boldsymbol{\varphi}^0, \boldsymbol{\varphi}^0\big) + k\big(\boldsymbol{\varphi}^0, \boldsymbol{\varphi}^0\big)\right) \\ &\leq c_{H,\delta}\left(\nu a_h\big(\boldsymbol{u}^\perp, \boldsymbol{u}^\perp\big) + \nu a_h\big(\boldsymbol{v}^\perp, \boldsymbol{v}^\perp\big) + k\big(\boldsymbol{u}^\perp, \boldsymbol{u}^\perp\big) + k\big(\boldsymbol{v}^\perp, \boldsymbol{v}^\perp\big)\right). \quad (4.18)\end{aligned}$$

By Lemma 3.9, Lemma 4.5 and Lemma 2.13 it follows

$$\begin{aligned}\sum_{j=0}^{J} \mathscr{A}_j^a\big(\boldsymbol{w}_j^2, \boldsymbol{w}_j^2\big) &= e_H\big(\boldsymbol{u}_0^1, \boldsymbol{u}_0^1\big) + \sum_{j=1}^{J} e_h\big(\boldsymbol{u}_j^1, \boldsymbol{u}_j^1\big) + \nu a_H\big(\boldsymbol{v}_0^1, \boldsymbol{v}_0^1\big) + \nu \sum_{j=1}^{J} a_h\big(\boldsymbol{v}_j^1, \boldsymbol{v}_j^1\big) \\ &\quad + \sum_{j=0}^{J} \big(k\big(\boldsymbol{u}_j^1, \boldsymbol{u}_j^1\big) + \lambda d\big(\boldsymbol{u}_j^1, \boldsymbol{u}_j^1\big)\big) \\ &\leq c_{H,\delta}\left(e_h\big(\boldsymbol{u}^\perp, \boldsymbol{u}^\perp\big) + \nu a_h\big(\boldsymbol{u}^\perp, \boldsymbol{u}^\perp\big) + k\big(\boldsymbol{u}^\perp, \boldsymbol{u}^\perp\big) + \lambda d\big(\boldsymbol{u}^\perp, \boldsymbol{u}^\perp\big)\right).\end{aligned}$$

According to Lemma 4.6 and Lemma 2.13, as well as the stability estimate (4.17), the following is obtained

$$\begin{aligned}\sum_{j=0}^{J} \mathscr{A}_j^a\big(\boldsymbol{w}_j^3, \boldsymbol{w}_j^3\big) &= \nu a_H\big(\boldsymbol{\varphi}_0^1, \boldsymbol{\varphi}_0^1\big) + \nu \sum_{j=1}^{J} a_h\big(\boldsymbol{\varphi}_j^1, \boldsymbol{\varphi}_j^1\big) \\ &\quad + \sum_{j=0}^{J} \big(k\big(\boldsymbol{\varphi}_j^1, \boldsymbol{\varphi}_j^1\big) + c_s^{-1} d\big(\boldsymbol{\varphi}_j^1, \boldsymbol{\varphi}_j^1\big)\big) \\ &\leq c_{H,\delta}\left(\nu a_h\big(\boldsymbol{\varphi}^\perp, \boldsymbol{\varphi}^\perp\big) + k\big(\boldsymbol{\varphi}^\perp, \boldsymbol{\varphi}^\perp\big) + c_s^{-1} d\big(\boldsymbol{\varphi}^\perp, \boldsymbol{\varphi}^\perp\big)\right) \quad (4.19) \\ &\leq c_{H,\delta}\Big(\nu a_h\big(\boldsymbol{u}^\perp, \boldsymbol{u}^\perp\big) + \nu a_h\big(\boldsymbol{v}^\perp, \boldsymbol{v}^\perp\big) + k\big(\boldsymbol{u}^\perp, \boldsymbol{u}^\perp\big) \\ &\qquad + k\big(\boldsymbol{v}^\perp, \boldsymbol{v}^\perp\big) + c_s^{-1} d\big(\boldsymbol{u}^\perp + \boldsymbol{v}^\perp, \boldsymbol{u}^\perp + \boldsymbol{v}^\perp\big)\Big).\end{aligned}$$

Due to the special choice of the decomposition (4.13), the terms $k\left(\boldsymbol{u}^\perp, \boldsymbol{u}^\perp\right)$ and $a_h\big(\boldsymbol{u}^\perp, \boldsymbol{u}^\perp\big)$ arise in (4.18)–(4.19), which we further estimate using Poincaré's inequality

$$k\big(\boldsymbol{u}^\perp, \boldsymbol{u}^\perp\big) \leq c_{\boldsymbol{K},\Omega} e_h\big(\boldsymbol{u}^\perp, \boldsymbol{u}^\perp\big)$$

with a constant $c_{\boldsymbol{K},\Omega}$ depending on the domain Ω and the inverse permeability coefficient $\boldsymbol{K}^{-1}$, and by Korn's inequality

$$\nu a_h\big(\boldsymbol{u}^\perp, \boldsymbol{u}^\perp\big) \leq c_\nu e_h\big(\boldsymbol{u}^\perp, \boldsymbol{u}^\perp\big) \tag{4.20}$$

with a constant depending on ν. Thus, collecting the estimates (4.14), (4.15), and (4.18)–(4.20), we obtain with $\boldsymbol{w}^\perp = (\boldsymbol{u}^\perp, \boldsymbol{v}^\perp)^T \in W_h^{\perp,a}$

$$\begin{aligned}
&\sum_{j=0}^{J} \mathscr{A}_j\left(\boldsymbol{w}_j, \boldsymbol{w}_j\right) \\
&\quad \leq c_{H,\delta}\Big(e_h\big(\boldsymbol{u}^0, \boldsymbol{u}^0\big) + \nu a_h\big(\boldsymbol{v}^0, \boldsymbol{v}^0\big) + k\big(\boldsymbol{v}^0, \boldsymbol{v}^0\big) + \nu a_h\big(\boldsymbol{u}^\perp, \boldsymbol{u}^\perp\big) + k\big(\boldsymbol{u}^\perp, \boldsymbol{u}^\perp\big) \\
&\qquad\quad + e_h\big(\boldsymbol{u}^\perp, \boldsymbol{u}^\perp\big) + \nu a_h\big(\boldsymbol{v}^\perp, \boldsymbol{v}^\perp\big) + k\big(\boldsymbol{v}^\perp, \boldsymbol{v}^\perp\big) + \lambda d\big(\boldsymbol{u}^\perp, \boldsymbol{u}^\perp\big) \\
&\qquad\quad + c_s^{-1} d\big(\boldsymbol{u}^\perp + \boldsymbol{v}^\perp, \boldsymbol{u}^\perp + \boldsymbol{v}^\perp\big)\Big) \\
&\quad \leq c_{H,\delta,\nu,\boldsymbol{K},\Omega}\Big(\mathscr{A}_h\left(\boldsymbol{w}^0, \boldsymbol{w}^0\right) + \mathscr{A}_h\left(\boldsymbol{w}^\perp, \boldsymbol{w}^\perp\right)\Big) \\
&\quad = c_{H,\delta,\nu,\boldsymbol{K},\Omega} \mathscr{A}_h\left(\boldsymbol{w}, \boldsymbol{w}\right)
\end{aligned}$$

where the constant $c_{H,\delta,\nu,\boldsymbol{K},\Omega}$ for a proper overlap δ depends only on ν, $\boldsymbol{K}$ and Ω. □

4.3 Numerical Tests

In this section, we test the performance of the discretization and the two-level Schwarz preconditioner.

We begin by examining the convergence of the discretization in Section 4.3.1. We then investigate the performance of the multiplicative two-level Schwarz preconditioner applied to a test case with mixed Dirichlet-Neumann boundary conditions in Section 4.3.2. We observe the continuity of the Schwarz method for the transition $\nu \to 0$ with respect to the iteration counts of GMRES, and test the robustness of the algorithm when the parameters in the system are varied. We can observe a stabilizing effect of the diffusion term on the performance of the method.

4.3.1 Convergence of the Discretization

To test the convergence of the discretization we choose a test setting with the force $\boldsymbol{f}$ and the source g given by

$$\boldsymbol{f} = \begin{pmatrix} \nu\kappa\partial_x\Delta\boldsymbol{\varphi} - \partial_x\boldsymbol{\varphi} - \frac{1}{2}\partial_y\Delta\boldsymbol{\varphi} \\ \nu\kappa\partial_y\Delta\boldsymbol{\varphi} - \partial_y\boldsymbol{\varphi} + \frac{1}{2}\partial_x\Delta\boldsymbol{\varphi} \end{pmatrix}, \qquad g = -\kappa\Delta\boldsymbol{\varphi} - c_s\left(\nu\kappa\Delta\boldsymbol{\varphi} - \boldsymbol{\varphi} + \frac{1}{30}\right),$$

where $\boldsymbol{\varphi}$ is defined on the square $\Omega = (0,1)\times(0,1)$ by

$$\boldsymbol{\varphi} = x^2(x-1)^2y^2(y-1)^2.$$

On the boundary $\partial\Omega$, homogeneous Dirichlet boundary conditions are prescribed for the solid displacement $\boldsymbol{u}$ as well as for the seepage velocity $\boldsymbol{v}$, i.e.,

$$\boldsymbol{u} = 0 \quad \text{on } \partial\Omega, \qquad \boldsymbol{v} = 0 \quad \text{on } \partial\Omega.$$

The solution of this test is defined only up to an additive constant. To make it unique we search for a mean-value free solution in the pressure component satisfying

$$\int_\Omega p\,dx = 0.$$

The solution to this system is then given by

$$\boldsymbol{u} = \begin{pmatrix} \partial_y\boldsymbol{\varphi} \\ -\partial_x\boldsymbol{\varphi} \end{pmatrix}, \qquad \boldsymbol{v} = \kappa\nabla\boldsymbol{\varphi}, \qquad p = \left(\nu\kappa\Delta\boldsymbol{\varphi} - \boldsymbol{\varphi} + \frac{1}{30}\right).$$

In Figure 4.1 we can observe the convergence orders of the finite element discretizations with $RT_1\times RT_1\times Q_1$ and $RT_2\times RT_2\times Q_2$. The calculations have been performed with the choice $\lambda = \kappa = 1$, $c_s = 10^{-4}$. The convergence analysis follows the same argumentation as in [KR18], cf. also [HKK$^+$22]. Thus, we expect the same convergence behavior as for the Biot system summarized in Section 3.2, which can be confirmed by observing Figure 4.1. In the left two plots we see linear convergence of the H^1-norms of the displacement $\boldsymbol{u}$, the seepage velocity $\boldsymbol{v}$ and the pressure p for polynomial degree $k = 1$, as well as second order convergence for their L^2-norms (note, that the slope of the L^2-norms is slightly less inclined). Additionally, the L^2-norm of the divergence of $\boldsymbol{u}$ and $\boldsymbol{v}$ are of second order,

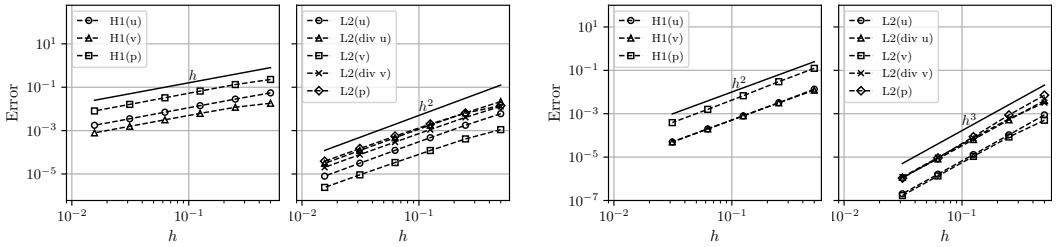

Figure 4.1: First and second order convergence of $RT_1 \times RT_1 \times Q_1$ (left). Second and third order convergence of $RT_2 \times RT_2 \times Q_2$ (right).

too. In the right two plots we see the corresponding convergence results for $k = 2$, which are one order higher than for $k = 1$, and therefore, the experimental results are in line with the convergence analysis of Biot's consolidation model.

4.3.2 Performance of the Multiplicative Two-level Schwarz Method

In this section we show test results for the Biot-Brinkman equations discretized with $RT_2 \times RT_2 \times Q_2$ finite elements and preconditioned with the multiplicative two-level Schwarz method. The convergence results for the hybrid two-level Schwarz preconditioner are qualitatively the same as for the multiplicative method, as we have already seen in Section 3.5. Thus, we will concentrate on the multiplicative two-level Schwarz method, only.

The performance tests are executed in the same scenario as in Section 3.5.3 from where we adopt the notation and refer to Figure 3.2 for an illustration of the setting. Mixed Dirichlet-Neumann boundary conditions are prescribed for the solid displacement and the seepage velocity, such that the medium is clamped from the left and the right, and free to move on top and bottom. The fluid flows into the poroelastic reservoir from the left, has a free outflow on the right and a no-slip condition on top and bottom. But instead of the normal components as for $\nu = 0$, the seepage velocity for the case $\nu > 0$ is given by $\boldsymbol{v} = \boldsymbol{v}_D$ on $\Gamma_{in} \cup \Gamma_{wall}$, where $\boldsymbol{v}_D$ is defined by

$$\boldsymbol{v}_D = \begin{pmatrix} 0.5 \\ 0 \end{pmatrix} \quad \text{on } \Gamma_{in}, \qquad \boldsymbol{v}_D = \begin{pmatrix} 0 \\ 0 \end{pmatrix} \quad \text{on } \Gamma_{wall}.$$

As in Section 3.5.3, the pressure is set to zero on Γ_{out}, no external forces are prescribed and

	ν						
h	0	10^{-12}	10^{-8}	10^{-4}	1	10^{4}	10^{8}
1/4	9	9	9	8	7	4	4
1/8	8	8	8	6	7	4	4
1/16	8	8	8	6	7	4	5
1/32	8	8	8	6	7	7	5

Table 4.1: Continuous transition of the Biot-Brinkman system to Biot's consolidation model for $\nu \to 0$ in terms of iteration counts of GMRES. Multiplicative two-level Schwarz, $RT_2 \times RT_2 \times Q_2$, $\lambda = \kappa^{-1} = 1$, $c_s = 0$.

no sinks or sources are located inside the medium. By this and due to the discontinuous Galerkin approximation of the diffusion term in the Brinkman equations we adjust the right hand side of (4.8) according to

$$\mathbb{F}_h\left(\begin{pmatrix}\boldsymbol{\varphi}\\ \boldsymbol{\psi}\\ q\end{pmatrix}\right) = \nu \sum_{B\in\Gamma_{B,h}} \left(\frac{\eta_a}{h}(\boldsymbol{v}_D, \boldsymbol{\psi})_B - (\boldsymbol{v}_D, \nabla\boldsymbol{\psi}\boldsymbol{n})_B\right)$$

to incorporate the inhomogeneous boundary condition of the seepage velocity, where $\Gamma_{B,h}$ is the set of all faces on $\Gamma_{in} \cup \Gamma_{wall}$.

To measure the performance of the multiplicative Schwarz preconditioner we count the number of iterations GMRES takes to converge, i.e., until the starting residual is reduced by a factor of 10^{-8}.

In Table 4.1 we see that the iterations of GMRES are robust in ν and the counts are even getting smaller for very large values of $\nu \gg 1$. Since ν is a rescaled quantity, see (4.3), the experiments need to cover a broad range of the parameter regime, even though the value of the viscosity-like constant ν might be much smaller in applications. Furthermore, the numbers in Table 4.1 show a continuous transition to the case $\nu = 0$ when ν tends to zero.

The main observation of the performance tests is that an added diffusion term to the Biot equations yields a stabilization of the iteration counts in κ^{-1} and that a scaling as in Table 3.14 is not necessary for very small values of κ^{-1}, which corresponds to the case of high permeabilities. Therefore, we investigate the iteration numbers for different values of $\nu > 0$ when κ^{-1} is varied and compare them to the case $\nu = 0$. The results are shown

		κ^{-1}								
	h	10^{-8}	10^{-6}	10^{-4}	10^{-2}	1	10^{2}	10^{4}	10^{6}	10^{8}
$\nu = 0$	1/4	21	15	10	8	9	6	6	4	4
	1/8	21	14	11	8	8	5	6	4	4
	1/16	33	15	12	8	8	5	5	4	4
	1/32	50	17	13	8	8	5	5	4	4
$\nu = 10^{-8}$	1/4	22	21	18	10	9	6	6	4	4
	1/8	19	19	18	11	8	5	6	4	4
	1/16	18	19	18	14	8	5	5	4	4
	1/32	17	17	17	16	8	5	5	4	3
$\nu = 10^{-4}$	1/4	9	9	9	12	8	6	6	4	4
	1/8	7	7	7	7	6	5	6	4	4
	1/16	8	8	8	8	6	5	5	4	4
	1/32	6	6	6	6	6	5	5	4	3
$\nu = 10^{-2}$	1/4	6	6	6	6	6	6	6	4	4
	1/8	6	6	6	6	6	5	6	4	4
	1/16	6	6	6	6	6	5	5	4	4
	1/32	6	6	6	6	6	6	5	4	3

Table 4.2: Performance with respect to κ^{-1} measured in iteration counts of GMRES, preconditioned by a multiplicative two-level Schwarz method. $RT_2 \times RT_2 \times Q_2$, $\lambda = 1$, $c_s = 0$.

in Table 4.2. For $\nu = 0$ we see robust iteration counts for $\kappa^{-1} > 1$, but the numbers are growing the smaller κ^{-1} becomes, deteriorating with a refinement of the mesh for $\kappa^{-1} \leq 10^{-4}$. By choosing $\nu > 0$ and thus switching to the Biot-Brinkman model, the iteration numbers of the system stabilize for all values of κ^{-1}, even in the case of a small $\nu = 10^{-8}$, where the counts are limited by a value of 17, instead of deteriorating with decreasing κ^{-1}. The stabilizing effect intensifies for larger ν, leading to robustness of the multiplicative two-level Schwarz method when varying the permeability constant κ^{-1}. In addition, we again observe the continuous transition of the Biot-Brinkman system to Biot's consolidation model in terms of iteration counts of GMRES, when $\nu \to 0$.

It still remains to test the other parameters in the system.

For varying λ, we do not see a significant difference of the iteration numbers between Biot's consolidation model ($\nu = 0$) and the Biot-Brinkman equations ($\nu > 0$) in Table 4.3. Both appear to be robust in ν with some sensitivity to numerical instabilities for very large values of $\lambda \geq 10^6$. As in Section 3.5.3, we observe numerical instabilities that can

		λ					
	h	0	1	10^2	10^4	10^6	10^8
$\nu = 0$	1/4	10	9	8	4	1	1
	1/8	9	8	6	4	1	1
	1/16	9	8	6	4	1	1
	1/32	8	8	6	4	1	1
$\nu = 10^{-2}$	1/4	6	6	5	4	2	1
	1/8	6	6	6	4	2	1
	1/16	6	6	6	4	2	1
	1/32	6	6	6	5	2	2

Table 4.3: Performance with respect to λ measured in iteration counts of GMRES, preconditioned by a multiplicative two-level Schwarz method. $RT_2 \times RT_2 \times Q_2$. $\kappa^{-1} = 1$, $c_s = 0$, scaling for $\lambda \geq 10^6$.

		$\lambda = \kappa^{-1}$								
	h	10^{-8}	10^{-6}	10^{-4}	10^{-2}	1	10^2	10^4	10^6	10^8
$\nu = 0$	1/4	23	13	10	10	9	5	4	4	4
	1/8	22	17	10	10	8	6	4	4	4
	1/16	31	16	13	8	8	6	4	3	5
	1/32	39	17	10	8	8	6	8	4	7
$\nu = 10^{-2}$	1/4	6	6	6	6	6	5	4	3	4
	1/8	6	6	6	6	6	6	4	3	4
	1/16	6	6	6	6	6	6	4	3	5
	1/32	6	6	6	6	6	6	8	4	8

Table 4.4: Performance with respect to $\lambda = \kappa^{-1}$ measured in iteration counts of GMRES, preconditioned by a multiplicative two-level Schwarz method. $RT_2 \times RT_2 \times Q_2$, $c_s = 0$, scaling for $\lambda \geq 10^6$.

	$\nu = 0$				$\nu = 10^{-2}$			
h	$c_s =$ 0	10^{-10}	10^{-5}	1	0	10^{-10}	10^{-5}	1
1/4	9	9	9	9	6	6	6	6
1/8	8	8	8	8	6	6	6	6
1/16	8	8	8	8	6	6	6	6
1/32	8	8	8	8	6	6	6	6

Table 4.5: Performance with respect to c_s measured in iteration counts of GMRES, preconditioned by a multiplicative two-level Schwarz method. $RT_2 \times RT_2 \times Q_2$. $\nu = \lambda = \kappa^{-1} = 1$.

be handled by using a scaling as in (3.46) with scaling matrix

$$\boldsymbol{S} = \begin{pmatrix} \frac{1}{\sqrt{\lambda}}\boldsymbol{I} & \mathbf{0} & \mathbf{0} \\ \mathbf{0} & \boldsymbol{I} & \mathbf{0} \\ \mathbf{0} & \mathbf{0} & \boldsymbol{I} \end{pmatrix},$$

for $\lambda \neq 0$. These numerical instabilities originate in the squaring of the diagonal entries of the system matrix within GMRES, whereas the growing iteration counts for smaller values of κ^{-1} in the case $\nu = 0$ are due to the dependence of the method on κ^{-1}. In Table 4.4 we can see how both effects accumulate as the iteration counts are growing when κ^{-1} tends to zero, and are deteriorating for $\lambda \geq 10^6$. The scaling captures the instabilities due to the squaring of the already large values of λ and the additional diffusion stabilizes for small κ^{-1}.

Finally, varying the storage capacity does not influence the iteration numbers of GMRES as can be seen in Table 4.5.

4.4 Conclusion

In this chapter we have extended the theory of the two-level Schwarz preconditioners for Biot's consolidation model to the case of a quasi-static Biot-Brinkman system and proved convergence of the algorithm. In the numerical experiments we observed that the additional diffusion term yields a stabilization of the iteration counts, when κ^{-1} is varied, whereas the method stays robust for all considered parameter ranges. Numerical instabilities due to extremely large values of λ, originating in the squaring of the diagonal entries of the system matrix within GMRES, can be handled by a scaling of the system, leading to an overall robust scheme in the practical application of the method.

Chapter 5

Homogenizing Two-scale Multilevel Schwarz Preconditioner for Pore-scale Porous Media Computations

In this chapter we provide an efficient multilevel Schwarz preconditioner for the iterative solution of pore-scale porous media flow models for the high-resolution simulation on a microscopic scale. Therefore, a steady Stokes flow is assumed as model problem in a periodically perforated domain. This kind of model has applications in the rather young field of computational microfluidics that aims to perform high-resolution computations of pore-scale dynamics in the exact microstructure geometry, see e.g. [SMR21] and the literature cited therein. Since the scale of interest quickly leads to immensely large systems of equations, sophisticated numerical methods are needed to efficiently solve the resulting systems. The idea we follow is that of a two-scale multigrid preconditioner that uses the knowledge of the effective homogenized behavior of the physical law on a coarse scale as smoothing operator. This approach originates in the work of Engquist and Luo in [Luo93, EL93] from 1993, and the work of Neuss, Jäger and Wittum in the late 1990's in [Neu96, NJW01]. Both developed multigrid solvers for second order elliptic diffusion equations with highly oscillating coefficients, using a homogenization approach to get an effective operator on the coarse scale. Whereas Engquist and Luo formulated the underlying basic idea of the method and applied it to finite difference discretizations, Neuss, Jäger and Wittum developed and refined the method for finite element discretizations, and set it on a solid analytical foundation.

Similar to the work of Neuss, Jäger and Wittum, a multigrid method with an effective coarse grid operator obtained by a numerical upscaling procedure has been developed in [Ebe03, EW05] by Eberhard and Wittum. Their approach uses Fourier analysis to obtain the effective permeability tensor, which is equivalent to homogenization in the

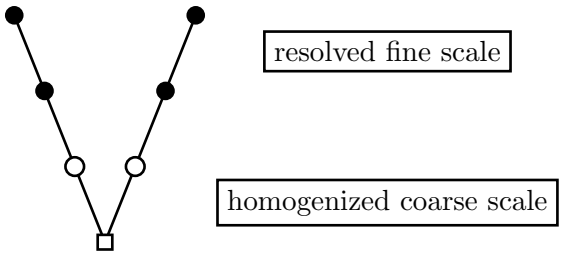

Figure 5.1: Homogenizing two-scale multilevel Schwarz method. The filled/empty circles denote the smoothing with a fine-scale/homogenized operator, respectively. The straight lines visualize the transfer between the levels, and the square refers to the application of the inverse or pseudo-inverse on the coarsest level.

case of periodic permeability fields.

Miehe and Bayreuther proposed a homogenization based multigrid solver with a problem dependent grid transfer operator in [MB07] and applied it to heterogeneous nonlinear inelastic model problems.

Sviercoski, Popov and Margenov reviewed the multiscale multigrid method in [SPM15] and applied it to flow problems in porous media by comparing it with different averaging techniques.

We are going to formulate the homogenizing two-scale multigrid method of [Neu96, NJW01] in a multilevel Schwarz context and apply it to H^{div}-conforming finite element discretizations of an extended Stokes problem on periodically perforated domains. To the best of our knowledge, this is novel in the literature and has not been done before. The basic idea is as follows:

1. Formulation of the microscopic problem on a perforated domain Ω^ε with periodically repeated obstacles of size ε.

2. Extension of the variables to the whole domain including the obstacles.

3. Homogenization of the microscopic equations to obtain effective operators on a macroscopic scale.

4. Discretization of extended problem and homogenized equations with the same type of finite element spaces.

5. Use the discretized effective coarse-scale operators inside a multilevel Schwarz preconditioner on levels, where the fine-scale behavior of the microscopic equations cannot be resolved anymore, see Figure 5.1.

As it turns out, the analytical homogenized operators cannot compete with the standard multigrid method, but an optimization process yields preconditioners that are superior with respect to convergence speed and efficiency for the intended case of small periods ε.

In the following we outline the structure of this chapter.

In Section 5.1 we introduce the model problem, which is a steady Stokes flow formulated on a periodically perforated domain with a period that is much smaller than the characteristic length of the reservoir. This system describes the resolved flow of an incompressible fluid through a system of connected pores, obtained by periodically repeating a standard periodicity cell over the whole domain. Since the perforation of the geometry limits the possibility to construct hierarchies of nested coarse-grid meshes, which can be used inside multigrid schemes, we extend the velocity and pressure of the system to the whole domain including the holes by a penalized Brinkman extension in Section 5.2. In Section 5.3 we discuss the choice of the extended model by investigating the convergence of the velocity with respect to the penalty factor. In Section 5.4 the extended system is discretized by an H^{div}-conforming mixed finite element method. The specifics of the homogenizing two-scale algorithm based on an overlapping multilevel Schwarz method are formulated in Section 5.5. Here, we use a homogenization of the fine-scale Stokes law as coarse-scale operator for the smoothing of the residual on mesh levels, on which the geometry of the micro-structure cannot be resolved anymore by standard multigrid approaches. There are several ways in the literature to derive the effective behavior of the model problem on a macroscopic coarse-scale, which are recapitulated in Section 5.6, where we focus on the famous two-scale convergence method (Section 5.6.1) as well as the energy method (Section 5.6.2). The limit of the homogenization process depends on the size and the ratio of the pores and the obstacles within the perforated domain, and as outcome we get four different homogenized operators. In Section 5.7 these operators are discretized with the same type of finite elements as the model problem. The assembly of the effective tensor derived by the two-scale convergence method by solving the cell-problems is presented in Section 5.7.1.

In the numerical experiments in Section 5.8 we compare the performance of the different homogenized operators against a standard multigrid operator that integrates the

fine-scale structure exactly and serves as a benchmark test. We begin with a discussion of a geometrically simple test case in Section 5.8.1. A direct application of the homogenizing two-scale multilevel Schwarz preconditioner with the effective operators obtained by the analysis leads to very different convergence results of GMRES in Section 5.8.2 originated in the non-optimality of the effective coefficients. An investigation of the choice of the permeability tensor by scanning the parameter spaces in Section 5.8.3 yields a dependence on the penalty factor coming from the Brinkman extension. Recalculating the performance tests with the optimal effective coefficients in the simple case of only one coarse-scale level shows improved convergence results for the homogenized Darcy operator and the homogenized Brinkman operator. In particular the optimized Brinkman operator performs as good as the benchmark test. Turning to the intended case of the full multilevel setup with the coarsest level set to zero in Section 5.8.4, the optimized Brinkman operator shows the best performance results and beats the iteration counts of the benchmark test by a factor of two for smaller periods of the periodic domain. This advantage of the performance reduces to some extent for a test case with a more anisotropic geometry in Section 5.8.5, when the same Brinkman operator is used. Nevertheless, the two-scale multilevel Schwarz preconditioner with the Brinkman operator still performs better than the standard multigrid preconditioner. Combining the Brinkman operator with the effective tensor derived by the two-scale convergence method, such that the effective tensor is rotated and scaled according to the geometry of the unit cell and optimized as in the axisymmetric case, finally leads to the best performance results for small periods.

5.1 Stokes Flow in Periodically Perforated Domain

The geometry of the porous medium, on which we are going to formulate the resolved porous media flow, is periodically arranged with obstacles inside a standard periodicity cell $Y = (0,1)^d$, which is repeated over the whole domain $\Omega \subset \mathbb{R}^d$, $d \in \{2,3\}$. For the description of this geometry we start with the definition of the standard periodicity cell

$$Y = \mathcal{F} \cup \mathcal{O}$$

as union of an open and connected fluid region $\mathcal{F}$, and a remaining obstacle part $\mathcal{O} = Y \setminus \mathcal{F}$ with a piecewise smooth boundary $\Gamma = \partial\mathcal{O}$. The open and bounded domain Y is also

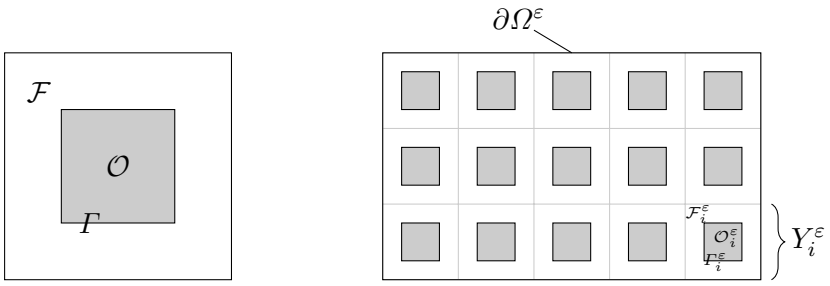

Figure 5.2: Periodically perforated domain Ω^ε consisting of repeated microcells Y_i^ε of size ε, where each Y_i^ε is the image of the scaled and shifted unit cell Y.

called the unit cell. The periodically perforated fluid domain $\Omega^\varepsilon \subset \Omega$ consists of the fluid parts $\mathcal{F}_i^\varepsilon$ of the periodically repeated microcells

$$Y_i^\varepsilon = \mathcal{F}_i^\varepsilon \cup \mathcal{O}_i^\varepsilon$$

of size ε, where each microcell $Y_i^\varepsilon = (0,\varepsilon)^d$, up to translation, is the image of the scaled and shifted unit cell Y. Therefore, Ω^ε is defined by

$$\Omega^\varepsilon = \Omega \setminus \bigcup_{i=1}^{N(\varepsilon)} \mathcal{O}_i^\varepsilon,$$

where

$$N(\varepsilon) = |\Omega|\,\varepsilon^{-d}(1+o(1)). \tag{5.1}$$

The outer boundary of Ω^ε is denoted by $\partial\Omega^\varepsilon$. An illustration of an example configuration is given in Figure 5.2. With these definitions, we now pose the problem of a resolved flow in porous media, which is a steady Stokes flow in the periodically perforated domain Ω^ε, by

$$\begin{aligned} -\nu\Delta \boldsymbol{v}^\varepsilon + \nabla p^\varepsilon &= \boldsymbol{f} \qquad \text{in } \Omega^\varepsilon, \\ \operatorname{div} \boldsymbol{v}^\varepsilon &= 0 \qquad \text{in } \Omega^\varepsilon, \end{aligned} \tag{5.2}$$

where $\nu > 0$ denotes the viscosity of the fluid, $\boldsymbol{v}^\varepsilon$ is the fluid velocity, p^ε is the pressure in the system and $\boldsymbol{f} \in [L^2(\Omega^\varepsilon)]^d$ is a given force. The impermeability of the obstacles is modeled by a no-slip condition at the obstacle boundaries Γ_i^ε

$$\boldsymbol{v}^\varepsilon = \boldsymbol{0} \quad \text{on } \Gamma_i^\varepsilon,$$

and the system is closed by a Dirichlet boundary condition

$$\boldsymbol{v}^\varepsilon = \boldsymbol{g} \quad \text{on } \partial\Omega^\varepsilon,$$

given as the trace of a divergence-free function in $[H^1(\Omega^\varepsilon)]^d$, which we denote again by $\boldsymbol{g}$ for convenience.

Define $V^\varepsilon = [H^1(\Omega^\varepsilon)]^d$ and $Q^\varepsilon = L^2(\Omega^\varepsilon)/\mathbb{R}$. The weak formulation of (5.2) is then: find $(\boldsymbol{v}^\varepsilon, p^\varepsilon) \in V^\varepsilon \times Q^\varepsilon$ such that $\boldsymbol{v}^\varepsilon = \boldsymbol{v}_0^\varepsilon + \boldsymbol{g}$ with $\boldsymbol{v}_0^\varepsilon \in [H_0^1(\Omega^\varepsilon)]^d$ given by

$$\begin{aligned} \nu\big(\nabla \boldsymbol{v}_0^\varepsilon, \nabla \boldsymbol{\varphi}^\varepsilon\big)_{\Omega^\varepsilon} - \big(p^\varepsilon, \operatorname{div} \boldsymbol{\varphi}^\varepsilon\big)_{\Omega^\varepsilon} &= \big(\boldsymbol{f}, \boldsymbol{\varphi}^\varepsilon\big)_{\Omega^\varepsilon} - \nu\big(\nabla \boldsymbol{g}, \nabla \boldsymbol{\varphi}^\varepsilon\big)_{\Omega^\varepsilon} \\ -\big(q^\varepsilon, \operatorname{div} \boldsymbol{v}_0^\varepsilon\big)_{\Omega^\varepsilon} &= 0 \end{aligned} \tag{5.3}$$

for all $\boldsymbol{\varphi}^\varepsilon \in [H_0^1(\Omega^\varepsilon)]^d$ and $q^\varepsilon \in L^2(\Omega^\varepsilon)/\mathbb{R}$. For existence and uniqueness of solutions see for example [Tem84, I.2.4].

5.2 Extension with Brinkman Law

Our aim is to use a multigrid preconditioner for solving the equations after we have discretized them with an H^{div}-conforming finite element method. But, the configuration of the domain including obstacles limits the possibility of defining a hierarchy of meshes with a coarsest level, where the grid is actually *coarse*. To bypass this problem we extend the unknowns of the system to the whole domain, including the obstacles, on which a hierarchy of nested meshes can be defined easily, see Figure 5.3.

Therefore, let

$$\Omega = \bigcup_{i=1}^{N(\varepsilon)} Y_i^\varepsilon$$

be the filled domain, i.e., the union of the fluid domain Ω^ε with all obstacles $\mathcal{O}_i^\varepsilon$. We

define an extension $\hat{\boldsymbol{v}}^\varepsilon$ of the velocity in $[H_0^1(\Omega)]^d$ to the whole domain Ω by

$$\hat{\boldsymbol{v}}^\varepsilon = \begin{cases} \boldsymbol{v}^\varepsilon & \text{in } \Omega^\varepsilon, \\ \boldsymbol{0} & \text{in } \Omega \backslash \Omega^\varepsilon. \end{cases} \tag{5.4}$$

The extension of the pressure needs more attention than the extension of the velocity. Following [AM97, Section 3.1.3], we define the pressure constant in the obstacle regions as

$$\hat{p}^\varepsilon = \begin{cases} p^\varepsilon & \text{in } \Omega^\varepsilon, \\ \bar{p}_i \in \mathbb{R} & \text{in each } \mathcal{O}_i^\varepsilon. \end{cases} \tag{5.5}$$

To derive a homogenized limit, the extension has to be chosen as the mean value of the surrounding fluid region, i.e., $\bar{p}_i = \frac{1}{|\mathcal{F}_i^\varepsilon|} \int_{\mathcal{F}_i^\varepsilon} p^\varepsilon \, d\boldsymbol{x}$. In this way, the pressure is bounded uniformly in ε, i.e.,

$$\left\| \hat{p}^\varepsilon \right\|_\Omega \leq c, \tag{5.6}$$

see [AM97, Lemma 1.3], and a homogenized limit of the system can be constructed for $\varepsilon \to 0$.

To realize the extensions (5.4) and (5.5), we use the Brinkman equations

$$\zeta \big(\tilde{\boldsymbol{v}}^\varepsilon, \boldsymbol{\varphi} \big)_{\mathcal{O}_i^\varepsilon} + \nu \big(\nabla \tilde{\boldsymbol{v}}^\varepsilon, \nabla \boldsymbol{\varphi} \big)_{\mathcal{O}_i^\varepsilon} - \big(\tilde{p}^\varepsilon, \operatorname{div} \boldsymbol{\varphi} \big)_{\mathcal{O}_i^\varepsilon} - \big(q, \operatorname{div} \tilde{\boldsymbol{v}}^\varepsilon \big)_{\mathcal{O}_i^\varepsilon} = 0$$

in each extended region $\mathcal{O}_i^\varepsilon$ and control the fluid velocity $\tilde{\boldsymbol{v}}^\varepsilon = \tilde{\boldsymbol{v}}_\zeta^\varepsilon$ by the scaled mass term $\zeta \, (\tilde{\boldsymbol{v}}^\varepsilon, \boldsymbol{\varphi})_{\mathcal{O}_i^\varepsilon}$ with a penalty constant $\zeta \geq 0$ chosen large enough to push the solution towards zero in the extended region. The combined set of equations is thus a coupled Stokes-Brinkman system

$$\begin{aligned} -\nu \Delta \tilde{\boldsymbol{v}}^\varepsilon + \mathbb{1}_{\Omega \backslash \Omega^\varepsilon} \zeta \tilde{\boldsymbol{v}}^\varepsilon + \nabla \tilde{p}^\varepsilon &= \mathbb{1}_{\Omega^\varepsilon} \boldsymbol{f} && \text{in } \Omega, \\ \operatorname{div} \tilde{\boldsymbol{v}}^\varepsilon &= 0 && \text{in } \Omega, \end{aligned} \tag{5.7}$$

closed by the Dirichlet boundary condition

$$\tilde{\boldsymbol{v}}^\varepsilon = \mathbb{1}_{\partial \Omega^\varepsilon} \boldsymbol{g} \quad \text{on } \partial \Omega,$$

written with the indicator function defined by

$$\mathbb{1}_D(\boldsymbol{x}) = \begin{cases} 1, & \text{for } \boldsymbol{x} \in D, \\ 0, & \text{in } \boldsymbol{x} \in \Omega \setminus D. \end{cases}$$

The boundary function $\mathbb{1}_{\partial\Omega^\varepsilon}\boldsymbol{g}$ is the trace of the $[H^1(\Omega)]^d$-function $\mathbb{1}_{\Omega^\varepsilon}\boldsymbol{g}$.

Let $X = V \times Q = [H^1(\Omega)]^d \times L^2(\Omega)/\mathbb{R}$. The variational formulation of (5.7) is then: find $(\tilde{\boldsymbol{v}}^\varepsilon, \tilde{p}^\varepsilon) \in V \times Q$ such that $\tilde{\boldsymbol{v}}^\varepsilon = \tilde{\boldsymbol{v}}_0^\varepsilon + \mathbb{1}_{\Omega^\varepsilon}\boldsymbol{g}$ with $\tilde{\boldsymbol{v}}_0^\varepsilon \in [H_0^1(\Omega)]^d$ given by

$$\begin{aligned} \nu a\big(\tilde{\boldsymbol{v}}_0^\varepsilon, \boldsymbol{\varphi}\big) + \sum_{i=1}^{N(\varepsilon)} \zeta\big(\tilde{\boldsymbol{v}}_0^\varepsilon, \boldsymbol{\varphi}\big)_{\mathcal{O}_i^\varepsilon} - b\big(\tilde{p}^\varepsilon, \boldsymbol{\varphi}\big) &= \big(\boldsymbol{f}, \boldsymbol{\varphi}\big)_{\Omega^\varepsilon} - \nu\big(\nabla \boldsymbol{g}, \nabla \boldsymbol{\varphi}\big)_{\Omega^\varepsilon}, \\ -b\big(q, \tilde{\boldsymbol{v}}_0^\varepsilon\big) &= 0, \end{aligned} \tag{5.8}$$

for all $\boldsymbol{\varphi} \in [H_0^1(\Omega)]^d$, $q \in Q$ with the bilinearforms

$$a\big(\tilde{\boldsymbol{v}}^\varepsilon, \boldsymbol{\varphi}\big) = \big(\nabla \tilde{\boldsymbol{v}}^\varepsilon, \nabla \boldsymbol{\varphi}\big)_\Omega, \qquad b\big(\tilde{p}^\varepsilon, \boldsymbol{\varphi}\big) = \big(\tilde{p}^\varepsilon, \operatorname{div} \boldsymbol{\varphi}\big)_\Omega.$$

According to the weak formulation, we define the bilinear form $\tilde{\mathbb{A}}^\varepsilon(\cdot,\cdot) : X \times X \to \mathbb{R}$ by

$$\tilde{\mathbb{A}}^\varepsilon\left(\begin{pmatrix} \tilde{\boldsymbol{v}}^\varepsilon \\ \tilde{p}^\varepsilon \end{pmatrix}, \begin{pmatrix} \boldsymbol{\varphi} \\ q \end{pmatrix}\right) = \nu a\big(\tilde{\boldsymbol{v}}^\varepsilon, \boldsymbol{\varphi}\big) + \sum_{i=1}^{N(\varepsilon)} \zeta\big(\tilde{\boldsymbol{v}}^\varepsilon, \boldsymbol{\varphi}\big)_{\mathcal{O}_i^\varepsilon} - b\big(\tilde{p}^\varepsilon, \boldsymbol{\varphi}\big) - b\big(q, \tilde{\boldsymbol{v}}^\varepsilon\big).$$

Remark 5.1. *Imposing strong or weak interface conditions inside the domain to accurately extend the solution to the obstacle regions will briefly be discussed in Section 6.2 in form of so-called virtual extensions.*

5.3 Discussion of the Extended Model

In this section we discuss the choice of the extended Stokes-Brinkman model as approximation for the Stokes problem on a perforated domain. This is done by deriving an error estimate for the velocity of the extended system in terms of the penalty factor. To simplify the notation and without loss of generality, we set $\boldsymbol{g} = 0$ in this section.

First, we note that the penalty formulation (5.8) is not consistent with the weak

formulation (5.3), since for the exact solution $(\hat{\boldsymbol{v}}^\varepsilon, \hat{p}^\varepsilon) \in V^\varepsilon \times Q^\varepsilon$ there holds

$$\begin{aligned}\tilde{\mathbb{A}}^\varepsilon\left(\begin{pmatrix}\hat{\boldsymbol{v}}^\varepsilon\\ \hat{p}^\varepsilon\end{pmatrix}, \begin{pmatrix}\boldsymbol{\varphi}\\ q\end{pmatrix}\right) &= \nu a(\hat{\boldsymbol{v}}^\varepsilon, \boldsymbol{\varphi}) + \sum_{i=1}^{N(\varepsilon)} \zeta(\hat{\boldsymbol{v}}^\varepsilon, \boldsymbol{\varphi})_{\mathcal{O}_i^\varepsilon} - b(\hat{p}^\varepsilon, \boldsymbol{\varphi}) - b(q, \hat{\boldsymbol{v}}^\varepsilon)\\ &= \nu(\nabla\hat{\boldsymbol{v}}^\varepsilon, \nabla\boldsymbol{\varphi})_{\Omega^\varepsilon} - (\hat{p}^\varepsilon, \operatorname{div}\boldsymbol{\varphi})_{\Omega^\varepsilon} - (\hat{p}^\varepsilon, \operatorname{div}\boldsymbol{\varphi})_{\Omega\setminus\Omega^\varepsilon} - (q, \operatorname{div}\hat{\boldsymbol{v}}^\varepsilon)_{\Omega^\varepsilon}\\ &= (\boldsymbol{f}, \boldsymbol{\varphi})_{\Omega^\varepsilon} - \sum_{i=1}^{N(\varepsilon)} (\bar{p}_i, \operatorname{div}\boldsymbol{\varphi})_{\mathcal{O}_i^\varepsilon}.\end{aligned}$$

Consequently, the error equation is

$$\tilde{\mathbb{A}}^\varepsilon\left(\begin{pmatrix}\tilde{\boldsymbol{v}}^\varepsilon\\ \tilde{p}^\varepsilon\end{pmatrix}, \begin{pmatrix}\boldsymbol{\varphi}\\ q\end{pmatrix}\right) - \tilde{\mathbb{A}}^\varepsilon\left(\begin{pmatrix}\hat{\boldsymbol{v}}^\varepsilon\\ \hat{p}^\varepsilon\end{pmatrix}, \begin{pmatrix}\boldsymbol{\varphi}\\ q\end{pmatrix}\right) = \sum_{i=1}^{N(\varepsilon)} (\bar{p}_i, \operatorname{div}\boldsymbol{\varphi})_{\mathcal{O}_i^\varepsilon}.$$

Thus, we can estimate

$$\begin{aligned}\|\nabla(\tilde{\boldsymbol{v}}^\varepsilon - \hat{\boldsymbol{v}}^\varepsilon)\|_\Omega^2 + \sum_{i=1}^{N(\varepsilon)} \zeta\|\tilde{\boldsymbol{v}}^\varepsilon - \hat{\boldsymbol{v}}^\varepsilon\|_{\mathcal{O}_i^\varepsilon}^2 &= \tilde{\mathbb{A}}^\varepsilon\left(\begin{pmatrix}\tilde{\boldsymbol{v}}^\varepsilon - \hat{\boldsymbol{v}}^\varepsilon\\ \tilde{p}^\varepsilon - \hat{p}^\varepsilon\end{pmatrix}, \begin{pmatrix}\tilde{\boldsymbol{v}}^\varepsilon - \hat{\boldsymbol{v}}^\varepsilon\\ -(\tilde{p}^\varepsilon - \hat{p}^\varepsilon)\end{pmatrix}\right)\\ &\le \sum_{i=1}^{N(\varepsilon)} \|\bar{p}_i\|_{\mathcal{O}_i^\varepsilon} \|\operatorname{div}(\tilde{\boldsymbol{v}}^\varepsilon - \hat{\boldsymbol{v}}^\varepsilon)\|_{\mathcal{O}_i^\varepsilon} \le c\sum_{i=1}^{N(\varepsilon)} \|\bar{p}_i\|_{\mathcal{O}_i^\varepsilon}^2 + \frac{1}{2}\|\nabla(\tilde{\boldsymbol{v}}^\varepsilon - \hat{\boldsymbol{v}}^\varepsilon)\|_\Omega^2, \quad (5.9)\end{aligned}$$

where we have used the Cauchy-Schwarz inequality and the basic Young's inequality. Including the last term of (5.9) into the left hand side yields

$$\frac{1}{2}\|\nabla(\tilde{\boldsymbol{v}}^\varepsilon - \hat{\boldsymbol{v}}^\varepsilon)\|_\Omega^2 + \sum_{i=1}^{N(\varepsilon)} \zeta\|\tilde{\boldsymbol{v}}^\varepsilon - \hat{\boldsymbol{v}}^\varepsilon\|_{\mathcal{O}_i^\varepsilon}^2 \le c\sum_{i=1}^{N(\varepsilon)} \|\bar{p}_i\|_{\mathcal{O}_i^\varepsilon}^2,$$

and finally by the pressure bound (5.6)

$$\sum_{i=1}^{N(\varepsilon)} \|\tilde{\boldsymbol{v}}^\varepsilon\|_{\mathcal{O}_i^\varepsilon}^2 = \sum_{i=1}^{N(\varepsilon)} \|\tilde{\boldsymbol{v}}^\varepsilon - \hat{\boldsymbol{v}}^\varepsilon\|_{\mathcal{O}_i^\varepsilon}^2 \le c\frac{1}{\zeta}. \quad (5.10)$$

From this we can conclude that the fluid extension $\tilde{\boldsymbol{v}}^\varepsilon \to \hat{\boldsymbol{v}}^\varepsilon$ in the obstacle regions $\mathcal{O}_i^\varepsilon$ for $\zeta \to \infty$ and thus the Stokes-Brinkman model (5.8) is a viable approximation for the Stokes model (5.3) on perforated domains.

5.4 H^{div}-conforming Discretization

As discretization we choose an H^{div}-conforming mixed finite element method as proposed in [CKS06].

We assume that the shape regular triangulation $\mathcal{T}_h$ of Ω is such that the boundary of the obstacles Γ_i^ε is aligned with $\mathcal{T}_h$. The alignment assures that the geometrical structure of Ω is resolved by the computational mesh $\mathcal{T}_h$. Let the discrete velocity space $V_h \subset H^{\mathrm{div}}(\Omega)$ contain the boundary condition in normal direction $\boldsymbol{g} \cdot \boldsymbol{n}$ and let $Q_h \subset L^2(\Omega)$ be the matching pressure space such that

$$\operatorname{div} V_h = Q_h.$$

The H^{div}-conforming discretization of the coupled Stokes-Brinkman system (5.8) based on the mixed finite element space

$$X_h = V_h \times Q_h \tag{5.11}$$

can then be represented as

$$\tilde{\mathbb{A}}_h^\varepsilon\left(\begin{pmatrix}\tilde{\boldsymbol{v}}_h^\varepsilon\\ \tilde{p}_h^\varepsilon\end{pmatrix}, \begin{pmatrix}\boldsymbol{\varphi}\\ q\end{pmatrix}\right) = \mathbb{F}_h\left(\begin{pmatrix}\boldsymbol{\varphi}\\ q\end{pmatrix}\right), \tag{5.12}$$

where the discrete bilinear form $\tilde{\mathbb{A}}_h^\varepsilon(\cdot,\cdot) : X_h \times X_h \to \mathbb{R}$ is defined by

$$\tilde{\mathbb{A}}_h^\varepsilon\left(\begin{pmatrix}\tilde{\boldsymbol{v}}_h^\varepsilon\\ \tilde{p}_h^\varepsilon\end{pmatrix}, \begin{pmatrix}\boldsymbol{\varphi}\\ q\end{pmatrix}\right) = \nu a_h\big(\tilde{\boldsymbol{v}}_h^\varepsilon, \boldsymbol{\varphi}\big) + \sum_{i=1}^{N(\varepsilon)} \zeta\big(\tilde{\boldsymbol{v}}_h^\varepsilon, \boldsymbol{\varphi}\big)_{\mathcal{O}_i^\varepsilon} - b\big(\tilde{p}_h^\varepsilon, \boldsymbol{\varphi}\big) - b\big(q, \tilde{\boldsymbol{v}}_h^\varepsilon\big)$$

and the right hand side is given by

$$\mathbb{F}_h\left(\begin{pmatrix}\boldsymbol{\varphi}\\ q\end{pmatrix}\right) = \big(\boldsymbol{f}, \boldsymbol{\varphi}\big)_{\Omega^\varepsilon} + \nu \sum_{B \in \Gamma_{B,h}} \Big(\frac{\eta_a}{h}\big(\boldsymbol{g}, \boldsymbol{\varphi}\big)_B - \big(\boldsymbol{g}, \nabla\boldsymbol{\varphi}\boldsymbol{n}\big)_B\Big). \tag{5.13}$$

The discrete bilinearform $a_h(\cdot,\cdot) : V_h \times V_h \to \mathbb{R}$, defined in (4.5), is the symmetric interior penalty discontinuous Galerkin approximation of $a(\cdot,\cdot) : V \times V \to \mathbb{R}$. The additional sum over all boundary terms in (5.13) is due to the discontinuous Galerkin formulation for inhomogeneous boundary values. Note, that the right hand side is only integrated on

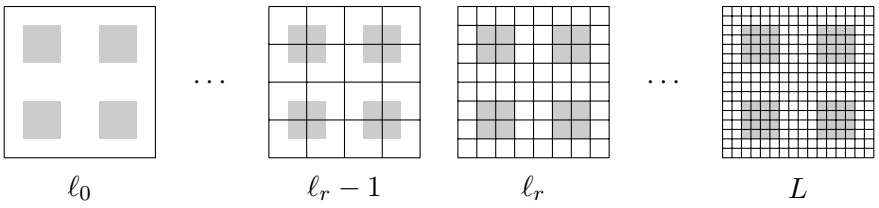

Figure 5.3: Hierarchy of meshes for extended domain Ω. L is the computational level, ℓ_r is the level on which the fine-scale structure of the domain is still resolved, and ℓ_0 is the coarsest level of the multigrid method.

the fluid region Ω^ε, such that $\mathbb{1}_{\Omega^\varepsilon}\boldsymbol{f}$ and $\mathbb{1}_{\Omega^\varepsilon}\boldsymbol{g}$ is realized.

By coercivity (4.6) of $a_h(\cdot,\cdot)$ it follows the coercivity estimate

$$\nu a_h(\boldsymbol{\varphi},\boldsymbol{\varphi}) + \sum_{i=1}^{N(\varepsilon)} \zeta(\boldsymbol{\varphi},\boldsymbol{\varphi})_{\mathcal{O}_i^\varepsilon} \geq c\nu \|\boldsymbol{\varphi}\|_{1,h}^2 \tag{5.14}$$

for all $\boldsymbol{\varphi} \in V_h$. Furthermore, let $\boldsymbol{\varphi}, \boldsymbol{\psi} \in V_h$, then it holds by a Poincaré inequality and (5.1)

$$\sum_{i=1}^{N(\varepsilon)} \zeta(\boldsymbol{\varphi},\boldsymbol{\psi})_{\mathcal{O}_i^\varepsilon} \leq \sum_{i=1}^{N(\varepsilon)} \zeta \|\boldsymbol{\varphi}\|_{\mathcal{O}_i^\varepsilon} \|\boldsymbol{\psi}\|_{\mathcal{O}_i^\varepsilon} \leq c\zeta\, |\Omega|\, \varepsilon^{2-d} \|\boldsymbol{\varphi}\|_{1,h} \|\boldsymbol{\psi}\|_{1,h}. \tag{5.15}$$

Thus, existence and uniqueness follows by coercivity (5.14), continuity (4.7) of $a_h(\cdot,\cdot)$ together with (5.15), as well as the discrete inf-sup condition (4.10).

5.5 Homogenizing Two-scale Multilevel Schwarz Algorithm

The homogenizing two-scale multilevel Schwarz algorithm presented in this section incorporates a homogenized operator on the effective coarse-scale and is otherwise based on Algorithm2.5 in form of a monolithic multigrid V-cycle with an overlapping Schwarz smoother. To sketch the idea of this approach Figure 5.1 serves as a reference.

We assume that $\mathcal{T}_h$ has emerged by a subdivision of a coarsest mesh $\mathcal{T}_{\ell_0}$ such that there is a hierarchy of nested meshes $\mathcal{T}_\ell = \mathcal{T}_{h_\ell}$ with

$$\mathcal{T}_{\ell_0} \subset \cdots \subset \mathcal{T}_{\ell_r - 1} \subset \mathcal{T}_{\ell_r} \subset \cdots \subset \mathcal{T}_L = \mathcal{T}_h,$$

Algorithm 5.1 Two-scale multigrid V-cycle

Let L be the computational level corresponding to $\mathcal{T}_h = \mathcal{T}_{h_L}$, and let ℓ_r be the coarsest level of the fine-scale, where the structure of the microscopic problem can still be resolved. Let ℓ_0 be the coarsest level of the multigrid scheme. Define

$$\boldsymbol{A}_\ell = \begin{cases} \boldsymbol{A}_\ell^\varepsilon, & \text{for } \ell \in \{\ell_r, \dots, L\}, \\ \bar{\boldsymbol{A}}_\ell, & \text{for } \ell \in \{\ell_0, \dots, \ell_r - 1\}. \end{cases}$$

Let $\boldsymbol{M}_{\ell_0}^{TS} = \boldsymbol{A}_{\ell_0}^{-1}$. Let $\boldsymbol{S}_\ell$ be a suitable smoother, and let $m_{\text{pre}}(\ell)$ and $m_{\text{post}}(\ell)$ be the number of pre-smoothing and post-smoothing steps, respectively, on each level. Recursively define the action of $\boldsymbol{M}_\ell^{TS}$ on a vector $\boldsymbol{b}_\ell$ as follows:

1. Pre-smoothing: let $\boldsymbol{x}_0 = \boldsymbol{0}$ and compute for $i = 1, \dots, m_{\text{pre}}(\ell)$

$$\boldsymbol{x}_i = \boldsymbol{x}_{i-1} + \boldsymbol{S}_\ell \left(\boldsymbol{b}_\ell - \boldsymbol{A}_\ell \boldsymbol{x}_{i-1}\right)$$

2. Coarse grid correction:

$$\boldsymbol{x}_{m_{\text{pre}}(\ell)+1} = \boldsymbol{x}_{m_{\text{pre}}(\ell)} + \boldsymbol{R}_{\ell-1}^T \boldsymbol{M}_{\ell-1}^{TS} \boldsymbol{R}_{\ell-1} \left(\boldsymbol{b}_\ell - \boldsymbol{A}_\ell \boldsymbol{x}_{m_{\text{pre}}(\ell)}\right)$$

3. Post-smoothing: for $i = m_{\text{pre}}(\ell) + 2, \dots, m_{\text{pre}}(\ell) + m_{\text{post}}(\ell) + 1$ compute

$$\boldsymbol{x}_i = \boldsymbol{x}_{i-1} + \boldsymbol{S}_\ell \left(\boldsymbol{b}_\ell - \boldsymbol{A}_\ell \boldsymbol{x}_{i-1}\right)$$

4. Assign: $\boldsymbol{M}_\ell^{TS} \boldsymbol{b}_\ell = \boldsymbol{x}_{m_{\text{pre}}(\ell)+m_{\text{post}}(\ell)+1}$

to mesh sizes

$$h_{\ell_0} < \cdots < h_{\ell_r - 1} < h_{\ell_r} < \cdots < h_L = h.$$

Here, L is the computational level on which the problem is going to be solved, and ℓ_0 is the coarsest level of the multigrid algorithm. We assume further that ℓ_r is the coarsest level on which the geometry of the fine-scale structure is still resolved exactly by the mesh $\mathcal{T}_{\ell_r}$, i.e., we assume that the boundary Γ_i^ε of the obstacles is aligned with $\mathcal{T}_{\ell_r}$, and not anymore with $\mathcal{T}_{\ell_r - 1}$. Therefore,

$$\{\ell_r, \dots, L\}$$

is the set of all levels, where the fine-scale geometry is resolved exactly by the correspond-

ing mesh, and

$$\{\ell_0, \ldots, \ell_r - 1\}$$

is the set of all coarse-scale levels. Compare Figure 5.3 for a visualization of the different mesh-levels, where the geometry of the domain is or is not resolved by the mesh.

Let $\boldsymbol{A}_\ell^\varepsilon$ be the system matrix corresponding to (5.12) to the mesh size h_ℓ, and let $\bar{\boldsymbol{A}}_\ell$ be one of the homogenized operators that will be defined in (5.19) in Section 5.7. As smoother we choose either the additive or the multiplicative Schwarz smoother introduced in Section 2.5. Both Schwarz smoothers depend on the level-matrix $\boldsymbol{A}_\ell$ that is chosen as

$$\boldsymbol{A}_\ell = \begin{cases} \boldsymbol{A}_\ell^\varepsilon, & \text{for } \ell \in \{\ell_r, \ldots, L\}, \\ \bar{\boldsymbol{A}}_\ell, & \text{for } \ell \in \{\ell_0, \ldots, \ell_r - 1\}, \end{cases}$$

depending on the level ℓ. The homogenizing two-scale multilevel Schwarz algorithm is then formulated in Algorithm 5.1.

5.6 Homogenized Coarse-scale Operators

In this section we review the results of the homogenization theory in the literature to provide coarse-scale operators for the perforated Stokes system (5.2) with the extensions defined in (5.4) and (5.5). Therefore, we recapitulate briefly the results of the homogenization theory in [AM97], where different homogenized limits of the steady Stokes system on a periodically perforated domain are derived based on two different homogenization methods.

The process of homogenization is illustrated in Figure 5.4 and describes different notions of upscaling or averaging techniques to derive laws for the effective behavior of equations with highly oscillating properties as coefficients or repeated geometric structures, when the size of the period ε tends to zero. Since the homogenized operators will enter the equations only in form of local patch problems or a coarse problem of an overlapping Schwarz preconditioner, it is sufficient to consider a homogeneous boundary condition $\boldsymbol{g} = \boldsymbol{0}$.

We start with presenting the limit for $\varepsilon \to 0$ obtained by the two-scale convergence method, which leads to a Darcy law, provided that the pore size is much smaller than

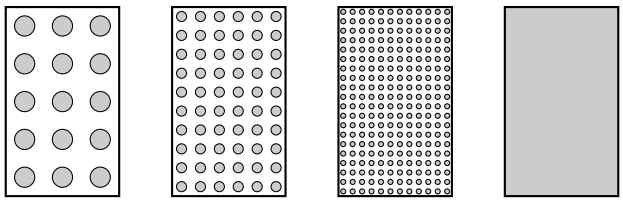

Figure 5.4: Homogenization limit of periodic domain Ω^ε as illustrated in [Hor97, Figure 1.1].

the characteristic length of the reservoir. After that, we present the results obtained by the energy method under the assumption that the obstacle size s_ε is much smaller than the period ε. In this case, the homogenized limit is depending on the size of the obstacles and leads at a critical size to a Brinkman law. For larger obstacles it results in a Darcy law, and for smaller obstacles in the Stokes equations again.

5.6.1 Homogenization with the Two-scale Convergence Method

The two-scale convergence method was introduced around 1990 by Nguetseng in [Ngu89] and by Allaire in [All92]. As a homogenization method it is restricted to periodic problems, where the geometry of the domain or the coefficients of the microscopic problem have a periodic structure that is repeated over the whole domain. A great advantage of the method is its close relation to the heuristic method of two-scale asymptotic expansions with which formal derivations of the homogenized problems are quite easy achievable. For example, if a sequence v^ε admits an asymptotic expansion of the form

$$v^\varepsilon(\boldsymbol{x}) = v_0(\boldsymbol{x}, \frac{\boldsymbol{x}}{\varepsilon}) + \varepsilon v_1(\boldsymbol{x}, \frac{\boldsymbol{x}}{\varepsilon}) + \varepsilon^2 v_2(\boldsymbol{x}, \frac{\boldsymbol{x}}{\varepsilon}) + \dots,$$

for $\boldsymbol{y}$-periodic and smooth functions $v_i(\boldsymbol{x}, \boldsymbol{y})$, then it two-scale converges to $v_0(\boldsymbol{x}, \boldsymbol{y})$. We refer to [Hor97, A.3] for an introduction to the method. The detailed proof of the two-scale convergence of system (5.12) can be found in [AM97]. The first formal derivations of Darcy's law using two-scale expansions are due to [Kel80, Lio81, SP80].

To derive a homogenized limit, one first needs to scale the fluid velocity $\boldsymbol{v}^\varepsilon$ by the factor ε^{-2} such that the viscosity ν is of order ε^2. This is possible due to the linearity of (5.2). Further, we need to assume that the pore size is much smaller than the characteristic length of the reservoir. The resulting homogenized limit for $\varepsilon \to 0$ obtained by the

two-scale convergence method is then Darcy's law

$$\begin{aligned} \nu \boldsymbol{L}^{-1} \bar{\boldsymbol{v}} + \nabla \bar{p} &= \boldsymbol{f} && \text{in } \Omega, \\ \operatorname{div} \bar{\boldsymbol{v}} &= 0 && \text{in } \Omega, \\ \bar{\boldsymbol{v}} \cdot \boldsymbol{n} &= 0 && \text{on } \partial\Omega, \end{aligned}$$

with the constant, symmetric and positive definite permeability tensor $\boldsymbol{L} = (\boldsymbol{L}_{ij})_{i,j=1}^{d}$ defined by

$$\boldsymbol{L}_{ij} = \int_{\mathcal{F}} \nabla \boldsymbol{\omega}_i(\boldsymbol{y}) \cdot \nabla \boldsymbol{\omega}_j(\boldsymbol{y}) \, d\boldsymbol{y} = \int_{\mathcal{F}} \boldsymbol{\omega}_i(\boldsymbol{y}) \cdot \boldsymbol{e}_j \, d\boldsymbol{y}, \tag{5.16}$$

where $\boldsymbol{\omega}_j$ are the solutions of the cell problems: find $\boldsymbol{y}$-periodic vector fields $\boldsymbol{\omega}_j$, and $\boldsymbol{y}$-periodic pressure fields π_j, such that

$$\begin{aligned} -\Delta \boldsymbol{\omega}_j + \nabla \pi_j &= \boldsymbol{e}_j && \text{in } \mathcal{F}, \\ \operatorname{div} \boldsymbol{\omega}_j &= 0 && \text{in } \mathcal{F}, \\ \boldsymbol{\omega}_j &= \boldsymbol{0} && \text{on } \partial\mathcal{F}. \end{aligned} \tag{5.17}$$

As one can see in the definition of the cell problems, the permeability $\boldsymbol{L}$ depends only on the geometry of the microstructure and not on the physical properties as the viscosity, or the acting forces.

5.6.2 Homogenization with the Energy Method

Next, we present the second method for the homogenization of system (5.2), called the energy method, that was introduced by Tartar and Murat in the late 1970's in [Tar78, MT78]. The key idea is to choose an oscillating test function in the variational formulation of the problem and pass to the limit in the notion of weak or strong convergence. The method is very general, since it is not restricted to periodicity of the domain or the coefficients in the system. We refer to [Hor97, A.2] for an introduction to the energy method and to [AM97] for the technical details about the homogenization of (5.2). The homogenized limit depends on the obstacle size s_ε and the equations can either result in a Brinkman law, a Darcy law, or again, a Stokes law.

For a proper presentation of the results we briefly introduce the concept of weak and strong convergence in Hilbert spaces. A sequence $\{v_n\}_{n\in\mathbb{N}}$ is said to be weakly convergent

to v in a Hilbert space V, if it converges with respect to the inner product $(\cdot,\cdot)$ of V, i.e.,

$$(v_n - v, \varphi) \to 0, \qquad \text{for } n \to \infty,$$

for all $\varphi \in V$. The sequence $\{v_n\}_{n\in\mathbb{N}}$ converges strongly in V, if it converges with respect to the norm $\|\cdot\| = \sqrt{(\cdot,\cdot)}$,

$$\|v_n - v\| \to 0, \qquad \text{for } n \to \infty.$$

The obstacle size s_ε is defined as a parameter that rescales the standard obstacle $\mathcal{O}$ to the size s_ε, i.e., $\mathcal{O}_i^\varepsilon = s_\varepsilon \mathcal{O}$. For the homogenization process the solid obstacles are assumed to be much smaller than the period ε, which is formulated in the form of a growth condition

$$\lim_{\varepsilon\to 0} \frac{s_\varepsilon}{\varepsilon} = 0.$$

The three different limits are distinguished by the ratio σ_ε defined by

$$\sigma_\varepsilon = \varepsilon \left| \log\left(\frac{s_\varepsilon}{\varepsilon}\right)\right|^{1/2} \qquad \text{for } d = 2, \tag{5.18}$$

and

$$\sigma_\varepsilon = \left(\frac{\varepsilon^d}{s_\varepsilon^{d-2}}\right)^{1/2} \qquad \text{for } d \geq 3,$$

and are formulated in the following.

1. At a critical size where $\lim_{\varepsilon\to 0} \sigma_\varepsilon = \sigma > 0$, the extended solution $(\tilde{\boldsymbol{v}}^\varepsilon, \tilde{p}^\varepsilon)$ of (5.2) converges weakly in $[H_0^1(\Omega)]^d \times L^2(\Omega)/\mathbb{R}$ to the unique solution $(\bar{\boldsymbol{v}}, \bar{p})$ of the Brinkman law

$$\begin{aligned} -\nu\Delta\bar{\boldsymbol{v}} + \frac{\nu}{\sigma^2}\boldsymbol{M}\bar{\boldsymbol{v}} + \nabla\bar{p} &= \boldsymbol{f} \qquad \text{in } \Omega, \\ \operatorname{div}\bar{\boldsymbol{v}} &= 0 \qquad \text{in } \Omega, \\ \bar{\boldsymbol{v}} &= 0 \qquad \text{on } \partial\Omega. \end{aligned}$$

2. For large obstacles, such that $\lim_{\varepsilon\to 0} \sigma_\varepsilon = 0$, the extended and rescaled solution $(\frac{\tilde{\boldsymbol{v}}^\varepsilon}{\sigma_\varepsilon^2}, \tilde{p}^\varepsilon)$ of (5.2) converges strongly in $[L^2(\Omega)]^d \times L^2(\Omega)/\mathbb{R}$ to the unique solution

$(\bar{\boldsymbol{v}}, \bar{p})$ of Darcy's law

$$\begin{aligned} \nu \boldsymbol{M} \bar{\boldsymbol{v}} + \nabla \bar{p} &= \boldsymbol{f} && \text{in } \Omega, \\ \operatorname{div} \bar{\boldsymbol{v}} &= 0 && \text{in } \Omega, \\ \bar{\boldsymbol{v}} \cdot \boldsymbol{n} &= 0 && \text{on } \partial\Omega. \end{aligned}$$

3. For very small obstacles, such that $\lim_{\varepsilon \to 0} \sigma_\varepsilon = +\infty$, the extended solution $(\tilde{\boldsymbol{v}}^\varepsilon, \tilde{p}^\varepsilon)$ of (5.2) converges strongly in $[H_0^1(\Omega)]^d \times L^2(\Omega)/\mathbb{R}$ to the unique solution $(\bar{\boldsymbol{v}}, \bar{p})$ of the homogenized Stokes equations

$$\begin{aligned} -\nu \Delta \bar{\boldsymbol{v}} + \nabla \bar{p} &= \boldsymbol{f} && \text{in } \Omega, \\ \operatorname{div} \bar{\boldsymbol{v}} &= 0 && \text{in } \Omega, \\ \bar{\boldsymbol{v}} &= 0 && \text{on } \partial\Omega. \end{aligned}$$

The definition of $\boldsymbol{M}$ is given by

$$\boldsymbol{M}_{ij} = \int_{\mathbb{R}^d \setminus \mathcal{O}} \nabla \boldsymbol{\omega}_i(\boldsymbol{y}) \cdot \nabla \boldsymbol{\omega}_j(\boldsymbol{y}) \, d\boldsymbol{y},$$

where $\boldsymbol{\omega}_i$, $1 \leq i \leq d$, are the solutions of the following cell problems, which differ in the choice of the boundary conditions with respect to the space dimension d. The cell problems are defined by: find vector fields $\boldsymbol{\omega}_j$ and pressure fields π_j, such that

$$\begin{aligned} -\Delta \boldsymbol{\omega}_i + \nabla \pi_i &= \boldsymbol{0} && \text{in } \mathbb{R}^d \setminus \mathcal{O}, \\ \operatorname{div} \boldsymbol{\omega}_i &= 0 && \text{in } \mathbb{R}^d \setminus \mathcal{O}, \\ \boldsymbol{\omega}_i &= \boldsymbol{0} && \text{in } \mathcal{O}, \end{aligned}$$

subject to the boundary conditions

$$\boldsymbol{\omega}_i(\boldsymbol{x}) \to \begin{cases} \boldsymbol{e}_i \log(|\boldsymbol{x}|) & \text{as } |\boldsymbol{x}| \to \infty \text{ for } d = 2, \\ \boldsymbol{e}_i & \text{as } |\boldsymbol{x}| \to \infty \text{ for } d \geq 3. \end{cases}$$

However, we have from [AM97, Proposition 3.2] that whatever the shape or the size

of the obstacle $\mathcal{O}$, in two space dimensions the matrix $\boldsymbol{M}$ is always the same

$$\boldsymbol{M} = 4\pi \boldsymbol{I}.$$

Note, that $\boldsymbol{L}$ from the two-scale periodic setting in Section 5.6.1, and $\boldsymbol{M}$ are totally different tensors, although they are not entirely unrelated, since $\boldsymbol{M}^{-1}$ is the rescaled limit of $\boldsymbol{L}$ for $s_\varepsilon \to 0$ in the unit cell Y, see [All91].

5.7 Discretization of the Homogenized Problems

The homogenized equations are discretized with the same type of H^{div}-conforming mixed finite element spaces as the microscopic Stokes system. The discretization follows again [CKS06].

Therefore, we choose the discretization spaces

$$X_\ell = V_\ell \times Q_\ell$$

from (5.11) equipped with a homogeneous Dirichlet boundary condition. We write the spaces to the mesh size $h_\ell > h$ to mark that we use the resulting operators inside the multilevel methods on the coarser mesh levels $\ell < L$.

This yields the following four discrete bilinearforms.

1. For Darcy's law derived with the two-scale convergence method we define $\bar{\mathbb{D}}_{\boldsymbol{L}^{-1},\ell}(\cdot,\cdot) : X_\ell \times X_\ell \to \mathbb{R}$ by

$$\bar{\mathbb{D}}_{\boldsymbol{L}^{-1},\ell}\left(\begin{pmatrix}\bar{\boldsymbol{v}}_\ell \\ \bar{p}_\ell\end{pmatrix}, \begin{pmatrix}\boldsymbol{\varphi} \\ q\end{pmatrix}\right) = \nu\big(\boldsymbol{L}^{-1}\bar{\boldsymbol{v}}_\ell, \boldsymbol{\varphi}\big)_\Omega - b\big(\bar{p}_\ell, \boldsymbol{\varphi}\big) - b\big(q, \bar{\boldsymbol{v}}_\ell\big).$$

2. For Brinkman's law we define $\bar{\mathbb{B}}_{\boldsymbol{M},\ell}(\cdot,\cdot) : X_\ell \times X_\ell \to \mathbb{R}$ by

$$\bar{\mathbb{B}}_{\boldsymbol{M},\ell}\left(\begin{pmatrix}\bar{\boldsymbol{v}}_\ell \\ \bar{p}_\ell\end{pmatrix}, \begin{pmatrix}\boldsymbol{\varphi} \\ q\end{pmatrix}\right) = \nu a_\ell\big(\bar{\boldsymbol{v}}_\ell, \boldsymbol{\varphi}\big) + \frac{\nu}{\sigma^2}\big(\boldsymbol{M}\bar{\boldsymbol{v}}_\ell, \boldsymbol{\varphi}\big)_\Omega - b\big(\bar{p}_\ell, \boldsymbol{\varphi}\big) - b\big(q, \bar{\boldsymbol{v}}_\ell\big).$$

3. For Darcy's law derived with the energy method we define $\bar{\mathbb{D}}_{\boldsymbol{M},\ell}(\cdot,\cdot) : X_\ell \times X_\ell \to \mathbb{R}$

by

$$\bar{\mathbb{D}}_{\boldsymbol{M},\ell}\left(\begin{pmatrix}\bar{\boldsymbol{v}}_\ell\\ \bar{p}_\ell\end{pmatrix},\begin{pmatrix}\boldsymbol{\varphi}\\ q\end{pmatrix}\right)=\nu\big(\boldsymbol{M}\bar{\boldsymbol{v}}_\ell,\boldsymbol{\varphi}\big)_\Omega-b\big(\bar{p}_\ell,\boldsymbol{\varphi}\big)-b\big(q,\bar{\boldsymbol{v}}_\ell\big).$$

4. For the Stokes equations we define $\bar{\mathbb{S}}_\ell(\cdot,\cdot):X_\ell\times X_\ell\to\mathbb{R}$ by

$$\bar{\mathbb{S}}_\ell\left(\begin{pmatrix}\bar{\boldsymbol{v}}_\ell\\ \bar{p}_\ell\end{pmatrix},\begin{pmatrix}\boldsymbol{\varphi}\\ q\end{pmatrix}\right)=\nu a_h\big(\bar{\boldsymbol{v}}_\ell,\boldsymbol{\varphi}\big)-b\big(\bar{p}_\ell,\boldsymbol{\varphi}\big)-b\big(q,\bar{\boldsymbol{v}}_\ell\big).$$

Corresponding to each of these four homogenized bilinearforms we denote their algebraic analogues by

$$\bar{\boldsymbol{D}}_{\boldsymbol{L}^{-1},\ell},\quad \bar{\boldsymbol{B}}_{\boldsymbol{M},\ell},\quad \bar{\boldsymbol{D}}_{\boldsymbol{M},\ell},\quad \text{and}\quad \bar{\boldsymbol{S}}_\ell. \tag{5.19}$$

Note that the two Darcy operators differ only in the choice of the permeability tensor.

5.7.1 Assembly of the Effective Tensor

As we have seen, the discrete homogenized operators $\bar{\boldsymbol{B}}_{\boldsymbol{M},\ell}$, $\bar{\boldsymbol{D}}_{\boldsymbol{M},\ell}$, and $\bar{\boldsymbol{S}}_\ell$ obtained by the energy method can directly be specified in the two-dimensional case, since their representation depends on the constant tensor $\boldsymbol{M}=4\pi\boldsymbol{I}$ and otherwise only on the ratio σ, that has to be specified. For the Darcy operator $\bar{\boldsymbol{D}}_{\boldsymbol{L}^{-1},\ell}$ obtained by the two-scale convergence method, however, we first need to solve d cell-problems to assemble the effective permeability tensor $\boldsymbol{L}$.

Therefore, let $\mathcal{T}_h^Y$ be a triangulation of the unit cell $Y=(0,1)^d$ such that the boundary of the obstacle is aligned with $\mathcal{T}_h^Y$. We extend the $\boldsymbol{y}$-periodic velocity and pressure fields of the cell-problems with the same Brinkman extension as formulated for the periodically perforated case in Section 5.2.

As discretization space we choose also H^{div}-conforming finite element basis functions and incorporate the periodicity of the boundary values into the discretization space which is realized by identifying opposite sides of the boundary ∂Y. The velocity and pressure

spaces are defined on Y with respect to $\mathcal{T}_h^Y$ by

$$V_h^\# = \{\boldsymbol{\varphi} \in V_h(Y) \ : \ \boldsymbol{\varphi} \text{ is } \boldsymbol{y}\text{-periodic}\},$$
$$Q_h^\# = \{q \in Q_h(Y) \ : \ q \text{ is } \boldsymbol{y}\text{-periodic}\},$$

and the discretization space is

$$X_h^\# = V_h^\# \times Q_h^\#.$$

The discrete cell-problems that need to be solved are then: for $j = 1, \dots, d$ find $(\boldsymbol{\omega}_{h,j}, \pi_{h,j}) \in X_h^\#$, such that

$$a_h(\tilde{\boldsymbol{\omega}}_{h,j}, \boldsymbol{\varphi}) + \zeta(\tilde{\boldsymbol{\omega}}_{h,j}, \boldsymbol{\varphi})_{\mathcal{O}} - b(\tilde{\pi}_h, \boldsymbol{\varphi}) - b(q, \tilde{\boldsymbol{\omega}}_{h,j}) = (\boldsymbol{e}_j, \boldsymbol{\varphi})_Y$$

for all $(\boldsymbol{\varphi}, q) \in X_h^\#$, where $a_h(\cdot,\cdot)$ and $b(\cdot,\cdot)$ are defined with respect to Y.

Following [Neu96] we solve the discrete cell-problems on a comparable mesh refinement level as in the periodically repeated setting, i.e., on the coarsest level where the geometric structure is resolved. Then the entries of the permeability tensor $\boldsymbol{L}$ are assembled as

$$\boldsymbol{L}_{ij} = \int_{\mathcal{F}} \tilde{\boldsymbol{\omega}}_{h,i}(\boldsymbol{y}) \cdot \boldsymbol{e}_j \, d\boldsymbol{y}.$$

Due to the periodicity of the problem, the solutions are defined only up to a constant, which has no influence on the permeability tensor, since the defining integral is equivalent to a formulation over the derivatives $\nabla\tilde{\boldsymbol{\omega}}_{h,i}$, see (5.16).

5.8 Numerical Tests

In this section, we test the performance of the introduced two-scale multilevel Schwarz preconditioner.

We will restrict the presentation to the case of two space dimensions and the choice of $RT_k \times Q_k$ mixed finite elements as H^{div}-conforming discretization space. Furthermore, we will only consider the multiplicative Schwarz algorithm as smoother.

To justify the effectiveness of the homogenizing two-scale multilevel Schwarz method we will compare the performance results to the standard multigrid method, where the fine-scale operator $\boldsymbol{A}_\ell^\varepsilon$ is evaluated on the coarse scale, as defined in the following. We

use a multigrid method with a quadrature rule designed such that the fine-scale structure of the domain is still resolved exactly by the integrals on the coarse-scale levels. To this end, we partition each cell $T \in \mathcal{T}_{h_\ell}$ on each coarse-scale level $\ell_0 \leq \ell \leq \ell_r - 1$ into at least $2^{d(\ell_r-\ell)}$ subcells (rectangles or hexahedra) of size h_{ℓ_r} and evaluate the coupled Stokes-Brinkman bilinearform $\tilde{\mathbb{A}}_h^\varepsilon(\cdot,\cdot)$ on each of the subcells with a Gaussian quadrature rule, such that the integration process is essentially the same as on the resolved level ℓ_r. Moreover, for ease of implementation, we divide each cell T into $2^{d(\ell_r+1)}$ subcells regardless of the level. This assures the accuracy of the integration on the coarsest level ℓ_0, since it resolves the fine-scale structure exactly and, consequently, on every other coarse-scale level, too.

Although this procedure slows down the assembly process of the code and is much more expensive than a normal multigrid algorithm would be, it preserves the information of the fine-scale structure in the integration process and therefore guarantees the performance of the standard multigrid scheme on the coarse-scale levels in terms of iteration counts of GMRES. Thus, it serves as a benchmark test for the homogenizing two-scale multilevel Schwarz methods.

The outline of the section is as follows.

In Section 5.8.1 we begin with the introduction of a geometrically simple, axisymmetric model problem on the unit cell, which is repeated over the whole domain Ω. For this geometry it is demonstrated that the solution is pushed towards zero inside the obstacle regions when the penalty factor ζ increases.

Then, in Section 5.8.2 we draw our attention to test the performance of the constructed two-scale multilevel Schwarz method with the different choices of operators on the effective coarse-scale, and test it against the standard multigrid using the fine-scale operator evaluated on the coarse scale that serves as a benchmark test. A first application of the method with the analytical coarse-scale operators does not lead to a convincing or even uniform result, and rises the question of how to choose the permeabilities optimally, which is tested in a series of test runs for various choices of the pore size ε, the penalty factor ζ, the mesh size h and the permeability tensor $\boldsymbol{K} = \kappa \boldsymbol{I}$, that is a multiple of the identity tensor in case of the axisymmetric model problem, also in the case of the Darcy operator derived by using the two-scale convergence method.

For the Brinkman operator we find in Section 5.8.3 a dependence of κ on the penalty factor ζ, whereas for the Darcy operator the performance tests do not lead to a clear view

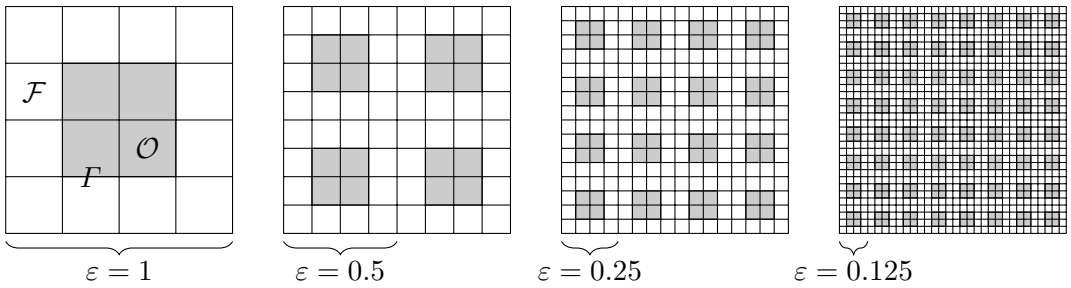

Figure 5.5: Periodic domains Ω^ε for different choices of ε.

on the dependencies. Nevertheless, we can choose an optimal κ in both cases, Brinkman as well as Darcy. As it turns out, the choice of the Brinkman operator within the two-scale multilevel Schwarz method leads to comparable performance results as the standard multigrid, when only one coarse-scale level is considered.

But with fixing the coarsest level to zero the Brinkman operator beats the standard multigrid method by yielding the best performance results, i.e., the lowest iteration counts of GMRES, as observed in Section 5.8.4.

This result is confirmed in Section 5.8.5 in a test with a more anisotropic geometry, where also another choice of $\boldsymbol{K}$ is considered, tailored to the shape and orientation of the obstacle inside the unit cell. As it turns out this method yields the best performance for small periods.

5.8.1 An Axisymmetric Model Problem

We start with the introduction of a geometrically simple model problem with an obstacle region that is completely contained within the fluid region. For this setting the assumptions on the geometry of the homogenization theory of Section 5.6 apply, and the homogenized permeability tensor is always a multiple of the identity tensor, also when calculated with the cell-problems in case of the two-scale convergence theory in Section 5.6.1.

Let the reservoir $\Omega = (0,1)^2$ be the open and bounded two-dimensional unit-square. The obstacle part $\mathcal{O}$ of the unit cell (or standard periodicity cell) $Y = (0,1)^2$ is defined as

$$\mathcal{O} = [0.25, 0.75]^2.$$

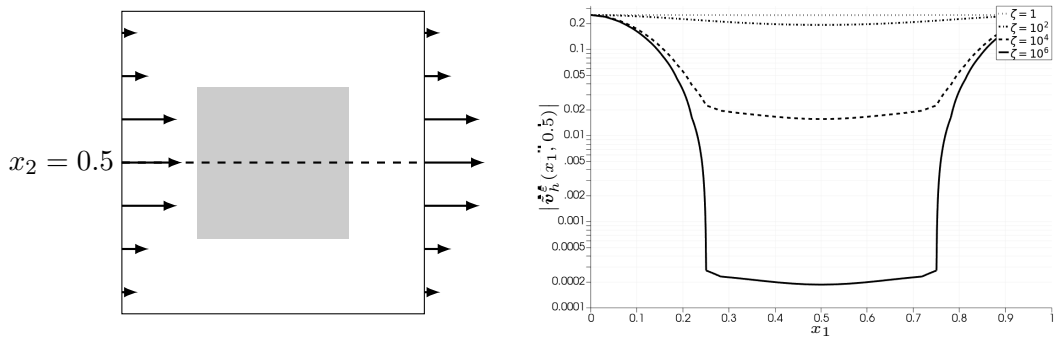

Figure 5.6: Sketch of the geometry and the flow setting of the axisymmetric model problem (left). Magnitude of the velocity for different values of the penalty constant ζ plotted logarithmically along the line $x_2 = 0.5$ (right). Samples calculated with $RT_0 \times Q_0$ on a mesh with $h = \frac{1}{32}$.

As in the construction of the geometry in Section 5.1 the periodically perforated domain Ω^ε consists of the repeated fine-scale structure determined by the definition of Y and period ε, see Figure 5.5. The calculations however are performed with the extended coupled Stokes-Brinkman problem on the whole domain Ω, where the definition of Ω^ε serves mainly the purpose of locating the obstacles inside Ω.

For the tests, the period is chosen as $\varepsilon = 2^{-r}$ with $r \in \{0, 1, 2, \ldots\}$ and the domain Ω is divided into $2^{2\ell}$ square mesh cells of size $h = 2^{-\ell}$, with the level $\ell \in \{\ell_0, \ldots, \ell_r - 1, \ell_r, \ldots, L\}$, where the coarsest and the resolved levels are given by $\ell_0 = 0$ and $\ell_r = r + 2$, respectively, compare also Figure 5.3. We consider a no-slip Dirichlet boundary condition on top and bottom, an inflow on the left, and an outflow on the right prescribed by an essential Dirichlet boundary condition on the velocity $\tilde{\boldsymbol{v}}_h^{\varepsilon}$. as visualized in the left part of Figure 5.6 for $\varepsilon = 1$. The force and the boundary condition are defined as

$$\boldsymbol{f} = \boldsymbol{0}, \qquad \boldsymbol{g} = \begin{pmatrix} x_2(1 - x_2) \\ 0 \end{pmatrix}, \tag{5.20}$$

and the fluid viscosity is set to $\nu = 1$. The test case is related to a pressure driven Poiseuille flow, assumed that there wouldn't be an obstacle.

By calculations with varying penalty factors

$$\zeta \in \left\{1, 10^2, 10^4, 10^6\right\},$$

and by observation of the magnitude of the velocity along the line $x_2 = 0.5$ we can clearly see in Figure 5.6 that the discrete velocity is pushed towards zero in the obstacle region $0.25 \leq x_1 \leq 075$ the more ζ increases. The calculations have been done using a discretization with $RT_0 \times Q_0$ finite elements to the mesh size $h = \frac{1}{32}$. Heuristically, this confirms the estimate (5.10) and validates the coupled Stokes-Brinkman model as an approximation to the periodically perforated fine-scale porous media flow equations (5.3).

5.8.2 Comparison of the Analytical Coarse-scale Operators

We now test the performance of the homogenizing two-scale multilevel Schwarz preconditioner by a comparison of the four different homogenized coarse-scale operators, as analytically derived by the homogenization theory in Section 5.6, and the resolved fine-scale operator. We will use a preconditioned GMRES to iteratively solve the linear system of equations until the starting residual has been reduced by a factor of 10^{-8}. As already mentioned, we will restrict the investigation to the case of a multiplicative Schwarz smoother $\boldsymbol{M}_{\mathrm{mu},\ell}$ and, in a first step, reduce the method to the case of only one coarse-scale level, such that we solve exactly on the finest coarse-scale level $\ell_r - 1$.

We choose the axisymmetric geometry for the standard periodicity cell Y along with the force and Dirichlet boundary condition as defined in Section 5.8.1, and test the performance of the preconditioner by counting the iterations GMRES takes to converge for different periods ε. As can be seen in Figure 5.5 the resolved level ℓ_r increases with decreasing ε, as does the coarsest level ℓ_0, since we set it as

$$\ell_0 = \ell_r - 1,$$

such that only one coarse-scale level is used. This has the advantage of minimizing the influence of the coarse-scale smoothing steps and allowing a more detailed view of the method. Furthermore, we set the penalty constant $\zeta = 10^4$. Although this choice seems arbitrary at first glance, it results in a good balance between accuracy and effort of the method, as we will see later in the discussion of this section.

As described in Section 5.7.1 we assemble the permeability tensor $\boldsymbol{L}$ of the Darcy operator $\bar{\boldsymbol{D}}_{\boldsymbol{L}^{-1},\ell}$ obtained by the two-scale convergence method by solving the two cell-problems on the unit cell on a mesh as in the left graph of Figure 5.5 for $\varepsilon = 1$ before running the calculations on the periodic domains with $\varepsilon < 1$. The inverse of the obtained permeability tensor is a multiple of the identity as expected and given by

$$\boldsymbol{L}^{-1} = 77.847\boldsymbol{I}. \tag{5.21}$$

The permeability tensor of the Darcy operator $\bar{\boldsymbol{D}}_{\boldsymbol{M},\ell}$ obtained by the energy method is given by $\boldsymbol{M} = 4\pi\boldsymbol{I}$, thus, we choose it as

$$\boldsymbol{M} = 12.566\boldsymbol{I}. \tag{5.22}$$

In case of the Brinkman operator $\bar{\boldsymbol{B}}_{\boldsymbol{M},\ell}$ the tensor $\boldsymbol{M}$ is divide by the square of the ratio $\sigma = \lim_{\varepsilon\to 0}\sigma_\varepsilon$. Since we are not in the limit case $\varepsilon \to 0$ but calculate with a fixed $\varepsilon > 0$ we decide in a first calculation to choose σ_ε^2 as defined in (5.18) instead of σ^2 to get a notion of how the method behaves for different permeabilities. This gives us for $\varepsilon_1 = \frac{1}{2}$ and $\varepsilon_2 = \frac{1}{8}$, respectively,

$$\frac{1}{\sigma_{\varepsilon_1}^2}\boldsymbol{M} = 290.071\boldsymbol{I}, \qquad \frac{1}{\sigma_{\varepsilon_2}^2}\boldsymbol{M} = 1160.280\boldsymbol{I}. \tag{5.23}$$

For the Stokes operator $\bar{\boldsymbol{S}}_\ell$ no tensor needs to be specified.

With the permeabilities as above, a first comparison of the two-scale multilevel Schwarz method is summarized in Table 5.1 with the four different homogenized operators $\bar{\boldsymbol{D}}_{\boldsymbol{L}^{-1},\ell}$, $\bar{\boldsymbol{D}}_{\boldsymbol{M},\ell}$, $\bar{\boldsymbol{B}}_{\boldsymbol{M},\ell}$, $\bar{\boldsymbol{S}}_\ell$, as well as the standard multigrid using the fine-scale operator $\boldsymbol{A}_\ell^\varepsilon$ evaluated on the coarse scale. The calculations have been done for polynomial degrees $k = 0$ and $k = 1$, with the fine-scale structure specified by $\varepsilon = \frac{1}{4}$ and $\varepsilon = \frac{1}{8}$ with corresponding resolved level $\ell_r = 4$ and $\ell_r = 5$, respectively, as well as coarse level $\ell_0 = \ell_r - 1$.

Since the resolved level grows for smaller values of ε, the coarsest level on which a resolved calculation of the porous media flow makes sense grows as well. That is why the presentation of the iteration counts always starts one level further below when decreasing ε.

For $k = 0$ the iteration counts do not really flatten out for increasing computational

		$\bar{\boldsymbol{D}}_{\boldsymbol{L}^{-1},\ell}$		$\bar{\boldsymbol{D}}_{\boldsymbol{M},\ell}$		$\bar{\boldsymbol{B}}_{\boldsymbol{M},\ell}$		$\bar{\boldsymbol{S}}_{\ell}$		$\boldsymbol{A}^{\varepsilon}_{\ell}$	
	ε	2^{-2}	2^{-3}	2^{-2}	2^{-3}	2^{-2}	2^{-3}	2^{-2}	2^{-3}	2^{-2}	2^{-3}
	ℓ_r	4	5	4	5	4	5	4	5	4	5
	ℓ_0	3	4	3	4	3	4	3	4	3	4
	$L=$										
	4	36		53		18		22		18	
	5	41	60	58	91	19	14	24	29	17	14
$k=0$	6	45	71	60	>100	22	16	27	29	20	16
	7	47	76	63	>100	25	19	30	31	24	19
	8	48	80	65	>100	27	23	32	33	28	23
	4	76		>100		20		26		15	
	5	90	>100	>100	>100	22	14	28	34	15	12
$k=1$	6	88	>100	>100	>100	22	15	28	36	15	12
	7	85	>100	>100	>100	23	16	29	37	14	13
	8	f	>100	>100	>100	22	16	28	37	14	13

Table 5.1: Iteration counts of GMRES preconditioned by the two-scale multilevel Schwarz method with analytically chosen effective tensors: Darcy with $\boldsymbol{L}^{-1}$ (1), Darcy with $\boldsymbol{M}$ (2), Brinkman (3), Stokes (4), standard multigrid (5). $\ell_0 = \ell_r - 1$, $RT_k \times Q_k$, $\zeta = 10^4$.

mesh level L for all operators, also for the resolved fine-scale operator, which is better for $k = 1$.

We observe poor convergence results for both Darcy operators $\bar{\boldsymbol{D}}_{\boldsymbol{L}^{-1},\ell}$ and $\bar{\boldsymbol{D}}_{\boldsymbol{M},\ell}$, which are especially growing with decreasing ε, and even exceed 100 iteration steps, or fail at all (marked with an f, because of failing SVD of the coarse matrix).

The Brinkman operator $\bar{\boldsymbol{B}}_{\boldsymbol{M},\ell}$ yields the best results of the homogenized operators and is equally good as $\boldsymbol{A}^{\varepsilon}_{\ell}$ when $k = 0$, but not for $k = 1$.

The results of the Stokes operator are not as poor as those of the Darcy operators, but not comparable to $\boldsymbol{A}^{\varepsilon}_{\ell}$, and for $k = 1$, even growing with decreasing ε. So far, the homogenization approach does not seem to give a remarkable improvement in any of the cases. But what needs to be noticed, is that the very different choices of the permeability tensors lead to quite different convergence results of the preconditioned GMRES method, which rises the question of how to choose the effective tensor to get the best convergence results, and finally beat the resolved fine-scale operator $\boldsymbol{A}^{\varepsilon}_{\ell}$.

5.8.3 Optimal Effective Tensors for Two-level Convergence

The different analytical approaches to homogenizing system (5.3) lead to very different performance results in the practical application of the two-scale multilevel Schwarz method. Moreover, the effective tensor varies widely, as observed in the last section. This raises the question of how to choose the effective tensor in Darcy's law or the Brinkman equations optimally with respect to the performance of the preconditioned GMRES method, i.e., such that GMRES requires the least number of iterations to converge.

Therefore, let $\boldsymbol{K}$ be the effective tensor of the homogenized equations for the model problem with geometric structure as specified in Figure 5.5, either regarding Darcy or Brinkman. Since the geometry of Y is axisymmetric, the effective tensor is a multiple of the identity, i.e.,

$$\boldsymbol{K} = \kappa \boldsymbol{I},$$

for some scalar value $\kappa > 0$, compare (5.21), (5.22) and (5.23).

By scanning the parameter spaces we test the dependencies of κ with respect to the penalty factor ζ and to the geometry of the reservoir measured by the pore size ε for the axisymmetric test case.

As it turns out, we find a linear dependence of κ on ζ in case of the Brinkman operator. The parameter study is accomplished for polynomial degree $k = 0$ and a two-scale two-level method to reduce its cost. The results are then confirmed in another more specific series of calculations for $k = 1$, as well as for different mesh refinement levels to exclude dependencies on the polynomial degree k or the mesh size h. In Section 5.8.5 the choice of $\boldsymbol{K}$ is also discussed for another geometric setting of Y.

We start with the parameter study for $k = 0$ using a two-scale two-level Schwarz preconditioner and count the iterations GMRES takes to converge for different values of κ as ζ is varied and ε decreases. We choose $L = \ell_r$ as the computational level and $\ell_0 = \ell_r - 1$ as the coarse-scale level.

The results for the Brinkman operator are shown in Table 5.2 and for the Darcy operator in Table 5.3. Here, all values that are close to the minimum are printed in bold and the proposed law is highlighted by a frame. We see that both methods become more and more sensitive to variations in κ the more ε decreases. But the iteration counts are not dependent on ε for an optimal choice of κ, what is expected, since the operators

	ζ κ	1	10	10^2	10^3	10^4	10^5	10^6
$\varepsilon = \frac{1}{2}$	1	**10**	**10**	**9**	13	14	14	15
	10	**10**	**10**	**9**	13	14	14	15
	10^2	**10**	**10**	**9**	13	14	14	15
	10^3	11	11	**9**	12	13	14	14
	10^4	15	15	**13**	**12**	**13**	14	14
	10^5	18	18	18	**16**	**15**	**15**	**16**
	10^6	22	22	22	21	19	**17**	**18**
$\varepsilon = \frac{1}{4}$	1	**12**	**12**	**13**	23	40	45	47
	10	**12**	**12**	**13**	23	40	45	47
	10^2	**12**	**12**	**12**	22	38	44	45
	10^3	15	15	**13**	16	31	36	37
	10^4	22	22	21	**16**	23	32	33
	10^5	33	33	31	**23**	**23**	29	33
	10^6	68	68	67	62	34	**30**	35
$\varepsilon = \frac{1}{8}$	1	**12**	**12**	14	25	64	>100	>100
	10	**12**	**12**	14	24	63	>100	>100
	10^2	**12**	**12**	**13**	23	60	>100	>100
	10^3	16	15	**13**	17	44	95	>100
	10^4	29	28	26	**15**	23	55	76
	10^5	43	43	40	27	**22**	35	61
	10^6	95	95	91	65	**33**	**34**	50
$\varepsilon = \frac{1}{16}$	1	**12**	**12**	14	25	61	>100	>100
	10	**12**	**12**	14	25	61	>100	>100
	10^2	**12**	**12**	**13**	24	58	>100	>100
	10^3	16	15	**13**	18	41	>100	>100
	10^4	31	30	28	**15**	20	60	>100
	10^5	55	55	52	34	**17**	30	86
	10^6	86	86	83	61	29	**27**	51
$\varepsilon = \frac{1}{32}$	1	**12**	**12**	14	26	61	>100	>100
	10	**12**	**12**	14	26	60	>100	>100
	10^2	**12**	**12**	**13**	25	59	>100	>100
	10^3	15	15	**13**	18	44	>100	>100
	10^4	31	31	28	**15**	21	59	59
	10^5	65	65	63	43	**15**	23	23
	10^6	>100	>100	>100	77	31	**21**	**21**

Table 5.2: Parameter study for Brinkman operator. Iteration counts of two-scale two-level preconditioner on computational level $L = \ell_r$ and coarse grid level $\ell_0 = \ell_r - 1$. $RT_0 \times Q_0$.

	ζ κ	1	10	10^2	10^3	10^4	10^5	10^6
$\varepsilon = \frac{1}{2}$	1	16	16	**11**	13	14	14	15
	10	16	16	**11**	**12**	14	14	15
	10^2	15	15	**11**	13	14	14	14
	10^3	15	15	**13**	**12**	**13**	14	14
	10^4	16	16	15	**12**	**13**	14	14
	10^5	20	20	19	17	**15**	**15**	**16**
	10^6	22	22	22	21	19	**17**	**17**
$\varepsilon = \frac{1}{4}$	1	51	40	**23**	**23**	40	45	47
	10	51	40	**23**	**22**	40	45	46
	10^2	50	39	**22**	**21**	38	44	45
	10^3	51	42	25	**15**	31	36	37
	10^4	56	54	33	**16**	23	32	33
	10^5	61	60	50	**24**	**23**	29	33
	10^6	79	78	78	64	34	**30**	36
$\varepsilon = \frac{1}{8}$	1	99	79	44	**32**	63	>100	>100
	10	98	79	44	**32**	62	>100	>100
	10^2	97	77	43	**31**	59	>100	>100
	10^3	92	73	44	**23**	44	95	>100
	10^4	>100	94	55	**21**	**23**	55	76
	10^5	>100	>100	80	32	**21**	35	61
	10^6	>100	>100	>100	>100	**35**	**34**	49
$\varepsilon = \frac{1}{16}$	1	>100	>100	85	**57**	66	>100	>100
	10	>100	>100	85	**57**	65	>100	>100
	10^2	>100	>100	84	**55**	63	>100	>100
	10^3	>100	>100	79	**42**	45	>100	>100
	10^4	>100	>100	76	33	**23**	60	>100
	10^5	>100	>100	>100	51	**19**	30	86
	10^6	>100	>100	>100	78	33	**27**	51
$\varepsilon = \frac{1}{32}$	1	>100	>100	>100	>100	f	f	>100
	10	>100	>100	>100	>100	f	f	>100
	10^2	>100	>100	>100	>100	f	f	>100
	10^3	>100	>100	>100	82	f	f	>100
	10^4	>100	>100	>100	58	f	f	>100
	10^5	>100	>100	>100	70	f	f	80
	10^6	>100	>100	>100	>100	f	f	43

Table 5.3: Parameter study for Darcy operator. Iteration counts of two-scale two-level preconditioner on computational level $L = \ell_r$ and coarse grid level $\ell_0 = \ell_r - 1$. $RT_0 \times Q_0$.

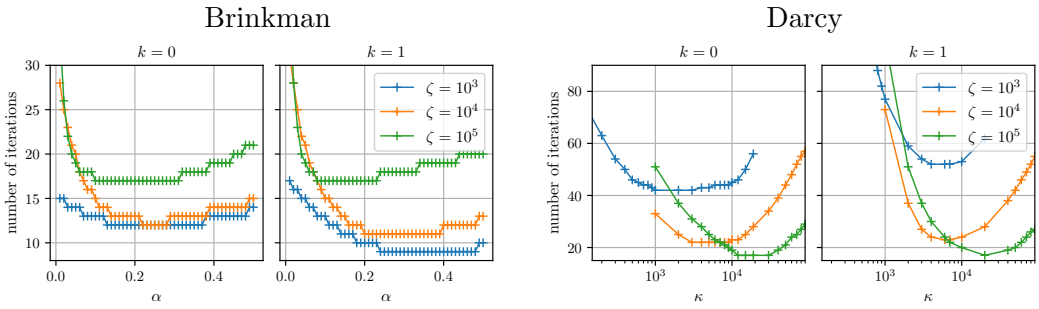

Figure 5.7: Refined parameter study for Brinkman operator with $\kappa = \alpha\zeta$ (left), and Darcy operator with $\kappa = \beta \cdot 10^3$ (right). $RT_k \times Q_k$, $\varepsilon = \frac{1}{16}$.

represent the effective behavior of the oscillating equations.

When Brinkman is chosen as coarse-scale operator, the results in Table 5.2 suggest a linear dependence of κ on ζ as by

$$\kappa(\zeta) = \alpha\zeta$$

with a constant $\alpha \approx 0.1$ to get optimal iteration counts. A refined series of calculations for $\varepsilon = \frac{1}{16}$ and $\zeta \in \{10^3, 10^4, 10^5\}$ yields $0.22 \leq \alpha \leq 0.28$ in the case of $RT_0 \times Q_0$ finite elements, see the left plot in Figure 5.7.

Another calculation with $RT_1 \times Q_1$ in Figure 5.7 confirms this observation also for polynomial degree $k = 1$. Here, we observe optimal iteration counts when α lies in the intervals $[0.24, 0.4]$ for $\zeta = 10^3$, $[0.2, 0.39]$ for $\zeta = 10^4$ and $[0.08, 0.23]$ for $\zeta = 10^5$.

To obtain the best choice for all considered values of ζ, we set $\alpha = 0.235$.

Darcy as coarse scale operator, on the other hand, appears to produce optimal iteration counts, when κ is roughly between 10^3 and 10^4 for $\zeta \leq 10^4$, with a shift to the range between 10^4 and 10^6, when $\zeta \geq 10^5$. A linear dependence of κ on ζ as for the Brinkman operator cannot be assumed. The Darcy operator is much more sensitive to variations in κ than Brinkman and relies on a correct choice of κ, especially for small ε-values.

We also encountered the case where LAPACK failed to produce the SVD of the coarse matrix, which is marked by an f in Table 5.3. In particular, with a further refinement of the periodic structure by choosing $\varepsilon = \frac{1}{32}$ the computation of the SVD of the coarse matrix failed in the range in focus, so that neither the hypothesis $10^3 \leq \kappa \leq 10^4$ can be validated for large $\zeta \geq 10^5$, nor a dependence of κ on ζ can be excluded. Nevertheless, we can

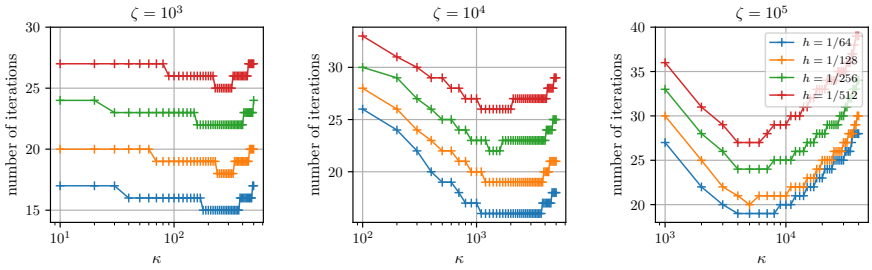

Figure 5.8: Independence of optimal κ on mesh size h for Brinkman operator. $RT_0 \times Q_0$, $\varepsilon = \frac{1}{8}$.

determine an optimal κ for fixed ζ in a refined series of calculations. For $RT_0 \times Q_0$ elements this yields optimal values of κ in the intervals $[10^3, 3 \cdot 10^3]$ for $\zeta = 10^3$, $[3 \cdot 10^3, 9 \cdot 10^3]$ for $\zeta = 10^4$, and $[1.2 \cdot 10^4, 2 \cdot 10^4]$ for $\zeta = 10^5$. Calculations with $RT_1 \times Q_1$ elements affirm this outcome for each ζ by observing the lowest iteration counts for values of κ in $[4 \cdot 10^3, 7 \cdot 10^3]$ for $\zeta = 10^3$, $[6 \cdot 10^3, 7 \cdot 10^3]$ for $\zeta = 10^4$, and $\kappa = 2 \cdot 10^4$ for $\zeta = 10^5$, see the right two plots in Figure 5.7.

The optimal choice of κ is not dependent on the mesh size h, as we can observe in another series of calculations for different mesh sizes to each $\zeta \in \{10^3, 10^4, 10^5\}$ visualized in Figure 5.8. The lowest iteration counts are always measured at the same κ, regardless of the choice of h. Only for $\zeta = 10^4$ do we see slight deviations from the optimum with a slight shift to smaller values of κ when $h \leq \frac{1}{256}$. However, since the values vary by only one iteration, this is within an acceptable tolerance in terms of performance of the method. Another observation in Figure 5.8 is that the optimal κ for $\zeta = 10^5$ differs from the calculated optimum 0.235 for $\zeta \leq 10^4$ and has a value of approximately 0.05. In the case $k = 1$ and $\varepsilon = \frac{1}{16}$ we already have seen this slight deviation to a smaller α, but there less sensitive to variations in κ, see the second left graph in Figure 5.7.

Recalculating Table 5.1 with the optimal permeabilities chosen as

$$\boldsymbol{M} = 0.235\zeta \boldsymbol{I} \tag{5.24}$$

for the Brinkman operator, and

$$\boldsymbol{M} = 6 \cdot 10^3 \boldsymbol{I}$$

		$\bar{\boldsymbol{D}}^*_{\boldsymbol{M},\ell}$			$\bar{\boldsymbol{B}}^*_{\boldsymbol{M},\ell}$			$\boldsymbol{A}^\varepsilon_\ell$		
	ε	2^{-2}	2^{-3}	2^{-4}	2^{-2}	2^{-3}	2^{-4}	2^{-2}	2^{-3}	2^{-4}
	ℓ_r	4	5	6	4	5	6	4	5	6
	ℓ_0	3	4	5	3	4	5	3	4	5
	$L=$									
	4	21			17			18		
	5	22	18		17	13		17	14	
$k=0$	6	24	20	22	19	16	12	20	16	12
	7	28	23	24	23	19	15	24	19	15
	8	33	27	28	27	23	19	28	23	19
	4	21			17			15		
	5	22	18		17	14		15	12	
$k=1$	6	22	18	23	18	14	11	15	12	10
	7	21	17	21	17	14	11	14	13	11
	8	20	17	20	16	14	12	14	13	12

Table 5.4: Iteration counts of GMRES preconditioned by the two-scale multilevel Schwarz method with optimized effective tensor for Darcy (left) and Brinkman (middle); standard multigrid (right). Coarsest level $\ell_0 = \ell_r - 1$. $RT_k \times Q_k$, $\zeta = 10^4$.

for the Darcy operator, leads to the improved results as shown in Table 5.4. The Darcy operator with optimal permeability performs much better than before and even shows lower iteration numbers than the Stokes operator, compare Table 5.1. In particular now it remains constant for $k = 1$ as ε decreases. Nevertheless, the Darcy and Stokes operators do not capture the oscillations of the residual at the coarse scale as well as the Brinkman or the resolved fine-scale operator, both of which show fewer iteration counts. Specifically, the performance of the optimized Brinkman operator $\bar{\boldsymbol{B}}_{\boldsymbol{M},\ell}$ is competitive with the benchmark test with $\boldsymbol{A}^\varepsilon_\ell$, showing broadly the same convergence results.

5.8.4 Two-scale Multilevel Schwarz with Optimized Effective Tensor

The results from the last section are promising with respect to the Brinkman operator compared to the resolved fine-scale operator, and we are going to test the behavior of both when applied to the actually intended case when the coarsest level of the multilevel algorithm is fixed to zero, instead of growing alongside the refinement of the periodic structure. Since the Darcy operators $\bar{\boldsymbol{D}}_{\boldsymbol{L}^{-1},\ell}$ and $\bar{\boldsymbol{D}}_{\boldsymbol{M},\ell}$, as well as the Stokes operator

	$\bar{\boldsymbol{B}}^*_{\boldsymbol{M},\ell}$				$\boldsymbol{A}^\varepsilon_\ell$			
ε	2^{-2}	2^{-3}	2^{-4}	2^{-5}	2^{-2}	2^{-3}	2^{-4}	2^{-5}
ℓ_r	4	5	6	7	4	5	6	7
$L=$								
4	17				15			
5	17	14			15	18		
6	18	14	11		15	18	22	
7	17	14	12	10	15	19	22	19
8	16	14	12	11	14	19	23	20

Table 5.5: Comparison of homogenizing two-scale multilevel Schwarz method with optimally chosen Brinkman operator (left) and standard multigrid (right), when coarse level $\ell_0 = 0$. $RT_1 \times Q_1$, $\zeta = 10^4$.

$\bar{\boldsymbol{S}}_\ell$ did not perform as well as the Brinkman operator $\bar{\boldsymbol{B}}_{\boldsymbol{M},\ell}$, we focus on the latter only, and restrict the presentation to the polynomial degree $k = 1$.

The results of the comparison of $\bar{\boldsymbol{B}}_{\boldsymbol{M},\ell}$ with optimally chosen permeability tensor as in (5.24), and $\boldsymbol{A}^\varepsilon_\ell$ for the case $\ell_0 = 0$ are given in Table 5.5. The Brinkman operator performs exactly the same as when applied on one coarse-scale level only, but the performance of the resolved fine-scale operator deteriorates. Whereas the iteration counts slightly decrease for smaller periods ε when $\bar{\boldsymbol{B}}_{\boldsymbol{M},\ell}$ is chosen, the numbers for $\boldsymbol{A}^\varepsilon_\ell$ rather grow, leading to approximately half of the iteration counts of the Brinkman operator compared to the benchmark test with the resolved fine-scale operator for $\varepsilon \leq 2^{-4}$.

5.8.5 Anisotropic Permeability

Finally, we want to test the performance of the two-scale multilevel Schwarz preconditioner with the Brinkman operator in a less simple setting. Therefore, we change the geometry of the unit cell as specified in Figure 5.9, such that the resulting effective tensor will not be isotropic anymore. For the performance tests, we again choose the force to be zero and a Dirichlet boundary condition as in (5.20) with an inflow on the left, an outflow on the right and a no-slip condition on top and bottom. Furthermore, we choose the penalty factor as $\zeta = 10^4$ and set the coarsest level to $\ell_0 = 0$.

In addition to the Brinkman operator $\bar{\boldsymbol{B}}^*_{\boldsymbol{M},\ell}$, that is designed and optimized with respect to the axisymmetric geometry, we introduce another Brinkman operator $\bar{\boldsymbol{B}}^*_{\boldsymbol{L}^{-1},\ell}$, where the effective tensor is derived via solving the unit cell problems so that it is rotated

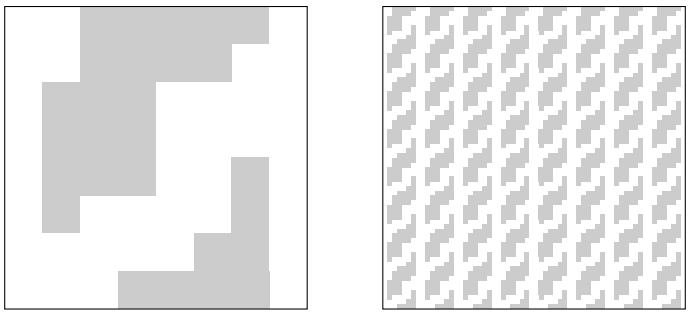

Y $\quad$ Ω^ε for $\varepsilon = \frac{1}{8}$

Figure 5.9: Geometry of unit cell Y and periodically perforated domain Ω^ε for anisotropic test case.

and scaled according to the orientation of the obstacles in the anisotropic example. To accomplish this approach, we solve the cell problems (5.17) as in the derivation of Darcy's law (via the two-scale convergence method) on the unit cell at the coarsest resolved level ℓ_r to obtain

$$\boldsymbol{L}^{-1} = \begin{pmatrix} 831.763 & -219.616 \\ -219.616 & 279.386 \end{pmatrix},$$

and adjust $\boldsymbol{L}^{-1}$ with a scaling factor α, obtained by scanning the parameter space as in Section 5.8.3. The best choice of α for the case $\zeta = 10^4$ lies in the interval $[13, 14]$, see Figure 5.10. Thus, we set $\alpha = 14$ and assemble the Brinkman equations on the coarse scale with the resulting effective tensor

$$\boldsymbol{K} = \alpha \boldsymbol{L}^{-1}.$$

In Table 5.6 we test both two-scale multilevel Schwarz methods, regarding $\bar{\boldsymbol{B}}^*_{\boldsymbol{M},\ell}$ and $\bar{\boldsymbol{B}}^*_{\boldsymbol{L}^{-1},\ell}$, as well as the standard multigrid method with respect to the anisotropic geometry. First, by a comparison of the results in Tables 5.6 and 5.5, we notice that the anisotropic geometry has an effect on the performance of the two-scale multilevel Schwarz method with the Brinkman operator $\bar{\boldsymbol{B}}^*_{\boldsymbol{M},\ell}$, as for the standard multigrid method. When using $\bar{\boldsymbol{B}}^*_{\boldsymbol{M},\ell}$, the iteration counts in the anisotropic test case are slightly greater than for the axisymmetric geometry. Still, for $\bar{\boldsymbol{B}}^*_{\boldsymbol{M},\ell}$ the numbers flatten out with decreasing period.

The standard multigrid performs slightly better for larger values of $\varepsilon \geq 2^{-4}$ in the

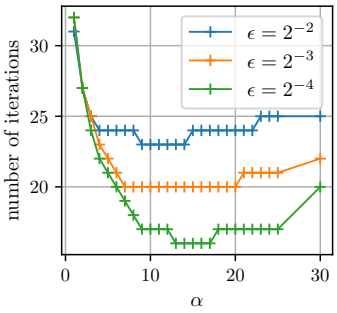

Figure 5.10: Anisotropic geometry. Optimal α for Brinkman operator with $\boldsymbol{K} = \alpha \boldsymbol{L}^{-1}$. $RT_1 \times Q_1$, $\zeta = 10^4$.

	$\bar{\boldsymbol{B}}^*_{\boldsymbol{M},\ell}$				$\boldsymbol{A}^{\varepsilon}_{\ell}$				$\bar{\boldsymbol{B}}^*_{\boldsymbol{L}^{-1},\ell}$			
ε	2^{-2}	2^{-3}	2^{-4}	2^{-5}	2^{-2}	2^{-3}	2^{-4}	2^{-5}	2^{-2}	2^{-3}	2^{-4}	2^{-5}
ℓ_r	4	5	6	7	4	5	6	7	4	5	6	7
$L =$												
5	21				12				23			
6	21	17			12	14			23	20		
7	20	17	15		13	15	17		22	19	16	
8	20	17	15	15	13	15	17	21	21	18	16	14

Table 5.6: Anisotropic case. Comparison of standard multigrid ($\boldsymbol{A}^{\varepsilon}_{\ell}$), two-scale multilevel Schwarz with operator optimized for axisymmetric test case ($\bar{\boldsymbol{B}}^*_{\boldsymbol{M},\ell}$), and two-scale multilevel Schwarz with operator optimized for anisotropic geometry ($\bar{\boldsymbol{B}}^*_{\boldsymbol{L}^{-1},\ell}$). $\ell_0 = 0$, $RT_1 \times Q_1$, $\zeta = 10^4$.

anisotropic test, but for decreasing ε, which is the intended situation, the numbers are growing and we see better test results for the two-scale multilevel Schwarz method with $\bar{\boldsymbol{B}}^*_{\boldsymbol{M},\ell}$ as operator.

Now, turning our attention to the two-scale multilevel Schwarz method with the newly introduced Brinkman operator $\bar{\boldsymbol{B}}^*_{\boldsymbol{L}^{-1},\ell}$ that is designed and optimized with respect to the non-symmetric geometry, we see, that it nearly performs the same as $\bar{\boldsymbol{B}}^*_{\boldsymbol{M},\ell}$ with about 1 iteration more for $\varepsilon \geq 2^{-4}$. But, for a smaller period $\bar{\boldsymbol{B}}^*_{\boldsymbol{L}^{-1},\ell}$ this method shows the best performance in this last test setting with only 14 iterations, which is slightly better than the 15 iterations of the Brinkman operator with $\bar{\boldsymbol{B}}^*_{\boldsymbol{M},\ell}$.

5.9 Conclusion

In this chapter we have developed and applied an efficient and performant two-scale multilevel Schwarz preconditioner to an H^{div}-conforming discretization of a coupled Stokes-Brinkman model that approximates the resolved flow of a fluid through a pore-system of periodically repeated perforated cells at pore-scale. The provided method develops the ideas in [Neu96] for diffusion problems and extends it to the case of a resolved Stokes flow in perforated domains. Different homogenized coarse-scale operators, known from the literature, have been compared to the standard multigrid preconditioner with respect to the convergence speed of GMRES preconditioned by the homogenizing two-scale multilevel Schwarz method. It was found that the performance of the analytical homogenized coarse grid operators is non-optimal when used within the two-scale multilevel Schwarz method. However, an optimization of the effective tensor with respect to the iteration counts of GMRES yields an excellent performance of the method, where the Brinkman operator appears to be the best choice regarding the pore size and the mesh size under consideration.

Chapter 6

Outlook and Summary

I conclude this thesis with an outlook on solving pore-scale computations of flow and deformation in nonlinear poroelastic media. In addition, the performance of the Schwarz method is discussed when interface conditions are imposed inside the domain.

In Section 6.1, a two-scale multilevel Schwarz preconditioner is considered for a nonlinear fluid-structure interaction problem on periodic domains that utilizes a homogenized model of linear poroelasticity as coarse-scale operator within a Newton method.

Section 6.2 briefly discusses the imposition of strong or weak interface conditions inside the domain to extend a physical phase accurately to an extended (virtual) region. We provide examples for Stokes flow, linear elasticity, and a fluid-structure interaction problem, and demonstrate that overlapping two-level Schwarz methods cannot be applied out of the box to these kinds of problems, which makes a more in-depth investigation of the Schwarz preconditioner necessary.

Finally, this thesis is briefly summarized in Section 6.3.

6.1 Two-scale Multilevel Schwarz Preconditioner for High-resolution FSI Problems in Poroelasticity

As model we assume a FSI (fluid-structure interaction) problem in an ALE (arbitrary Lagrangian-Eulerian) framework of a coupled laminar Stokes flow and an elastic solid body that allows for nonlinear deformations described by a St. Venant-Kirchhoff material law.

Let the open and bounded, three-dimensional computational domain

$$\Omega = \Omega_f \cup \Gamma \cup \Omega_s$$

consist of a connected fluid part Ω_f, a connected solid matrix Ω_s and an interface Γ,

arranged by periodically repeated microcells $Y_i^\varepsilon = (0,\varepsilon)^3$ of size ε, such that

$$\Omega = \bigcup Y_i^\varepsilon.$$

Each microcell is the image of a scaled and shifted standard periodicity cell $Y = (0,1)^3$ consisting of an open and bounded fluid domain Y_f and an open and bounded solid matrix Y_s, such that

$$Y = Y_f \cup \Gamma_Y \cup Y_s,$$

where Γ_Y is the interface between Y_f and Y_s. Let $\boldsymbol{u}$ denote the solid displacement, p the fluid pressure in the system, and $\boldsymbol{w} = \boldsymbol{v} - \partial_t \boldsymbol{u}$ the relative velocity where $\boldsymbol{v}$ is the seepage velocity of the fluid. Furthermore, the deformation gradient $\boldsymbol{F}$ and its determinant J are defined by

$$\boldsymbol{F} = \boldsymbol{I} + \nabla \boldsymbol{u}, \qquad J = \det(\boldsymbol{F}).$$

$\boldsymbol{F}$ describes the local change of relative position under deformation and J denotes the local change of volume at a given time t, cf. [Ric17, Chapter 2].

The ALE formulation of the fluid-structure interaction problem we focus on is given in dimensionless form by

$$\begin{aligned} -\operatorname{div}\left(\boldsymbol{F}\left(\lambda \operatorname{tr}(\boldsymbol{\varepsilon}(\boldsymbol{u}))\boldsymbol{I} + 2\mu\boldsymbol{\varepsilon}(\boldsymbol{u})\right)\right) &= \boldsymbol{f}_s && \text{in } \Omega_s, \\ -\operatorname{div}\Big(\varepsilon^2 J\Big(\nabla\left(\boldsymbol{w} + \eta\partial_t\boldsymbol{u}\right)\boldsymbol{F}^{-1} + \left(\nabla\left(\boldsymbol{w} + \eta\partial_t\boldsymbol{u}\right)\boldsymbol{F}^{-1}\right)^T\Big)\boldsymbol{F}^{-T} & \\ -Jp\boldsymbol{F}^{-T}\Big) &= J\boldsymbol{f}_f && \text{in } \Omega_f, \\ \operatorname{div}\left(J\boldsymbol{F}^{-1}\left(\boldsymbol{w} + \eta\partial_t\boldsymbol{u}\right)\right) &= 0 && \text{in } \Omega_f, \end{aligned} \tag{6.1}$$

where the strain $\boldsymbol{\varepsilon}(\boldsymbol{u}) = \frac{1}{2}\left(\nabla\boldsymbol{u} + \nabla\boldsymbol{u}^T\right)$ is the symmetric gradient and $\boldsymbol{f}_s$ and $\boldsymbol{f}_f$ are given forces acting on the solid and fluid domain, respectively. Furthermore, λ and μ denote the Lamé constants of elasticity and $\eta = \frac{T_T}{T_c}$ is the ratio of the so-called Terzaghi time $T_T = \frac{\nu}{\Lambda\varepsilon^2}$ and the characteristic time T_c, for given fluid viscosity ν and characteristic Young's modulus Λ.

Additionally, a no-slip condition for the relative velocity and equivalence of the normal

stresses are prescribed on the interface Γ, i.e.,

$$\boldsymbol{w} = 0 \quad \text{on } \Gamma, \qquad \boldsymbol{\sigma}_s \boldsymbol{n} = \boldsymbol{\sigma}_f \boldsymbol{n} \quad \text{on } \Gamma,$$

where the solid and fluid stress fields are defined by

$$\begin{aligned}
\boldsymbol{\sigma}_s &= \boldsymbol{F}\left(\lambda \operatorname{tr}(\boldsymbol{\varepsilon}(\boldsymbol{u}))\boldsymbol{I} + 2\mu\boldsymbol{\varepsilon}(\boldsymbol{u})\right), \\
\boldsymbol{\sigma}_f &= \varepsilon^2 J \left(\nabla\left(\boldsymbol{w} + \eta\partial_t \boldsymbol{u}\right)\boldsymbol{F}^{-1} + \left(\nabla\left(\boldsymbol{w} + \eta\partial_t \boldsymbol{u}\right)\boldsymbol{F}^{-1}\right)^T\right)\boldsymbol{F}^{-T} - Jp\boldsymbol{F}^{-T}.
\end{aligned}$$

Moreover, boundary conditions are prescribed on $\partial\Omega$ to close the system.

6.1.1 Towards Highly Resolved Poroelastic Media Computations

In the case of small deformations of the solid body, and even up to order ε, the homogenization of the fluid-structure interaction problem leads to Biot's linear consolidation model, even when the elastic solid deformation is assumed to obey the nonlinear St. Venant-Kirchhoff material law. When solving the discrete system with Newton's method, a linearized problem needs to be solved algebraically, which is typically done by the application of an iterative Krylov-subspace method as GMRES. This makes the use of an effective preconditioner necessary.

As we have seen in Chapter 5, a two-scale multilevel Schwarz method with a homogenized operator on the coarse scale is promising. Thus, the idea of solving highly resolved models of poroelastic media is as follows:

1. Formulation of the microscopic nonlinear fluid-structure interaction problem in ALE coordinates on a domain with periodically repeated elastic obstacles as in (6.1).
2. Extension of the variables to the whole domain alongside Chapter 5 with a Brinkman model for the fluid velocity.
3. Discretization of the whole system with an H^{div}-conforming finite element method.
4. Iterative solution of the nonlinear equations with Newton's method.
5. Preconditioning of the linearized equations inside Newton with a two-scale multilevel Schwarz method using either Biot's consolidation model as coarse-scale operator, or the Biot-Brinkman equations, with optimized effective parameters.

In view of the results of Chapter 5, an optimized Biot-Brinkman model has the best chances of yielding an effective preconditioner. We note, that even though system (6.1) is nonlinear the application of Newton's method leads to a linear system that needs to be solved, which is expected to be similar to Biot's consolidation model at least for deformations up to order ε.

This argumentation is due to the application of the two-scale convergence method to system (6.1) that we will not examine here, but briefly explain some of the details. With the assumption that the deformation gradient remains small (up to order ε), the formal two-scale expansion yields Biot's linear consolidation model. Without smallness assumption on the deformation, a two-scale expansion of system (6.1) leads to a large system with several unknowns that depend on both scales, the macroscopic and the microscopic scale. The missing scale-separation in this case makes it necessary to resolve the heterogeneous structure, cf. [MB07].

6.2 Extensions to Virtual Regions

Instead of extending the physical phases with a Brinkman law, one could also follow another monolithic approach by using the same laws in the extended regions as in the physical domain and prescribe interface conditions on Γ directly via constraining the corresponding degrees of freedom that are located at the interface. This leads to problems when the multilevel Schwarz methods are applied out of the box and makes a further in-depth investigation of the method necessary. Nevertheless, we will outline the approach in the following concluding section for a steady Stokes flow in Section 6.2.1, linear elasticity in Section 6.2.2, and a simplified fluid-structure interaction problem in Section 6.2.3, and demonstrate the performance of the multiplicative two-level Schwarz method in Section 6.2.4.

To extend a given physical phase like a fluid velocity or solid displacement stated in a domain $\mathcal{D} \subset \Omega$ to the whole computational domain Ω we introduce so-called virtual regions $\mathcal{D}_{\text{virtual}} = \Omega \setminus \mathcal{D}$, with $\mathcal{D} \cap \mathcal{D}_{\text{virtual}} = \emptyset$. These regions are meant to be parts of Ω, where we prescribe the same physical equations, but decouple it from the physically meaningful part of the domain $\mathcal{D}$ such that the boundary condition on the interface is met and the phase in the extended region $\mathcal{D}_{\text{virtual}} \subset \Omega$ will not have any physical influence to the phase in $\mathcal{D}$. We realize this by prescribing interface conditions tailored to the needs of the specific equations and choosing the discretization spaces accordingly.

6.2.1 Stokes Flow

First, we assume a Stokes fluid flowing against non-elastic obstacles without interaction between the fluid and solid phase, where the obstacles are aligned with the computational grid. On the interface Γ between the fluid domain $\mathcal{F}$ and the obstacle domain $\mathcal{O}$ we assume a no-slip boundary condition of the fluid. For a sketch of a possible configuration of the domain see Figure 6.1. In strong form we have Stokes flow given by

$$\begin{aligned} -\Delta \boldsymbol{v} + \nabla p &= \boldsymbol{f} && \text{in } \mathcal{F}, \\ \operatorname{div} \boldsymbol{v} &= 0 && \text{in } \mathcal{F}, \end{aligned}$$

complemented by a Dirichlet boundary condition $\boldsymbol{g}$ prescribed on $\partial\Omega$. The solution is defined up to an additive constant, which is determined by the constraint

$$\int_{\mathcal{F}} p \, dx = 0.$$

The fluid velocity $\boldsymbol{v}$ is then extended by $\mathbf{0}$ to the obstacles $\mathcal{O}$ by choosing the same equations, i.e., Stokes flow, but with a no-slip interface and boundary condition

$$\begin{aligned} -\Delta \boldsymbol{v} + \nabla p &= \mathbf{0} && \text{in } \mathcal{O}, \\ \operatorname{div} \boldsymbol{v} &= 0 && \text{in } \mathcal{O}, \\ \boldsymbol{v} &= \mathbf{0} && \text{on } \Gamma \cup \partial\mathcal{O}. \end{aligned}$$

As discretization we choose an inf-sup-stable finite element pair such as Taylor-Hood $S_k \times S_{k-1}$, or the H^{div}-conforming pair $RT_k \times Q_k$. In the latter, we have to use an interior penalty discontinuous Galerkin formulation to discretize the Laplacian as in (4.5). With both discretizations we incorporate the zero boundary values directly into the system matrix by constraining those degrees of freedom that lie on the interface Γ. To give an example, consider a configuration of the domain $\Omega = \mathcal{F} \cup \mathcal{O}$, consisting of a fluid region $\mathcal{F}$, where we aim to solve a system of equations, and an extended region $\mathcal{O}$. For ease of explanation we consider the continuous finite element space S_1 of piecewise linear polynomials in a configuration with only two cells, where the degrees of freedom are distributed as in Figure 6.2. When the system gets assembled, each degree of freedom that lies on the interface Γ gets constrained to zero. This is achieved as with a normal Dirichlet boundary condition by setting the whole row to zero except for the diagonal

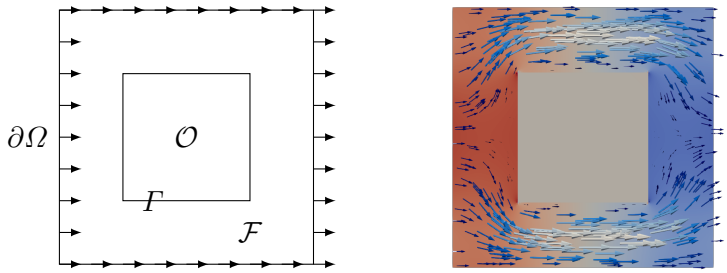

Figure 6.1: Stokes flow against inelastic obstacle with extension to virtual region, discretized with $RT_2 \times Q_2$ finite elements.

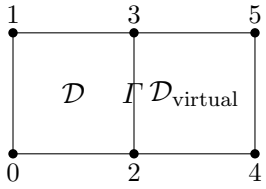

Figure 6.2: Degrees of freedom on computational domain $\mathcal{D}$ and extended virtual region $\mathcal{D}_{\text{virtual}}$ with interface Γ.

entry, which is set to one. The resulting system then is

$$\begin{pmatrix} * & * & & & & \\ * & * & & & & \\ & & 1 & & & \\ & & & 1 & & \\ & & & & * & * \\ & & & & * & * \end{pmatrix} \begin{pmatrix} x_0 \\ x_1 \\ x_2 \\ x_3 \\ x_4 \\ x_5 \end{pmatrix} = \begin{pmatrix} f_0 \\ f_1 \\ 0 \\ 0 \\ f_4 \\ f_5 \end{pmatrix}.$$

In the H^{div}-conforming case, we additionally have to decouple the interior face terms that lie on Γ. This is achieved by choosing boundary terms for $\Gamma_{\mathcal{F}} = \partial\mathcal{F} \cap \Gamma$, as well as for $\Gamma_{\mathcal{O}} = \partial\mathcal{O} \cap \Gamma$ instead of the usual jump terms on faces on Γ. For an improved readability we introduce bilinear forms $a^f_{h,\Gamma}(\cdot,\cdot)$ and $a^b_{h,\Gamma}(\cdot,\cdot)$ that define the face terms

and the boundary terms of $a_h(\cdot,\cdot)$, respectively, on a given set S by

$$\begin{aligned} a^f_{h,S}(\boldsymbol{v}_h,\boldsymbol{\varphi}) &= \sum_{F\in S}\frac{\eta_a}{h}\big([\![\boldsymbol{v}_h]\!],[\![\boldsymbol{\varphi}]\!]\big)_F - \sum_{F\in S}\big(\{\!\{\nabla\boldsymbol{v}_h\boldsymbol{n}\}\!\},[\![\boldsymbol{\varphi}]\!]\big)_F \\ &\quad - \sum_{F\in S}\big([\![\boldsymbol{v}_h]\!],\{\!\{\nabla\boldsymbol{\varphi}\boldsymbol{n}\}\!\}\big)_F, \\ a^b_{h,S}(\boldsymbol{v}_h,\boldsymbol{\varphi}) &= \sum_{B\in S}\frac{\eta_a}{h}\big(\boldsymbol{v}_h,\boldsymbol{\varphi}\big)_B - \sum_{B\in S}\big(\nabla\boldsymbol{v}_h\boldsymbol{n},\boldsymbol{\varphi}\big)_B - \sum_{B\in S}\big(\boldsymbol{v}_h,\nabla\boldsymbol{\varphi}\boldsymbol{n}\big)_B. \end{aligned}$$

With these bilinear forms the decoupling of the virtual region is realized by choosing

$$\begin{aligned} a_h(\boldsymbol{v}_h,\boldsymbol{\varphi}) &= \sum_{T\in\mathcal{T}_h}\big(\nabla\boldsymbol{v}_h,\nabla\boldsymbol{\varphi}\big)_T + a^f_{h,\Gamma_{I,h}\setminus\Gamma}(\boldsymbol{v}_h,\boldsymbol{\varphi}) \\ &\quad + a^b_{h,\Gamma_{\mathcal{F}}}(\boldsymbol{v}_h,\boldsymbol{\varphi}) + a^b_{h,\Gamma_{\mathcal{O}}}(\boldsymbol{v}_h,\boldsymbol{\varphi}) + a^b_{h,\Gamma_{B,h}}(\boldsymbol{v}_h,\boldsymbol{\varphi}). \end{aligned} \tag{6.2}$$

An example calculation with $RT_2 \times Q_2$ finite elements can be seen in Figure 6.1. The fluid velocity as well as the pressure are zero in the extended region in the middle of the domain. As a result, the fluid flows around the obstacle as intended.

6.2.2 Linear Elasticity

Next, we consider an elastic solid body, where the stress-strain relation is given by Hooke's law, i.e.,

$$\boldsymbol{\sigma}(\boldsymbol{u}) = 2\mu\boldsymbol{\varepsilon}(\boldsymbol{u}) + \lambda\,\mathrm{div}(\boldsymbol{u})\boldsymbol{I}, \qquad \boldsymbol{\varepsilon}(\boldsymbol{u}) = \frac{1}{2}\left(\nabla\boldsymbol{u} + \nabla\boldsymbol{u}^T\right).$$

For a given force $\boldsymbol{f}$ the constitutive equations are prescribed in terms of the displacement $\boldsymbol{u}$ by

$$-\,\mathrm{div}\left(2\mu\boldsymbol{\varepsilon}(\boldsymbol{u}) + \lambda\,\mathrm{div}(\boldsymbol{u})\boldsymbol{I}\right) = \boldsymbol{f} \qquad \text{in } \mathcal{O}, \tag{6.3}$$

where $\mathcal{O}$ is the solid domain. We consider displacement-traction problems, where (6.3) is closed by a combination of a Dirichlet boundary condition $\boldsymbol{g}_D$ on Γ_D, and a zero Neumann boundary condition on Γ_N, i.e.,

$$\boldsymbol{u} = \boldsymbol{g}_D \quad \text{on } \Gamma_D, \qquad\qquad \boldsymbol{\sigma}(\boldsymbol{u})\boldsymbol{n} = \boldsymbol{0} \quad \text{on } \Gamma_N,$$

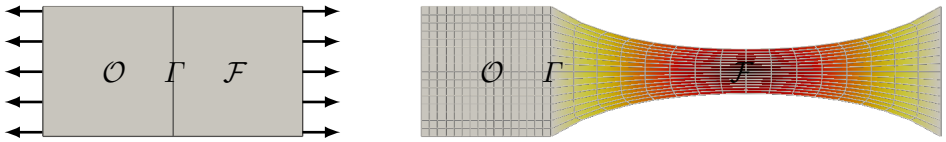

Figure 6.3: Movement of an elastic solid block $\mathcal{O}$ with extension to a virtual region $\mathcal{F}$ via interface constraints. Undeformed state (left), deformed state (right).

on disjoint parts Γ_D and Γ_N of the boundary $\partial\mathcal{O}$ of the solid domain $\mathcal{O}$, for which we assume that $\Gamma_D \cap \Gamma_N = \emptyset$, and $\Gamma_D \neq \emptyset$ to exclude rigid body movements.

Along the Neumann boundary part Γ_N the solid domain $\mathcal{O}$ is extended to a larger domain $\Omega = \mathcal{O} \cup \Gamma \cup \mathcal{F}$, with $\mathcal{O} \cap \mathcal{F} = \emptyset$, such that the interface Γ between $\mathcal{O}$ and $\mathcal{F}$ is part of the Neumann boundary Γ_N, i.e., $\Gamma \subset \Gamma_N$. $\mathcal{F}$ plays the role of a virtual region, that shall not affect the physically meaningful region $\mathcal{O}$. To achieve this, the displacement in $\mathcal{F}$ is prescribed with the same material law as in $\mathcal{O}$, but the boundary conditions are changed to a one-sided continuity condition on Γ, i.e.,

$$\begin{aligned} -\operatorname{div}\left(2\mu\boldsymbol{\varepsilon}(\boldsymbol{u}_{\mathcal{F}}) + \lambda \operatorname{div}(\boldsymbol{u}_{\mathcal{F}})\boldsymbol{I}\right) &= \boldsymbol{f}_{\mathcal{F}} \qquad \text{in } \mathcal{F}, \\ \boldsymbol{u}_{\mathcal{F}} &= \boldsymbol{u} \qquad \text{on } \Gamma. \end{aligned}$$

where $\boldsymbol{u}_{\mathcal{F}}$ denotes the extension of the solid displacement $\boldsymbol{u}$ to the virtual region $\mathcal{F}$. Since the boundary condition on Γ is sufficient to decouple the virtual region from $\mathcal{O}$ without affecting it, the force $\boldsymbol{f}_{\mathcal{F}}$ can be chosen arbitrarily. For example, $\boldsymbol{f}_{\mathcal{F}} = \boldsymbol{0}$, or $\boldsymbol{f}_{\mathcal{F}} = \boldsymbol{f}$, depending on what might be more convenient. To make it clear, the one-sided continuity condition on Γ is prescribed as a combination of the present free Neumann boundary condition on $\Gamma \cap \partial\mathcal{O}$ and a Dirichlet boundary condition on $\Gamma \cap \partial\mathcal{F}$ to assure continuity of the extended phase $\boldsymbol{u}_{\mathcal{F}}$. In summary

$$\begin{aligned} \boldsymbol{\sigma}(\boldsymbol{u})\boldsymbol{n} &= \boldsymbol{0} \qquad \text{on } \Gamma \cap \partial\mathcal{O}, \\ \boldsymbol{u}_{\mathcal{F}} &= \boldsymbol{u} \qquad \text{on } \Gamma \cap \partial\mathcal{F}. \end{aligned}$$

The assembled system matrix expressed in the same setting as in Figure 6.2 is then given

by

$$\begin{pmatrix} * & * & * & * & & \\ * & * & * & * & & \\ * & * & * & * & & \\ * & * & * & * & & \\ & & * & * & * & * \\ & & * & * & * & * \end{pmatrix} \begin{pmatrix} x_0 \\ x_1 \\ x_2 \\ x_3 \\ x_4 \\ x_5 \end{pmatrix} = \begin{pmatrix} f_0 \\ f_1 \\ f_2 \\ f_3 \\ 0 \\ 0 \end{pmatrix}.$$

One can see very clearly that the physically meaningful upper part of the system, corresponding to $\mathcal{D}$, gets solved independently from the extension in the last two rows.

In Figure 6.3, we demonstrate this strategy in a sample calculation with S_2 finite elements. The setting is as shown in the left picture of Figure 6.3 with a Dirichlet boundary condition pulling to the left, a free Neumann boundary condition at the remaining part of $\partial\mathcal{O}$ and an extension to the virtual region $\mathcal{F}$ that is complemented by another Dirichlet boundary condition pulling to the right. The result is as expected, a translation of $\mathcal{O}$ to the left without changing its shape and a deformation of the virtual region that does not affect $\mathcal{O}$.

Note, that if the discretization is realized with a locking free H^{div}-conforming discontinuous Galerkin finite element method, one needs to take care of the correct decoupling of the deformation in the face terms of the interior penalty formulation similar to (6.2), but taking the Neumann boundary into account and prescribing weak boundary conditions only for the deformation in the virtual region.

6.2.3 Simplified Fluid-Structure Interaction Problem

We now combine both approaches in a simplified nonlinear fluid-structure interaction problem,

$$\begin{aligned} -\operatorname{div}\left(\lambda \operatorname{tr}\left(\boldsymbol{\varepsilon}(\boldsymbol{u})\right)\boldsymbol{I} + 2\mu\boldsymbol{\varepsilon}(\boldsymbol{u})\right) &= \mathbf{0} \quad \text{in } Y_s \\ -\operatorname{div}\left(J\left[\nabla \boldsymbol{w}\boldsymbol{F}^{-1} + \left(\nabla \boldsymbol{w}\boldsymbol{F}^{-1}\right)^T\right] - Jp\boldsymbol{F}^{-1}\right) &= \mathbf{0} \quad \text{in } Y_f \\ \operatorname{div}\boldsymbol{w} &= 0 \quad \text{in } Y_f \end{aligned}$$

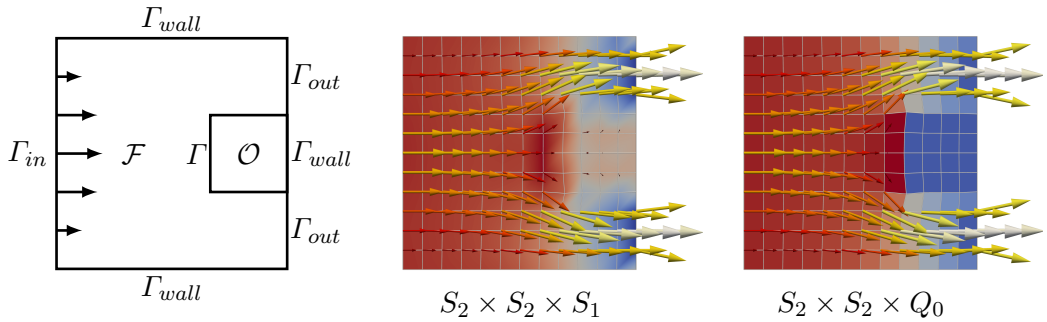

Figure 6.4: Fluid-structure interaction with virtual extensions of fluid velocity and solid displacement. Continuous pressure space (middle), discontinuous pressure space (right).

with interface conditions

$$\boldsymbol{w} = 0 \quad \text{on } \Gamma, \qquad\qquad \boldsymbol{\sigma}_s \boldsymbol{n} = \boldsymbol{\sigma}_f \boldsymbol{n} \quad \text{on } \Gamma,$$

closed by mixed Dirichlet-Neumann boundary conditions as sketched in Figure 6.4, where the solid stress $\boldsymbol{\sigma}_s$ and fluid stress $\boldsymbol{\sigma}_f$ are defined by

$$\begin{aligned} \boldsymbol{\sigma}_s &= \lambda \operatorname{tr}(\boldsymbol{\varepsilon}(\boldsymbol{u}))\, \boldsymbol{I} + 2\mu \boldsymbol{\varepsilon}(\boldsymbol{u}), \\ \boldsymbol{\sigma}_f &= J \left[\nabla \boldsymbol{w} \boldsymbol{F}^{-1} + \left(\nabla \boldsymbol{w} \boldsymbol{F}^{-1} \right)^T \right] - J p \boldsymbol{F}^{-1}. \end{aligned}$$

We need to take care of the pressure component that couples the fluid velocity with the solid displacement, when using continuous inf-sup stable mixed finite element spaces $S_2 \times S_2 \times S_1$. A decoupling by using a discontinuous pressure space Q_0 yields the desired result of a properly decoupled velocity field, as one can see in Figure 6.4.

6.2.4 Performance of the Two-level Schwarz Method

In Table 6.1 we observe the performance of the multiplicative overlapping two-level Schwarz method used as preconditioner for GMRES, where we solve until the starting residual is reduced by a factor of 10^{-8}.

We see that the iteration numbers deteriorate with a refinement of the mesh for the Stokes flow example and the elasticity problem when virtual extensions are used as explained above. If no interface condition is incorporated, the counts are uniform, as can

	Stokes		Elasticity		FSI
h	no interf.	virt. ext.	no interf.	virt. ext.	average
1/8	7	42	6	11	48.0
1/16	8	46	6	13	59.2
1/32	8	44	6	14	72.0
1/64	9	49	6	15	94.0
1/128	9	50	6	16	133.8

Table 6.1: Iteration counts of GMRES preconditioned with a multiplicative two-level Schwarz method applied to Stokes, linear elasticity, and a simplified FSI problem. Without interface incorporated (no interf.), or extended with virtual regions (virt. ext.). Averaged iteration counts for FSI problem.

be seen in the comparison calculations. Moreover, the numbers are much larger when virtual regions are included.

In addition, an example calculation is performed with the fluid-structure interaction problem discretized by $S_2 \times S_2 \times Q_0$ finite element spaces. Due to the nonlinear nature of the model, a Newton method is used to solve the discrete system. Since our focus is on the performance of the preconditioner and to make the results comparable, the iteration counts of GMRES are averaged over the first five Newton steps. The iteration counts are deteriorating corresponding to the previous cases.

This demonstrates that the overlapping two-level Schwarz method cannot be applied out of the box to interface problems occurring in the extension of a domain with a virtual region, which makes a more in-depth investigation of the Schwarz preconditioner necessary in this particular case, which is left as an open task for future research.

6.3 Summary

In this thesis we have successfully applied overlapping two-level and multilevel Schwarz methods as preconditioner to H^{div}-conforming discretizations of Biot's consolidation model and a Biot-Brinkman model. We have proved convergence of the two-level methods and investigated the performance and robustness of the proposed methods in various numerical test scenarios.

Moreover, we have developed a homogenizing two-scale multilevel Schwarz method as

preconditioner for the calculation of a pore-scale porous media flow problem that resolves the microstructure of the medium, i.e., a Stokes flow in a periodically perforated domain.

List of Figures

List of Tables

Bibliography

[ABB+99] E. Anderson, Z. Bai, C. Bischof, S. Blackford, J. Demmel, J. Dongarra, J. Du Croz, A. Greenbaum, S. Hammarling, A. McKenney, and D. Sorensen. *LAPACK Users' Guide*. Society for Industrial and Applied Mathematics, Philadelphia, PA, third edition, 1999.

[ABB12] O. Axelsson, R. Blaheta, and P. Byczanski. Stable discretization of poroelasticity problems and efficient preconditioners for arising saddle point type matrices. *Comput. Visual. Sci.*, 15:191–207, 2012.

[ABF02] D. N. Arnold, D. Boffi, and R. S. Falk. Approximation by quadrilateral finite elements. *Math. Comput.*, 71:909–922, 2002.

[ABF+22] D. Arndt, W. Bangerth, M. Feder, M. Fehling, R. Gassmöller, T. Heister, L. Heltai, M. Kronbichler, M. Maier, P. Munch, J.-P. Pelteret, S. Sticko, B. Turcksin, and D. Wells. The `deal.II` library, version 9.4. *J. Numer. Math.*, 30(3):231–246, 2022.

[AFW97] D. N. Arnold, R. S. Falk, and R. Winther. Preconditioning in $H(\mathrm{div})$ and applications. *Math. Comput.*, 66(219):957–984, 1997.

[AFW98] D. N. Arnold, R. S. Falk, and R. Winther. Multigrid preconditioning in $H(\mathrm{div})$ on non-convex polygons. *Comput. Appl. Math.*, 17(3):303–315, 1998.

[AFW00] D. N. Arnold, R. S. Falk, and R. Winther. Multigrid in $H(\mathrm{div})$ and $H(\mathrm{curl})$. *Numer. Math.*, 85(2):197–217, 2000.

[AFW06] D. N. Arnold, R. S. Falk, and R. Winther. Finite element exterior calculus, homological techniques, and applications. *Acta Numerica*, 15:1–155, 2006.

[AFW10] D. N. Arnold, R. S. Falk, and R. Winther. Finite element exterior calculus: from Hodge theory to numerical stability. *Bull. Amer. Math. Soc. (N.S.)*, 47(2):281–354, 2010.

[AGH+19] J. H. Adler, F. J. Gaspar, X. Hu, C. Rodrigo, and L. T. Zikatanov. Robust block preconditioners for Biot's model. In *Domain Decomposition Methods in Science and Engineering XXIV. DD 2017. Lecture Notes in Computational Science and Engineering*, volume 125, pages 3–16. Springer, Cham, 2019.

[AGLR08] G. Aguilar, F. Gaspar, F. Lisbona, and C. Rodrigo. Numerical stabilization of Biot's consolidation model by a perturbation on the flow equation. *Int. J. Numer. Meth. in Engng.*, 75:1282–1300, 2008.

[AHH+22] J. H. Adler, Y. He, X. Hu, S. Maclachlan, and P. Ohm. Monolithic multigrid for a reduced-quadrature discretization of poroelasticity. *arXiv preprint arXiv:2107.04060v3*, 2022.

[AKW23] T. Almani, K. Kumar, and M. F. Wheeler. Convergence analysis of single rate and multirate fixed stress split iterative coupling schemes in heterogeneous poroelastic media. *Numer. Methods Partial Differential Eq.*, pages 1–25, 2023.

[All91] G. Allaire. Continuity of the Darcy's law in the low-volume fraction limit. *Annali della Scuola Norm. Sup. di Pisa - Classe di Scienze, Serie 4*, 18(4):475–499, 1991.

[All92] G. Allaire. Homogenization and two-scale convergence. *SIAM J. Math. Anal.*, 23(6):1482–1518, 1992.

[Alt06] H. W. Alt. *Lineare Funktionalanalysis*, volume 5. Springer, Berlin Heidelberg, 2006.

[AM97] G. Allaire and A. Mikelić. One-phase Netonian flow. In U. Hornung, editor, *Homogenization and Porous Media*, volume 6 of *Interdisciplinary Applied Mathematics*, chapter 3, pages 45–76. Springer, New York, 1997.

[Arn81] D. N. Arnold. Discretization by finite elements of a model parameter dependent problem. *Numer. Math.*, 37:405–421, 1981.

[Arn82] D. N. Arnold. An interior penalty finite element method with discontinuous elements. *SIAM J. Numer. Anal.*, 19(4):742–760, 1982.

[BBF13] D. Boffi, F. Brezzi, and M. Fortin. *Mixed finite element methods and applications*. Springer Series in Computational Mathematics. Springer, Berlin, Heidelberg, 2013.

[BBN+17] J. W. Both, M. Borregales, J. M. Nordbotten, K. Kumar, and F. A. Radu. Robust fixed stress splitting for Biot's equations in heterogeneous media. *Applied Mathematics Letters*, 68:101–108, 2017.

[BDFM87] F. Brezzi, J. Douglas, M. Fortin, and L. D. Marini. Efficient rectangular mixed finite elements in two and three space variables. *Math. Model. Numer. Anal.*, 21(4):581–604, 1987.

[BDM85] F. Brezzi, J. Douglas, and L. D. Marini. Two families of mixed finite elements for second order elliptic problems. *Numer. Math.*, 47:217–235, 1985.

[Bio35] M. A. Biot. Le problème de la consildation des matières argileuses sous une charge. *Ann. Soc. Sci. Bruxelles*, 55:110–113, 1935.

[Bio41] M. A. Biot. General theory of three-dimensional consolidation. *J. Appl. Phys.*, 12(2):155–164, 1941.

[Bio55] M. A. Biot. Theory of elasticity and consolidation for a porous anisotropic solid. *J. Appl. Phys.*, 26(2):182–185, 1955.

[Bio72] M. A. Biot. Theory of finite deformations of porous solids. *Indiana University Mathematics Journal*, 21(7):597–620, 1972.

[BK81] R. Burridge and J. B. Keller. Poroelasticity equations derived from microstructure. *J. of the acoustical society of America*, 70(4):1140–1146, 1981.

[BKMRB21] W. M. Boon, M. Kuchta, K.-A. Mardal, and R. Ruiz-Baier. Robust preconditioners for perturbed saddle-point problems and conservative discretizations of Biot's equations utilizing total pressure. *SIAM J. Sci. Comput.*, 43(4):B961–B983, 2021.

[Bra93] J. H. Bramble. *Multigrid methods*. Longman Group, UK, 1993.

[Bra13] D. Braess. *Finite Elemente. Theorie, schnelle Löser und Anwendungen in der Elastizitätstheorie*. Number 5 in Masterclass. Springer Spektrum, Berlin Heidelberg, 2013.

[Bre74] F. Brezzi. On the existence, uniqueness and approximation of saddle-point problems arising from Lagrangian multipliers. *ESAIM: Mathematical Modelling and Numerical Analysis - Modélisation Mathématique et Analyse Numérique*, 8(R2):129–151, 1974.

[Bre04] S. C. Brenner. Korn's inequalities for piecewise H^1 vector fields. *Math. Comput.*, 73(247):1067–1087, 2004.

[Bri49] H. C. Brinkman. A calculation of the viscous force exerted by a flowing fluid on a dense swarm of particles. *Appl. Sci. Res.*, 1(27), 1949.

[BRK17] M. Bause, F. A. Radu, and U. Kocher. Space–time finite element approximation of the Biot poroelasticity system with iterative coupling. *Comput. Methods Appl. Mech. Engrg.*, 320:745–768, 2017.

[Bru94] M. L. Brusseau. Transport of reactive contaminants in heterogeneous porous media. *Rev. Geophys.*, 32(3):285–313, 1994.

[BS92] I. Babuška and M. Suri. On locking and robustness in the finite element method. *SIAM J. Numer. Anal.*, 29(5):1261–1293, 1992.

[BW57] M. A. Biot and D. Willis. The elastic coefficients of the theory of consolidation. *J. Appl. Mech.*, 24:594–601, 1957.

[BW05] S. C. Brenner and K. Wang. Two-level additive Schwarz preconditioners for C^0 interior penalty methods. *Numer. Math.*, 102:231–255, 2005.

[Chr68] J. T. Christian. Undrained stress distribution by numerical methods. *J. of the Soil Mechanics and Foundations Division*, 94(6):1333–1245, 1968.

[Cia88] P. G. Ciarlet. *Mathematical elasticity Volume I: Three-dimensional elasticity*, volume 20 of *Studies in mathematics and its applications*. Elsevier Science Publishers B.V., Amsterdam, 1988.

[CKS05] B. Cockburn, G. Kanschat, and D. Schötzau. A locally conservative LDG method for the incompressible Navier-Stokes equations. *Math. Comput.*, 74:1067–1095, 2005.

[CKS06] B. Cockburn, G. Kanschat, and D. Schötzau. A note on discontinuous Galerkin divergence-free solutions of the Navier-Stokes equations. *J. Sci. Comput.*, 31:61–73, 2006.

[Cou04] O. Coussy. *Poromechanics*. John Wiley & Sons Ltd, The Atrium, Southern Gate, Chichester, West Sussex PO19 8SQ, England, 2004.

[CWF16] N. Castelletto, J. A. White, and M. Ferronato. Scalable algorithms for three-field mixed finite element coupled poromechanics. *J. Comp. Phys.*, 327:894–918, 2016.

[CWT15] N. Castelletto, J. A. White, and H. A. Tchelepi. Accuracy and convergence properties of the fixed-stress iterative solution of two-way coupled poromechanics. *Int. J. Numer. Anal. Meth. Geomech.*, 39:1593–1618, 2015.

[Dar56] H. Darcy. *Exposition et application des principes à suivre et des formules à employer dans les questions de distribution d'eau*. Les fontaines publiques de la ville de Dijon. Victor Dalmont, éditeur, Paris, 1856.

[DC93] E. Detournay and A. H.-D. Cheng. Fundamentals of poroelasticity. In C. Fairhurst, editor, *Analysis and Design Methods*, volume 2 of *Comprehensive Rock Engineering: Principles, Practice and Projects*, chapter 5, pages 113–171. Pergamon, Oxford, 1993.

[DFS17] S. Dörsam, E. Friedmann, and J. Stein. Modeling and simulations of drug distribution in the human vitreous. In D. Šimurda and T. Bodnár, editors, *Topical Problems of Fluid Mechanics 2017*, pages 95–102, Prague, 2017.

[DGTZ07] H.-Y. Duan, S.-Q. Gao, R. C. E. Tan, and S. Zhang. A generalized BPX multigrid framework covering nonnested V-cycle methods. *Mathemathics of Computation*, 76(257):137–152, 2007.

[Dob10] M. Dobrowolski. *Angewandte Funktionalanalysis*, volume 2. Springer, Berlin Heidelberg, 2010.

[DTDPP16] P. Druetta, P. Tesi, C. De Persis, and F. Picchioni. Methods in oil recovery processes and reservoir simulation. *Advances in Chemical Engineering and Science*, 6:399–435, 2016.

[DV02] L. Desvillettes and C. Villani. On a variant of Korn's inequality arising in statistical mechanics. *ESAIM: Control, Optimisation and Calculus of Variations*, 8:603–619, 2002.

[DW87] M. Dryja and O. B. Widlund. *An additive variant of the Schwarz alternating method for the case of many subregions.* Technical Report 339, Ultracomputer Note 131. Department of Computer Science, Courant Institute, 1987.

[DW94] M. Dryja and O. B. Widlund. Domain decomposition algorithms with small overlap. *SIAM J. Numer. Anal.*, 15(3):604–620, 1994.

[Ebe03] J. Eberhard. *Upscaling und Mehrgitterverfahren für Strömungen in heterogenen porösen Medien.* Dissertation, Universität Heidelberg, 2003.

[EG10] A. Ern and J.-L. Guermond. *Theory and practice of finite elements.* Applied mathematical sciences. Springer-Verlag, New York, Berlin, Heidelberg, 2010.

[EL93] B. Engquist and E. Luo. Multigrid methods for differential equations with highly oscillatory coefficients. In *The Sixth Copper Mountain Conference on Multigrid Methods*, pages 175–189, 1993.

[Eva10] L. C. Evans. *Partial differential equations.* Graduate studies in mathematics. American Mathematical Society, Providence, RI, 2. ed. edition, 2010.

[EW92] R. E. Ewing and J. Wang. Analysis of the Schwarz algorithm for mixed finite elements methods. *M2AN - Modélisation mathématique et analyse numérique*, 26(6):739–756, 1992.

[EW05] J. Eberhard and G. Wittum. A coarsening multigrid method for flow in heterogeneous porous media. In Björn Engquist, Olof Runborg, and Per Lötstedt, editors, *Multiscale Methods in Science and Engineering*, pages 111–132, Berlin, Heidelberg, 2005. Springer Berlin Heidelberg.

[FB91] M. Fortin and F. Brezzi. *Mixed and hybrid finite element methods*, volume 3. New York: Springer-Verlag, 1991.

[FBG10] M. Ferronato, L. Bergamaschi, and G. Gambolati. Performance and robustness of block constraint preconditioners in finite element coupled consolidation problems. *Int. J. Numer. Methods in Engrg.*, 81:381—-402, 2010.

[FC18] M. Fraldi and A. R. Carotenuto. Cells competition in tumor growth poroelasticity. *J. of the Mechanics and Physics of Solids*, 112:345–367, 2018.

[Fed64] R. P. Fedorenko. The speed of convergence of one iterative process. *USSR Comput. Math. and Math. Phys.*, 4(3):227–235, 1964.

[FK01] X. Feng and O. Karakashian. Analysis of two-level overlapping additive Schwarz preconditioners for a discontinuous Galerkin method. In *Proceedings of the thirteenth international conference on domain decomposition methods*, pages 235–243. DDM.org Press, 2001.

[Flo18] H. Florez. About revisiting domain decomposition methods for poroelasticity. *Mathematics*, 6(10), 2018.

[FWR13] H. Florez, M. F. Wheeler, and A. A. Rodriguez. Domain decomposition methods in geomechanics. *Society of Petroleum Engineers - SPE Reservoir Simulation Symposium*, 2, 2013. SPE-163674-MS.

[GR11] S. Gross and A. Reusken. *Numerical methods for two-phase incompressible flows*. Springer, Berlin Heidelberg, 2011.

[GR17] F. J. Gaspar and C. Rodrigo. On the fixed-stress split scheme as smoother in multigrid methods for coupling flow and geomechanics. *Comput. Methods Appl. Mech. Engrg.*, 326:536–540, 2017.

[GRH+19] F. J. Gaspar, C. Rodrigo, X. Hu, P. Ohm, J. Adler, and L. Zikatanov. New stabilized discretizations for poroelasticity equations. In G. Nikolov, N. Kolkovska, and K. Georgiev, editors, *Numerical Methods and Applications*, pages 3–14, Cham, 2019. Springer International Publishing.

[GW14] M. J. Gander and G. Wanner. The origins of the alternating Schwarz method. In *Domain Decomposition Methods in Science and Engineering XXI*, pages 487–495, 2014.

[HH99] R. Hiptmair and R. H. W. Hoppe. Multilevel methods for mixed finite elements in three dimensions. *Numer. Math.*, 82(2):253–279, 1999.

[Hip96] R. Hiptmair. *Multilevel preconditioning for mixed problems in three dimensions.* Dissertation, Univesität Augsburg, 1996.

[Hip97] R. Hiptmair. Multigrid method for $H(div)$ in three dimensions. *Electronic Transactions on Numerical Analysis*, 6:133–152, 1997.

[HK18] Q. Hong and J. Kraus. Parameter-robust stability of classical three-field formulation of Biot's consolidation model. *Electron. Trans. Numer. Anal.*, 48:202–226, 2018.

[HKK+22] Q. Hong, J. Kraus, M. Kuchta, M. Lymbery, K.-A. Mardal, and M. E. Rognes. Robust approximation of generalized Biot-Brinkman problems. *J. Sci. Comput.*, 93(77), 2022.

[HKLP19] Q. Hong, J. Kraus, M. Lymbery, and F. Philo. Conservative discretizations and parameter-robust preconditioners for Biot and multiple-network flux-based poroelasticity models. *Numerical Linear Algebra with Applications*, 26(4):e2242, 2019.

[HKLP20] Q. Hong, J. Kraus, M. Lymbery, and F. Philo. Parameter-robust Uzawa-type iterative methods for double saddle point problems arising in Biot's consolidation and multiple-network poroelasticity models. *Math. Models Methods Appl. Sci.*, 30(13):2523–2555, 2020.

[HKLW20] Q. Hong, J. Kraus, M. Lymbery, and M. F. Wheeler. Parameter-robust convergence analysis of fixed-stress split iterative method for multiple-permeability poroelasticity systems. *Multiscale Model. Simul.*, 18(2):916–941, 2020.

[HKXZ15] Q. Hong, J. Kraus, J. Xu, and L. Zikatanov. A robust multigrid method for discontinuous Galerkin discretizations of Stokes and linear elasticity equations. *Numer. Math.*, 132:23–49, 2015.

[HL02] P. Hansbo and M. G. Larson. Discontinuous Galerkin methods for incompressible and nearly incompressible elasticity by Nitsche's method. *Comput. Methods Appl. Mech. Engrg.*, 191(17–18):1895–1908, 2002.

[HMH+19] K. Hanser, S. Meggendorfer, P. Hügel, F. Fallenbüchel, H. M. Fahad, and F. Sadlo. Energy-based visualization of 2D flow fields. In *Proceedings of International Conference on Information Visualization Theory and Applications (IVAPP)*, pages 250–258, 2019.

[Hor97] U. Hornung, editor. *Homogenization and Porous Media*, volume 6 of *Interdisciplinary Applied Mathematics*. Springer, New York, 1997.

[HRGZ17] X. Hu, C. Rodrigo, F. J. Gaspar, and L. T. Zikatanov. A nonconforming finite element method for the Biot's consolidation model in poroelasticity. *J. Comput. Appl. Math.*, 310:143–154, 2017.

[HS52] M. R. Hestenes and E. Stiefel. Methods of conjugate gradients for solving linear systems. *J. of Research of the National Bureau of Standards*, 49(6):409–436, 1952.

[HW11] J. S. Howell and N. J. Walkington. Inf–sup conditions for twofold saddle point problems. *Numer. Math.*, 118:663–693, 2011.

[JKY21] M. Jayadharan, E. Khattatov, and I. Yotov. Domain decomposition and partitioning methods for mixed finite element discretizations of the Biot system of poroelasticity. *Comput. Geosci.*, 25:1919–1938, 2021.

[Kel80] J. B. Keller. Darcy's law for flow in porous media and the two-space method. In R. L. Sternberg, editor, *Nonlinear Partial Differential Equations in Engineering and Applied Science*, Lecture Notes in Pure and Appl. Math., pages 429–443. Dekker, New York, 1980.

[KLM17] G. Kanschat, R. Lazarov, and Y. Mao. Geometric multigrid for Darcy and Brinkman models of flows in highly heterogeneous porous media: A numerical study. *J. of Comput. and Appl. Math.*, 310:174–185, 2017. Numerical Algorithms for Scientific and Engineering Applications.

[KM15] G. Kanschat and Y. Mao. Multigrid methods for H^{div}-conforming discontinuous Galerkin methods for the Stokes equations. *J. Numer. Math.*, 23(1):51–66, 2015.

[Kor08] A. Korn. Solution générale du problème d'équilibre dans la théorie de l'élasticité, dans le cas ou les efforts sont donnés à la surface. *Annales de la Faculté des sciences de l'Université de Toulouse pour les sciences mathématiques et les sciences physiques*, 2e série, 10:165–269, 1908.

[KR10] G. Kanschat and B. Riviere. A strongly conservative finite element method for the coupling of Stokes and Darcy flow. *J. of Computational Physics*, 229(17):5933–5943, 2010.

[KR18] G. Kanschat and B. Riviere. A finite element method with strong mass conservation for Biot's linear consolidation model. *J. of Scientific Computing*, 77(3):1762–1779, dec 2018.

[KS14] G. Kanschat and N. Sharma. Divergence-conforming discontinuous Galerkin methods and C^0 interior penalty methods. *SIAM J. Numer. Anal.*, 52(4):1822–1842, 2014.

[Lee16] J. J. Lee. Robust error analysis of coupled mixed methods for Biot's consolidation model. *J. Sci. Comput.*, 69(2):610–632, 2016.

[Lee18] J. J. Lee. Robust three-field finite element methods for Biot's consolidation model in poroelasticity. *BIT Numerical Mathematics*, 58(2):347–372, 2018.

[Lio81] J.-L. Lions. *Some Methods in the Mathematical Analysis of Systems and Their Control*. Science Press, Gordon and Breach, Beijing, New York, 1981.

[LMW17] J. J. Lee, K.-A. Mardal, and R. Winther. Parameter-robust discretization and preconditioning of Biot's consolidation model. *SIAM J. Sci. Comput.*, 39(1):A1–A24, 2017.

[Luo93] E. Luo. *Multigrid method for elliptic equations with oscillatory coefficients*. Phd thesis, UCLA, 1993.

[LWXZ07] Y.-J. Lee, J. Wu, J. Xu, and L. Zikatanov. Robust subspace correction methods for nearly singular systems. *Math. Models Methods Appl. Sci.*, 17(11):1937–1963, 2007.

[LY22] S. Lee and S.-Y. Yi. Locking-free and locally-conservative enriched Galerkin method for poroelasticity. *J. of Scientific Computing*, 94(26), 2022.

[Mal15] V. Malieva. *Mathematical Modelling and Simulations of Brain Cell Swelling Under Ischaemic Conditions.* Dissertation, Universität Heidelberg, 2015.

[Man53] J. Mandel. Consolidation des sols (étude mathématique). *Géotechnique*, 3(7):287–299, 1953.

[Man94] J. Mandel. Hybrid domain decomposition with unstructured subdomains. In Alfio Quarteroni, Jacques Periaux, Yuri A. Kuznetsov, and Olof B. Widlund, editors, *Domain decomposition methods in science and engineering. The Sixth International Conference on Domain Decomposition, June 15-19, 1992, Como, Italy*, volume 157 of *Contemporary mathematics*, pages 103–112. American Math. Soc., Providence, RI, 1994.

[MB07] C. Miehe and C. G. Bayreuther. On multiscale fe analyses of heterogeneous structures: From homogenization to multigrid solvers. *Int. J. Numer. Meth. in Engng.*, 71:1135–1180, 2007.

[MT78] F. Murat and L. Tartar. H-convergence. Séminaire d'Analyse Fonctionnelle et Numérique de l'Université d'Alger 1977/78. English translation in [MT97], 1978.

[MT97] F. Murat and L. Tartar. H-convergence. In A. Cherkaev and R. Kohn, editors, *Topics in the Mathematical Modelling of Composite Materials*, volume 31, pages 21–43. Birkhäuser, Boston, MA, 1997.

[MW13] A. Mikelić and M. F. Wheeler. Convergence of iterative coupling for coupled flow and geomechanics. *Comput. Geosci.*, 17:455–461, 2013.

[MWW14] A. Mikelić, B. Wang, and M. F. Wheeler. Numerical convergence study of iterative coupling for coupled flow and geomechanics. *Comput. Geosci.*, 18:325–341, 2014.

[Ned80] J. C. Nedelec. Mixed finite elements in $\mathbb{R}^3$. *Numer. Math.*, 35:315–341, 1980.

[Ned86] J. C. Nedelec. A new family of mixed finite elements in $\mathbb{R}^3$. *Numer. Math.*, 50:57–81, 1986.

[Neu96] N. Neuß. *Homogenisierung und Mehrgitter*. Dissertation, Universität Heidelberg, 1996.

[Ngu89] G. Nguetseng. A general convergence result for a functional related to the theory of homogenization. *SIAM J. Math. Anal.*, 20:608–629, 1989.

[Ngu90] G. Nguetseng. Asymptotic analysis for a stiff variational problem arising in mechanics. *SIAM J. Math. Anal.*, 21(6):1394–1414, 1990.

[Nit71] J. Nitsche. Über ein Variationsprinzip zur Lösung von Dirichlet-Problemen bei Verwendung von Teilräumen, die keinen Randbedingungen unterworfen sind. *Abh. Math. Semin. Univ. Hamburg*, 36:9–15, 1971.

[NJW01] N. Neuß, W. Jäger, and G. Wittum. Homogenization and multigrid. *Computing*, 66:1–26, 2001.

[NRH19] C. Niu, H. Rui, and X. Hu. A stabilized hybrid mixed finite element method for poroelasticity. *Comput. Geosci.*, 25:757–774, 2019.

[ORB16] R. Oyarzúa and R. Ruiz-Baier. Locking-free finite element methods for poroelasticity. *SIAM J. Numer. Anal.*, 54(5):2951–2973, 2016.

[Phi05] P. J. Phillips. *Finite Element Methods in Linear Poroelasticity: Theoretical and Computational Results*. Phd thesis, The University of Texas at Austin, 2005.

[PS75] C. C. Paige and M. A. Saunders. Solution of sparse indefinite systems of linear equations. *SIAM J. Numer. Anal.*, 12(4):617–629, 1975.

[PW07a] P. J. Phillips and M. F. Wheeler. A coupling of mixed and continuous Galerkin finite element methods for poroelasticity. I. The continuous in time case. *Comput. Geosci.*, 11(2):131–144, 2007.

[PW07b] P. J. Phillips and M. F. Wheeler. A coupling of mixed and continuous Galerkin finite element methods for poroelasticity. II. The discrete-in-time case. *Comput. Geosci.*, 11(2):145–158, 2007.

[PW08] P. J. Phillips and M. F. Wheeler. A coupling of mixed and discontinuous Galerkin finite-element methods for poroelasticity. *Comput. Geosci.*, 12(4):417–435, 2008.

[RGHZ16] C. Rodrigo, F.J. Gaspar, X. Hu, and L.T. Zikatanov. Stability and monotonicity for some discretizations of the Biot's consolidation model. *Comput. Methods Appl. Mech. Engrg.*, 298:183–204, 2016.

[Ric17] T. Richter. *Fluid-structure interactions*, volume 118 of *Lecture Notes in Computational Science and Engineering*. Springer, Cham, 2017.

[RT77] P.-A. Raviart and J. M. Thomas. A mixed method for second order elliptic problems. In I. Galligani and E. Magenes, editors, *Mathematical Aspects of the Finite Element Method*, pages 292—-315. Springer, New York, 1977.

[RTL19] E. Rohana, J. Turjanicová, and V. Lukeš. The Biot-Darcy-Brinkman model of flow in deformable doubleporous media; homogenization and numerical modelling. *Computers & Mathematics with Applications*, 78(9):3044—-3066, 2019.

[Saa03] Y. Saad. *Iterative methods for sparse linear systems*. Society for Industrial and Applied Mathematics, second edition, 2003.

[SBG96] B. F. Smith, P. E. Bjørstad, and W. D. Gropp. *Domain Decomposition*. Cambridge University Press, Cambridge, 1996.

[Sch70] H. A. Schwarz. Über einen Grenzübergang durch alternirendes Verfahren. *Vierteljahrsschrift der Naturforschenden Gesellschaft in Zürich*, 15(3):272–286, 1870.

[Sch99] J. Schöberl. *Robust Multigrid Methods for Parameter Dependent Problems*. Dissertation, Johannes Kepler Universität Linz, 1999.

[Sho00] R. E. Showalter. Diffusion in poro-elastic media. *J. Math. Anal. Appl.*, 251(1):310–340, 2000.

[SMR21] C. Soulaine, J. Maes, and S. Roman. Computational microfluidics for geosciences. *Frontiers in Water*, 3, 2021.

[SP80] E. Sanchez-Palencia. *Non-Homogeneous Media and Vibration Theory*. Lecture Notes in Physics. Springer, Berlin, Heidelberg, 1 edition, 1980.

[SPM15] R. F. Sviercoski, P. Popov, and S. Margenov. An analytical coarse grid operator applied to a multiscale multigrid method. *J. of Comput. and Appl. Math.*, 287:207–219, 2015.

[SS86] Y. Saad and M. H. Schultz. GMRES: a generalized minimal residual algorithm for solving nonsymmetric linear systems. *SIAM J. Sci. Stat. Comput.*, 7(3):856–869, 1986.

[SST03] D. Schötzau, C. Schwab, and A. Toselli. hp-DGFEM for incompressible flows. *SIAM J. Numer. Anal.*, 40:2171–2194, 2003.

[SW69] R. S. Sandhu and E. L. Wilson. Finite element analysis of seepage in elastic media. *J. Eng. Mech. Div.*, 95:641–652, 1969.

[SWZY23] X. Shu, Y. Wu, X. Zhang, and F. Yu. Experiments and models for contaminant transport in unsaturated and saturated porous media – a review. *Chemical Engineering Research and Design*, 192:606–621, 2023.

[Tar78] L. Tartar. Quelques remarques sur l'homogénéisation. In H. Fujita, editor, *Functional Analysis and Numerical Analysis, Proceedings of the Japan-France Seminar 1976*, pages 469–481, Tokyo, 1978. Japan Society for the Promotion of Science.

[Tem84] R. Temam. *Navier-Stokes equations*, volume 2 of *Studies in mathematics and its applications*. Elsevier Science Publishers B.V., North-Holland Amsterdam, New York, Oxford, third (revised) edition, 1984.

[Ter25] K. Terzaghi. *Erdbaumechanik auf bodenphysikalischer Grundlage*. F. Deuticke, Leipzig u. Wien, 1925.

[TPS08] M. Tchonkova, J. F. Peters, and S. Sture. A new mixed finite element method for poro-elasticity. *Int. J. for Numerical and Analytical Methods in Geomechanics*, 32, 2008.

[TW10] A. Toselli and O. Widlund. *Domain decomposition methods - algorithms and theory*. Springer-Verlag, Berlin Heidelberg, 2010.

[VW92] P. S. Vassilevski and J. Wang. Multilevel iterative methods for mixed finite element discretizations of elliptic problems. *Numer. Math.*, 63:503–520, 1992.

[WAK21] J. Witte, D. Arndt, and G. Kanschat. Fast tensor product Schwarz smoothers for high-order discontinuous Galerkin methods. *Comput. Methods Appl. Math.*, 21(3):709–728, 2021.

[WCWZ22] F. Wang, M. Cai, G. Wang, and Y. Zeng. A mixed virtual element method for Biot's consolidation model. *Computers & Mathematics with Applications*, 126:31–42, 2022.

[Wit22] J. Witte. *Fast and Robust Multilevel Schwarz Methods using Tensor Structure for High-Order Finite Elements*. Dissertation, Universität Heidelberg, 2022.

[Xu92] J. Xu. Iterative methods by space decomposition and subspace correction. *SIAM Review*, 34(4):581–613, 1992.

[Yi13] S.-Y. Yi. A coupling of nonconforming and mixed finite element methods for Biot's consolidation model. *Numer. Methods Partial Differential Equations*, 29(5):1749–1777, 2013.

[Yi14] S.-Y. Yi. Convergence analysis of a new mixed finite element method for Biot's consolidation model. *Numer. Methods Partial Differential Equations*, 30(4):1189–1210, 2014.

[Yi17] S.-Y. Yi. A study of two modes of locking in poroelasticity. *SIAM J. Numer. Anal.*, 55(4):1915–1936, 2017.

[Yse93] H. Yserentant. Old and new convergence proofs for multigrid methods. *Acta numerica*, 2:285–326, 1993.

[YYN71] Y. Yokoo, K. Yamagata, and H. Nagaoka. Finite element method apllied to biot's consolidation theory. *Soils and foundations*, 11(1), 1971.

[Žen84] A. Ženíšek. The existence and uniqueness theorem in Biot's consolidation theory. *Aplikace matematiky*, 29(3):194–211, 1984.